Modelling of flow and heat transfer of nanofluids

Satwik Mukherjee

Modelling of flow and heat transfer of nanofluids

Thesis submitted for the award
of the degree of

Doctor of Philosophy

by

Satwik Mukherjee

Under the guidance of

Prof. G. C. Shit

DEPARTMENT OF MATHEMATICS
Jadavpur University
Kolkata- 700032, India

September 2022

Dr. Gopal Chandra Shit
Professor
Department of Mathematics

JADAVPUR UNIVERSITY
188, RAJA S.C. MALLICK ROAD
KOLKATA 700 032, INDIA

CERTIFICATE FROM THE SUPERVISOR

This is to certify that the thesis entitled "Modelling of flow and heat transfer of nanofluids" Submitted by **Sri Satwik Mukherjee** got his name registered on 18-05-2017 for the award of Ph. D. (Science) degree of Jadavpur University, is absolutely based upon his own work under the supervision of Prof. Gopal Chandra Shit and that neither this thesis nor any part of it has been submitted for either any degree / diploma or any other academic award anywhere before.

Gopal Ch. Shit
15/9/2022

(Signature of the Supervisor(s) date with official seal)

Prof. Gopal Chandra Shit
Department of Mathematics,
Jadavpur University, Kolkata - 700032

Dr. Gopal Chandra Shit
Professor
Department of Mathematics
Jadavpur University
Kolkata - 700 032. (India)

Declaration

I certify that,

a. The work contained in this thesis is original and has been done by myself under the guidance of my supervisor.
b. The work has not been submitted to any other institute for any degree or diploma.
c. I have followed the guidelines provided by the institute in preparing the thesis.
d. I have conformed to the norms and guidelines given in the *ethical code of conduct* of the institute.
e. Whenever I have used materials (data, theoretical analysis, and text) from other sources, I have given due credit by citing them in the text of the thesis as well as in the references.
f. Whenever I have quoted written materials from other sources, I have put them under quotation marks and given due credit to the sources by citing them and giving required details in the references. Further, I have taken permission from the copyright owners of the sources, whenever necessary.

Sastwik Mukherji

Signature of the Student

15/09/2022

Dedicated To

My Mother Smt. Jaya Mukherjee

Acknowledgments

I would like to express my sincere gratitude to Prof. Gopal Chandra Shit whom I had the privilege to have as my supervisor. He helped me at a very difficult time in my academic life. I am immensely grateful to him for his support, advice and encouragement. I will always remember his contribution throughout my life.

I would like to thank Gourab Bhattacharya for his valuable advice and many helpful discussions that I have had with him. I am thankful to Prof. Bodhayan Roy for sharing with me his knowledge and wisdom whenever I had the pleasure of meeting him.

I am grateful to all the teachers of the Department of Mathematics, Jadavpur University who have taught me. I would also like to thank all the members and office staffs of Jadavpur University for all their help.

Next, I would like to thank my labmates Susanta Mondal, Subrata Maiti, Amit Mondal, Sreeparna Majee and Pallab Dey.

For the last 5 years or so, Jadavpur University has been my second home where I have met so many wonderful people across various domains. I would like to mention Kaustav Bose, Ranendu Adhikary, Kaushik Chakraborty, Archak Das and Subhadeep Naskar among others with whom I share many beautiful memories that I will treasure forever.

I would like to thank my parents :- Mr. Prabir Kumar Mukherjee and Smt. Jaya Mukherjee and Titam for their unconditional love, blessings and many sacrifices.

Finally, I would like to acknowledge Jadavpur University, Kolkata for their assistance and the Council for Scientific and Industrial Research (CSIR), Government of India for their financial support in the form of research fellowship to carry out this work.

Satwik Mukherjee

Date: 15/09/2022

Satwik Mukherjee

Abstract

Title: Modelling of flow and heat transfer of nanofluids

Index Number: 41/17/Math./25

The present thesis is devoted to the study of heat and mass transfer phenomena in nanofluid flow process by applying semi-analytic and purely analytical methods. A significant part of this thesis is centered around the study of electroosmotic nanofluid flow in a micro-nano channel. The study considers the presence of an external magnetic field with an aim to analyze entropy generation. The semi-analytical methods such as differential transform method and homotopy analysis method have been utilised to solve the fluid flow problems. The selected problems in the thesis bear potential applications in plastic extrusion process and building microfluidic devices. The entire thesis is divided into eight chapters as described below:

The **Chapter 1** is an introductory section that briefly discusses the numerical methods and topics concerned with the problems considered in subsequent chapters in this thesis. This chapter also defines and presents an overview of the properties and terminology used in this thesis such as heat and mass transfer phenomena, electroosmosis, magneto-hydrodynamic flow and basic ideas on entropy generation.

The **Chapter 2** presents the effects of ion diffusion coefficient on steady electroosmotic couple stress nanofluid flow and heat transfer in a porous microchannel bounded by two permeable beds. The study considers the nanofluid injection process through porous beds. The combined effects of ion diffusivity and injected nanofluid velocity on EDL (Electric double layer) thickness are analytically expressed. The differential transform method (DTM) is used to solve the flow equations. The DTM solution is then compared with the exact analytical solution of velocity, Zeta potential function. Moreover, a square averaged residual analysis is conducted. The bulk nanofluid flow rate is found to follow a quadratic like relationship with the couple stress parameter. The nanofluid temperature is found to increase with an enhancement of ion diffusion coefficient, which is related with experimental results observed by Kong et al. (Phys. Chem. Chem. Phys. 19 (2017) 7678) for NaCl electrolyte solution confined in a graphene nanochannel. Moreover, the nanofluid temperature decreases with enhancement of both porous permeability of the medium and couple stress parameter.

The **Chapter 3** aims to study the electroosmotic nanofluid flow and heat transfer phenomena in a microchannel with porous walls by paying due attention to the interaction of the injected fluid velocity and the net charge density in the base fluid on the development of Zeta potential and electroosmotic slip velocity. The novelty of this study is to obtain the integral expression for electroosmotic slip velocity which is found to converge to Smoluchowski velocity when the injected fluid velocity is low and porous permeability of the channel wall becomes negligible. Under a weak electric field condition, the enhancement of pressure gradient is found to increase the normalized temperature and decrease the normalized nanoparticle concentration. The bulk

nanofluid temperature is found to follow an almost quadratic relationship with applied pressure gradient. Additionally, in the absence of injection velocity, we observed a new expression for Soret number as a ratio of the cross sectional nanoparticle concentration to the Joule heating parameter.

In **Chapter 4**, we examine the pulsating electroosmotic nanofluid flow phenomena in a microchannel with porous walls. The combined effects of injected nanofluid velocity and ion diffusion coefficients on the Zeta potential formation is considered. The novel boundary condition is introduced so as to examine the effects of electroosmotic parameters and frictional forces on thermal profiles as well as nanoparticle volume fractions present in the nanofluid.

In **Chapter 5**, we study the magnetohydrodynamic graphene-(PDMS) nanofluid flow between two squeezing parallel plates in the presence of thermal radiation effects. The energy efficiency of the system via the Bejan number is studied extensively. The entropy generation in terms of the Bejan number, the coefficient of skin-friction, and the heat transfer rate is furthermore investigated under the effects of various physical parameters of interest. The present study shows that the entropy generation due to frictional forces is higher than that of due to thermal effects. Thus, the study bears the potential application in powder technology as well as in biomedical engineering.

The **Chapter 6** examines the energy efficiency of the squeezing Cu-water nanofluid flow that takes place within two parallel plates having externally applied magnetic field. The effects of thermal radiation are taken into account. The non-linear partial differential equations are converted into a set of coupled ordinary differential equations by the self-similarity transformations. The differential transform method (DTM) is used to solve the set of coupled differential equations, which gives rise to a series solution. The convergence analysis has been made and two theorems are presented to confirm the validity of the obtained series solution.

The **Chapter 7** investigates the unsteady Maxwell nanofluid flow past a stretching surface, embedded in a porous medium, in the presence of magnetic field and thermal radiation effects. The Navier's slip boundary condition is considered at the nanofluid-surface interface. Entropy analysis for the energy efficiency of the system in terms of the Bejan number is carried out extensively. By employing suitable similarity transformations on the set of partial differential equations; describing the flow regimes, we have transformed them into a set of coupled ordinary differential equations. These transformed equations are then solved by using the homotopy analysis method (HAM). The findings show that the rise in time relaxation parameter has adverse effects on nanofluid velocity but enhances the entropy generation in the system.

Finally, the **Chapter 8** summarizes the overall important findings of the thesis and discusses the future scope of research in this direction.

Gopal Ch. Shit
15.9.2022

Dr. Gopal Chandra Shit
Professor
Department of Mathematics
Jadavpur University
Kolkata - 700 032. (India)

Satwik Mukherjee
15/09/2022

Contents

List of Symbols and Abbreviations

Nomenclature

Symbols	Definition
$(u,\ v)$	The velocity components along x and y directions
h	Channel height
Ve	The velocity component along y-direction
t	Time
ρ	Density
p	Hydro-static pressure
e	Charge of proton
$\zeta_{1,2}$	Electrical Potential at the walls
ρ_e	Charge density
E_0	Electric field strength
ν	Kinematic viscosity
K_B	Boltzmann Constant
η_0	Ion density
T	Temperature
z	Valency of ions
ϵ_0	Permittivity of the free space
σ	Electrical Conductivity
Ec	Eckert number
k	Thermal Conductivity
μ	Dynamic Viscosity
C	Nanoparticle Concentration
$\tilde{k}$	Dielectric Constant
ψ	Electrical potential distribution
C_p	Specific heat
α	Material parameter, Plate squeezing rate, Stretching rate
u_{ref}	Reference velocity
$k_{1,2}$	Porous permeability
u_p	Velocity through porous bed
O_+	Surface limit point

Symbols	**Definition**
$u_{B_{1,2}}$	Slip velocity
$\phi^*_{1,2}$	Boundary deposition parameter
M	Molar mass
C_{ref}	Reference concentration
D_B	Brownian Diffusion Coefficient
D_T	Thermophoretic Diffusion Coefficient
D	Ion Diffusion Coefficient
R_D	Diffusive Reynolds number
Re	Reynolds number
M_D	Molecular diffusivity parameter
$\kappa,\ m$	Electroosmotic Parameter
λ_D	Debye Length
Sc	Schmidt number
S_t	Soret number
Pr	Prandtl number
$\gamma,\ \Gamma$	Joule heating parameter in context of electroosmotic flow
$\Phi,\ \Phi_1$	Non dimensional Zeta potential distribution
Π	Pressure parameter
Q	Flow rate
E_{Total}	Total entropy generation
θ_{bulk}	Bulk temperature
f_{bulk}	Bulk concentration
$\tilde{U}_{HS}$	Electroosmotic slip velocity
U_{HS}	Smoluchowski velocity
T_{av}	Average nanofluid temperature
$n^{\pm}$	Density of positive/negative ions
N_A	Avogadro number
η	Couple stress viscosity coefficient
ϵ	Permittivity of the medium
k_p	Porous permeability of the medium
S	Sensitivity parameter, Squeeze number
λ	material parameter in context of electroosmotic flow
L_i	dimensionless porous permeability parameter
γ	Inverse couple stress parameter
Br	Brinkman number
δ	Temperature ratio parameter
δ_1	Fractional ratio parameter
χ_1	Mass transfer parameter
$\phi_{1,2}$	Deposition parameter at beds
Da	Inverse Darcy number
$Z_{1,2}$	Dimensionless Zeta potential
$f^{'}$	Dimensionless velocity

Nomenclature

Symbols	Definition
d_L	electric double layer thickness near lower microchannel wall
$A,\ B$	steady and unsteady parts of the pressure gradient
ω	frequency
F_r	time dependent viscous drag force
λ_1	proportionality constant, relaxation time
$\tilde{\omega}$	Womersley number
b	frictional constant
$\mathcal{N}(x) = 0$	Non-linear ODE
B_0	Magnetic field
$\rho_f,\ \rho_{nf}$	density of base fluid or nanofluid
ρ_s	density of solid nanoparticles
μ_{nf}	coefficient of dynamic viscosity of nanofluid
ν_f, ν_{nf}	coefficient of kinematic viscosity
k_{nf}	thermal conductivity of the nanofluid
k_f	thermal conductivity of the base fluid
k_s	thermal conductivity of the nanoparticles
σ	Electrical conductivity
$(\rho C_p)_f,\ (\rho C_p)_{nf}$	effective heat capacity of the fluid and nanofluid
q_r	Radiative heat flux
σ_1	Stefan-Boltzmann constant
k_1	Mean absorption coefficient
T_H	Plate temperature
ϕ	Volume fraction of the nanoparticle
M	Magnetic number
De	Deborah number
R	Radiation parameter
C_f	Coefficient of skin-friction
Nu	Nusselt number
$E_S,\ N_S$	Dimensionless total entropy generation
$N_{ST},\ N_{SFF}$	Entropy generation due to thermal effects and friction
Be	Bejan number
q'''	Heat source/sink term
h_f	Convective heat transfer coefficient
U_w	Velocity at the sheet
T_w	Temperature at the sheet
u_∞	Free stream velocity
T_∞	Free stream temperature
Bi	Biot number
N	Navier slip coefficient
Re_x	Local Reynolds number
S_{Total}	Entropy generation rate per unit volume

Symbols	**Definition**
m	mass of the fluid medium
$S(t)$	Surface area
$\tau(t)$	volume of a closed medium
$\vec{v}$	velocity vector
$\vec{f_b}$	body force per unit volume
(f_x, f_y, f_z)	component of body force along x, y and z axis
$\bar{\bar{\sigma}}$	stress tensor
$\vec{F_e}$	total external body force
$\vec{F_\sigma}$	total surface force
τ	shear stress
$\vec{S}$	Cauchy stress tensor
$\vec{E}$	electric field vector
$\vec{j}$	total current density
h_x	local heat transfer coefficient
$\vec{q}$	heat flux
E	total energy per unit volume
q	reference fluid pressure
J_A	molar flux
D_{AB}	the mass diffusivity of A in B
x_A	mole fraction of A in the mixture
$\vec{\tau}$	deviatoric extra tensor
u^*, v^*, p^*, x^*, y^*	dimensionless form of the corresponding variables
δ_{99}	overall boundary layer thickness
δ^*	displacement thickness
δ^{**}	momentum thickness
$\sigma_{xx}, \sigma_{yy}, \sigma_{zz},$	normal stresses
$\tau_{yx},\ \tau_{zx}$	tangential stresses
τ_{xx}	normal viscous stress component
Φ	dissipative function
$\dot{W}$	rate of work done
$\dot{H}$	rate of heat generation

Chapter 1

Introduction

1.1 Introduction

Fluid mechanics plays an integral role behind the developments of most of the modern state of the art scientific technology. It describes the physical laws of motion for fluid particles. Starting from the flow dynamics in cellular organisms to complex ocean and climate dynamics along with the majority of the technological applications in this real world are accomplished by studying the fundamental fluid flow equations. Scientists across every field, engineers and even modern films, entertainment industry have keen interest in the study of fluid mechanics to improve their respective domain of expertise. Many basic idea of physics have emerged from the understanding of the fluid flow equations. Since time immemorial, people have been interested to know, how the birds fly, what originates the ocean waves that don't repeat again, how the fish swims beneath the deep sea to the modern queries of how a rocket goes up, what factors make a cricket ball swing, and all these questions can be answered at least partially from the knowledge of fluid flow mechanics which is the theme of this thesis.

The fundamental equations describing the fluid flow dynamics follows a set of highly nonlinear equations aka the "Navier Stokes Equations". This non-linearity and chaotic nature of the solutions obtained from these equations has made this subject so challenging that the Millennium Prize is associated with this field of science as declared by the Clay Mathematical Research Institute in May, 2000. Now a days, with the advancement of the computers and new computational techniques, numerical methods have become the principal tool that is used mostly to tackle the situation. On the contrary, there have been serious efforts made by mathematicians to develop new and useful analytical techniques that can serve as alternatives to known computational methods. However, the need for new mathematical techniques as well as novel experiments will always remain the utmost importance for the development of this subject as well as the study of any other discipline of applied sciences.

1.2 Fluid Flow Equations

The fluid flow dynamics is governed by a set of mathematical equations in terms of different flow variables. These equations describe the physical conservation laws for the mass and motion of fluid particles. These laws are presented below.

1.2.1 The Continuity Equation

The continuity equation (also known as transport equation) is a statement about the mass conservation principle. It says that, inside a closed immovable control volume, the rate of change in fluid mass equals to the same amount of mass that goes out of the control volume through its boundary surface. From the conservation of mass principle we get,

$$\frac{dm}{dt} = \frac{d}{dt}\int_{\tau(t)} \rho d\tau = 0, \tag{1.1}$$

where m denotes the fluid mass, ρ the density of the fluid, $\tau(t)$ the arbitrary control at time t. We know that, $d\tau = (\vec{v}.\vec{n})dS$. Thus, applying the Reynolds transport theorem we get,

$$\frac{d}{dt}\int_{\tau(t)} \rho d\tau = \int_{\tau(t)} \frac{\partial \rho}{\partial t} d\tau + \int_{S(t)} \rho(\vec{v}.\vec{n})dS = \int_{\tau(t)} \Big[\frac{\partial \rho}{\partial t} + div(\rho\vec{v})\Big] d\tau = 0, \tag{1.2}$$

where $S(t)$ denotes the bounded closed surface of the control volume. The above volume integral is zero for any arbitrary volume $\tau(t)$ thereby making $\frac{\partial \rho}{\partial t} + div(\rho\vec{v})$ equals to zero everywhere in the flow field. Therefore,

$$\frac{\partial \rho}{\partial t} + \rho\ div(\vec{v}) = 0. \tag{1.3}$$

The equation 1.3 is known as the continuity equation. For incompressible fluid, i.e. when fluid density does not vary with time t:

$$\rho = constant,$$

the continuity equation becomes,

$$div(\vec{v}) = 0. \tag{1.4}$$

1.2.2 The Momentum Equation

The momentum equations were formulated by M. Navier and G.G. Stokes. The conservation principle of linear momentum is used to obtain these set of equations. The statement goes like this: in a closed immovable control volume, the rate of change

of the linear momentum is same as the sum of the external force components acting on the volume,

$$\frac{D}{Dt}\int_{\tau(t)}(\rho\vec{v})d\tau = \Sigma\ body\ forces + \Sigma\ surface\ forces. \tag{1.5}$$

From the above equation, we further get,

$$\int_{\tau(t)}\rho\Big[\frac{\partial\vec{v}}{\partial t} + (\vec{v}.\vec{\nabla})\vec{v}\Big]d\tau = \vec{F}_e + \vec{F}_\sigma, \tag{1.6}$$

where $\frac{D}{Dt}$ denotes the material derivative, $\vec{F}_e$ the external forces acting on fluid and $\vec{F}_\sigma$ the net force caused due to stress tensor $\bar{\bar{\sigma}}$.
We know that, $\vec{F}_\sigma = -\int_{S(t)}(\vec{n}.\bar{\bar{\sigma}})dS = -\int_{\tau(t)}(\vec{\nabla}.\bar{\bar{\sigma}})d\tau$. Let $\vec{f}_b$ denotes the body force per unit volume. Then, (1.6) takes the form,

$$\frac{\partial\vec{v}}{\partial t} + (\vec{v}.\vec{\nabla})\vec{v} = \rho\vec{f}_b - \vec{\nabla}.\bar{\bar{\sigma}}. \tag{1.7}$$

In the Cartesian coordinate system, the above equation takes the form:

$$\rho(\frac{\partial u}{\partial t} + u\frac{\partial u}{\partial x} + v\frac{\partial u}{\partial y} + w\frac{\partial u}{\partial z}) = \rho f_x - \frac{\partial\sigma_{xx}}{\partial x} - \frac{\partial\tau_{xy}}{\partial y} - \frac{\partial\tau_{xz}}{\partial z}, \tag{1.8}$$

$$\rho(\frac{\partial v}{\partial t} + u\frac{\partial v}{\partial x} + v\frac{\partial v}{\partial y} + w\frac{\partial v}{\partial z}) = \rho f_y - \frac{\partial\tau_{yx}}{\partial x} - \frac{\partial\sigma_{yy}}{\partial y} - \frac{\partial\tau_{yz}}{\partial z}, \tag{1.9}$$

$$\rho(\frac{\partial w}{\partial t} + u\frac{\partial w}{\partial x} + v\frac{\partial w}{\partial y} + w\frac{\partial w}{\partial z}) = \rho f_z - \frac{\partial\sigma_{zx}}{\partial x} - \frac{\partial\tau_{zy}}{\partial y} - \frac{\partial\sigma_{zz}}{\partial z}. \tag{1.10}$$

where $\vec{f}_b = (f_x, f_y, f_z)$, $\vec{v} = (u, v, w)$ and

$$\bar{\bar{\sigma}} = \begin{pmatrix} \sigma_{xx} & \tau_{xy} & \tau_{xz} \\ \tau_{yx} & \sigma_{yy} & \tau_{yz} \\ \tau_{zx} & \tau_{zy} & \sigma_{zz} \end{pmatrix}.$$

The expressions for the stress tensor $\bar{\bar{\sigma}}$ differs for the Newtonian and Non Newtonian fluids.

1.2.3 The Energy Equation

The principle of conservation of energy is used to calculate fluid temperature distribution in a system. The first law of thermodynamics is used to obtain this equation, which reads:

- Rate of change of energy with time = Heat source/sink added + Rate of work done by/on the system

This law is described below,

$$\rho\frac{DE}{Dt}\Delta x\Delta y\Delta z = \Sigma\dot{Q} + \Sigma\dot{W}, \tag{1.11}$$

where E denotes the total energy, $\Sigma\dot{Q}$ the rate of heat added in the control volume, $\Sigma\dot{W}$ the net rate of work done by the surface force on fluid. The rate of work done in the x direction by fluid with velocity u inside a control volume element with volume $\Delta x\Delta y\Delta z$ equals to the product of the velocity component u and the surface forces σ_{xj}. We obtain the following expression for this term as,

$$\Sigma\dot{W} = \Delta x\Delta y\Delta z\Big[\frac{\partial(u\sigma_{xx})}{\partial x} + \frac{\partial(v\sigma_{yy})}{\partial y} + \frac{\partial(w\sigma_{zz})}{\partial z} + \frac{\partial(u\sigma_{yx})}{\partial y} + \frac{\partial(u\sigma_{zx})}{\partial z} + \frac{\partial(u\sigma_{xy})}{\partial x} + \frac{\partial(v\sigma_{zy})}{\partial z} + \frac{\partial(w\sigma_{xz})}{\partial x} + \frac{\partial(w\sigma_{yz})}{\partial z}\Big]. \tag{1.12}$$

Now, we would like to add the energy fluxes to our system. Let q_x, q_y, q_z denote the fluxes in the x, y, z direction respectively. Then the rate of heat added to the fluid control volume takes the following form,

$$\Sigma\dot{Q} = -\Delta x\Delta y\Delta z\Big[\frac{\partial q_x}{\partial x} + \frac{\partial q_y}{\partial y} + \frac{\partial q_z}{\partial z}\Big]. \tag{1.13}$$

From the Fourier's law of heat conduction we get,

$$\vec{q} = -k\nabla T \tag{1.14}$$

where k is the thermal conductivity. We finally express the surface forces as follows,

$$\begin{aligned}\sigma_{xx} &= -p + \tau_{xx},\\ \sigma_{yy} &= -p + \tau_{yy},\\ \sigma_{zz} &= -p + \tau_{zz}.\end{aligned} \tag{1.15}$$

where p denotes the normal pressure and τ_{xx}, τ_{yy} and τ_{zz} the normal viscous stress components acting perpendicular on the control volume. After substituting the above terms along with the expression 1.13 into 1.11, we get,

$$\rho\frac{DE}{Dt} = \frac{\partial}{\partial x}\Big[k\frac{\partial T}{\partial x}\Big] + \frac{\partial}{\partial y}\Big[k\frac{\partial T}{\partial y}\Big] + \frac{\partial}{\partial z}\Big[k\frac{\partial T}{\partial z}\Big] - \frac{\partial(up)}{\partial x} - \frac{\partial(vp)}{\partial y} - \frac{\partial(wp)}{\partial z} + \Phi, \tag{1.16}$$

where Φ represents a dissipation function denoting a source of energy due to drag forces acting on fluid flow. The expression of Φ is given below,

$$\Phi = \frac{\partial(u\tau_{xx})}{\partial x} + \frac{\partial(u\tau_{yx})}{\partial y} + \frac{\partial(u\tau_{zx})}{\partial z} + \frac{\partial(v\tau_{xy})}{\partial x} + \frac{\partial(v\tau_{yy})}{\partial y} + \frac{\partial(v\tau_{zy})}{\partial z} + \frac{\partial(w\tau_{xz})}{\partial x} + \frac{\partial(w\tau_{yz})}{\partial y} + \frac{\partial(w\tau_{zz})}{\partial z}.$$

1.2.4 Classification of Fluids

The fluid can be broadly classified in terms of its viscous nature. An incompressible fluid with neither viscosity nor surface tension is termed as inviscid fluid or ideal fluid. However, most of the fluid in nature has certain amount of viscosity and can be again classified into two categories,

- Newtonian fluids
- Non-Newtonian fluids

1.2.4.1 Newtonian fluid models

Internal friction between adjacent fluid layers is the root cause of viscosity. Viscosity measures the cohesive nature of a fluid. The fluid with a high viscosity opposes shear stress. The Newtonian fluid follows the principle that shear stress for a fluid across a plane is proportional to its velocity gradient. This statement is described below,

$$\tau = \mu \frac{du}{dy}, \tag{1.17}$$

where τ denotes the shear stress, du the change in fluid velocity, dy the change of distance dy and μ, a proportionality constant. The term, τ is called the dynamic viscosity coefficient.

1.2.4.2 Non Newtonian fluid models

There are fluids that do not follow the linear relationship between shear stress and the rate of strain. Some examples of such fluids are presented below,
(i) Power Law Fluid Model: The stress-strain relationship for a Power law fluid follows the following relation of the form:

$$\tau = \mu(\dot{\gamma})^n, \tag{1.18}$$

where τ denotes the shear stress, $\dot{\gamma}$ the rate of shear strain and n the power law index. We call a fluid dilatant if $n > 1$ and pseudoplastic if $n < 1$.
(ii) Bingham Plastic Fluid Model: This fluid model follows the following relation:

$$\begin{aligned} \tau &= \mu\dot{\gamma} + \tau_0; \quad \tau \geq \tau_0 \\ \dot{\gamma} &= 0; \qquad\qquad \tau < \tau_0, \end{aligned} \tag{1.19}$$

where τ_0 is called the minimum yield stress.
(v) Maxwell Fluid Model: Several polymer materials such as Polydimethylsiloxane follows the Maxwell fluid behaviour as described below,

$$\mathbf{T_1} + \lambda_1 \hat{T_1} = -2\mu\mathbf{D}, \tag{1.20}$$

Table 1.1: Values of material properties of PDMS, Water, Cu, Graphene.

Physical properties	PDMS	Water	Cu	Graphene
$\rho \ \ (Kg/m^3)$	816	997.1	8933	2250
$C_p \ \ (J.Kg^{-1})$	2000	4179	385	710
$k \ \ (W.m^{-1}.K^{-1})$	0.15	0.613	401	3000
$\sigma \ \ (S/m)$		5.5×10^{-6}	59.6×10^6	

where λ_1 represents relaxation time, D the Rivlin-Ericksen tensor given by $\mathbf{D} = \frac{1}{2}(\nabla V + (\nabla V)^T)$, T_1 the stress tensor and $\hat{T_1}$ its upper-convected time derivative, which is expressed as,

$$\hat{T_1} = \frac{D}{Dt}T_1 - (\nabla V)^T \cdot T_1 - T_1 \cdot (\nabla V),$$

where $\frac{D}{Dt}$ is the material derivative. The term $\lambda_1 = 0$ reduces it to the Newtonian model.

1.2.4.3 Nanofluid

Nanofluid is a homogenous mixture of a base fluid with the nano-sized particles. Choi and Eastman [1995] first suggested the concept of nanofluid and experimentally verified that the augmentation of small amount of nanoparticles into the fluid increases the heat transfer capacity of the fluid. Angayarkanni and Philip [2015] provided a review article on nanofluids. Their survey include different techniques of preparing nanofluids, stability conditions of nanofluids, different methods of measuring the thermal conductivity of nanofluids. They discussed the thermal properties of nanofluids based on various experimental results. The study of nanofluid flow between two squeezing plates is an important topic of research in the recent years because of its many engineering and industrial applications. For example, the external magnetic field is applied to resist the deviation of the lubrication viscosity in some engineering cases. Nanofluids are also used as coolants in nuclear reactors, radiation therapy, geothermal energy extraction. It has wide range of applications in polymer processing, injection modeling, load capacity related problems in many mechanical systems. In this thesis, we have utilized Cu and Graphene as nanoparticles, and the base fluids are taken as Newtonian as well as non-Newtonian fluids. The Table 1.1 provides the physical values of Cu, graphene, water and polydimethylsiloxane (PDMS).

1.3 Magnetohydrodynamics

The MHD or magnetohydrodynamics studies the motion of an electrically conducting fluid in the presence of a magnetic field. It has immense applications in the field

of biological fluid flow such as blood flow, plasma flow, liquid metal processing etc. Presently, the biggest nuclear reactor, called the TOKAMAK is built on the principles of MHD. The foundation of the MHD is based on the consideration of Lorentz force, which says that when a charged fluid particle move in a magnetic field of strength $\vec{B}$ and an electric field $\vec{E}$ with charge q and velocity $\vec{v}$, then it experiences a force $\vec{f}$, which is given by,

$$\vec{f} = q\vec{E} + q\vec{E'} + q\vec{v} \times \vec{B}, \tag{1.21}$$

where $\vec{E}$ represents the electrostatic field, $\vec{E'}$ the induced electric field by changing magnetic field and the last term is due to the Lorentz force. In the absence of an electric field $\vec{E}, \vec{E'} = 0$, the force for a charge becomes,

$$\vec{F} = q\vec{v} \times \vec{B} = \vec{j} \times \vec{B}, \tag{1.22}$$

where $\vec{j}$ is the current density. The MHD Navier-Stokes equation can be expressed as follows,

$$\rho \frac{D\vec{v}}{Dt} = \vec{F} - \nabla p + \rho\nu\nabla^2\vec{v}, \tag{1.23}$$

where $\frac{D}{Dt} = \frac{\partial}{\partial t} + (\vec{v}.\vec{\nabla})$ represents the material derivative, ρ the fluid density, $\vec{F}$ the body force per unit volume, p the fluid pressure, $\vec{v}$ the fluid velocity and ν the kinematic coefficient of viscosity. In the relativistic analogy, with a moving reference frame for a charged particle, the electromagnetic force experienced by it can be viewed as a electric field force E'', which can be expressed below,

$$\vec{E''} = \vec{E} + \vec{v} \times \vec{B}. \tag{1.24}$$

Thus, the current produced by this field will be of the form,

$$\vec{j_c} = \sigma\vec{E''} = \sigma(\vec{E} + \vec{v} \times \vec{B}). \tag{1.25}$$

Additionally, we can also assume the current due to ions is present in the fluid as,

$$\vec{j'} = \rho_e\vec{v}, \tag{1.26}$$

where ρ_e is the charge density. Thus the total current density in the fluid is equal to

$$\vec{j} = \vec{j_c} + \vec{j'} = \sigma(\vec{E} + \vec{v} \times \vec{B}) + \rho_e\vec{v}. \tag{1.27}$$

For an electrically neutral fluid, $\rho_e = 0$, we get,

$$\vec{j} = \vec{j_c} + \vec{j'} = \sigma(\vec{E} + \vec{v} \times \vec{B}). \tag{1.28}$$

In the absence of an external electric field $\vec{E}$, the Navier-Stoke's equation reduces to,

$$\rho \frac{D\vec{v}}{Dt} = \rho\vec{g} + \vec{j} \times \vec{B} - \nabla p + \rho\nu\nabla^2\vec{v}. \tag{1.29}$$

$$\nabla.\vec{v} = 0 \tag{1.30}$$

$$\nabla \times \vec{E} = -\frac{\partial \vec{B}}{\partial t}, \tag{1.31}$$

$$\nabla \times \vec{B} = \vec{j}, \nabla \cdot \vec{j} = 0 \quad and \quad \nabla \cdot \vec{B} = 0. \tag{1.32}$$

1.4 Electroosmotic Flow

In general, it is observed that an externally applied electric field induces an electroosmotic fluid flow in a microchannel, apart from the pressure difference. A thin charged layer (known as electric double layer or EDL), formed near the channel walls due to ion separation, starts to migrate under the influence of an applied electric field. The fluid-channel interface exhibits trapped charges in the channel wall and consequently attracts oppositely charged ions present in the fluid. Far away from the wall, the fluid is assumed to have a zero net charge. The charged fluid in the EDL layer starts to move when an electric field is applied and consequently drags the fluid layers adjacent to the edge of the EDL.

1.4.1 Zeta Potential Distribution

The electric potential distribution in a microchannel is described by the Poisson equation (Ranjit and Shit [2017]) as,

$$\frac{\partial^2 \psi}{\partial y^2} = -\frac{\rho_e}{\epsilon}, \tag{1.33}$$

where ψ denotes the electric potential distribution, ρ_e the net charge density, ϵ the permittivity of the medium. The $1:1$ symmetric electrolyte is assumed for our study. The net charge density (Ranjit and Shit [2017]) has the following expression,

$$\rho_e = ezN_A(n^+ - n^-), \tag{1.34}$$

where, e denotes the electron charge, z the valence of the ions, N_A the Avogadro number and $n^{\pm}$ the average number of positive/negative ions. The electroosmotic hydrodynamic flow equations can be expressed as,

$$\rho \frac{D\vec{v}}{Dt} = \vec{F} - \nabla p - \rho_e \nabla \psi + \rho \nu \nabla^2 \vec{v}, \tag{1.35}$$

$$\nabla \cdot \vec{V} = 0. \tag{1.36}$$

This kind of fluid flow has enormous applications in biomedical engineering such as building micro and nano fluidic devices.

1.5 Heat-Mass Transfer and Entropy generation

1.5.1 Heat Transfer

The heat transfer phenomena is an important event in an engineering system. To make a system energy efficient, it is required to consume the supplied energy efficiently so that the loss due to irreversible heat transfer diminish. There are different physical

mechanisms how heat get transferred from one part of the body to another. Some of these physical process are described below.

Conduction

By the conduction heat transfer process heat gets transferred in a stationary body due to temperature gradient, without the movements of the fluid particles. The Fourier's law governs this phenomena by the following statement,

$$\vec{q} = -k\nabla T. \tag{1.37}$$

where k is called the thermal conductivity of the medium. It says that the heat transfer rate in normal direction is proportional to the temperature gradient present in that direction.

Convection

By the convection heat transfer process heat gets transmitted by the motion of fluid particles from the higher temperature zone to a lower temperature region. This process is prevalent when a fluid comes in the presence of a hotter solid interface or multiple layer of fluids, having different temperature, are mixed.

Radiation

Through the radiation, heat energy is emitted by a substance in the form of electromagnetic wave within a specified band of wavelength ranges from 0.1-100 μ. This mode of transmission may not require a medium, thus can also take place in vacuum. The body receiving this electromagnetic wave gets hotter by the following Stefan-Boltzmann law:

$$E_R = \sigma A T^4, \tag{1.38}$$

where A is the surface area, T the absolute emitting surface temperature and σ the Stefan-Boltzmann constant.

1.5.1.1 Mass Transfer

The mass transfer phenomena takes place due to diffusion of species from a higher concentration to a lower concentration region in a heterogeneous system. Diffusion can occur due to variation in temperature gradient or because of variation in concentration gradient. In case of a very low fluid velocity, diffusion can dominate the mass transfer due to advection process. Fick's law describes the law of diffusion between two species A and B as follows,

$$J_A = -\bar{c} D_{AB} \frac{dx_A}{dx}, \tag{1.39}$$

where, J_A denotes the molar diffusion flux of the species A, x_A the mole fraction of A and $\bar{c}$ the molar concentration, D_{AB} the mass diffusivity of A in another species B. It says that the difussion flux is proportional to the concentration gradient.

1.5.1.2 Entropy Generation

The irreversible loss of thermal energy in an engineering system, also termed as entropy generation, is investigated in this thesis with respect to different important

physical regulatory parameters. It is important to minimize the entropy generation in any engineering process to make it energy efficient. The review article by Mahian et al. [2013] on entropy generation presented many possible research directions along with a thorough literature survey.

Rate of entropy generation

The rate of volumetric rate (E_{gen}) is expressed as,

$$E_{gen} = \frac{k}{T^2}(\nabla T)^2 + \frac{\mu}{T}\phi, \tag{1.40}$$

where T is the medium temperature, ϕ the viscous dissipation part, k the thermal conductivity and μ the viscosity. The expression of (1.40) in two dimensional Cartesian coordinates take the following form,

$$E_{gen} = \frac{k}{T^2}\Big[(\frac{\partial T}{\partial x})^2 + (\frac{\partial T}{\partial y})^2\Big] + \frac{\mu}{T}\Big\{2\big[(\frac{\partial u}{\partial x})^2 + (\frac{\partial v}{\partial y})^2\big] + (\frac{\partial u}{\partial x} + \frac{\partial v}{\partial y})^2\Big\} + \frac{\mu}{k_p T}(u^2 + v^2), \tag{1.41}$$

where u, v are the velocity components.

1.6 Methods of Solution

1.6.1 Differential Transform Method

We have implemented a semi-analytic power series like method, termed as "Diferential Transform Method" (DTM), which is a very useful tool to solve non-linear differential equations with boundary conditions. In this introduction, we have applied this method to solve a particular ODE, governing the equation of the Zeta potential distribution in a microchannel, for the study of an electroosmotic fluid flow phenomena between two permeable channel walls in the presence of injection process. This analytic method is very useful when there is a requirement for obtaining an explicit solution to ODE, however only a limited number of these highly non-linear problems can be handled analytically. Henceforth numerical methods have become the principal tool that is used mostly to tackle the situation. On the contrary, there have been serious efforts made by mathematicians to develop new and useful analytical techniques that can serve as alternatives to known computational methods. In this regard, we would like to start our discussion on the DTM, pioneered by Zhou [1986] who employed the basic idea of DTM for solving linear and nonlinear differential equations in electrical circuit problems. The differential transform method is an iterative process to obtain analytical Taylor series solutions for the corresponding linear and non-linear differential equations. Chen and Ho [1999] further developed DTM method for solving partial differential equations. The graphical abstract of this method can be best described in the following figure 1.1. Our objective is twofold, in (I) we have explained the above mentioned flow chart, and in (II) we have employed

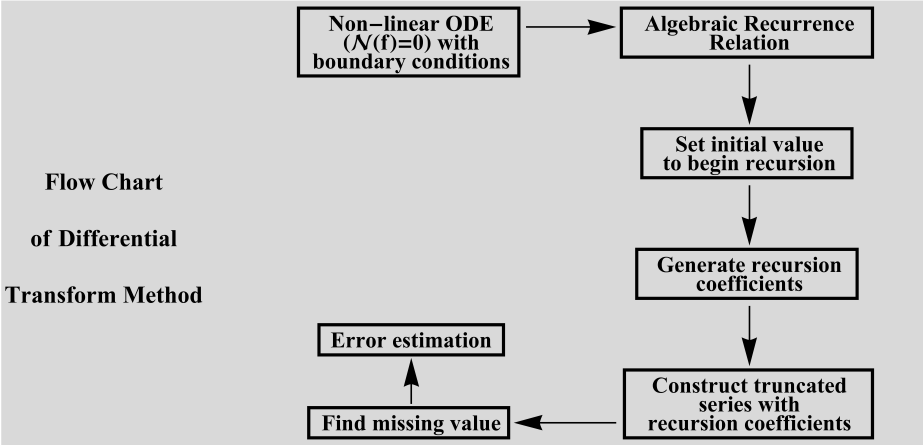

Figure 1.1: Graphical abstract of the DTM.

DTM to solve the following equation (1.42) describing the distribution of the Zeta potential problem,

$$\frac{\partial^2 \psi}{\partial y^2} = m^2 e^{R_D y}\psi, \;\; \psi(0) = Z_1, \;\; \psi(1) = Z_2. \tag{1.42}$$

I. Description of the flow chart in figure 1.1: In general, let us denote a non-linear ODE as $\mathcal{N}(f) = 0$. The first principal is to investigate the Taylor's expansion, expressed in equation (1.43), of the function $f(\eta)$ around the point η_0, where η_0 is the point at which most of the boundary values are available,

$$f(\eta) = \sum_{k=0}^{\infty} F(k)(\eta - \eta_0)^k, \tag{1.43}$$

where the k^{th} order DTM coefficient of $f(\eta)$ is defined as,

$$F(k) = \frac{1}{k!}\frac{d^k f(\eta)}{d\eta^k}|_{\eta=\eta_0}, \tag{1.44}$$

where $f(\eta)$ is the original function and $F(k)$ is the k^{th} order differential transform of $f(\eta)$. It is worthwhile to mention here that the DTM coefficients $F(k)$ are calculated symbolically, by providing a set of recursive algebraic relations of the transformed ODE with boundary values, by using the identities in Table 1.2. We are required to set dummy unknown variables for the unknown $F(k)$ to initiate the recursion process, and this variable has been calculated following the algorithm, explained in the next section. After expressing all the $F(k)$ in terms of the dummy variables, the next step is to truncate the equation (1.43) into a finite sum $\tilde{f}(\eta)$,

$$\tilde{f}(\eta) = \sum_{k=0}^{P} F(k)(\eta - \eta_0)^k, \tag{1.45}$$

Table 1.2: The differential transform identities used in this study

Differentiable function	DTM expression
$w(r) = \frac{d^m g(r)}{dr^m}$	$W(l) = \frac{(l+m)!}{l!} G(l+m)$
$w(r) = m(r)n(r)$	$W(l) = \sum_{i=0}^{l} M(i)N(l-i)$
$w(r) = r^n$	$W(l) = \delta(l-n)$
$w(r) = cp(r) \pm dq(r)$	$W(l) = cP(l) \pm dQ(l)$

where P is called the series length. The series length P is required to be a large number, however its effectiveness will be revealed only after estimating the error terms produced due to its truncated approximation.

II. Details of DTM to solve equation (1.42)

The DTM solution of the equation (1.42) takes the form $\tilde{\psi}(\eta) = \sum_{k=0}^{P} \Psi(k)\eta^k$, where $\Psi(k) = \frac{1}{k!}\frac{\partial^k \psi(\eta)}{\partial \eta^k}|_{\eta=0}$ and $\tilde{\psi}$ satisfies the boundary conditions $\tilde{\psi}(0) = Z_1$ and $\tilde{\psi}(1) = Z_2$. Now, $\tilde{\psi}(0) = Z_1$ and

$$\tilde{\psi}(1) = Z_2 \rightarrow \sum_{k=0}^{P} \Psi(k) = Z_2. \tag{1.46}$$

Thus, we need to find $\Psi(k), 0 \leq k \leq P$ to solve the equation (1.46). Using the identities as described in Table 1.2, from equation (1.42) we obtain the following relation,

$$\Psi(k+2) = \frac{m^2 \sum_{i=0}^{k} \frac{{R_D}^i}{i!} \Psi(k-i)}{(k+1)(k+2)}, \ 0 \leq k \leq P. \tag{1.47}$$

Therefore, to calculate all the $\Psi(k)$, we need two initial values $\Psi(0)$ and $\Psi(1)$ where $\Psi(0) = Z_1$ is already known. Thus, we only need the value of $\Psi(1)$, however this value cannot be obtained from the boundary conditions directly as described in equation (1.46). This is the reason to introduce a dummy unknown variable in this method. So, we assign $\Psi(1) = a$, and we find this unknown value a by utilising the relation $\tilde{\psi}(1) = Z_2 \rightarrow \sum_{k=0}^{P} \Psi(k) = Z_2$, as described in (1.46). The following expressions show the values of $\Psi(k)$, calculated after setting the dummy variable as follows,

$$\Psi(0) = Z_1, \Psi(1) = a, \Psi(2) = \frac{m^2 Z_1}{2}, \Psi(3) = \frac{m^2}{6}(a + R_D Z_1), \cdots \tag{1.48}$$

Using the expressions in (1.48), the relation $\sum_{k=0}^{P} \Psi(k) = Z_2$, as described in (1.46), becomes an equation in variable a. Therefore, solving equation (1.46) numerically to obtain the value 'a' completes the task of DTM.

Table 1.3: Variations in square averaged error terms with series length parameter P when $R_D = 2, m = 1.5, Z_{1,2} = -1$.

P	ϵ_ψ
15	0.00177057
20	3.82093×10^{-6}
25	3.57474×10^{-9}

Finally, obtained solution is expressed in the form,

$$\tilde{\psi}(\eta) = \sum_{k=0}^{P} \Psi(k)\eta^k. \tag{1.49}$$

With the following parametric values, $P = 25, R_D = 2, m = 3, Z_{1,2} = -1$, we obtain $a = 3.40974$. For this value of 'a', equation (1.49) has the following expression,

$$\tilde{\psi}(\eta) = -1 + 3.40974\eta - \frac{9\eta^2}{2} + 2.1146\eta^3 + 0.239604\eta^4 - \cdots - 0.000219034\eta^{25} \tag{1.50}$$

Thus, we need to estimate the error produced after truncating the series at step P. The square averaged error term is expressed as

$$\epsilon_\psi = \frac{1}{K+1} \sum_{i=0}^{K} [\mathcal{N}_\psi(\tilde{\psi}(\frac{i}{K}))]^2, \tag{1.51}$$

where K is a relaxation parameter and $\mathcal{N}_\psi(\eta) = \frac{\partial^2 \psi}{\partial \eta^2} - m^2 e^{R_D \eta}\psi$. In our case, $K = 1000$. The following Table 1.3 shows that an error term decreases rapidly as we increase the series length parameter by indicating that $\tilde{\psi}$ is well approximating the non-linear ODE $\mathcal{N}_\psi$.

1.6.2 Homotopy Analysis Method

The Homotopy Analysis Method, an analytic method which is also abbreviated as HAM, is applied in our thesis to solve the non-linear differential equations arising from the governing equations that describe the nanofluid flow behaviour over a stretching surface. Liao [2010], first employed the idea of HAM, successfully used HAM for solving several non-linear differential equations. The HAM, a recursive analytical method, is used to obtain an approximate series solution with respect to a set of suitable basis functions for the corresponding linear and non-linear differential equations. The application of this method for the following differential equations is discussed here,

$$f''' - (M+K)f' + A_1(1-\phi)^{2.5}\left[ff'' - f'^2 - \lambda(f' + \frac{\eta}{2}f'') + De(2ff'f'' - f^2 f''')\right] = 0, \tag{1.52}$$

$$\frac{1}{Pr}\left(1+\frac{4R}{3}\right)\theta'' + \frac{A_2}{A_3}(f\theta' - \frac{\lambda\eta}{2}\theta') + \frac{Ec}{A_3(1-\phi)^{2.5}}(f''^2 + (M+K)f'^2)$$
$$+\frac{A_1(1-\phi)^{2.5}}{Pr}(Af' + B\theta) = 0. \tag{1.53}$$

The boundary conditions are given as follows,

$$f'(0) = 1 + \gamma f''(0),\ f(0) = S,\ \theta'(0) = -Bi\big(1-\theta(0)\big), \tag{1.54}$$
$$f'(\infty) = 0,\ \theta(\infty) = 0. \tag{1.55}$$

The Homotopy Analysis Method is applied to obtain approximate solutions of the equations (1.52) and (1.53) with respect to the boundary conditions (1.54) and (1.55). Based on the boundary conditions, the following set of basis functions are chosen to solve the ODEs,

$$\{\eta^i exp(-j\eta)|i \geq 0, j \geq 0\}. \tag{1.56}$$

These exponential decay functions help to converge the solutions faster when η takes large values. The approximate solutions with respect these basis functions take the following form,

$$f(\eta) = p_{0,0} + \sum_{i=0}^{\infty}\sum_{j=1}^{\infty} p_{i,j}\eta^i exp(-j\eta),$$
$$g(\eta) = q_{0,0} + \sum_{i=0}^{\infty}\sum_{j=1}^{\infty} q_{i,j}\eta^i exp(-j\eta), \tag{1.57}$$

where $p_{i,j}, q_{i,j}$ are coefficients that need to be obtained from the equations (1.52)-(1.55). Following the method of Liao with respect to the boundary conditions, we need to find guess solutions that satisfy the boundary conditions. The initial approximate guess solutions are chosen as,

$$f_0(\eta) = \frac{S + S\gamma + 1 - e^{-\eta}}{1+\gamma},\ g_0(\eta) = \frac{Bi}{1+Bi}e^{-\eta}. \tag{1.58}$$

The following auxiliary functions are selected to initiate the recursion process,

$$L_f = f''' + f'',\ L_\theta = \theta'' + \theta' \tag{1.59}$$

that satisfy the following properties,

$$L_f[c_1 + c_2\eta + c_3e^{-\eta}] = 0,\ L_\theta[c_5 + c_5e^{-\eta}] = 0, \tag{1.60}$$

where c_i are unknown constants.
The zeroth order deformation of the problem is expressed as,

$$(1-q)L_f[\tilde{f}(\eta,q)-f_0(\eta)] = qh_f H_f \mathcal{N}_f(\tilde{f}(\eta,q)) \tag{1.61}$$
$$(1-q)L_\theta[\tilde{\theta}(\eta,q)-\theta_0(\eta)] = qh_\theta H_\theta \mathcal{N}_\theta(\tilde{f}(\eta,q),\tilde{\theta}(\eta,q)) \tag{1.62}$$
$$\tilde{f}(\eta,q) = f_0(\eta)+\sum_{m=1}^{\infty} f_m(\eta)q^m,\ \ \tilde{\theta}(\eta,q) = \theta_0(\eta)+\sum_{m=1}^{\infty}\theta_m(\eta)q^m,$$
$$f_m(\eta) = \frac{1}{m!}\frac{\partial^m \tilde{f}}{\partial q^m}\bigg|_{q=0},\ \ \theta_m(\eta) = \frac{1}{m!}\frac{\partial^m \tilde{\theta}}{\partial q^m}\bigg|_{q=0}$$

with respect to the following boundary conditions,

$$\tilde{f}(0,q) = S,\ \ \tilde{f}^{'}(0,q) = 1+\gamma\tilde{f}^{''}(0,q),\ \ \tilde{f}^{'}(\infty,q) = 0,\ \ \tilde{\theta}(\infty,q) = 0,$$
$$\tilde{\theta}^{'}(0,q) = -Bi(1-\tilde{\theta}(0,q)). \tag{1.63}$$

where $q \in [0,1]$, $\mathcal{N}_{f,\theta}$ denotes the non-linear ODEs (1.52), (1.53) and $h_{f,\theta}, H_{f,\theta}$ are convergence control parameters. In this study, we have considered $H_{f,\theta} = e^{-\eta}$ and $h_f = h_\theta = h$. The value of h is chosen in such a way that both $\tilde{f}, \tilde{\theta}$ converge when $q = 1$. The only remaining parameters (f_m, θ_m) that we need to define are obtained from the following m-th order deformation equations,

$$L_f\Big[f_m-\chi_m f_{m-1}\Big] = h_f H_f R_m^f,\ \ L_\theta\Big[\theta_m-\chi_m\theta_{m-1}\Big] = h_\theta H_\theta R_m^\theta, \tag{1.64}$$
$$f_m(0) = 0,\ \ f_m^{'}(0) = \gamma f_m^{''}(0),\ \ f_m^{'}(\infty) = 0,\ \ \theta_m(\infty) = 0,$$
$$\theta_m^{'}(0) = Bi\theta_m(0), \tag{1.65}$$

where

$$\begin{aligned} R_m^f(\eta) \;=\; & f_{m-1}^{'''} - (M+K)f_{m-1}^{'} + A_1(1-\phi)^{2.5}\Bigg[\sum_{i=0}^{m-1} f_i f_{m-1-i}^{''} - \sum_{i=0}^{m-1} f_i^{'} f_{m-1-i}^{'} - \\ & \lambda(f_{m-1}^{'} + \frac{\eta}{2}f_{m-1}^{''}) + De\Bigg(2\sum_{i=0}^{m-1} f_{m-1-i}\sum_{j=0}^{i} f_j^{'} f_{j-i}^{''} - \\ & \sum_{i=0}^{m-1} f_{m-1-i}\sum_{j=0}^{i} f_j f_{j-i}^{'''}\Bigg)\Bigg], \end{aligned} \tag{1.66}$$

$$\begin{aligned} R_m^\theta(\eta) \;=\; & \frac{1}{Pr}\Big(1+\frac{4R}{3}\Big)\theta_{m-1}^{''} + \frac{A_2}{A_3}\Bigg(\sum_{i=0}^{m-1} f_i\theta_{m-1-i}^{'} - \frac{\lambda\eta}{2}\theta_{m-1}^{'}\Bigg) \\ & + \frac{A_1(1-\phi)^{2.5}}{Pr}(Af_{m-1}^{'} + B\theta_{m-1}) \\ & + \frac{Ec}{A_3(1-\phi)^{2.5}}\Bigg(\sum_{i=0}^{m-1}\Big[f_i^{''} f_{m-1-i}^{''} + (M+K)f_i^{'} f_{m-1-i}^{'}\Big]\Bigg). \end{aligned} \tag{1.67}$$

Table 1.4: Error estimation with series iteration number when $h = -0.6, S = 0.3, \phi = 0.1, M, K = 0.7, R = 0.1, Pr = 10, A, B = -0.5, De = 0.1, Ec = 0.03, Bi = 0.2, \gamma = 0.1, \lambda = 0.05$.

P	ϵ_P^f	ϵ_P^θ
2	0.00149238	0.000163246
4	0.000196797	0.0000990327
6	0.0000570259	0.0000649834
8	0.0000224567	0.0000438791

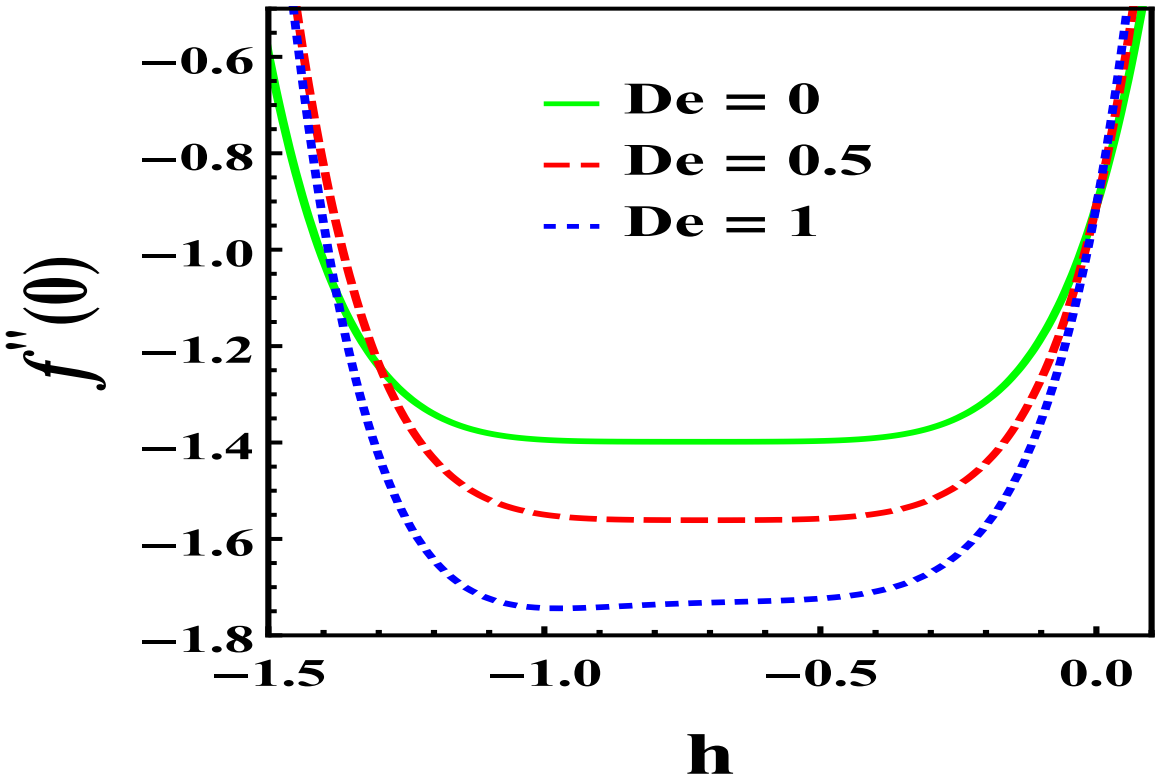

Figure 1.2: h-plot for different values of the Deborah number De when $P = 6,\ S = 0.3,\ \gamma = 0.1,\ \lambda = 0.05,\ \phi = 0.1, M, K = 0.7$.

The functions f, θ are then approximated by finite sums of the following form,

$$\overline{f} = f_0 + \sum_{i=1}^{P} f_i,\ \overline{\theta} = \theta_0 + \sum_{i=1}^{P} \theta_i, \tag{1.68}$$

where P denotes the number of iteration. The convergence control parameter h is determined from the above series by first observing the h-plot and then considering the error minimizing table where error terms are defined as,

$$\epsilon_P^f = \frac{1}{L+1} \sum_{j=0}^{L} \left[\mathcal{N}_f(\sum_{i=0}^{P} f_i)(\eta_j) \right]^2,\ \epsilon_P^\theta = \frac{1}{L+1} \sum_{j=0}^{L} \left[\mathcal{N}_\theta(\sum_{i=0}^{P} \theta_i)(\eta_j) \right]^2 \tag{1.69}$$

where $\eta_j = jr,\ r = \frac{\eta_{max}}{L+1},\ \eta_{max} = 6,\ L = 1000$ are chosen for this study. The value $h = -0.6$ is chosen based on the h-plot (figure 1.2) which shows that $[-1, -0.5]$ is a admissible interval of h-values for which the series $\overline{f}, \overline{\theta}$ will converge subject to small variations of the physical parameters. An error estimation with such a choice of h is presented in Table 1.4. The decrements in error terms with the increasing iteration value, presented in Table 1.4, indicates that $\overline{f}, \overline{\theta}$ are converging to the exact solution. The amount of precision of the iterated approximate solution as compared to the exact solution increases with the rise in number of iterations.

Chapter 2

Mathematical modeling and entropy generation of electrothermal couple stress nanofluid [1]

2.1 Introduction

A significant amount of scientific research is being conducted in building electrical double layer capacitors (EDLCS) in the last few decades (Conway [1991], Miller and Simon [2008]). The electrolyte conductivity and adsorption, diffusion of ions at aqueous electrolyte-electrode interface are principal factors that determines energy efficiency of EDLCS devices. The electric charge density and the ion diffusion coefficient in such a solution are related by the Nernst-Planck equation (Zheng and Wei [2011]). The study of ion diffusion coefficient in electrolyte solution has been experimentally investigated by several researchers Nielsen et al. [1952], Sato et al. [2012], Zhong and Friedman [1988]. The study on electrolyte fluid flow in micro/nano channels is immensely important to build micro-nanofluidic devices that are found to be economical as well as beneficial for the rapid development of EDCLS, medicines and medical equipment (Selvaganapathy et al. [2002], Johnson and Locascio [2002], Wang et al. [2004]). Recently, Kong et al. [2017] have investigated the effects of temperature on ion diffusion coefficient in NaCl electrolyte solution confined in a graphene nanochannel. It is revealed from their study that the enhancement of temperature will increase ion diffusion coefficient. In this chapter, we have shown that the temperature of couple stress nanofluid (CHOI [1995], Narla et al. [2020b], Akram et al. [2020b,a]) rises with enhancement of ion diffusion coefficient. Moreover, the effects of ion diffusion coefficient becomes more prominent in a nanochannel compared to a

[1] The content of this chapter has been published in *Applied Mathematics and Computation* (Elsevier), 426 (2022).

microchannel. The effects of ion diffusion coefficient on nanoparticle concentration and entropy generation in the system are also analyzed in this chapter.

This chapter investigates the effects of ion diffusion coefficient on electrothermal flow of couple stress nanofluid in a porous medium between two permeable beds of micrometer width under nanofluid injection process at the bottom bed. The fluid flow phenomena in such micro-sized channels under the influence of an external electric field are termed as electroosmotic flow (EOF). This flow is generated by the electric field-driven movements of freely moving ions near microchannel beds. A thin immobile layer (Stern layer) of charged ions is formed in an aqueous solution at the fluid-bed interface due to charged surface. This further attracts the oppositely charged ions in the solution, thereby forming an electric double layer (EDL). The relatively free ions (diffused layer) in EDL start migrating under an externally applied electric force, resulting in a bulk movement of fluid particles. Under the assumption of high ion concentration in fluid and no-slip boundary conditions at the fluid-bed interface, the fluid flow is governed by Smoluchowski slip velocity at the edge of EDL in the absence of a pressure gradient. However, the presence of intrinsic couple stress due to rotational substructure in the fluid can deter the electroosmotic nanofluid velocity at the edge of EDL from reaching the Smoluchowski slip velocity value. The diminution of nanofluid velocity with enhancement of couple stress parameter is discussed in Section 2.4 in this chapter.

Cosserat and Cosserat [1909] first investigated the effects of couple stress in the continuum theory of the solid body. This theory was further extended to incorporate the study of couple stress effects on rheology of visco-elastic materials by several researchers Toupin [1962], Dahler and Scriven [1963], Stokes [1966], Ariman and Cakmak [1967], Hadjesfandiari et al. [2015]. It is often found that industrial/biological fluids contain molecules of variable size that bind together, thereby forming molecular chains in the fluid. These additional structures manifest couple stress effects in the fluid. The presence of intrinsic couple stress is well accounted in complex non-Newtonian fluids, granular fluids, liquid crystals, colloid suspensions etc. The consideration of the classical Newtonian fluid model does not consider this micro behavior in fluid. The subject "couple stress fluid theory" was pioneered by Stokes [1966] whose model studied couple stress effect along with fluid displacement field in the presence of usual stress in fluid, thereby not identifying rotation of micro substructure phenomena by a separate equation. This intrinsic stress parameter significantly influences fluid velocity profiles, which are well studied in the literature (Tripathi et al. [2017], Subramaniam and Mondal [2020], Siva et al. [2020]). The existence of couple stress is found to have an inverse relationship with fluid velocity as energy consumption by rotating fluid particles due to couple stress is responsible for such phenomena. The present study shows that the fluid flow rate follows a non-linear quadratic-like relationship with a couple stress parameters. Therefore, the effects of such a stress parameter would also influence heat and mass transfer phenomena in a flow process. Recently, several researchers Tripathi et al. [2021], Ramesh et al. [2021] have investigated the thermophysical effects of couple stress on heat and mass transfer process in an elec-

troosmotic nanofluid flow. However, they have used long wavelength type approximations to reduce the flow equations thereby ignored the effects of convective parts of the flow profiles in their studies. The present study focuses on studying the effects of ion diffusion coefficient and couple stress in electrolyte nanofluid on the thermal and mass flow process in a porous medium under nanofluid injection process at lower permeable bed. Moreover, this study considers the effects of convective flow behaviour in the direction in which nanofluid is injected. A significant amount of research has been carried out to understand the pressure-driven fluid flow behaviour through permeable beds that has important applications in designing engineering machines pertaining to applications in Hydrogeology, gaseous diffusion process, building medical devices dependent on filtration mechanism etc. (Berman [1953], Sellars [1955], Yuan [1956], Morduchow [1956], Esmond and Clark [1966], Beavers and Joseph [1967], Dutta and Beskok [2001], Wang [1971], Radhakrishnamacharya and Maiti [1977], Shaw et al. [2014], Maiti et al. [2019], Rajagopal and Tao [1995], Elshehawey et al. [2000], Vajravelu et al. [2003], Malathy and Srinivas [2008], Bitla and Iyenger [2014], Bhandari et al. [2020], Tripathi et al. [2021])

The non-linear differential equations governing the nanofluid flow are solved by applying the differential transform method (DTM). The idea of DTM was invented and popularized by Zhou [1986]. Chen and Ho [1999] have used this method to solve partial differential equations. It is an analytical power series type method that calculates the Taylor coefficients of a function recursively by applying algebraic identities. We have briefly described this method in Section 2.3. This chapter analyzes the effects of ion diffusion coefficient, porous permeability of the medium and couple stress on total entropy generation in the system. Recently, Siddabasappa et al. [2021] have conducted a study on entropy generation and heat transfer process in a MHD couple stress fluid flow in a channel. A detailed discussion on the utility of entropy generation is found in these papers. Bejan [1979], Herwig [2018], Narla and Tripathi [2020], Narla et al. [2020a]

Being motivated by the above findings, this chapter analytically examines the effect of ion diffusion coefficient, couple stress and porous permeability of the medium on steady electroosmotic nanofluid flow, heat and mass transfer process in a micro-nano channel between two permeable beds in the presence of slip-velocity generated at edges of the EDL. We also examine the entropy generation in the system. The temperature distribution in microchannel depends on heat generation due to the Joule heating and temperature at the channel surface. A great amount of research in electroosmotic flow theory has focused on non-porous microchannels in the absence of both substructure in fluid and fluid injection process at channel beds. However, the present study attempts to explore the effects of ion diffusion coefficient and substructures present in nanofluid on its velocity profiles, temperature profiles and mass migration process under nanofluid injection process. The effects of injection velocity and ion diffusion coefficient are found to have considerable influence on Zeta potential formation in microchannel. Moreover, an analytical study is carried out to express EDL thickness as a function of injection velocity and ion diffusion coefficient in terms

of a newly introduced metric the diffusive Reynolds number. The effects of diffusive Reynolds number on temperature, nanoparticle concentration profile and total entropy generation are extensively analyzed graphically in this chapter.

2.2 Description of the Problem

This chapter examines the steady, viscous and incompressible couple stress nanofluid flow in a porous microchannel between two permeable beds. The microchannel height is denoted by distance h. The flow takes place in the presence of an externally applied electric field of strength E_0. A physical diagram of this problem in the rectilinear Cartesian coordinates is depicted in Figure-2.1. The nanofluid is driven by a uniform pressure gradient in the horizontal axis direction. Moreover, this same pressure gradient also drives the nanofluid flow through the permeable beds. The temperature difference between two channel beds is assumed to be small. The nanofluid is assumed to be injected at lower bed in the vertical direction with a uniform velocity Ve. Thus, the injected velocity influences fluid flow behaviour through the porous beds, impacting the fluid-bed slip velocity boundary conditions. Moreover, the electric charge distribution in the microchannel is affected by the injected velocity, which influences the electroosmotic slip velocity at the edge of EDL.

2.2.1 Zeta Potential Distribution

The electric potential distribution in a microchannel is described by the Poisson equation (Ranjit and Shit [2017]) as,

$$\frac{\partial^2 \psi}{\partial y^2} = -\frac{\rho_e}{\epsilon}, \tag{2.1}$$

where Ψ denotes the electric potential distribution, ρ_e the net charge density, ϵ the permittivity of the medium. The $1:1$ symmetric electrolyte is assumed for this study. The net charge density (Ranjit and Shit [2017]) has the following expression,

$$\rho_e = ezN_A(n^+ - n^-). \tag{2.2}$$

where, e denotes the electron charge, z the valence of the ions, N_A the Avogadro number and $n^{\pm}$ the average number of positive/negative ions. The ion distribution is calculated by using the following Nernst-Planck equation,

$$Ve\,\frac{\partial n^{\pm}}{\partial y} = D\,\frac{\partial^2 n^{\pm}}{\partial y^2} \pm \frac{D\;z\;e}{K_B\;T_{av}}\frac{\partial}{\partial y}(n^{\pm}\,\frac{\partial \psi}{\partial y}), \tag{2.3}$$

where D represents the ion diffusivity, K_B the Boltzmann constant and T_{av} the average temperature of the nanofluid. Equation 2.3 is solved with the following boundary

conditions,

$$\begin{aligned} n^{\pm} &= 0 \quad \text{at } \frac{\partial \psi}{\partial y} = 0, \\ n^{\pm} &= n_0\, e^{\frac{Ve}{D}y} \quad \text{at } \psi = 0. \end{aligned} \tag{2.4}$$

The ionic expression shows that its distribution in microchannel is inversely related to diffusivity parameter and enhances with increasing injected nanofluid velocity. The solution of equations 2.4 is expressed as follows,

$$n^{\pm} = n_0\, e^{\mp \frac{z\ e}{K_B\ T_{av}}\psi + \frac{Ve}{D}y}. \tag{2.5}$$

Under the Debye-Hückel approximations (Bandopadhyay et al. [2013]) and lower Zeta potential approximation, equations 2.1,2.2,2.5 are converted to the following ordinary differential equation,

$$\begin{aligned} \frac{\partial^2 \psi}{\partial y^2} &= \frac{2n_0\ ez\ N_A}{\tilde{k}\epsilon_0}\, e^{\frac{Ve}{D}y} \left(\frac{ez}{K_B T_{av}}\psi\right), \\ \psi &= \zeta_1 \quad \text{at } y = 0, \\ \psi &= \zeta_2 \quad \text{at } y = h, \end{aligned} \tag{2.6}$$

where $\zeta_{1,2}$ are the uniform zeta potentials at the channel beds. The following set of transformations are applied to make the equations dimensionless (see Table 2.2),

$$\begin{aligned} &Y = \frac{y}{h},\ U = \frac{u}{\lambda U_{HS}},\ \theta = \frac{T - T_0}{Br(T_h - T_0)},\ f = \frac{C - C_h}{Br(C_0 - C_h)}, \\ &Z_1 = \frac{ez}{K_B T_{av}}\zeta_1,\ Z_2 = \frac{ez}{K_B T_{av}}\zeta_2,\ \Phi_1 = \frac{ez}{K_B T_{av}}\psi. \end{aligned}$$

where $\lambda = \frac{h}{\epsilon\zeta_1}\sqrt{\frac{\sigma\mu}{S}}$ is a material parameter that depends on microchannel heights and S denotes a sensitivity parameter. Equation 2.6 has the following dimensionless form,

$$\begin{aligned} &\frac{\partial^2 \Phi_1}{\partial Y^2} = \kappa^2 e^{R_D\ Y}\Phi_1, \\ &\Phi_1 = Z_1 \quad \text{at } Y = 0, \\ &\Phi_1 = Z_2 \quad \text{at } Y = 1, \end{aligned} \tag{2.7}$$

where $\kappa = \frac{h}{\lambda_D}$ denotes the electroosmotic parameter, $R_D = \frac{Ve\ h}{D}$ the diffusive Reynolds number and $\lambda_D = \left(\frac{\epsilon K_B T_{av}}{2e^2 z^2 n_0\ N_A}\right)^{\frac{1}{2}}$ denotes the Debye length.

2.2.2 Assumptions and Governing Equations

The following set of assumptions is considered while analyzing this physical problem,

- The nanofluid flow is considered to be fully developed and laminar.
- The microchannel height is considered to be very small compared to the channel length. It implies that the horizontal gradient ($\frac{\partial}{\partial x}$) of a field is much smaller than its vertical gradient value $\frac{\partial}{\partial y}$. Moreover, under the assumption that E_0 is small, the horizontal convective term $u\ \frac{\partial}{\partial x}$ is ignored. The nanofluid velocity profiles are represented by $q = (u(y), Ve)$ (in microchannel) and $q_1 = (u_p(y), Ve)$ through permeable bed.
- Permeable beds are assumed to be homogeneous.
- Body couple forces are ignored.

Based on the above assumptions, the equations for couple stress nanofluid flow in the Cartesian coordinates can be expressed as follows (Bitla and Iyenger [2014], Ranjit and Shit [2017], Seth et al. [2018], Siva et al. [2020]),

$$Ve\frac{\partial u}{\partial y} = -\frac{1}{\rho}\frac{\partial p}{\partial x} + \frac{\mu}{\rho}\frac{\partial^2 u}{\partial y^2} - \frac{\eta}{\rho}\frac{\partial^4 u}{\partial y^4} + \frac{\rho_e}{\rho}E_0 - \frac{\mu}{\rho\ k_p}u, \tag{2.8}$$

$$\frac{\partial p}{\partial y} = 0, \tag{2.9}$$

$$Ve\frac{\partial T}{\partial y} = \frac{k}{\rho\ C_p}\frac{\partial^2 T}{\partial y^2} + \sigma\frac{{E_0}^2}{\rho\ C_p} + \frac{\mu}{\rho\ C_p}\left(\frac{\partial u}{\partial y}\right)^2 + \frac{\mu}{k_p \rho C_p}u^2, \tag{2.10}$$

$$Ve\frac{\partial C}{\partial y} = D_B\frac{\partial^2 C}{\partial y^2} + \frac{D_T}{T_0}\frac{\partial^2 T}{\partial y^2}, \tag{2.11}$$

where T and C denote the nanofluid temperature and nanoparticle concentration respectively. Here, ρ denotes the density, ν the kinematic viscosity, η the couple stress viscosity coefficient, C_p the specific heat and k the thermal conductivity of the nanofluid. The electroosmotic parameters ρ_e represents the net charge density, D_B the Brownian diffusion parameter and D_T the thermophoresis parameter respectively. The contributions of both thermophoresis and the Brownian diffusion terms are found to be very small in the thermal energy equation (because $D_T, D_B \approx 10^{-6}$ is small compared to injected velocity Ve *i.e.* $D_B\ \frac{\partial C}{\partial y}\frac{\partial T}{\partial y}, \frac{D_T}{T_0}\left(\frac{\partial T}{\partial y}\right)^2 << Ve\frac{\partial T}{\partial y}$, ref. Table-2.1) thereby ignored. The physical parameter values used in this study are based on Table-2.1.

Table 2.1: Physical parameters used in this study (Ranjit et al. [2019], Zhao et al. [2014])

Physical Parameters	Values [Unit]
Channel height (h)	100 μm
Density of the fluid (ρ)	1000 kg/m^3
Charge of proton (e)	1.6×10^{-19} C
Electrical Potential at the walls (ζ_1, ζ_2)	-25 mV
Boltzmann Constant (K_B)	1.38×10^{-23} J/K
Average absolute fluid temperature (T_{av})	300 K
Valency of ions (z)	1
Permittivity of the medium (ϵ)	8×10^{-10} C/Vm
Kinematic viscosity of the fluid (ν)	10^{-6} m^2/s
Electrical Conductivity (σ_e)	5×10^{-3} S/m
Thermal Conductivity (k)	0.5 W/mK
Specific heat (C_p)	3000 J/kgK
Material parameter (α)	0.1
Permeability of the beds (k_1, k_2)	10^{-7} m^2
Brownian Diffusion Coefficient (D_B)	2×10^{-6} m^2/s
Thermophoretic Diffusion Coefficient (D_T)	10^{-6} m^2/s
Permeability of the medium (k_p)	10^{-4} m^2

2.2.3 Nanofluid Flow Through Porous Beds

The injected nanofluid velocity hinders the horizontal nanofluid flow velocity through the porous bed. Under the assumption of both very small permeability k_i and couple stress parameter η, the nanofluid flow through a porous medium can be described by the Darcy-Brinkman equation as (Seth et al. [2018]),

$$Ve\frac{\partial u_p}{\partial y} = -\frac{1}{\rho}\frac{\partial p}{\partial x} - \frac{\nu}{k_i}u_p, \qquad (2.12)$$
$$u_p = 0 \text{ as } \frac{\partial p}{\partial x} = 0.$$

The solution of equations 2.12 is expressed as follows,

$$u_p = -\frac{1}{\rho\, Ve}\, e^{-\frac{\nu}{k_i\, Ve}y} \int e^{\frac{\nu}{k_i\, Ve}y}\, \frac{\partial p}{\partial x}\, dy = -\frac{k_i}{\mu}\, \frac{\partial p}{\partial x}. \qquad (2.13)$$

The above expression is only valid when k_i is a very small number. Moreover, it is to be noted that, the term Ve has to be included in the integral expression when $\frac{\partial p}{\partial x}$ is a function of y *i.e.* Ve cannot be taken entirely as a constant value in the flow region. At the fluid-bed interface the slip velocity is expressed as described by Beavers and Joseph [1967],

$$\frac{\partial u}{\partial y}\Big|_{y=O} = \frac{\alpha}{\sqrt{k_i}}\,(u_{B_1} - u_p) \qquad (2.14)$$

Table 2.2: Expression for the non-dimensional parameters used in this study

Nomenclature	Expression	Abbreviation
Reynolds number	$\frac{\rho\ Ve\ h}{\mu}$	Re
Permeability parameter	$\frac{k_i}{h^2}$	L_i
Inverse couple stress parameter	$\frac{\mu\ h^2}{\eta}$	γ
Prandtl number	$\frac{\mu\ C_p}{k}$	Pr
Eckert number	$\frac{\lambda^2 {U_{HS}}^2}{C_p\ (T_h - T_0)}$	Ec
Brinkman number	$Pr \times Ec$	Br
Joule heating parameter	$\frac{\sigma h^2 {E_0}^2}{k\ (T_h - T_0)}$	Γ
Temperature ratio parameter	$\frac{T_0}{T_h - T_0}$	δ
Fractional ratio parameter	$\frac{C_h}{C_0 - C_h}$	δ_1
Mass transfer parameter	$\frac{\rho\ C_p\ D_B\ (C_0 - C_h)}{k}$	χ_1
Helmhotz-Smoluchowski velocity	$-\frac{\epsilon E_0 \zeta_1}{\mu}$	U_{HS}
Pressure parameter	$\frac{h^2 \frac{\partial p}{\partial x}}{\mu \lambda U_{HS}}$	Π
Schmidt number	$\frac{\mu}{\rho\ D_B}$	Sc
Soret number	$\frac{D_T\ (T_h - T_0)}{T_0\ D_B\ (C_0 - C_h)}$	S_t
Deposition parameter at lower bed	$\frac{h\ \mu\ {\phi_1}^*}{M\ n_0\ (C_0 - C_h)}$	ϕ_1
Deposition parameter at upper bed	$\frac{h^2\ \mu\ {\phi_2}^*}{M\ n_0\ (C_0 - C_h)}$	ϕ_2
Inverse Darcy number	$\frac{h^2}{k_p}$	Da
Electroosmotic Parameter	$\frac{h}{\lambda_D}$	κ
Diffusive Reynolds number	$\frac{Veh}{D}$	R_D
Debye Length	$\sqrt{\frac{\epsilon K_B T_{av}}{2e^2 z^2 n_0 N_A}}$	λ_D
Zeta Potential	$\frac{ez}{K_B T_{av}} \zeta_{1,2}$	$Z_{1,2}$
Material Parameter	$\frac{h}{\epsilon \zeta_1} \sqrt{\frac{\sigma \mu}{S}}$	λ

where O denotes the lower bed limit point, α a non-dimensional material parameter, u_{B_1} the slip velocity at fluid-bed boundary. The expressions for the non-dimensional parameters used in this study are described in Table-2.2.

2.2.4 Boundary Conditions at Fluid-bed Interface

i. Velocity boundary conditions:

$$\begin{aligned} \frac{\partial u}{\partial y} &= \frac{\alpha}{\sqrt{k_1}}\left(u + \frac{k_1}{\mu}\frac{\partial p}{\partial x}\right),\ \frac{\partial^2 u}{\partial y^2} = 0 \text{ at } y = 0, \\ \frac{\partial u}{\partial y} &= -\frac{\alpha}{\sqrt{k_2}}\left(u + \frac{k_2}{\mu}\frac{\partial p}{\partial x}\right),\ \frac{\partial^2 u}{\partial y^2} = 0 \text{ at } y = h. \end{aligned} \tag{2.15}$$

where $k_{1,2}$ denote permeability of channel beds. The variations in velocity gradient between adjacent fluid layers near channel beds is linearly dependent on velocity change across the fluid-bed interface, thereby making the second derivative of velocity

field zero at the fluid-bed boundary. The non-dimensional form of the equations 2.8, 2.15 are as follows,

$$
\begin{aligned}
&-\frac{1}{\gamma}\frac{\partial^4 U}{\partial Y^4}+\frac{\partial^2 U}{\partial Y^2}-Re\frac{\partial U}{\partial Y}-\Pi+\frac{\kappa^2}{\lambda Z_1}\Phi_1-Da\ U=0,\\
&\frac{\partial U}{\partial Y}-\frac{\alpha}{\sqrt{L_1}}(U+L_1\Pi)=0 \quad \text{at Y} = 0,\\
&\frac{\partial U}{\partial Y}+\frac{\alpha}{\sqrt{L_2}}(U+L_2\Pi)=0 \quad \text{at Y=1},\\
&\frac{\partial^2 U}{\partial Y^2}=0, \quad \text{at Y} = 0,1.
\end{aligned}
\tag{2.16}
$$

ii. Temperature Boundary conditions: (Eshaghi et al. [2021], Dogonchi et al. [2021a], Moshfegh and Sandberg [1996])

$$
\begin{aligned}
T &= T_0 \quad \text{at } y=0,\\
\frac{\partial T}{\partial y} &= 0 \quad \text{at } y=h.
\end{aligned}
\tag{2.17}
$$

The lower bed is assumed to have a fixed temperature. The variations of temperature at upper channel bed is assumed to be unchanged as the upper bed is assumed to be insulated. The non-dimensional form of the equations 2.10,2.17 are as follows,

$$
\begin{aligned}
&\omega+\frac{S}{RePr}Y=\theta,\\
&\omega=0 \quad \text{at} \quad \text{Y}=0,\\
&\frac{\partial\omega}{\partial Y}=-\frac{S}{RePr} \quad \text{at} \quad \text{Y}=1,\\
&\frac{\partial^2\omega}{\partial Y^2}+\left(\frac{\partial U}{\partial Y}\right)^2-RePr\frac{\partial\omega}{\partial Y}+Da\ U^2=0.
\end{aligned}
\tag{2.18}
$$

iii. Nanoparticle concentration boundary conditions:

$$
\begin{aligned}
C &= C_h+\phi_1^*\ k_1\ \frac{\rho\ Ve}{M\ n_0} \quad \text{at } y=0,\\
\frac{\partial C}{\partial y} &= -\phi_2^*\ k_2\ \frac{\rho\ Ve}{M\ n_0} \quad \text{at } y=h.
\end{aligned}
\tag{2.19}
$$

where C_h represents nanoparticle concentration at lower channel bed, ${\phi_1}^*$ and ${\phi_2}^*$ the boundary deposition parameters, M the nanoparticles molar mass and n_0 the ion density in nanofluid. The non-dimensional form of equations 2.11,2.19 are as follows,

$$
\begin{aligned}
&\frac{\partial^2 f}{\partial Y^2}-ReSc\frac{\partial f}{\partial Y}+S_t\frac{\partial^2\Omega}{\partial Y^2}=0,\\
&f=ReL_1\phi_1 \quad \text{at} \quad \text{Y}=0,\\
&\frac{\partial f}{\partial Y}=-ReL_2\phi_2 \quad \text{at} \quad \text{Y}=1.
\end{aligned}
\tag{2.20}
$$

Table 2.3: The differential transform identities used in this study

Differentiable function	DTM expression
$w(r) = \frac{d^m g(r)}{dr^m}$	$W(l) = \frac{(l+m)!}{l!} G(l+m)$
$w(r) = m(r)n(r)$	$W(l) = \sum_{i=0}^{l} M(i)N(l-i)$
$w(r) = r^n$	$W(l) = \delta(l-n)$
$w(r) = cp(r) \pm dq(r)$	$W(l) = cP(l) \pm dQ(l)$

2.3 Analytical Method of Solution and its convergence

2.3.1 Differential Transform Method (DTM)

The approximate analytical solutions of the equations 2.16,2.18,2.20 are obtained by applying the Differential transform method (DTM), which was first presented by Zhou [1986]. For an analytical function $w(x)$ satisfying a differential equation $\mathcal{N}_w(x) = 0$, its n^{th} order DTM transformation is expressed by $W(n)$ as follows,

$$W(n) = \frac{1}{n!}\left[\frac{d^n w(x)}{dx^n}\right]_{x=x_0}, \tag{2.21}$$

where x_0 is a particular point of interest, determined by the differential equations. The Taylor series expansion of $w(x)$ around x_0 gives

$$w(x) = \sum_{l=0}^{\infty} \frac{1}{l!}\left[\frac{d^l w(x)}{dx^l}\right]_{x=x_0} (x-x_0)^l. \tag{2.22}$$

Thus, equation 2.22 can be rewritten using notation 2.21 as follows,

$$w(x) = \sum_{l=0}^{\infty} W(l)(x-x_0)^l. \tag{2.23}$$

The DTM transformation coefficients $W(l)$ are recursively calculated by transforming the differential equations into an algebraic set of relations by using the identities presented in Table-2.3.
The idea of DTM is to truncate the exact solution $w(x)$, expressed in 2.23, into a finite sum $\tilde{w}(x)$ in the following form,

$$\tilde{w}(x) = \sum_{l=0}^{N} W(l)(x-x_0)^l, \tag{2.24}$$

where, N is the series characteristic length. The square averaged error term generated due to this approximation is expressed as,

$$\epsilon_w = \frac{1}{K+1}\sum_{i=0}^{K}[\mathcal{N}_w(\tilde{w}(\frac{i}{K+1}))]^2$$

Table 2.4: Average squared individual residual error terms for the Zeta potential, velocity, temperature and nanoparticle concentration with number of iterations in DTM when $R_D = 2,\ Re = 10^{-2},\ \gamma = 0.1,\ \kappa = 2,\ \Pi = -1,\ L_i = 10,\ Da = 10^{-4}, Z_{1,2} = -1,\ \lambda = \frac{10^4}{2},\ \phi_1 = 10,\ \phi_2 = 10^{-3},\ S_t = 1,\ Pr = 6,\ S = 1,\ Sc = 0.5,\ K = 1000.$

N	ϵ_{Φ_1}	ϵ_U	ϵ_ω	ϵ_f
20	0.000266815	1.03571×10^{-13}	4.34637×10^{-25}	2.79027×10^{-32}
23	7.9153×10^{-6}	2.56772×10^{-15}	7.05674×10^{-27}	3.4426×10^{-33}
25	6.51909×10^{-7}	1.8998×10^{-16}	4.02968×10^{-28}	2.56249×10^{-35}

The purpose of DTM is to minimize ϵ_w for suitably selecting a large N for a particular choice of parameters as presented in Table-2.2. Using the relations in Table-2.3, at $x_0 = 0$, the functions satisfying equations 2.16,2.18,2.20 are approximated by the expressions $\tilde{U} = \sum_{k=0}^{N} U(k)x^k,\ \tilde{\omega} = \sum_{k=0}^{N} \Omega(k)x^k,\ \tilde{f} = \sum_{k=0}^{N} F(k)x^k$. Moreover, the boundary conditions are also transformed in the DTM form as follows,

$$\begin{aligned}
&\tilde{U}'(0) + \frac{\alpha}{\sqrt{L_1}}(\tilde{U}(0) + L_1\Pi) = 0, \tilde{U}''(0) = 0, \tilde{\omega}(0) = 0, \tilde{f}(0) = ReL_1\phi_1,\\
&\tilde{U}'(1) + \frac{\alpha}{\sqrt{L_2}}(\tilde{U}(1) + L_2\Pi) = 0, \tilde{U}''(1) = 0, \tilde{\omega}'(1) = -\frac{S}{RePr},\\
&\tilde{f}'(1) = -ReL_2\phi_2.
\end{aligned} \tag{2.25}$$

As an example, the l-th DTM coefficient of f satisfying the equation 2.20 at $x_0 = 0$ are obtained by using the relations presented in Table-2.3 as follows,

$$\begin{aligned}
&F(l+2) = \frac{ReSc(l+1)F(l+1) - S_t(l+1)(l+2)\Omega(l+2)}{(l+1)(l+2)},\\
&F(0) = ReL_1\phi_1,\ F(1) = a.
\end{aligned} \tag{2.26}$$

The missing initial a is used to calculate the values $F(l), \forall l \geq 0$ recursively by using the relations 2.26. The value for a is calculated from the boundary condition $\tilde{f}'(1) = -ReL_2\phi_2$ as described in equation 2.25.

2.3.2 Convergence of the Results

The averaged squared residual error estimations are presented in Table-2.4, which indicates the error terms are decreasing rapidly with increasing series length parameter thereby showing convergence criterion for the DTM series solution. Figures 2.2 and 2.3 show a comparison between the DTM solutions (when $R_D \to 0,\ Da = 0$) and the exact analytic solutions (*i.e.* when $R_D = 0,\ Da = 0$), presented in appendix, of 2.7 and 2.16, which show excellent agreement. Based on Table-2.4, we have selected $N = 25$ for our study.

2.4 Results and Discussion

This study focuses on examining the effects of the ion diffusivity in terms of diffusive Reynolds number (R_D), inverse darcy number (Da) and inverse couple stress parameter (γ) on nanofluid flow profiles. The following set of default parameter values (based on Table-2.1) are used for numerical calculations conducted in this chapter,

$$\begin{aligned} &Re = 10^{-2},\ \kappa = 2,\ \Pi = -0.1,\ Pr = 6,\ \phi_1 = 10,\ Sc = 0.5,\\ &S_t = 1,\ L_{1,2} = 10,\ Z_{1,2} = -1,\ Da = 10^{-4},\ R_D = 2,\ \gamma = 0.1,\\ &S = 1,\ \phi_2 = 10^{-3},\ N = 25,\ K = 1000. \end{aligned} \tag{2.27}$$

For OH^- ions, its ion diffusion coefficient D is found to be around $5\times10^{-9}\ m^2/s$, which makes the diffusive Reynolds number $R_D = \frac{Veh}{D} = \frac{10^{-4}\times10^{-4}}{5\times10^{-9}} = 2$ for a microchannel of height $100\mu m$ with injected velocity $10^{-4}\ ms^{-1}$. Figure 2.4 shows that the Zeta potential decreases with enhancement of diffusive Reynolds number, which is inversely related to the ion diffusion coefficient, for a fixed Reynolds number. Moreover, a shift in the Zeta potential distribution is observed towards the upper channel bed with increasing diffusive Reynolds number. The EDL thickness (denoted by $d_{L,U}$ for EDL thickness near lower and upper beds respectively) is affected by diffusive Reynolds number as shown in equation 2.7. After ignoring the term $\Phi^{'}(d_L)$ and keeping κ fixed, from equation 2.7 we obtain,

$$\begin{aligned} &\int_0^{d_L} {\Phi_1}^{''}\, dY = \int_0^{d_L} \kappa^2\ e^{R_D\ Y}\ \Phi_1\ dY,\\ &\Rightarrow d_L \approx \frac{1}{R_D}\ ln\frac{Z_1 - {\Phi_1}^{'}(0)(\frac{R_D}{\kappa^2} + \frac{1}{R_D})}{\Phi_1(d_L)}. \end{aligned} \tag{2.28}$$

when $R_D > 1$. Here, ${\Phi_1}^{'}(0),\ \Phi_1(d_L) > 0$ depends on $Z_{1,2},\ \kappa$ and Φ_1 attains its minimum non-zero lower bound in the interval $[0, 1]$. Therefore, under the assumptions of fixed ion concentration in the aqueous nanofluid and uniform surface charge, equation 2.28 can be expressed in a logarithmic form, $d_L \approx \frac{1}{R_D}\ ln|a\ (\frac{R_D}{\kappa^2} + \frac{1}{R_D}) + b|,\ a, b \in \mathbb{R}$, which is a decreasing function of R_D, κ.

2.4.1 Flow Analysis

Figures 2.5-2.7 illustrate the combined effects of the material parameters (permeability, ion diffusivity and couple stress parameters) on nanofluid flow profiles in a microchannel. Figure 2.5 shows that the enhancement of porous permeability of microchannel medium in terms of inverse Darcy number increases nanofluid velocity inside microchannel. Figure 2.6 shows that axial velocity increases with enhancement of the inverse couple stress parameter. The increment in couple stress in nanofluid enhances the micro-rotation phenomena of nanofluid particles, resulting in the diminution of nanofluid velocity due to additional rotational energy consumption. The findings suggest that couple stress opposes the nanofluid flow inside the microchannel,

which is in agreement with other researchers. The following analytical expression shows the dependence of bulk nanofluid flow rate on couple stress parameter in the absence of both injected velocity, porous permeability and applied electric field,

$$\int_0^1 u\ dY = \frac{h^2\ \frac{\partial p}{\partial x}}{\mu}\ \left(-25.8947 + \frac{1}{\gamma} + \left(31.6228 - \frac{2}{\gamma}\right)\ \frac{1}{\sqrt{\gamma}}\ Tanh\frac{\sqrt{\gamma}}{2}\right). \tag{2.29}$$

Figure 2.7 shows that nanofluid velocity decreases with enhancement of the diffusive Reynolds number. The diminution of the ion diffusion coefficient is responsible for formation of a weaker Zeta potential distribution in microchannel thereby reducing the charge density inside microchannel, hence the electroosmotic force driving nanofluid flow diminishes.

2.4.2 Thermophysical Quantities

The effects of inverse couple stress parameter, inverse Darcy number and diffusive Reynolds number in nanofluid on its thermal properties are investigated in figures 2.8 - 2.16. The energy efficiency in terms of entropy generation is studied under a weak electric field assumption. Entropy generation measures the amount of irreversible heat generation in a thermal process. The expression for total volumetric entropy generation rate (Ranjit et al. [2019], Bejan [1979], Falade et al. [2016], Seth et al. [2018]) is expressed as,

$$\begin{aligned} E_{Total} &= E_{HT} + E_{VS} + E_{JH} + E_{MT} + E_{CS} + E_P, \\ E_{HT} &= \frac{k}{T^2}\left(\frac{\partial T}{\partial y}\right)^2,\ E_{VS} = \frac{\mu}{T}\left(\frac{\partial u}{\partial y}\right)^2,\ E_{JH} = \frac{\sigma E_0^2}{T}, \\ E_{MT} &= \frac{(\rho\ C_p)\ D_B}{C}\left(\frac{\partial C}{\partial y}\right)^2 + \frac{(\rho\ C_p)\ D_B}{T}\left(\frac{\partial T}{\partial y}\right)\left(\frac{\partial C}{\partial y}\right), \\ E_{CS} &= \frac{\eta}{T}\left(\frac{\partial^2 u}{\partial y^2}\right)^2,\ E_P = \frac{\mu}{k_p T}u^2. \end{aligned} \tag{2.30}$$

where E_{Total} denotes the total entropy generation, E_{HT} the entropy generation due to the heat transfer, E_{VS} the entropy generation due to the fluid friction, E_{JH} the entropy generation due to the Joule heating effect, E_{CS} the entropy generation due to couple stress parameter, E_{MT} the entropy generation due to mass transfer phenomena and E_P the entropy generation due to porous medium. The non-dimensionless form of the entropy generation (S_{Total}) is expressed as follows (ref. 2.2),

$$S_{Total} = \frac{h^2}{k}\, E_{Total} = \frac{Br^2}{(Br\theta+\delta)^2}\left(\frac{\partial\theta}{\partial Y}\right)^2 + \frac{1}{Br\theta+\delta}\left(\Gamma + Br\left(\left(\frac{\partial U}{\partial Y}\right)^2 + \frac{1}{\gamma}\left(\frac{\partial^2 U}{\partial Y^2}\right)^2 + DaU^2\right)\right) + \chi_1\left(\frac{Br^2}{Brf+\delta_1}\left(\frac{\partial f}{\partial Y}\right)^2 + \frac{Br^2}{Br\theta+\delta}\frac{\partial\theta}{\partial Y}\frac{\partial f}{\partial Y}\right). \tag{2.31}$$

Under a weak electric field consideration along with an additional assumption $S = 1$ *i.e.* $Br = \Gamma$, we find $Br << 1$. Thus, ignoring Br^2 in the equation 2.31 reduces the expression of the total entropy generation to,

$$S_{Total} \approx \frac{Br}{\delta}\left(1 + \left(\frac{\partial U}{\partial Y}\right)^2 + \frac{1}{\gamma}\left(\frac{\partial^2 U}{\partial Y^2}\right)^2 + DaU^2\right) \tag{2.32}$$

The Joule heating parameter is found to be the principal contributor of entropy generation in microchannel even under a weak electric field. The following metric S_R measures the contribution of total entropy generation to entropy generation due to the Joule heating parameter,

$$S_R = \frac{\delta S_{Total}}{Br}. \tag{2.33}$$

Figures 2.8,2.11,2.14 show that the temperature increases with increasing values of both the inverse couple stress parameter and inverse Darcy parameter but decreases with enhancement of diffusive Reynolds number. The enhancement of both inverse couple stress and inverse permeability of the medium in nanofluid increases heat generation due to fluid friction. The diminution of ion diffusion coefficient diminishes net charge density thereby producing lesser frictional heat generation due to reduced velocity gradient. The effect of ion diffusion on heat generation is prominent in a nanometer height channel, which is achieved by considering $S = \lambda = 1$ *i.e.* $Br = \Gamma$ (it is possible when $h = \frac{10^{-7}}{5}$ keeping other parameter values fixed in table 2.1), as under the above consideration the heat generation due to Joule heating remains small. Moreover, the condition on h is not mandatory to get an effective result for ion diffusion coefficient on temperature as increment in electroosmotic parameter values may furnish similar result without the assumption of $S = \lambda = 1$. Figures 2.9,2.12,2.15 depict a completely opposite behaviour for the nanoparticle concentration profiles compared to 2.8,2.11,2.14. The enhancement of temperature gradient pushes away nanoparticles to a lower temperature gradient region thereby reducing mass transfer rate due to thermophoretic diffusion process. Figures 2.10,2.13,2.16 show that the entropy generation decreases with a rise in the diffusive Reynolds number in nanofluid but increases with enhancement of the inverse couple stress and inverse Darcy number. The lower permeability of the medium produces more irreversible heat loss due to the viscous drag force. A similar trend is observed when the ion diffusivity is high.

However, the enhancement of the couple stress parameter diminishes both velocity and temperature thereby reduces the total entropy generation. Figure 2.13 shows that shape of the entropy generation graphs are dependent on couple stress parameter. Moreover, it suggests that entropy generation flattens near EDL region. This trend is a consequence of the fact that heat generation due to frictional drag force increases near microchannel beds.

2.5 Conclusions

We have examined the impact of ion diffusion coefficient, couple stress and permeability of the medium on steady electroosmotic nanofluid flow in a microchannel between two permeable beds. The findings show that the enhancement of both diffusive Reynolds number and inverse permeability of the medium diminishes bulk nanofluid flow rate in a microchannel. The principal objective of this study is to understand the effects of ion diffusion coefficient on thermal and nanoparticle concentration profiles in a nanofluid. It is found that nanofluid temperature increases with enhancement of ion diffusion coefficient. Moreover, It is observed that nanofluid temperature increases with diminution of couple stress parameter. This phenomena is attributed to additional energy consumption by rotating fluid particles due to enhancement of couple stress. Finally, a comparative study on the effects of couple stress parameter, ion diffusion coefficient and porous permeability of the medium on the entropy generation is investigated. The important findings from our study are summarized below,

1. The Zeta potential decreases with enhancement of the diffusive Reynolds number.

2. The nanofluid velocity increases with enhancement of porous permeability parameter, inverse couple stress parameter but decreases with diffusive Reynolds number. The bulk nanofluid flow rate is expressed as a non-linear function of couple stress parameter.

3. The nanofluid temperature increases with diminution of couple stress parameter, porous permeability of the medium but decreases with diminution of ion diffusion coefficient.

4. The nanoparticle concentration decreases with diminution of couple stress parameter, porous permeability of the medium but increases with diminution of ion diffusion coefficient.

5. The total entropy generation decreases with enhancement of the diffusive Reynolds number but increases with the enhancement of inverse couple stress parameter and inverse Darcy number. The increase in entropy generation is significantly influenced due to increment in friction produced by nanofluid particles during

migration through the porous media. The shape of the entropy generation graph depends on couple stress parameter.

2.6 Appendix

Exact analytical solution of velocity profile: The solution U has the following form when $Da = 0$,

$$U = Real[C_1 + C_2 e^{y_2\ Y} + C_3 e^{y_3\ Y} + C_4 e^{y_4\ Y} - \frac{\Pi}{Re}\ Y - \tilde{\Phi}], \tag{2.34}$$

$$\tilde{\Phi} = (d_1\ \cosh \kappa Y + d_2\ \sinh \kappa Y),$$

$$\begin{pmatrix} -\kappa^4 + \gamma\kappa^2 & -\kappa\ \gamma\ Re \\ -\kappa\ \gamma\ Re & -\kappa^4 + \gamma\kappa^2 \end{pmatrix} \begin{pmatrix} d_1 \\ d_2 \end{pmatrix} = \begin{pmatrix} \frac{\gamma\kappa^2}{\lambda} \\ \frac{\gamma\kappa^2\beta(Z_2 - Z_1 Cosh\kappa)\ Csch\kappa}{\lambda Z_1} \end{pmatrix}$$

where,

$$y_i^3 - \gamma\ y_i + Re\ \gamma = 0,\ E_{ij} = e^{y_j} - e^{y_i},\ L_{ij} = L_j - L_i,\ T_3 = \tilde{\Phi}''|_{Y=0},$$

$$F_1 = \alpha\sqrt{L_1}\Pi + \frac{\Pi}{Re} + \tilde{\Phi}'|_{Y=0},\ F_2 = -\alpha\sqrt{L_2}\Pi + \frac{\Pi}{Re} + \tilde{\Phi}'|_{Y=1},$$

$$F_3 = \frac{1}{E_{23}}(F_2 - e^{y_2}F_1),\ F_4 = L_{23}\frac{e^{y_2}\alpha}{E_{23}\sqrt{L_1}} - \frac{\alpha y_2}{\sqrt{L_1}},$$

$$F_5 = T_3 - y_2 F_1 - L_{23}F_3,\ T_1 = \frac{\alpha U_{B_1}}{\sqrt{L_1}} + F_1,\ T_2 = -\frac{\alpha U_{B_2}}{\sqrt{L_2}} + F_2,$$

$$T_4 = \frac{T_2 - T_1 e^{y2}}{E_{23}},\ T_5 = T_3 - T_1 y_2 - \frac{L_{23}(T_2 - T_1 e^{y_2})}{E_{23}},\ y_5 = \frac{E_{24}y_4}{E_{23}},$$

$$y_6 = L_{24}y_4 - \frac{E_{24}L_{23}y_4}{E_{23}},\ C_4 = \frac{T_5}{y_6},\ C_3 = \frac{T_4 - C_4 y_5}{y_3},$$

$$C_2 = \frac{T_1 - C_4 y_4 - C_3 y_3}{y_2},\ C_1 = U_{B_1} - C_2 - C_3 - C_4 + \tilde{\Phi}|_{Y=0},$$

$$T_5 = \tilde{\Phi}''|_{Y=1},\ U_{B_1} = \frac{FF_5FF_3 - FF_2FF_6}{det},$$

$$U_{B_2} = \frac{FF_1FF_6 - FF_3FF_4}{det},\ det = FF_1FF_5 - FF_2FF_4,$$

$$FF_1 = C_{1B_1} + e^{y_2}C_{2B_1} + e^{y_3}C_{3B_1} + e^{y_4}C_{4B_1},$$

$$
\begin{aligned}
FF_2 &= C_{1B_2} + e^{y_2}C_{2B_2} + e^{y_3}C_{3B_2} + e^{y_4}C_{4B_2} - 1,\\
FF_3 &= -(C_{1B_0} + e^{y_2}C_{2B_0} + e^{y_3}C_{3B_0} + e^{y_4}C_{4B_0}) + \tilde{\Phi}|_{Y=1} + \frac{\Pi}{Re},\\
FF_4 &= {y_2}^2 e^{y_2}C_{2B_1} + {y_3}^2 e^{y_3}C_{3B_1} + {y_4}^2 e^{y_4}C_{4B_1},\\
FF_5 &= {y_2}^2 e^{y_2}C_{2B_2} + {y_3}^2 e^{y_3}C_{3B_2} + {y_4}^2 e^{y_4}C_{4B_2},\\
FF_6 &= -({y_2}^2 e^{y_2}C_{2B_0} + {y_3}^2 e^{y_3}C_{3B_0} + {y_4}^2 e^{y_4}C_{4B_0}) + T_5,\\
C_{4B_1} &= \frac{F_4}{y_6},\ C_{4B_2} = \frac{\alpha L_{23}}{E_{23}y_6\sqrt{L_2}},\ C_{4B_0} = \frac{5}{y_6},\\
C_{3B_1} &= \frac{\frac{-\alpha e^{y_2}}{E_{23}\sqrt{L_1}} - \frac{F_4 y_5}{y_6}}{y_3},\\
C_{3B_2} &= \frac{\frac{-\alpha}{E_{23}\sqrt{L_2}} - \frac{L_{23}\alpha y_5}{E_{23}\sqrt{L_2}y_6}}{y_3},\ C_{3B_0} = \frac{F_3 - \frac{F_5 y_5}{y_6}}{y_3},\\
C_{2B_1} &= \frac{\frac{\alpha}{\sqrt{L_1}} - C_{4B_1}y_4 - C_{3B_1}y_3}{y_2},\ C_{2B_2} = \frac{-C_{4B_2}y_4 - C_{3B_2}y_3}{y_2},\\
C_{2B_0} &= \frac{F_1 - C_{4B_0}y_4 - C_{3B_0}y_3}{y_2},\ C_{1B_1} = 1 - C_{2B_1} - C_{3B_1} - C_{4B_1},\\
C_{1B_2} &= -C_{2B_2} - C_{3B_2} - C_{4B_2},\\
C_{1B_0} &= -C_{2B_0} - C_{3B_0} - C_{4B_0} + \tilde{\Phi}|_{Y=0}.
\end{aligned}
$$

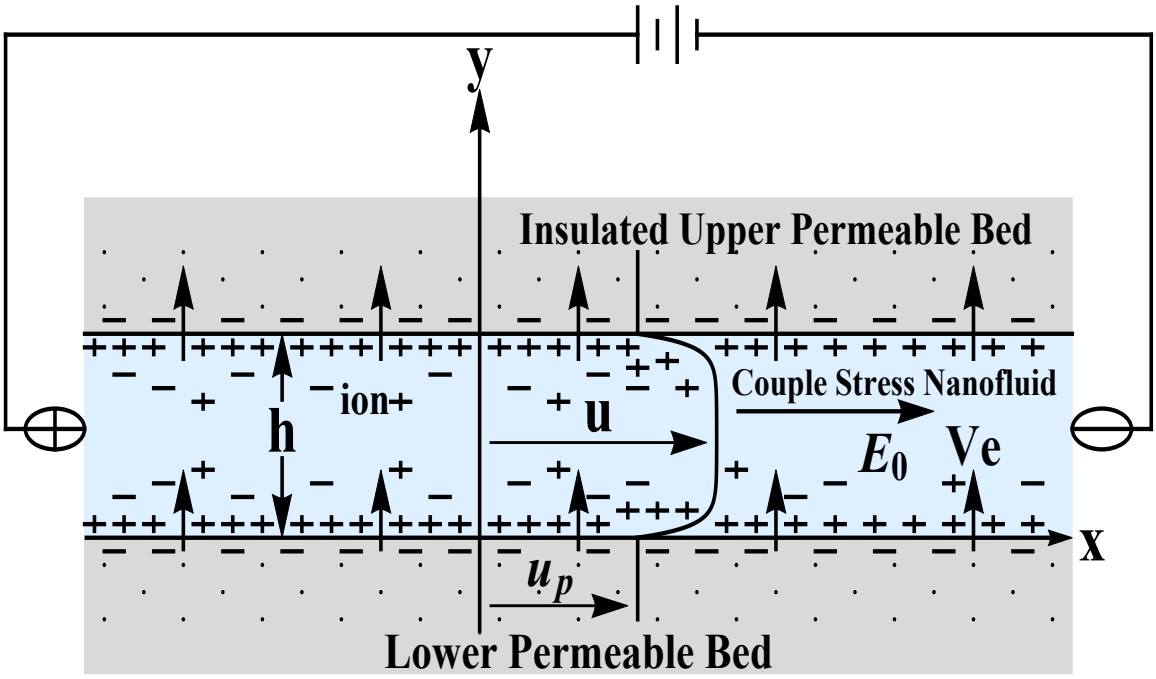

Figure 2.1: Physical diagram of the steady couple stress nanofluid flow in a microchannel between two permeable beds.

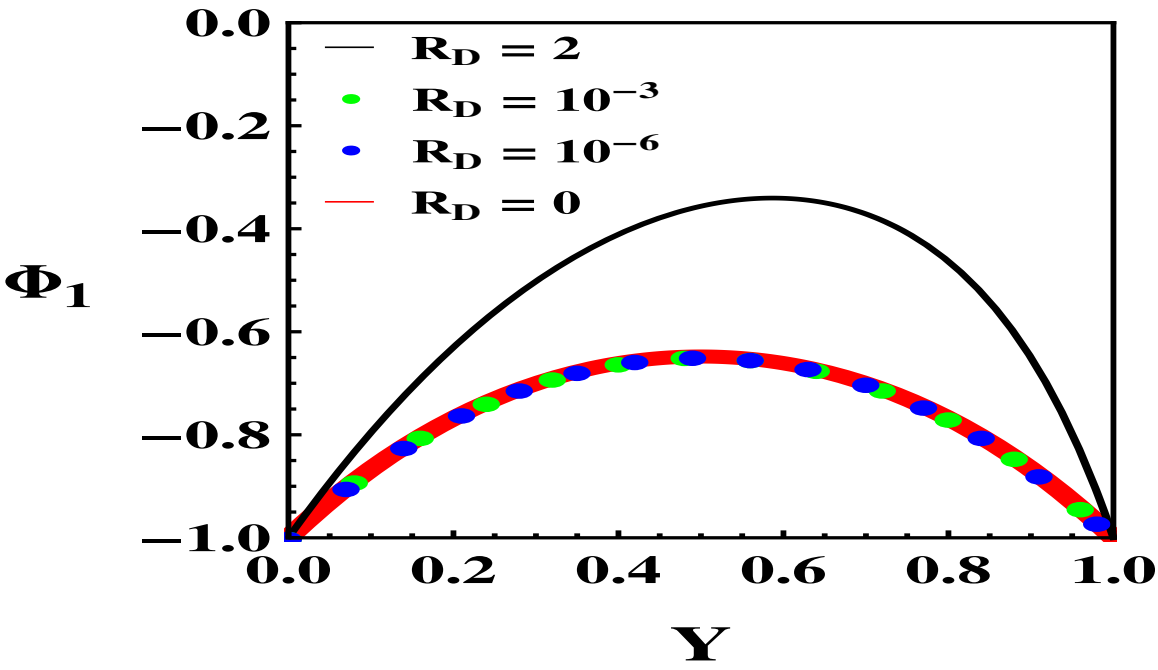

Figure 2.2: An illustrative comparison between the DTM solution Φ_1 for different values of the diffusive Reynolds number R_D. For, $R_D = 0$ we obtain the exact solution of the equation (7) namely Φ which satisfies $\frac{\partial^2 \Phi}{\partial Y^2} = \kappa^2 \Phi$, plotted in red colour.

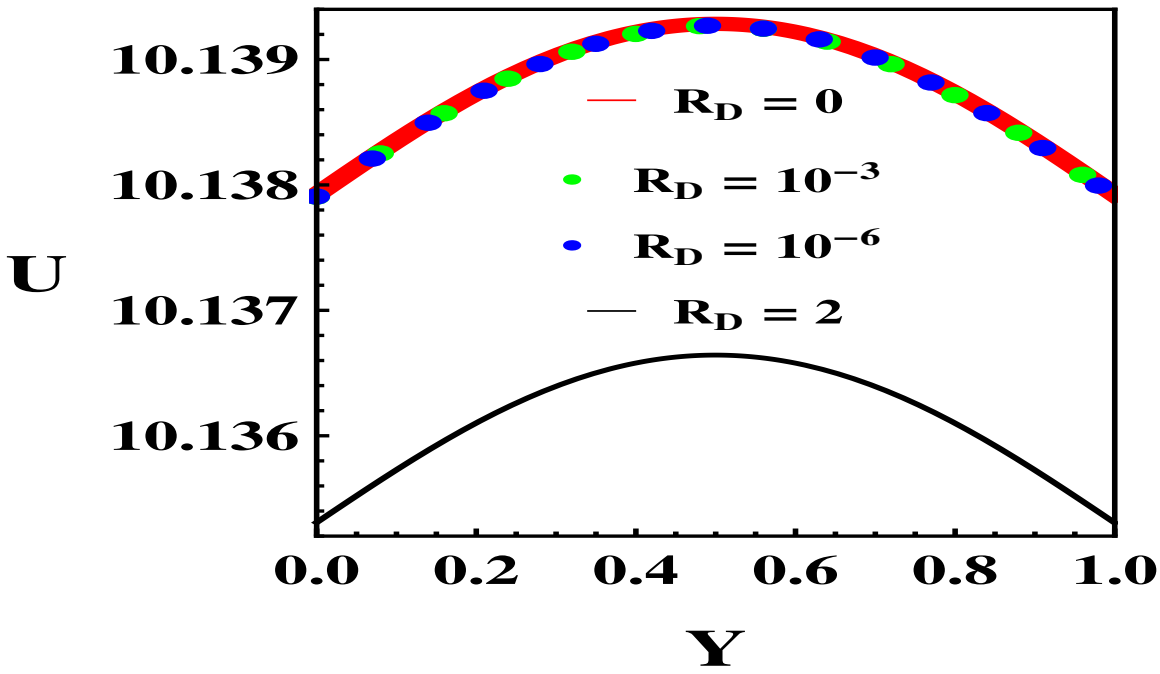

Figure 2.3: An illustrative comparison between the DTM solution U with the Zeta potential Φ_1 for different values of the diffusive Reynolds number R_D when $Da = 0$. For, $R_D = 0, Da = 0$ we obtain the exact solution of the equation (16), plotted in red colour, which is presented in appendix 6.

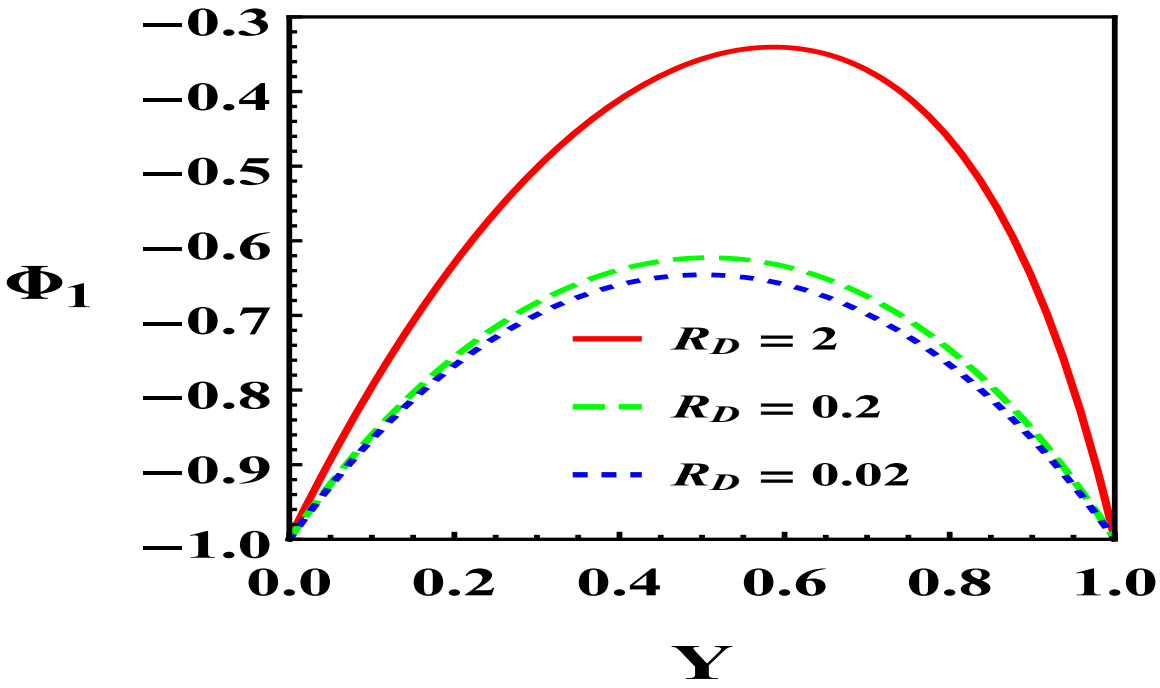

Figure 2.4: Effects of the ion diffusion coefficient in terms of the diffusive Reynolds number on formation of the Zeta potential is illustrated when $\kappa = 2$.

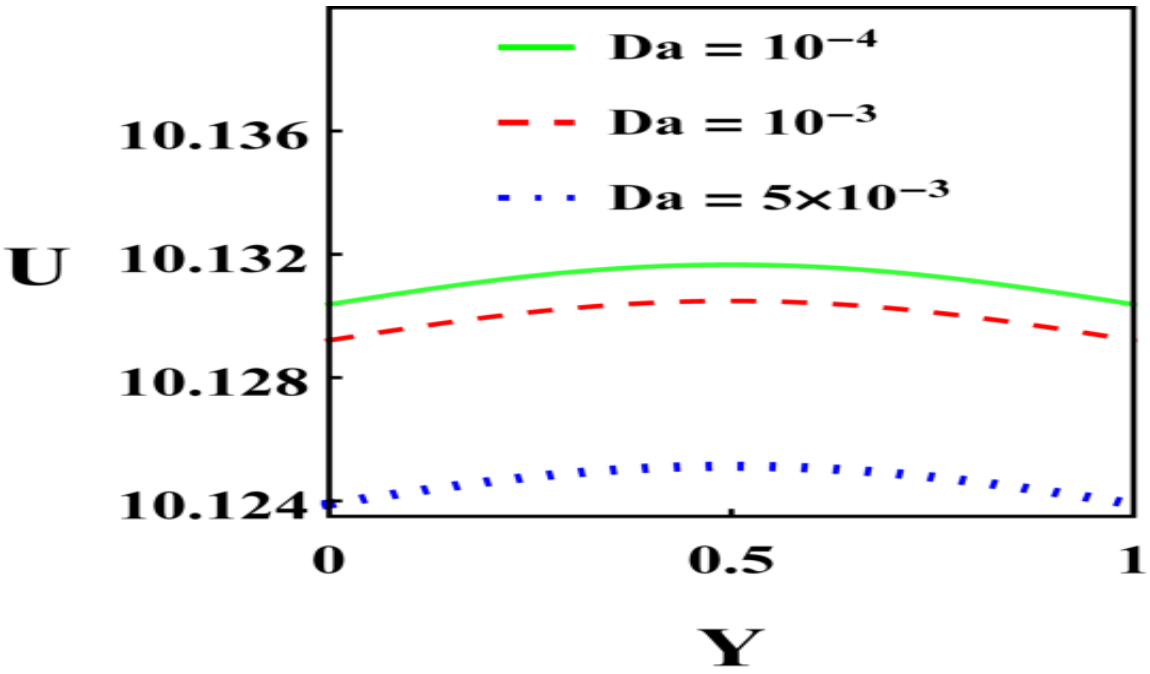

Figure 2.5: The variations of axial velocity with inverse Darcy number is illustrated. The parameter values used for this illustration are: $\gamma = 0.1,\ \lambda = \frac{10^4}{2},\ S = 1,\ \kappa = 2,\ R_D = 0.2,\ \phi_1 = 10,\ \phi_2 = 10^{-3},\ \Pi = -1.$

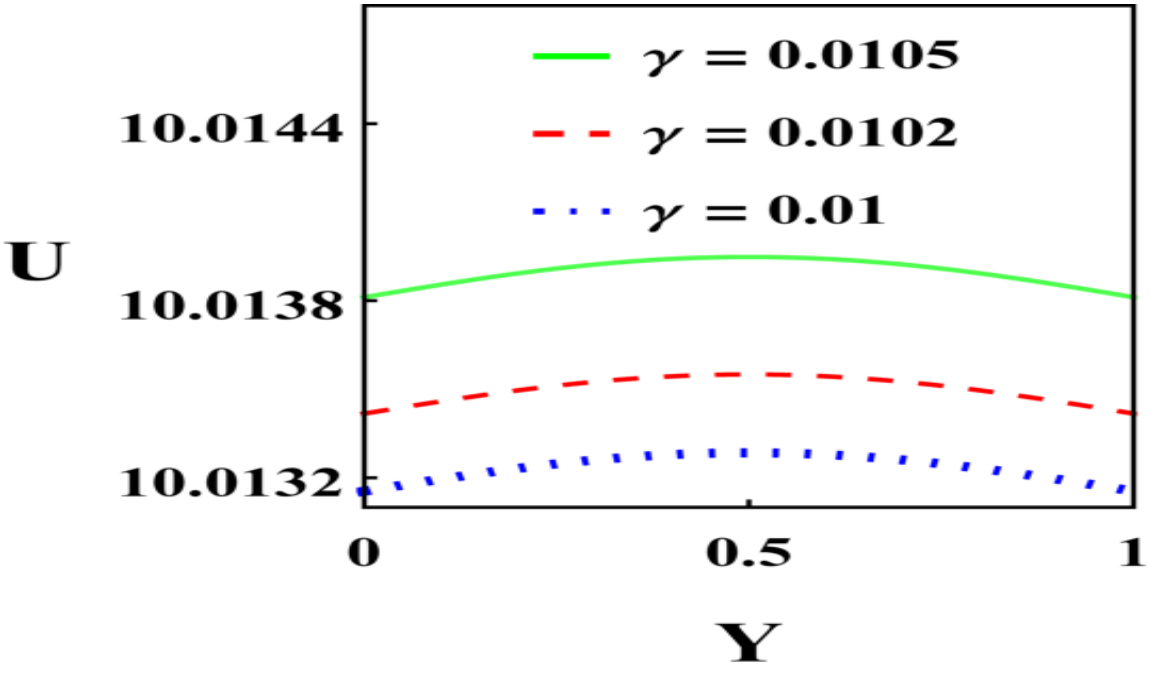

Figure 2.6: The variations of axial velocity with inverse couple stress parameter is illustrated. The parameter values used for this illustration are: $Da = 10^{-4},\ \lambda = \frac{10^4}{2},\ S = 1,\ \kappa = 2,\ R_D = 2,\ \phi_1 = 10,\ \phi_2 = 10^{-3},\ \Pi = -1.$

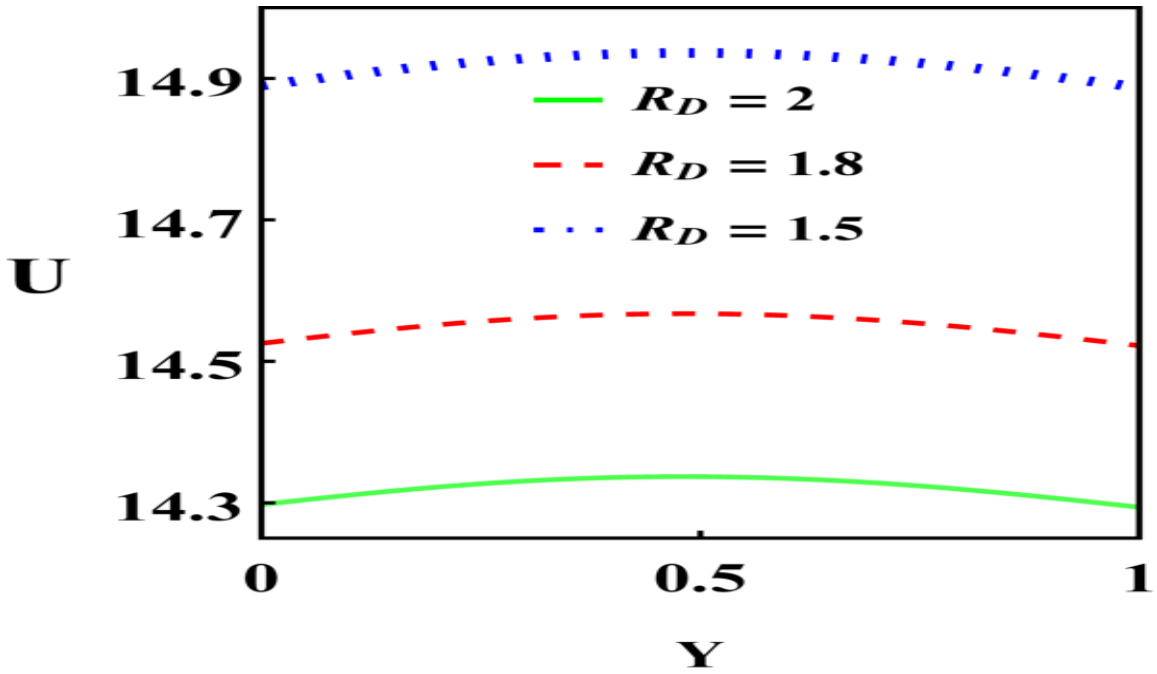

Figure 2.7: The variations of axial velocity with diffusive Reynolds number is illustrated. The parameter values used for this illustration are: $\gamma = 1,\ \lambda = 1,\ S = 1,\ \kappa = 3,\ Da = 10^{-4},\ \phi_1 = 20,\ \phi_2 = 2 \times 10^{-3},\ \Pi = -1.$

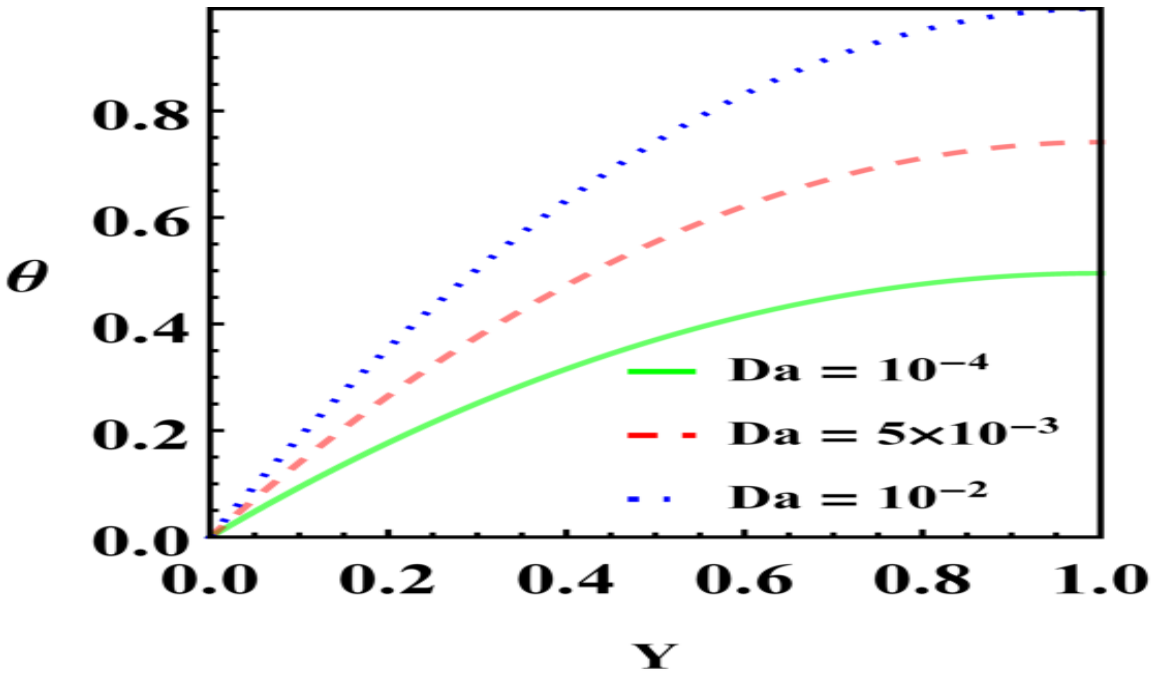

Figure 2.8: The variations of nanofluid temperature with inverse Darcy number is illustrated. The parameter values used for this illustration are: $\gamma = 0.1,\ \lambda = \frac{10^4}{2},\ S = 1,\ \kappa = 2,\ R_D = 0.2,\ \phi_1 = 10,\ \phi_2 = 10^{-3},\ \Pi = -1.$

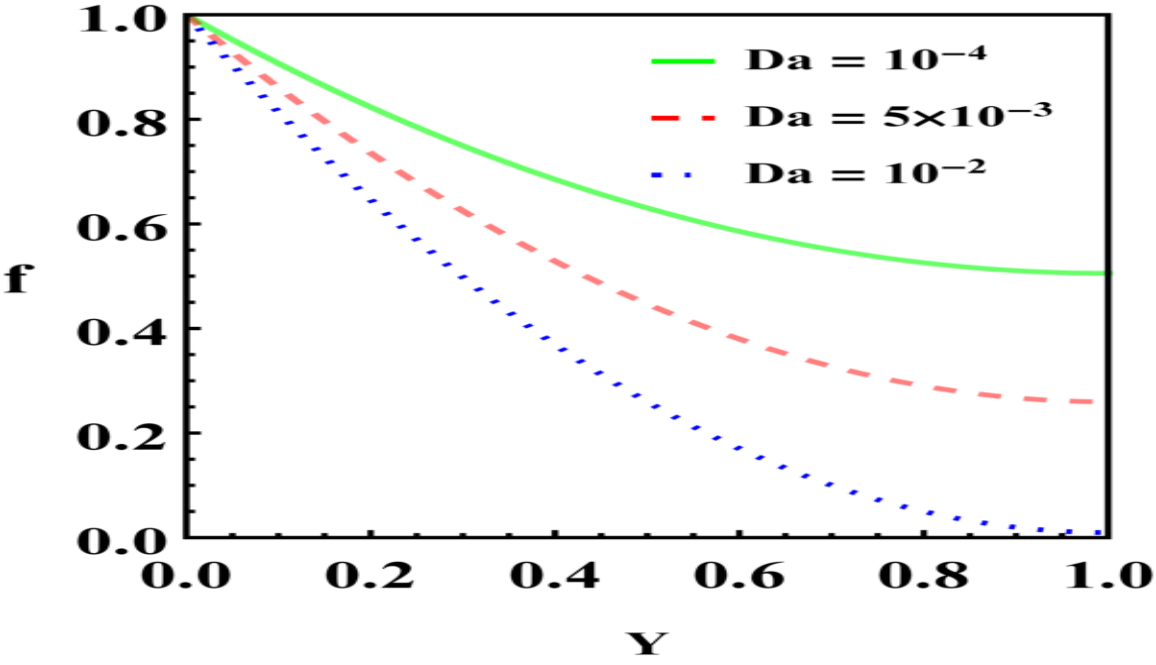

Figure 2.9: The variations of nanoparticle concentration with inverse Darcy number is illustrated. The parameter values used for this illustration are: $\gamma = 0.1,\ \lambda = \frac{10^4}{2},\ S = 1,\ \kappa = 2,\ R_D = 0.2,\ \phi_1 = 10,\ \phi_2 = 10^{-3},\ \Pi = -1.$

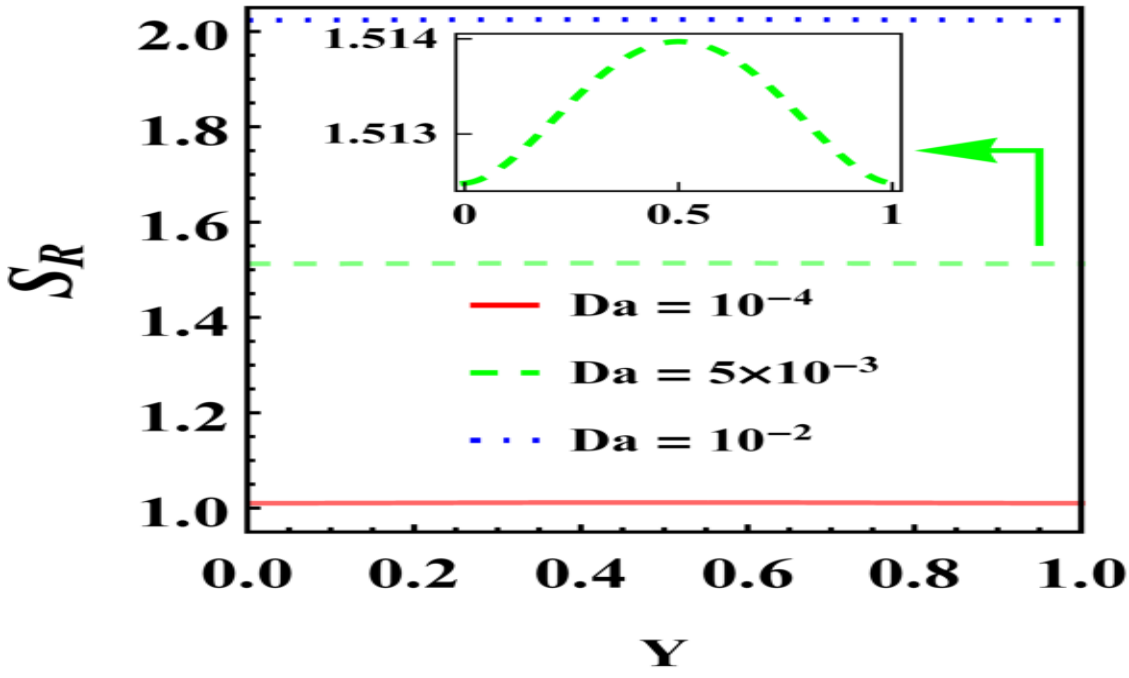

Figure 2.10: The variations of entropy generation with inverse Darcy number is illustrated. The parameter values used for this illustration are: $\gamma = 0.1,\ \lambda = \frac{10^4}{2},\ S = 1,\ \kappa = 2,\ R_D = 0.2,\ \phi_1 = 10,\ \phi_2 = 10^{-3},\ \Pi = -1.$

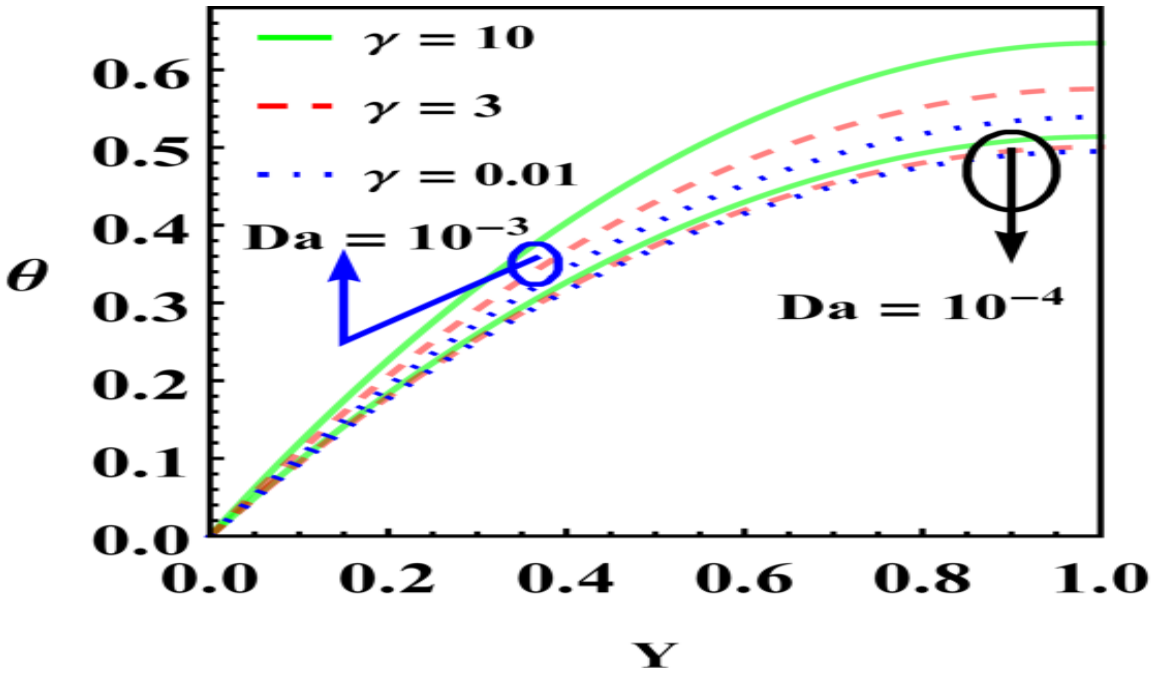

Figure 2.11: The variations of nanofluid temperature with inverse couple stress parameter is illustrated. The parameter values used for this illustration are: $\lambda = \frac{10^4}{2}$, $S = 1$, $\kappa = 2$, $R_D = 2$, $\phi_1 = 10$, $\phi_2 = 10^{-3}$, $\Pi = -1$.

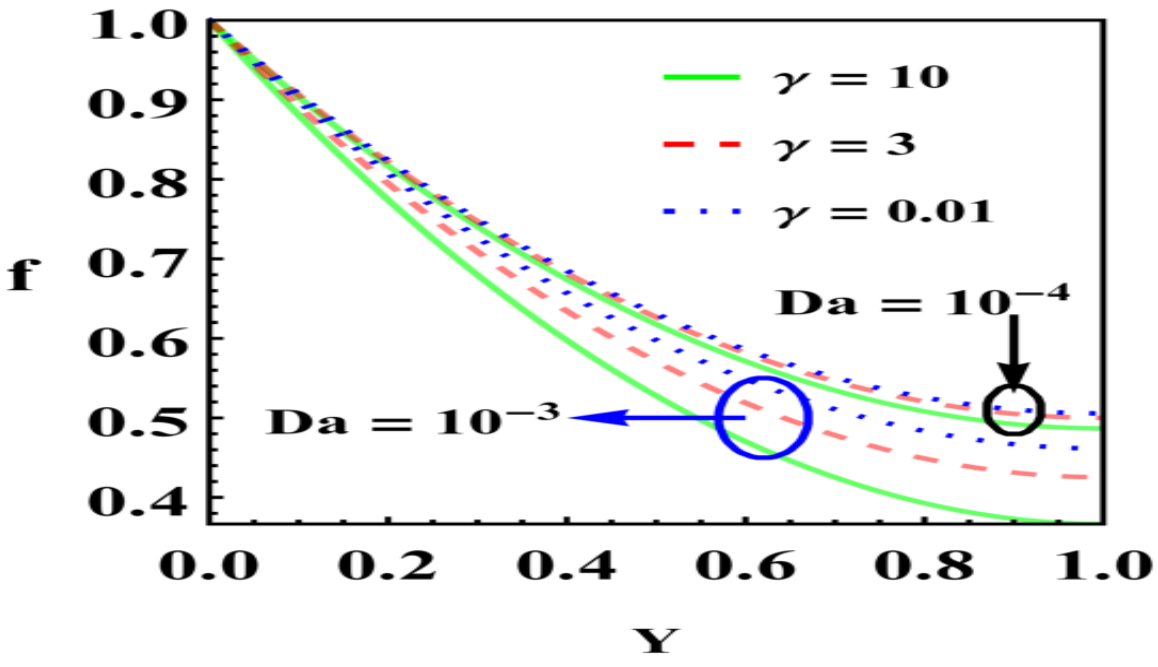

Figure 2.12: The variations of nanoparticle concentration with inverse couple stress parameter is illustrated. The parameter values used for this illustration are: $\lambda = \frac{10^4}{2}$, $S = 1$, $\kappa = 2$, $R_D = 2$, $\phi_1 = 10$, $\phi_2 = 10^{-3}$, $\Pi = -1$.

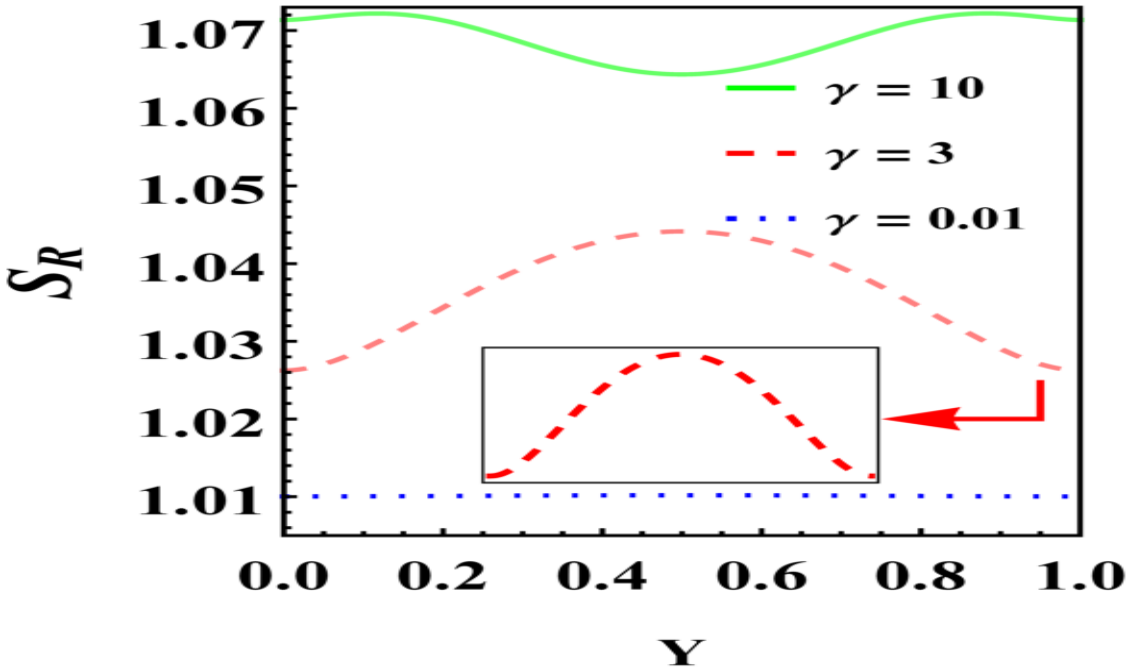

Figure 2.13: The variations of entropy generation with inverse couple stress parameter is illustrated. The parameter values used for this illustration are: $Da = 10^{-4}$, $\lambda = \frac{10^4}{2}$, $S = 1$, $\kappa = 2$, $R_D = 2$, $\phi_1 = 10$, $\phi_2 = 10^{-3}$, $\Pi = -1$.

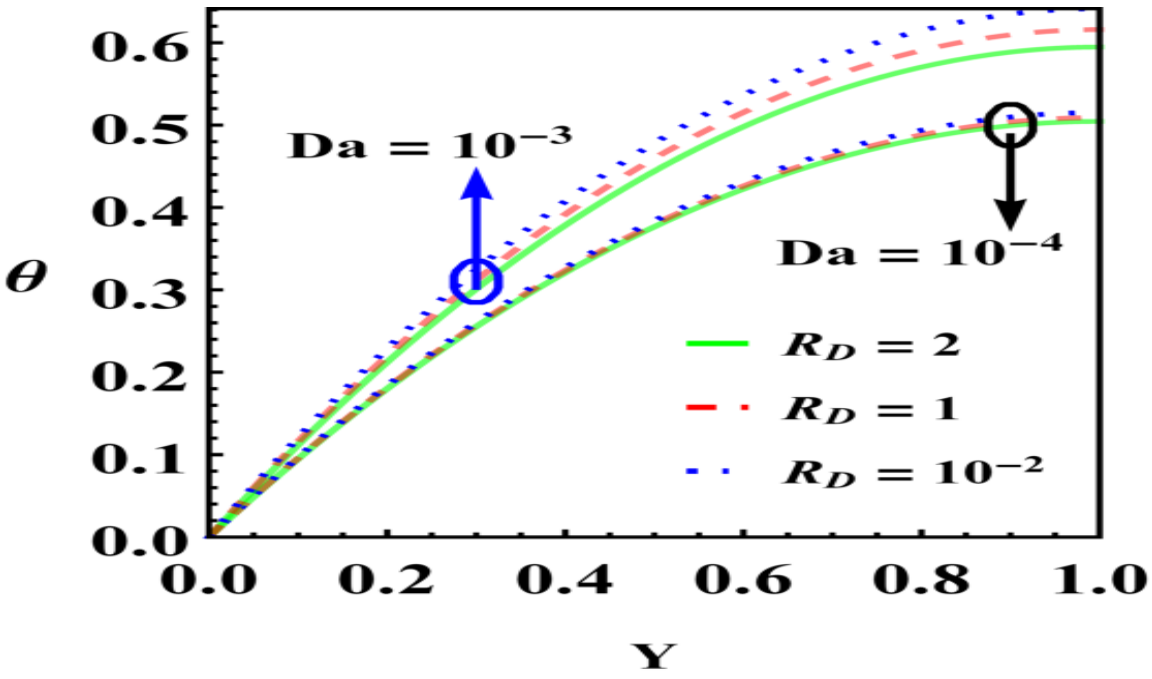

Figure 2.14: The variations of nanofluid temperature with diffusive Reynolds number is illustrated. The parameter values used for this illustration are: $\gamma = 1$, $\lambda = 1$, $S = 1$, $\kappa = 3$, $\phi_1 = 20$, $\phi_2 = 2 \times 10^{-3}$, $\Pi = -1$.

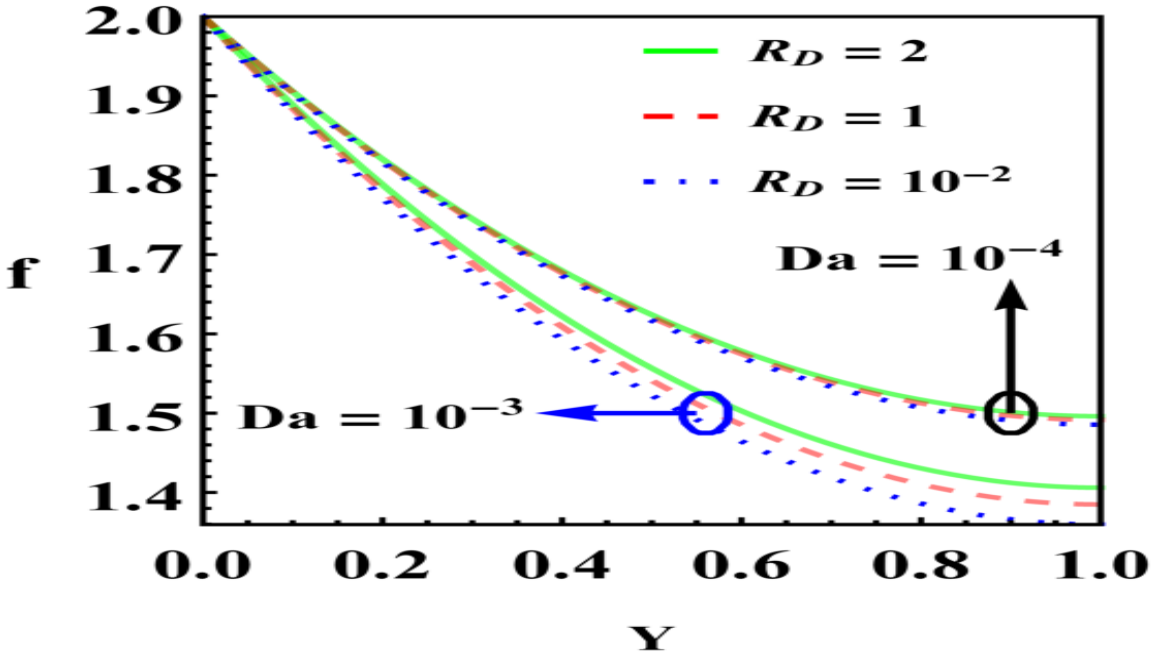

Figure 2.15: The variations of nanoparticle concentration with diffusive Reynolds number is illustrated. The parameter values used for this illustration are: $\gamma = 1,\ \lambda = 1,\ S = 1,\ \kappa = 3,\ \phi_1 = 20,\ \phi_2 = 2 \times 10^{-3},\ \Pi = -1$.

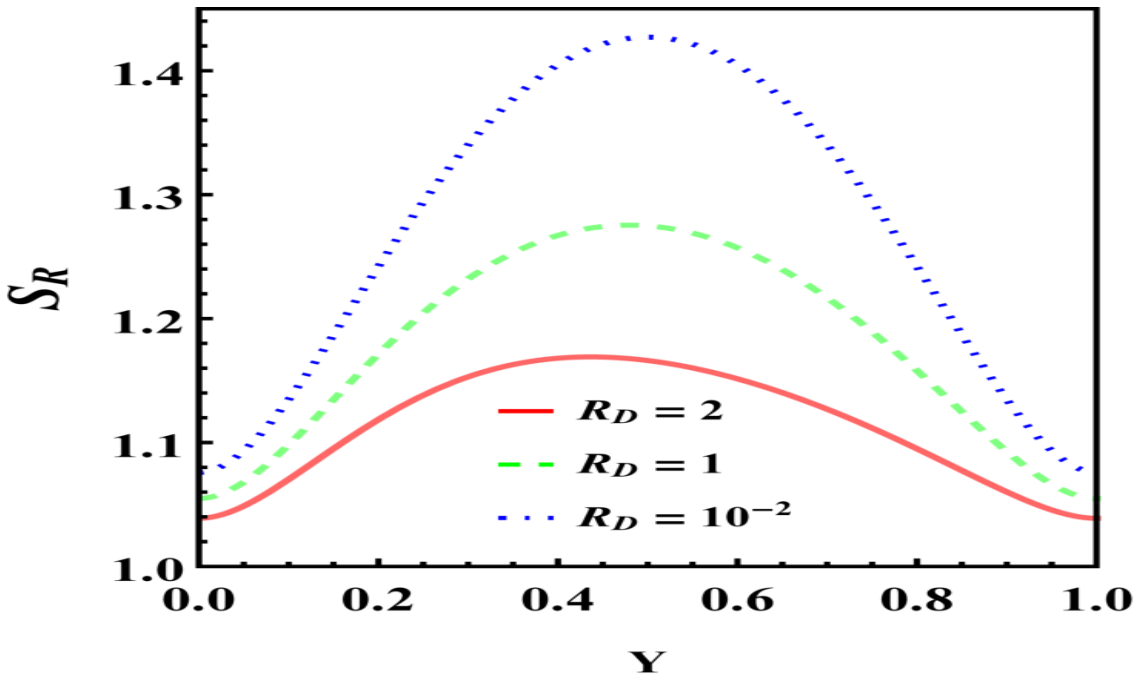

Figure 2.16: The variations of entropy generation with diffusive Reynolds number is illustrated. The parameter values used for this illustration are: $\gamma = 1,\ \lambda = 1,\ S = 1,\ \kappa = 3,\ Da = 10^{-4},\ \phi_1 = 20,\ \phi_2 = 2 \times 10^{-3},\ \Pi = -1$.

Chapter 3

Entropy generation of electrothermal nanofluid flow between two permeable walls under injection process [2]

3.1 Introduction

The fluid flow and heat transfer phenomena in a laboratory-on-a-chip device with micrometer channel width is currently an important topic of scientific research. Low production cost and small amount (micro litre) of sample requirement make it a viable option for conducting medical experiments in recent times. Such microfluidic devices have gained importance in applications related to pumping, mixing and separation of chemical/biological species (Selvaganapathy et al. [2002], Johnson and Locascio [2002], Wang et al. [2004]). The study of ion diffusion coefficients (Nielsen et al. [1952], Sato et al. [2012], Zhong and Friedman [1988]) on electrolyte liquid flow in the channels with micro/nano meter heights is a current trends of research. The study of electrolyte flow in micro-nano devices is essential to design electric discharge convection lasers (EDCLs), medical equipment (Conway [1991], Miller and Simon [2008]). Kong et al. [2017] investigated the effects of temperature on the ion diffusion coefficients. They have shown that enhancement in temperature increases the ion diffusion coefficient. We have investigated the effects of ion diffusion coefficient on nanofluid velocity. The increment in ion diffusion coefficient is found to increase nanofluid velocity inside microchannel. Thus, frictional heat generation is expected to increase with enhancement of ion diffusion coefficient which is in line with the work of Kong et al. In this chapter, a unidirectional fluid flow model (Vajravelu et al. [2003], Malathy and Srinivas [2008], Bitla and Iyenger [2014]) is considered in the

[2]The content of this chapter has been published in *Journal of nanofluid* (American Scientific Publishers), 11 (2022) 714-727.

presence of injection to incorporate the effects of ion diffusion coefficient on velocity.

In general, it is observed that an externally applied electric field induces an electroosmotic fluid flow in a microchannel, apart from the pressure difference. A thin charged layer (known as electric double layer or EDL), formed near the channel walls due to ion separation, starts to migrate under the influence of an applied electric field. The fluid-channel interface exhibits trapped charges in the channel wall and consequently attracts oppositely charged ions present in the fluid. Far away from the wall, the fluid is assumed to have a zero net charge. The charged fluid in the EDL layer starts to move when an electric field is applied and consequently drags the fluid layers adjacent to the edge of the EDL. The no-slip boundary condition at the channel walls and assumption of high ion concentration in the fluid makes Smoluchowski slip velocity a favourable choice to be considered as the electroosmotic velocity at the edge of the EDL. However, the no-slip boundary assumption may not yield accurate results for strongly hydrophobic surfaces (Park and Kim [2009]). Such effects of the injected fluid velocity and charge distribution on electroosmotic slip velocity at the edge of the EDL may cause it to deviate from Smoluchowski velocity, making it therefore an important topic of investigation.

The term "nanofluid" was first coined by CHOI [1995] who showed that augmentation of a tiny percentage of nanoparticles in the base fluid can significantly enhance its heat transfer capacity. The nano-sized ($10^{-9}m - 10^{-7}m$) particles (metallic, nonmetallic or organic) are often present in the base fluid in a microchannel either as impurities or added additionally to improve its heat transfer capacity (the fluid material may carry nanoparticle or sediments). These particles under the influence of an externally applied electric field manifests electroosmotic nanofluid flow phenomena such as the blood circulation mechanism wherein deposition of nutrients present in blood to tissues can be representative of such an electroosmotic nanofluid flow. A list of articles on the applications of nanofluid can be found in Alagumalai et al. [2022], Tayebi et al. [2021], Dogonchi et al. [2021b], Sadeghi et al. [2021], Veera Krishna et al. [2021b], Tayebi and Chamkha [2020], Chamkha et al. [2018], Dogonchi et al. [2019], Eshaghi et al. [2021], Dogonchi et al. [2021a], Veera Krishna et al. [2021a]. In a microchannel, the Joule heating effect is the principle contributor of heat generation in the presence of an externally applied strong electric field. However, under a weak electric field the contribution of convective heat transfer process and viscous dissipation in heat production starts to get manifested as observed in Section 3.3 of this chapter. It is observed in the findings that the normalized temperature follows an increasing trend with enhancement of the pressure gradient, whereas, the reverse trend is visible in the case of normalized nanoparticle concentration, when the electric field strength is very small. Moreover, it is found that the bulk nanofluid temperature is an almost quadratic function of the applied pressure gradient. The variations in the temperature distribution influences the nanoparticle diffusion rate through thermophoresis in the nanofluid. An interesting finding in this direction is presented below (discussed

in detail in Section 3.3),

$$\frac{D_T}{D_B} \approx \frac{3\ C_{ref}\ \delta}{\gamma}\ (1 - \int_0^1 f\ dY).$$

The above expression depicts a relationship between thermophoresis coefficient and the Brownian motion coefficient of nanoparticles in terms of the cross sectional nanoparticle concentration and Joule heating parameter, in the absence of injection velocity. The expression on the right hand side measures the nanoparticle distribution with variations in electric field strength; whereas left hand side carries information about nanoparticle diameter. These findings can potentially reveal new intrinsic physical relationships of the temperature and mass distribution in a microchannel.

The presence of porosity at the microchannel walls gives rise to many intricate physical discoveries in a pressure-driven fluid-flow phenomena. In fact, the pressure drop phenomena across porous channel walls (in a pipe or channel) is of principle interest for the engineers to design engineering and medical devices pertaining to applications such as oil extraction process, fixed bed catalytic reactors, gaseous diffusion, transpiration cooling, dialysis of blood in artificial kidney etc. (cf. Berman [1953], Sellars [1955], Turan and Cuhadaroglu [2020], Morduchow [1956], Beavers and Joseph [1967], Dutta and Beskok [2001], Wang [1971], Radhakrishnamacharya and Maiti [1977], Rajagopal and Tao [1995], Dhivya et al. [2021], Vajravelu et al. [2003], Malathy and Srinivas [2008], Bitla and Iyenger [2014], Krishna and Chamkha [2020], Veera Krishna and Chamkha [2019], Krishna et al. [2020], Krishna [2020a,b], Veera Krishna [2020], Veera Krishna et al. [2018], Veera Krishna and Chamkha [2018]). Thus, the flow behaviour at the fluid-porous wall interface is an important domain of scientific research. Some of the important results in this direction are: (1) fluid flow through a porous media follows Darcy's law and (2) the Beavers and Joseph [1967] boundary condition best describes the flow behaviour at the fluid-porous bed interface when fluid flow is parallel to the channel surface. The injected fluid velocity introduces us into the realm of discovering the flow behaviour through the porous wall and finding new physical boundary conditions at the fluid-wall interface. An extensive discussion on this topic is devoted in Section 3.2.1 of this chapter. The findings suggest that the injected fluid velocity term must be incorporated in the Darcy law to express the flow behaviour through the porous medium in the presence of both high injection fluid velocity and large porous permeability value.

It is of utmost importance for engineers and medical device developers to minimize the irreversible thermal loss in a system, thereby making it energy efficient (Misra et al. [2020], Afshar et al. [2021]). The importance of entropy generation and its contribution to the understanding of heat transfer process is described by Herwig [2018]. The electric current passing through a solid/fluid medium of finite conductivity, converts applied electric energy to thermal energy in micro scale by collisions between conducting electrons and atoms constituting the conductor. In microfluidic

devices Joule heating effect (Horiuchi and Dutta [2004], Khan et al. [2022]) is found to be a major contributor of entropy generation when a strong electric field of strength 1 $kVcm^{-1}$ or above is applied. However, under a weak electric field it is observed that the fluid friction, heat transfer and mass transfer also affect entropy generation besides Joule heating effect. A comparative study on the total entropy generation is conducted to comprehend the most sensitive factors responsible for enhancement of entropy generation in the system in Section 3.3.2.2. Moreover, it is found that the total entropy generation follows a quadratic relationship with the Joule heating parameter in the absence of both injection velocity and the viscous dissipation.

This article is devoted to study the effects of nanofluid injection velocity on EDL formation, slip velocities generated at both fluid-wall interface and edge of the EDL, temperature/nanoparticle distribution in a microchannel and total entropy generation of the steady electroosmotic nanofluid flow between permeable walls. The heat flow inside microchannel takes place due to the Joule heating, viscous dissipation and the prescribed temperature at the channel walls. A significant number of studies in electroosmotic flow theory is conducted on non-porous channels in the absence of fluid injection process through channel walls. However, the present study can model fluid filtration process through micro porous membranes in a microchannel, which has resemblance with the model used by Beavers and Joseph [1967] except the considerations of injection process (Abate et al. [2010]) and nanofluid flow phenomena under a mild electric field. Recently, several researchers Vajravelu et al. [2003], Malathy and Srinivas [2008], Bitla and Iyenger [2014] have carried out the investigation of pulsating fluid flow process between permeable beds with fluid injection at the lower channel bed using Beavers-Joseph boundary condition (Beavers and Joseph [1967]) for both Newtonian and Non-Newtonian fluid models. However, their studies have not considered the presence of an external electric field into their model. Moreover, these studies are restricted to analyze the velocity profiles, whereas, the present chapter is devoted to analyze the effects of injected velocity on the thermal as well as nanoparticle concentration profiles in such a flow. The consideration of nanofluid injection process through porous channel walls is shown to influence on formation of Zeta potential inside microchannel thereby impacting fluid flow behaviour inside EDL. Moreover, the electroosmotic velocity at the edge of EDL is studied under slip boundary condition. The present study attempts to explore filtration flow behaviour under a weak electric field through micro porous membranes in microchannel, which can guide researchers to make designs/experiments thereby bearing potential for developing microfluidic devices. This theoretical study is carried out from a general point of view that bears the promise of important applications in biomicrofluidics. The novelty of this chapter lies on the following facts:

1. The effects of slip boundary condition at the solid-fluid interface, injection velocity and ion diffusivity on formation of electric potential distribution and electroosmotic slip velocity are discussed in Sections 3.2.1-3.2.4. The electroosmotic slip velocity is calculated by solving the Nernst-Planck equation and the

traditional Smoluchowski slip velocity has been derived from it. The increment in ion diffusion coefficient enhances nanofluid velocity.

2. The effects of the pressure gradient and frictional forces on the normalized temperature profiles are vividly visible when a weak electric field is applied. The nanofluid bulk temperature follows an almost quadratic relationship with pressure gradient.

3. The nanoparticle diffusion behaviour is analyzed in the absence of injection velocity. The Soret number is represented as a ratio of the total cross-sectional nanoparticle concentration to the Joule heating parameter.

4. A comparative study on the total entropy generation is conducted to identify the principle factors responsible for entropy generation under a weak electric field. Analytical expression for the total entropy generation follows a quadratic relationship with the Joule heating parameter in the absence of both injection velocity and the viscous dissipation as presented in equation 3.29.

The structure of this chapter can be summarized as follows. Section 3.2 discusses the approximate forms of the governing flow equations. Section 3.2.2 explains the boundary conditions used to solve thermophysical equations describing the present study. The impact of fluid friction force on heat generation under a low electric field strength inside microchannel is also assessed in this section. Section 3.2.4 introduces approximation conditions used to solve the Zeta potential distribution equation. An error analysis is carried out graphically to show the effectiveness of using an approximate expression for potential distribution over the exact solution (which can be expressed in terms of Bessel functions) in the same section. Section 3.3 is devoted to discussion of the graphical results on flow characteristics and total entropy generation obtained in the present study. The overall findings of this chapter are summarized in Section 3.3.3. The physical parameter values used in this study are presented in Table 3.3.2.1 in Section 3.3. The non-dimensional forms of the equations and their solutions are presented in Appendix.

3.2 Flow Analysis

The rectilinear steady flow of the viscous incompressible Newtonian nanofluid between two permeable walls (h denotes the distance between the walls) is considered for this study in the presence of an externally applied weak electric field of strength E_0 (the schematic diagram of the problem in the Cartesian coordinates is presented in Figure 3.1). It is assumed that the fluid-flow is driven by a uniform pressure gradient in the longitudinal direction in both microchannel and permeable walls. The fluid is assumed to have a small amount of nanoparticle and the temperature difference between channel walls is considered to be small. The nanofluid is injected at the lower wall with a velocity Ve that influences the pressure-driven flow through

the permeable walls thereby impacting the slip velocity generated at the fluid-wall interface. The existence of electroosmotic flow near the edge of the channel walls (beds) is governed by a newly derived slip condition that is a generalized version of the well-known Smoluchowski slip velocity condition. The following assumptions are made in conducting the analysis of the fluid flow model considered for study in this chapter:

1. The flow is fully developed, steady, laminar and incompressible.
2. The flow takes place between two parallel plates and microchannel height is assumed to be very small in comparison to channel length, which implies, $\frac{\partial}{\partial x} << \frac{\partial}{\partial y}$. Hence, the term $\frac{\partial}{\partial x}$ is neglected in this study.
3. The velocity fields in microchannel and through permeable bed are assumed to be $q = (u(y), Ve),\ q_1 = (u_p(y), Ve)$ respectively.
4. The thermophoresis and the Brownian diffusion terms are ignored in the thermal energy equation.
5. Homogeneous permeable walls are considered for study.

Under the above assumptions, the governing equations for the nanofluid flow in our study, in the Cartesian coordinates can be expressed as follows, (Bitla and Iyenger [2014], Ranjit and Shit [2017], Seth et al. [2018], Vajravelu et al. [2003], Malathy and Srinivas [2008])

$$Ve\ \frac{\partial u}{\partial y} = -\frac{1}{\rho}\ \frac{\partial p}{\partial x} + \nu\ \frac{\partial^2 u}{\partial y^2} + \frac{\rho_e}{\rho}\ E_0, \tag{3.1}$$

$$\frac{\partial p}{\partial y} = 0, \tag{3.2}$$

$$Ve\ \frac{\partial T}{\partial y} = \frac{k}{\rho\ C_p}\ \frac{\partial^2 T}{\partial y^2} + \sigma\ \frac{{E_0}^2}{\rho\ C_p} + \frac{\mu}{\rho\ C_p}\left(\frac{\partial u}{\partial y}\right)^2, \tag{3.3}$$

$$Ve\ \frac{\partial C}{\partial y} = D_B\ \frac{\partial^2 C}{\partial y^2} + \frac{D_T}{T_h}\ \frac{\partial^2 T}{\partial y^2}, \tag{3.4}$$

where, u denotes the velocity of the nanofluid in x direction, Ve the velocity of the nanofluid injected at the lower wall in y direction, T denotes the nanofluid temperature, C denotes concentration of nanoparticles present in the nanofluid. The physical parameters ν denotes kinematic viscosity, ρ the density, k the thermal conductivity, C_p the specific heat of the nanofluid. Here, ρ_e represents the net charge density, D_B

the Brownian diffusion parameter and D_T the thermophoresis parameter respectively. The contribution of the drag force $\frac{\nu}{C_p}\left(\frac{\partial u}{\partial y}\right)^2$ is very small (except near the channel walls) in the temperature equation as the longitudinal velocity gradient is small (and $\frac{\nu}{C_p} = \frac{10^{-9}}{3}$ is a small number, ref. Table 3.3.2.1) under bounded pressure gradient. The contributions of both longitudinal convective temperature and concentration gradients (denoted by $u\,\frac{\partial T}{\partial x}$ and $u\,\frac{\partial C}{\partial x}$ respectively) are ignored under an additional weak electric field consideration while analyzing the temperature and nanoparticle distribution (at a higher electric field, longitudinal velocity u increases with enhancement of electric field and only the contribution of the Joule heating parameter prevails but this article aims to examine the thermal behaviour at a low electric field strength). The thermophoresis and the Brownian diffusion terms are ignored in the thermal energy equation as $\frac{D_T}{T_h}\,\frac{\partial T}{\partial y},\ D_B\,\frac{\partial C}{\partial y} << Ve$ (ref. Table 3.3.2.1 in Section 3.3 of this article takes $D_B = 2 \times 10^{-6}\ m^2 s^{-1},\ D_T = 10^{-6}\ m^2 s^{-1}$).

3.2.1 Flow through the porous wall

The effect of the injected velocity Ve on the longitudinal fluid flow velocity through the porous wall, denoted by u_p with an assumption of very small permeability k_i can be described as (Seth et al. [2018]),

$$\begin{aligned} Ve\,\frac{\partial u_p}{\partial y} &= -\frac{1}{\rho}\,\frac{\partial p}{\partial x} - \frac{\nu}{k_i}\,u_p, \\ u_p &= 0 \text{ as } \frac{\partial p}{\partial x} = 0. \end{aligned} \tag{3.5}$$

Equation 3.5 along with equation 3.2 gives rise to the following solution,

$$u_p = -\frac{1}{\rho\,Ve}\,e^{-\frac{\nu}{k_i\,Ve}y}\int e^{\frac{\nu}{k_i\,Ve}y}\,\frac{\partial p}{\partial x}\,dy = -\frac{k_i}{\mu}\,\frac{\partial p}{\partial x}, \tag{3.6}$$

which is the well-known Darcy velocity. The slip velocity at the fluid-wall interface can be described in the sense of Beavers and Joseph [1967] as follows,

$$\frac{\partial u}{\partial y}\Big|_{y=O_+} = \tilde{\alpha}\,(u_{B_1} - u_p), \tag{3.7}$$

where O_+ denotes the lower surface limit point from exterior nanofluid, $\tilde{\alpha}$ denotes a proportionality number of dimension L^{-1} and can be written in the form $\tilde{\alpha} = \frac{\alpha}{\sqrt{k_i}}$ where α denotes a non-dimensional material coefficient, u_{B_1} denotes the slip velocity of nanofluid at the fluid-wall interface. All the above notations and a relationship between α and k_i have been mentioned by Beavers and Joseph [1967] in their foundational paper.

3.2.2 Boundary conditions at fluid-surface interface

i. The following boundary conditions at the channel walls are imposed as per discussion on equation 3.7 in Section 3.2.1: (Beavers and Joseph [1967], Vajravelu et al. [2003])

$$\begin{aligned} \frac{\partial u}{\partial y} &= \frac{\alpha}{\sqrt{k_1}}\left(u + \frac{k_1}{\mu}\frac{\partial p}{\partial x}\right) \text{ at } y = 0, \\ \frac{\partial u}{\partial y} &= -\frac{\alpha}{\sqrt{k_2}}\left(u + \frac{k_2}{\mu}\frac{\partial p}{\partial x}\right) \text{ at } y = h, \end{aligned} \tag{3.8}$$

where k_1, k_2 denote permeability of the lower and upper walls respectively.

ii. The lower channel wall is kept at a fixed temperature, whereas, the temperature variations near upper channel wall is assumed to be zero: (Moshfegh and Sandberg [1996], Abu Talib and Hilo [2021], Eshaghi et al. [2021], Dogonchi et al. [2021a])

$$\begin{aligned} T &= T_0 \quad \text{at } y = 0, \\ \frac{\partial T}{\partial y} &= 0 \quad \text{at } y = h. \end{aligned} \tag{3.9}$$

The lower channel wall is assumed to be kept at a fixed temperature and the temperature variation remains negligible near the upper wall. The viscous dissipation term in equation 3.3 indicates the influence of the electroosmotic parameters along with the frictional drag forces on the temperature distribution in the system when the electric field strength is low along with a low temperature diffusion consideration (nanofluid channel walls have similar temperature). In such a situation we can assume that the rate of change of the net heat energy is proportional to the viscous dissipation energy as the Joule heating effect is low (E_0 is small) and the second order temperature diffusion term is low (T, T_0 are almost same; therefore, the heat transfer due to diffusion is low). For the higher electric field values, the temperature due to the Joule heating will be much higher as compared to the temperature variation condition at the upper wall, hence, the impact of the viscous dissipation term won't be reflected significantly in the temperature profile; in both situations the assumption $\frac{\partial T}{\partial y}|_{y=h} = 0$ can be a meaningful choice.

iii. Fractional distribution of nanoparticles at the channel walls:

$$\begin{aligned} C &= C_{ref} + \phi_1^* \, k_1 \, \frac{\rho \, Ve}{M \, n_0} \quad \text{at } y = 0, \\ \frac{\partial C}{\partial y} &= -\phi_2^* \, k_2 \, \frac{\rho \, Ve}{M \, n_0} \quad \text{at } y = h, \end{aligned} \tag{3.10}$$

where C_{ref} denotes a reference nanoparticle concentration at the lower wall. Here, ${\phi_1}^*$ and ${\phi_2}^*$, called boundary deposition parameters, are numbers that control the amount of the nanoparticle coming into (going out of) the channel through the wall

pores that are also subject to getting blocked by the sedimentation of the nanoparticle (or EDL resistance). M is the molar mass of the nanoparticle in the nanofluid and n_0 denotes the ion density in the nanofluid. The nanoparticle concentration at the lower wall is proportional to the amount of nanoparticles present in injected nanofluid. The amount of nanoparticles present at the bottom of microchannel is assumed to be higher than the nanoparticle concentration in the nanofluid due to continuous upward injection of nanofluid at the lower wall. The variation of nanoparticle concentration near the upper wall is proportional to the amount of nanoparticles getting absorbed through upper porous wall. The solutions of equations 3.1-3.4 are presented in Appendix.

3.2.3 Electric potential distribution

The electric potential distribution ψ is developed inside the microchannel due to formation of EDL by separating the ions adjacent to the channel walls. The Poisson-Boltzmann equation (Ranjit and Shit [2017]) describes the electrical potential distribution inside the channel as,

$$\frac{\partial^2 \psi}{\partial y^2} = -\frac{\rho_e}{\tilde{k}\epsilon_0}, \tag{3.11}$$

where ρ_e denotes the net charge density, ϵ_0 the permittivity of the free space and $\tilde{k}$ denotes the dielectric constant. The electrolytes are assumed to be $1:1$ symmetric for the present study. The net charge density (Ranjit and Shit [2017]) can be expressed as,

$$\rho_e = ezN_A(n^+ - n^-). \tag{3.12}$$

The following Nernst-Planck equation for the ionic distributions is used to calculate $n^{\pm}$,

$$Ve\,\frac{\partial n^{\pm}}{\partial y} = D\,\frac{\partial^2 n^{\pm}}{\partial y^2} \pm \frac{D\;z\;e}{K_B\;T_{av}}\frac{\partial}{\partial y}(n^{\pm}\;\frac{\partial \psi}{\partial y}), \tag{3.13}$$

where D represents the ion diffusion coefficient, N_A the Avogadro number, z the valence of the ions, e the electron charge, K_B the Boltzmann constant, T_{av} the average temperature of the nanofluid, n_0 the average number of the positive (n^+) or negative (n^-) ions. Under the assumptions that the ion concentration varies with injection velocity, the above equation can be reduced to:

$$\begin{aligned} Ve\,\frac{\partial n^{\pm}}{\partial y} &= D\,\frac{\partial^2 n^{\pm}}{\partial y^2} \pm \frac{D\;z\;e}{K_B\;T_{av}}\frac{\partial}{\partial y}(n^{\pm}\;\frac{\partial \psi}{\partial y}), \\ n^{\pm} &= 0 \quad \text{at } \tfrac{\partial \psi}{\partial y} = 0, \\ n^{\pm} &= n_0\, e^{\frac{Ve}{D}y} \quad \text{at } \psi = 0. \end{aligned} \tag{3.14}$$

We have obtained the following expressions for the ion concentration,

$$n^{\pm} = n_0 \; e^{\mp \frac{z \; e}{K_B \; T_{av}} \psi + \frac{Ve}{D} y}. \tag{3.15}$$

Combining equations 3.11, 3.15 and using the Debye-Hückel approximations (Bandopadhyay et al. [2013]), we obtain,

$$\frac{\partial^2 \psi}{\partial y^2} = \frac{2 n_0 \; ez \; N_A}{\tilde{k} \epsilon_0} \; e^{\frac{Ve}{D} y} \left(\frac{ez}{K_B T_{av}} \psi \right). \tag{3.16}$$

Let ψ satisfies the following boundary conditions,

$$\begin{aligned} \psi &= \zeta_1 \quad \text{at } y = 0, \\ \psi &= \zeta_2 \quad \text{at } y = h, \end{aligned}$$

where ζ_1, ζ_2 are the different Zeta potentials at the channel walls (channels are assumed to have uniform Zeta potentials) respectively.

3.2.4 Electroosmotic Velocity

The ion concentration is assumed to be in the range $[10^{-2}M - 1M]$, therefore, leading to formation of a thin EDL. The upwardly injected velocity is responsible for formation of a low density stern layer. The effects of the injected velocity on the diffused layer in terms of Smoluchowski velocity is calculated in this section by solving the following equation (obtained by reducing equation 3.1 with the assumption that $\frac{\partial p}{\partial x} = 0$),

$$Ve \; \frac{\partial u}{\partial y} = \nu \; \frac{\partial^2 u}{\partial y^2} - \frac{E_0 \tilde{k} \epsilon_0}{\rho} \; \frac{\partial^2 \psi}{\partial y^2}. \tag{3.17}$$

Under an additional assumption that the electroosmotic parameter is very high (which indicates the presence of very high ion concentration in the nanofluid and essentially suggests the formation of a very thin double layer), equation 3.17 can be solved with the boundary condition $y \to \infty$, $\frac{\partial u}{\partial y} \to 0$, $\frac{\partial \psi}{\partial y} \to 0$, which gives,

$$\frac{\partial u}{\partial y} = \frac{E_0 \tilde{k} \epsilon_0}{\mu} \; e^{\frac{Ve}{\nu} y} \; \int e^{-\frac{Ve}{\nu} y} \frac{\partial^2 \psi}{\partial y^2} dy, \tag{3.18}$$

where $\frac{Ve}{\nu} \approx 10^3$ (ref. Table 3.3.2.1). After integrating 3.18 one more time, the following expression for the electroosmotic slip velocity is obtained by considering equation 3.7 at the lower wall,

$$\begin{aligned} \int_0^{\infty} \frac{\partial u}{\partial y} dy &= \frac{E_0 \tilde{k} \epsilon_0}{\mu} \; \int_0^{\infty} e^{\frac{Ve}{\nu} y} \; \int e^{-\frac{Ve}{\nu} y} \frac{\partial^2 \psi}{\partial y^2} dy dy, \\ \tilde{U}_{HS} &= \frac{\sqrt{k_1}}{\alpha} \; \frac{\partial u}{\partial y}\bigg|_{y=0} - \frac{E_0 \tilde{k} \epsilon_0}{\mu} \; \int e^{\frac{Ve}{\nu} y} \; \int e^{-\frac{Ve}{\nu} y} \frac{\partial^2 \psi}{\partial y^2} dy dy \bigg|_{y=0}, \end{aligned} \tag{3.19}$$

where $\tilde{U}_{HS}$ denotes the electroosmotic slip velocity and k_1 denotes permeability of the lower wall. The well-known form of Smoluchowski velocity can be obtained from 3.19 by considering porous permeability at the lower plate is negligible (in such a case, the boundary condition in equation 3.8 is reduced to no-slip boundary condition) along with the fact that $Ve \to 0$ as shown in figure 3.4.

The following transformations are applied to make the equations dimensionless.

$$Y = \frac{y}{h},\ U = \frac{u}{u_{ref}},\ \theta = \frac{T - T_h}{T_0 - T_h},\ f = \frac{C}{C_{ref}},$$
$$Z_1 = \frac{ez}{K_B T_{av}}\zeta_1,\ Z_2 = \frac{ez}{K_B T_{av}}\zeta_2,\ \Phi = \frac{ez}{K_B T_{av}}\psi,$$

where u_{ref} denotes a reference nanofluid velocity.

The dimensionless forms of the electric potential distribution equation along with the wall Zeta potential are presented as follows,

$$\begin{aligned} &\frac{\partial^2 \Phi}{\partial Y^2} = \kappa^2 e^{R_D\ Y}\Phi, \\ &\Phi = Z_1 \quad \text{at } Y = 0, \\ &\Phi = Z_2 \quad \text{at } Y = 1, \end{aligned} \tag{3.20}$$

where $Re = \frac{\rho V e h}{\mu}$ denotes the Reynolds number, $\kappa = \frac{h}{\lambda_D}$ denotes the electroosmotic parameter, $M_D = \frac{\nu}{D}$ denotes the molecular diffusivity parameter, $R_D = Re\ M_D$ denotes diffusive Reynolds number and $\lambda_D = \left(\frac{\tilde{k}\epsilon_0 K_B T_{av}}{2e^2 z^2 n_0\ N_A}\right)^{\frac{1}{2}}$ denotes the Debye length. A solution Φ_1 for 3.20 can be found in terms of the Bessel functions; however, the study is further simplified under the following conditions on the newly introduced diffusive-Reynolds number R_D,

$$R_D << 1,\ e^{R_D\ Y} \approx 1\ \forall\ Y \in [0, 1]. \tag{3.21}$$

Figure 3.2 depicts the magnitude of the error terms generated due to this approximation. Figure 3.2 and equation 3.1 show that the approximation will ultimately produce a point wise error $E_r(Y)$ term to the non-dimensional form of equation 3.1 as follows,

$$Re\ \frac{\partial U}{\partial Y} = -\Pi + \nu\ \frac{\partial^2 U}{\partial Y^2} + \frac{\kappa^2 \beta}{Z_1}\Phi + E_r(Y), \tag{3.22}$$

where, $E_r(Y) = \frac{\kappa^2\beta}{Z_1}(\Phi - \Phi_1) < Max_Y|\frac{\kappa^2\beta}{Z_1}\ (\Phi_1 - \Phi)| < 2 \times 10^{-5}$ (when $Re = 1$, κ, Z_1, D and β are as defined in Section 3.3) based on Table 3.3.2.1, which is a justifiable choice.

Under the above assumptions 3.21, the solution of 3.20 is expressed as,

$$\Phi = Z_1 \cosh(\kappa Y) + \frac{Z_2 - Z_1 \cosh\kappa}{\sinh\kappa}\sinh(\kappa Y). \tag{3.23}$$

Figure 3.3 shows the variations of Zeta potential distribution with diffusive Reynolds number. The charge distribution flattens faster with increment in diffusive Reynolds number as the increment in fluid velocity pushes more ions towards the upper wall based on boundary condition 3.14 which is responsible for formation of a thinner EDL near the upper wall. The increment in ion diffusion coefficient increases ion transportation near the charged walls and consequently diminishes the presence of ions in the potential free region as described in equation 3.14. Thus, a symmetrical behaviour in Potential distribution is visible with diminution of diffusive Reynolds number in Figure 3.3. Moreover, figure 3.3 shows that, $\Phi_1 \approx \Phi$, when $R_D = 10^{-5}$ (under the assumptions of $Ve \leq 1$ along with parameter values from Table 3.3.2.1, it is found that, $R_D \leq 10^{-5}$). Throughout this chapter, Φ is used in place of Φ_1 to simplify the numerical computations except in figure 3.7, where, the effects of diffusive Reynolds number on nanofluid velocity profile is illustrated.

3.3 Discussion on results

3.3.1 Validation

All the figures except the figures 3.2, 3.3, 3.7 are drawn based on the exact solutions, expressed in Appendix, of the ODEs 3.1-3.4 along with the conditions 3.21, 3.23. Figures 3.2 and 3.3 are drawn by using the DSolve package in Mathematica. In figure 3.3, a graphical comparison is made between the numerical solutions Φ_1 and the exact solution Φ, where Φ_1 denotes the solution with $R_D \neq 0$ and $\Phi = Z_1 \cosh(\kappa Y) + \frac{Z_2 - Z_1 \cosh\kappa}{\sinh\kappa} \sinh(\kappa Y)$. Moreover, figure 3.3 validates that $\Phi_1 \to \Phi$ as $R_D \to 0$. The differential transform method (DTM) is used to draw the Figure 3.7. We will briefly mention the DTM method in this Section, whereas, a much detailed discussion on this method can be found in Shit and Mukherjee [2019], Zhou [1986]. By using this method, an approximate solution U of the non-dimensional form of equation 3.1, denoted by $\mathcal{N}_U(Y)$, can be expressed as a finite series of the following form,

$$U = \sum_{i=0}^{P} a_i Y^i$$

where the unknown coefficients a_i are obtained recursively from the boundary conditions and P denotes series iteration length. We define a square averaged error term to study the convergence of our solution with increasing iteration values,

$$error_U = \frac{1}{K+1} \sum_{i=0}^{K} \left| \mathcal{N}_U \left(U \left(\frac{i}{K+1} \right) \right) \right|^2.$$

The following comparison table shows that the error term decreases with enhancement of iteration length which indicates convergence,

Error estimation with iteration length P when
$R_D = 2,\ \beta = 2.5 \times 10^{-3},\ \kappa = 2,\ Re = 10^{-2},\ L_{1,2} = 6,\ \Pi = -0.01,\ K = 1000$

Iteration length (P)	$error_U$	$error_{\Phi_1}$
20	8.28101×10^{-13}	0.000256358
25	1.20971×10^{-15}	6.2024×10^{-7}
30	9.65159×10^{-19}	7.61996×10^{-10}

3.3.2 Analysis of the results

It is found that, under the assumptions of high electric field in the absence of injection velocity (*i.e.* $Ve \approx 0$) and the viscous dissipation term in the energy equation 3.3, the equations 3.3-3.4 along with 3.9-3.10 are reduced to the following expressions,

1. $\int_0^1 \theta \, dY = 1 + \frac{\gamma}{3}$,
2. $\int_0^1 f \, dY = 1 - \frac{\gamma \, S_t}{3}$,

where $\gamma,\ S_t$, denote the Joule heating parameter and the Soret number respectively, are formally described below. The Joule heating parameter is proportional to the square of electric field strength thereby making the above two expressions solely dependent on applied electric field strength in the presence of a strong electric field when $Ve \approx 0$ and the viscous dissipation term in neglected. This chapter analyzes nanofluid flow phenomena under a weak electric field to incorporate the effects of various thermophysical parameters whose impacts are shadowed under a strong electric field. The present study focuses on examining the combined effects of an externally applied electric field (E_0), pressure gradient ($\frac{\partial p}{\partial x}$), Zeta potential developed at the wall (ζ_1), dielectric constant ($\tilde{k}$) and ion density (η_0) in terms of the electroosmotic parameter (κ) on the flow rate (Q), normalized temperature ($\overline{\theta}$), normalized bulk temperature (θ_{bulk}), normalized nanoparticle concentration ($\overline{f}$) and normalized bulk nanoparticle concentration (f_{bulk}). The contributions of the material parameters *i.e.* the permeability ($L_i = \frac{k_i}{h^2}$) of the channel wall, Brownian motion coefficient of the nanoparticle (D_B) along with the thermophoresis parameter (D_t) and the nanofluid velocity (Ve) on the entropy production and heat production phenomena are investigated. The following key metrics are used for the present study,

$$Q = \int_0^1 U dY,\ \theta_{bulk} = \frac{\int_0^1 \overline{\theta}\, U dY}{Q},\ f_{bulk} = \frac{\int_0^1 \overline{f}\, U dY}{Q},$$
$$\overline{\theta} = \frac{\theta - 1}{\gamma},\ \overline{f} = \frac{f - 1}{\gamma}. \tag{3.24}$$

in which the physical parameter values are selected from the Table 3.3.2.1 (Note that a larger range of the parameter values is chosen to accommodate a larger set of the fluids into our study). The following set of the parametric values (default parameter values unless stated otherwise) are taken for the present study based on the Table

3.3.2.1,

$$\begin{aligned} &Re = 10^{-3},\ \kappa = 12,\ \gamma = 4 \times 10^{-10},\ \beta = 2.5 \times 10^{-3}, \\ &\Pi = -0.01,\ Br = 2 \times 10^{-10},\ \chi_1 = 1.2,\ \phi_1 = 2 \times 10^{-10}, \\ &S_t = 0.16,\ L_{1,2} = 6,\ Z_{1,2} = -1,\ \delta = 30,\ \phi_2 = 10^{-12}, \\ &Sc = 0.5,\ Pr = 6. \end{aligned} \tag{3.25}$$

where $Br = Pr \times Ec$ denotes the Brinkman number, $Pr = \frac{\mu\ C_p}{k}$ denotes the Prandtl number, $Ec = \frac{{u_{ref}}^2}{C_p\ (T_0 - T_h)}$ denotes the Eckert number, $\gamma = \frac{\sigma h^2 {E_0}^2}{k\ (T_0 - T_h)}$ denotes the Joule heating parameter, $\delta = \frac{T_h}{T_0 - T_h}$ denotes the temperature ratio parameter and $\chi_1 = \frac{\rho\ C_p\ D_B\ C_{ref}}{k}$ represents the mass transfer parameter. The permeability of the walls are assumed to be around 6 darcys (permeability of the unconsolidated sand), which gives us the parameter range for L_1, L_2. Dielectric constant value ($\tilde{k}$) is taken as 50 in the calculation of electroosmotic mobility parameter ($\beta = \frac{U_{HS}}{u_{ref}}$) where $U_{HS} = -\frac{\tilde{k}\epsilon_0 E_0 \zeta_1}{\mu}$ denotes the Helmholtz-Smoluchowski velocity at the edge of the EDL near the lower plate, The hydro static pressure gradient is considered as $10^4\ Pa$ for the present study which gives us the range of pressure parameter $\Pi = \frac{h^2 \frac{\partial p}{\partial x}}{\mu u_{ref}}$. We found the Soret coefficient value $S_t = \frac{D_T\ (T_0 - T_h)}{T_h\ D_B\ C_{ref}} = 0.16$ under the assumption that $C_{ref} \approx 0.1$, $T_0 - T_h \approx 10$. The Schmidt number $Sc = \frac{\mu}{\rho\ D_B}$ is calculated based on Table 3.3.2.1 for nanoparticles of diameter size 100 nm (Zhao et al. [2014]). The boundary deposition parameters $\phi_1 = \frac{h\ \mu\ {\phi_1}^*}{M\ n_0\ C_{ref}}$, $\phi_2 = \frac{h^2\ \mu\ {\phi_2}^*}{M\ n_0\ C_{ref}}$ are assumed to take values 2×10^{-10}, 10^{-12} respectively.

3.3.2.1 Flow characteristics

Figures 3.4-3.7 elucidate the combined effects of the applied electric field strength, pressure gradient, injected fluid velocity and material parameters (permeability, ion diffusion coefficient and ion concentration) on the fluid-flow profiles. Figure 3.4 shows an interesting finding on the Smoluchowski velocity formulation presented in Section 3.2.4. It shows that the newly formulated $\tilde{U}_{HS} \to U_{HS}$ as the permeability value $k_1 \to 0$ *i.e.* the no-slip boundary velocity condition starts to get satisfied. This velocity follows an inverse relationship with the increasing velocity of the injected fluid in terms of Reynolds number. The increment in injected velocity in the transverse direction reduces the electroosmotic mobility of the fluid thereby diminishing electroosmotic velocity. Moreover, it is observed that nanofluid velocity increases with enhancement of permeability parameter. Figures 3.5, 3.6 show that the net flow amount increases with enhancement of the electric field strength, absolute value of the externally applied pressure gradient and electroosmotic parameter, whereas, decreases with enhancement of Reynolds number. The higher electroosmotic parameter value indicates the presence of higher ion concentration (in base fluid) which is responsible for formation of a thinner EDL layer thereby producing a lesser velocity drag force and consequently fluid flow rate increases.

Table 1. Physical parameters used in this study (Zhao et al. [2014], Ranjit et al. [2019], Craven et al. [2008])

Physical Parameters	Values [Unit]
Channel height (h)	$1\ \mu m$
Density of the fluid (ρ)	$1000\ kg/m^3$
Charge of proton (e)	$1.6 \times 10^{-19}\ C$
Electrical Potential at the walls (ζ_1, ζ_2)	$-25\ mV$
Electric field force in the axial direction (E_0)	$200\ V/m$
Boltzmann Constant (K_B)	$1.38 \times 10^{-23}\ J/K$
Ion density (η_0)	$10^{-2}\ mol/m^3$
Average absolute fluid temperature (T_{av})	$300\ K$
Valency of ions (z)	1
Permittivity of the free space (ϵ_0)	$10^{-11}\ C/Vm$
Kinematic viscosity of the fluid (ν)	$10^{-6}\ m^2/s$
Electrical Conductivity (σ_e)	$5 \times 10^{-2}\ S/m$
Thermal Conductivity (k)	$0.5\ W/mK$
Specific heat (C_p)	$3000\ J/kgK$
Material parameter (α)	0.1
Reference velocity of the fluid (u_{ref})	$1\ mm/s$
Permeability of the beds (k_1, k_2)	$6 \times 10^{-12}\ m^2$
Pressure gradient ($\frac{\partial p}{\partial x}$)	$-10^4\ N/m^3$
Brownian Diffusion Coefficient (D_B)	$2 \times 10^{-6}\ m^2/s$
Thermophoretic Diffusion Coefficient (D_T)	$10^{-6}\ m^2/s$
Ion Diffusion Coefficient (D)	$0.1\ m^2/s$

The increasing absolute values of the pressure gradient increases the kinetic energy of the fluid and increases the flow rate. Moreover, it is to be noted that the negative pressure gradients $\frac{\partial p}{\partial x}$ drive the fluid flow in the positive x direction thereby resulting in enhancement of longitudinal velocity component u. The increasing values of the electric field strength will increase Smoluchowski slip velocity which increases the net flow rate of the fluid. Figure 3.7 shows that nanofluid velocity decreases with enhancement of diffusive Reynolds number when Reynolds number is fixed thereby showing that enhancement in ion diffusivity coefficient increases nanofluid velocity. The increment in ion diffusion coefficient increases ion mobility towards the charged channel walls thereby forming a thinner EDL layer as shown in figure 3.3. This phenomena forms a overall weaker Zeta potential distribution in microchannel thereby reduces the net charge density inside microchannel. The diminution of electroosmotic force reduces nanofluid velocity. Figure 3.8 shows that the normalized temperature increases with increasing values of pressure gradient, whereas, the reverse trend is observed for normalized nanoparticle concentration in figure 3.9. The enhancement in pressure gradient increases the kinetic energy of the fluid and increases the flow rate. Hence, increasing values of the pressure gradient increases viscous drag force at the walls of microchannel and consequently increases heat generation due to fluid friction. The effects of the pressure gradient and the fluid friction on heat generation is vividly visible at a low electric field as the heat generation due to Joule heating is small.

The diminishing nanoparticle concentration is due to the reduction of thermophore-

sis phenomena in nanofluid, which, diminishes nanoparticle diffusion process, which is in agreement with other experimental findings (Yang et al. [2018]). The following equation represents an almost quadratic nonlinear dependence of bulk temperature on pressure gradient. The functional representation of normalized bulk temperature θ_{bulk} as a function of pressure gradient $(\frac{\partial p}{\partial x})$ when $E_0 = 200$ Volts/m and $Ve = 1\ m/s$ is given by

$$\theta_{bulk} = \frac{3231.35 - 0.0788593\ \frac{\partial p}{\partial x} + 1.93249 \times 10^{-10}\ \frac{\partial p}{\partial x}^2 - 2.48662 \times 10^{-15}\ \frac{\partial p}{\partial x}^3}{40994.7 - \frac{\partial p}{\partial x}}.$$

Figures 3.10, 3.11 show that the normalized bulk concentration value of the nanoparticle decreases with enhancement of electric field strength and Schmidt number. The increasing value of Schmidt number indicates that the nanoparticle diameter is increasing *i.e.* the Brownian coefficient is decreasing. The diminishing nanoparticle diffusion process takes place in the base fluid consequently decreasing the bulk concentration of the nanoparticle. The increment in electric field makes temperature a function of the Joule heating parameter as it becomes the most dominant source of heat production in the system. Therefore, the temperature gradient in the fluid decreases with the channel height (away from the channel wall). Hence, the change in the temperature gradient decreases with a rise in the Joule heating effect, which ultimately reduces the thermophoresis phenomena in the fluid. This phenomena reduces the nanoparticle diffusion process and results in lowering of bulk nanoparticle concentration value. Under the assumption, $Ve \approx 0$ and neglecting the contribution of heat generation due to viscous dissipation in thermal energy equation 3.3, we obtain the following expressions,

$$S_t \approx \frac{3}{\gamma}\ (1 - \int_0^1 f\ dY),\ \ \frac{D_T}{D_B} \approx C_{ref}\ \delta\ S_t. \tag{3.26}$$

This above expressions represent the Soret number as a ratio of the cross sectional nanoparticle concentration to Joule heating parameter. It also shows an increment in both Schmidt number and Joule heating parameter diminishes nanoparticle concentration in nanofluid in the absence of injection velocity. Moreover, equation 3.26 assists us to obtain a relation between thermophoresis coefficient and Brownian motion coefficient of nanoparticles when temperature ratio parameter $(\delta = \frac{T_h}{T_0 - T_h})$ and reference concentration value at lower wall (C_{ref}) are well estimated. Table 3.3.2.1 depicts a well-known observation that the increasing value of Prandtl number increases the normalized heat transfer rate $(-\frac{1}{\gamma}\frac{\partial \theta}{\partial Y}\big|_{Y=0})$. Fluid absorbs higher amount of heat to increase its temperature with increase in specific heat value. Thus an increment rate in temperature within fluid layers slows down, resulting an increase in heat transfer rate value. Moreover, it is observed that heat transfer rate follows an increasing relationship with injected velocity. The normalized nanoparticle mass transfer rate $(-\frac{1}{\gamma}\frac{\partial f}{\partial Y}\big|_{Y=0})$ decreases with higher viscosity value in terms of Prandtl number of the fluid as higher drag force between the fluid layers hinders mass diffusion process. The

higher injection velocity at lower porous wall enhances nanoparticle inflow rate in microchannel as described in condition 3.10.

Table 2. Variations of heat and mass transfer rate with Reynolds number and Prandtl number when $E_0 = 20\ Volts/m$

Re	Pr	$-\frac{1}{\gamma}\frac{\partial\theta}{\partial Y}\big\vert_{Y=0}$	$-\frac{1}{\gamma}\frac{\partial f}{\partial Y}\big\vert_{Y=0}$
10^{-2}	6	−0.971234	0.169931
	7	−0.966549	0.169183
	8	−0.961895	0.168439
10^{-1}	6	−0.752488	0.259831
	7	−0.719734	0.254686
	8	−0.688967	0.249854
1	6	−0.166461	0.927397
	7	−0.142951	0.924735
	8	−0.125196	0.922762

3.3.2.2 A Comparative Study on the total entropy generation in the system

The occurrences of irreversible heat loss in a physical system is termed as entropy generation. This study focuses on identifying the parameters most responsible for entropy generation when a weak electric field is applied in our system. The principal factors for the irreversible heat loss in the chosen model are friction due to viscous dissipation, irreversible heat transfer phenomena and Joule heating effect. The expression for total volumetric entropy generation rate (Ranjit et al. [2019], Bejan [1979]) is expressed as,

$$\begin{aligned} E_{Total} &= E_{HT} + E_{VS} + E_{JH} + E_{MT}, \\ E_{HT} &= \frac{k}{T^2}\left(\frac{\partial T}{\partial y}\right)^2,\ E_{VS} = \frac{\mu}{T}\left(\frac{\partial u}{\partial y}\right)^2,\ E_{JH} = \frac{\sigma E_0^2}{T}, \\ E_{MT} &= \frac{(\rho\ C_p)\ D_B}{C}\left(\frac{\partial C}{\partial y}\right)^2 + \frac{(\rho\ C_p)\ D_B}{T}\left(\frac{\partial T}{\partial y}\right)\left(\frac{\partial C}{\partial y}\right), \end{aligned} \tag{3.27}$$

where E_{Total} denotes total entropy generation, E_{HT} denotes entropy generation due to the heat transfer, E_{VS} denotes entropy generation on account of the fluid friction, E_{JH} denotes entropy generation due to the Joule heating effect and E_{MT} denotes entropy generation as a consequence of the mass transfer phenomena. The dimensionless form of the entropy generation is obtained by dividing E_{Total} by the characteristic entropy transfer rate $\frac{k}{h^2}$. The contribution of the normalized form of total entropy generation S_{Total} is expressed as follows,

$$\begin{aligned} S_{Total} &= \frac{E_{Total}}{E_{JH}} \\ &= \frac{1}{\gamma}\Bigg[\frac{1}{(\theta+\delta)}\left(\frac{\partial\theta}{\partial Y}\right)^2 + \left(\gamma + Br\left(\frac{\partial U}{\partial Y}\right)^2\right) + \\ &\chi_1\left(\frac{\theta+\delta}{f}\left(\frac{\partial f}{\partial Y}\right)^2 + \frac{\partial\theta}{\partial Y}\frac{\partial f}{\partial Y}\right)\Bigg], \end{aligned} \tag{3.28}$$

A comparative study on total entropy generation with small variations of the electroosmotic parameter, injection velocity and pressure gradient are graphically illustrated in Figures 3.12-3.14. The increment of the pressure gradient enhances the total entropy generation when a weak electric field is applied as shown in figure 3.12. The increase in absolute pressure gradient value enhances velocity gradient near the walls, thereby increasing the nanofluid temperature gradient due to friction. A discussion on the dependence of nanofluid temperature on pressure gradient is presented in figure 3.8. Figure 3.13 shows that the increment of ion concentration increases the total entropy generation near channel walls, whereas entropy decreases in a middle like region. The result is evident as the amount of materials passing through a particular cross-section is fixed. The rising trend of entropy generation near channel walls is a consequence of increase in heat generation by friction drag force at the walls. The increment in ion concentration near channel walls decreases EDL thickness, thereby enhancing velocity gradient near the channel walls. This phenomena is responsible for the temperature rise in nanofluid due to friction. Figure 3.14 shows an increment in injection velocity in terms of Reynolds number diminishes total entropy generation near channel walls, whereas, the reverse trend is visible in middle like region. Moreover, the variations in magnitude of contribution of injection velocity in total entropy generation near channel walls is the least significant. The following expression 3.29 shows that the total entropy generation follows a quadratic relationship with electric field in the absence of injection velocity and viscous dissipation. Moreover, the sensitivity of E_{Total} with an enhancement of electric field strength is vividly visible from the following expression when $Ve \approx 0$ and the viscous dissipation term is neglected in equations 3.3, 3.27,

$$\int_0^1 \frac{h^2}{k}\, E_{Total}\, dy \approx \frac{\gamma}{31} + 0.00852234\, \gamma^2. \tag{3.29}$$

3.3.3 Conclusions

The steady electroosmotic flow of nanofluid between two permeable walls in a microchannel has been analytically examined in this chapter. The combined effects of the injected fluid velocity and an externally applied electric field on formation of the Zeta potential is expressed analytically. The electroosmotic slip velocity at an edge of the EDL is integrally expressed under pressure drop boundary condition at the channel wall. This velocity is found to converge to the well-known Smoluchowski velocity when the fluid velocity is low and permeability of the channel tends to zero. The contribution of viscous drag force during heat generation under a weak electric field is investigated. The effects of the thermophoresis phenomena in nanoparticle diffusion process is investigated by varying the electric field strength. The effects of the electric field, pressure gradient, injection velocity and ion concentration in total entropy generation are thereafter illustrated. The main findings from our study can be summarized as follows,

3.3. Discussion on results

1. The electroosmotic slip velocity converges to Smoluchowski velocity when the injection velocity is low and permeability $k_1 \to 0$.

2. The nanofluid velocity decreases with enhancement of injected nanofluid velocity.

3. The net flow amount increases with enhancement of the electric field strength, externally applied pressure gradient and electroosmotic parameter.

4. The nanofluid velocity decreases with enhancement of diffusive Reynolds number.

5. The increment in normalized fluid temperature with enhancement of the pressure gradient is visible when a weak electric field is applied.

6. The bulk nanofluid temperature shows an almost quadratic nonlinear relationship with the applied pressure gradient.

7. The normalized heat transfer rate increases with enhancement of both Prandtl number and Reynolds number as shown in Table 3.3.2.1.

8. The decrements in normalized nanoparticle concentration with enhancement of the pressure gradient is visible when a weak electric field is applied.

9. The normalized bulk concentration value of the nanoparticle decreases with enhancement of the electric field strength and Schmidt number.

10. When $Ve \approx 0$, a relationship between thermophoresis coefficient and Brownian motion coefficient of nanoparticles in terms of the cross sectional nanoparticle concentration and Joule heating parameter is depicted in equation 3.26 as Soret number.

11. The normalized nanoparticle mass transfer rate rises with enhancement of Reynolds number and diminishes with Prandtl number as shown in Table 3.3.2.1.

12. A comparative study of normalized total entropy generation shows that the entropy generation near microchannel walls increases with the absolute pressure gradient parameter, electroosmotic parameter but decreases with injected velocity in terms of Reynolds number.

13. The total entropy generation follows a quadratic relationship with the Joule heating parameter in the absence of injection velocity and neglecting the viscous dissipation term in thermal energy equation 3.3, 3.27 as shown in equation 3.29.

Appendix A: Head of First Appendix

1. Velocity Profiles

The solution U has the following form,

$$\begin{aligned} U &= d_1 + d_2 e^{Re\ Y} - \frac{\Pi}{Re}\ Y - \tilde{\Phi}, \\ \tilde{\Phi} &= \Big(\frac{T_1}{\kappa^2} + Re\ \frac{\kappa\ T_2 + Re\ T_1}{\kappa^2\ (\kappa^2 - Re^2)}\Big)\cosh\kappa Y \\ &+ \frac{\kappa\ T_2 + Re\ T_1}{\kappa\ (\kappa^2 - Re^2)}\sinh\kappa Y, \\ \kappa^2\beta\frac{\Phi}{Z_1} &= T_1\cosh\kappa Y + T_2\sinh\kappa Y, \end{aligned} \tag{3.30}$$

where,

$$\begin{aligned} &d_1 = \frac{c_1 d - b c_2}{ad - bc},\ d_2 = \frac{c c_1 - a c_2}{bc - ad},\ a = -\frac{\alpha}{\sqrt{L_1}}, \\ &b = Re - \frac{\alpha}{\sqrt{L_1}},\ c = \frac{\alpha}{\sqrt{L_2}},\ d = Re\ e^{Re} + \frac{\alpha\ e^{Re}}{\sqrt{L_2}}, \\ &c_1 = \frac{\Pi}{Re} + \tilde{\Phi}'|_{Y=0} + \frac{\alpha}{\sqrt{L_1}}(L_1\ \Pi - \tilde{\Phi}|_{Y=0}), \\ &c_2 = \frac{\Pi}{Re} + \tilde{\Phi}'|_{Y=1} - \frac{\alpha}{\sqrt{L_2}}(L_2\ \Pi - \tilde{\Phi}|_{Y=1} - \frac{\Pi}{Re}). \end{aligned} \tag{3.31}$$

2. Temperature Profiles

The solution has the form,

$$\begin{aligned} \theta &= -\int e^{Pr\ Re\ Y}\Big(\int e^{-Pr\ Re\ Y}\ \Big(\gamma + Br\ \Big(\frac{\partial U}{\partial Y}\Big)^2\Big)dY\Big)dY \\ &+ \frac{R_2}{Pr\ Re}\ e^{Pr\ Re\ Y} + R_1, \end{aligned} \tag{3.32}$$

where,

$$\begin{aligned} &G = \int e^{Pr\ Re\ Y}\Big(\int e^{-Pr\ Re\ Y}\ \Big(\gamma + Br\ \Big(\frac{\partial U}{\partial Y}\Big)^2\Big)dY\Big)dY, \\ &R_1 = 1 - \frac{R_2}{Re\ Pr} + G\big|_{Y=0},\ R_2 = \frac{G'\big|_{Y=1}}{e^{Re\ Pr}}. \end{aligned} \tag{3.33}$$

3. Concentration Profiles

The solution has the following form:

$$\begin{aligned} f &= -S_t \int e^{Sc\ Re\ Y} \left(\int e^{-Sc\ Re\ Y}\ \frac{\partial^2 \theta}{\partial Y^2} dY \right) dY \\ &\quad + \frac{I_1}{Sc\ Re}\ e^{Sc\ Re\ Y} + I_2, \end{aligned} \tag{3.34}$$

where,

$$F = -S_t \int e^{Sc\ Re\ Y} \left(\int e^{-Sc\ Re\ Y}\ \frac{\partial^2 \theta}{\partial Y^2} dY \right) dY, \tag{3.35}$$

$$I_1 = -\frac{Re\ L_2\ \phi_2 + F'\big|_{Y=1}}{e^{Sc\ Re}},$$

$$I_2 = 1 + Re\ L_1\ \phi_1 - \frac{I_1}{Sc\ Re} - F\big|_{Y=0}.$$

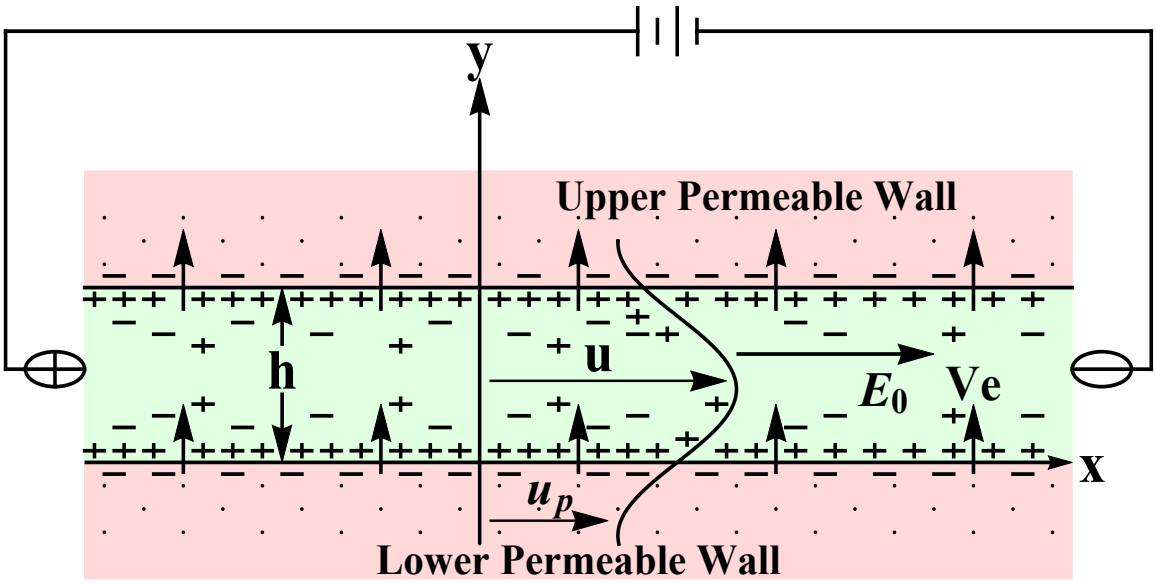

Figure 3.1: Schematic illustration of the nanofluid flow between two permeable walls separated by distance h. A weak electric field of strength E_0 is applied in the longitudinal direction. The injected nanofluid velocity at the lower permeable wall is Ve. The velocity fields in microchannel and through permeable beds are taken as $q = (u(y), Ve)$, $q_1 = (u_p(y), Ve)$ respectively.

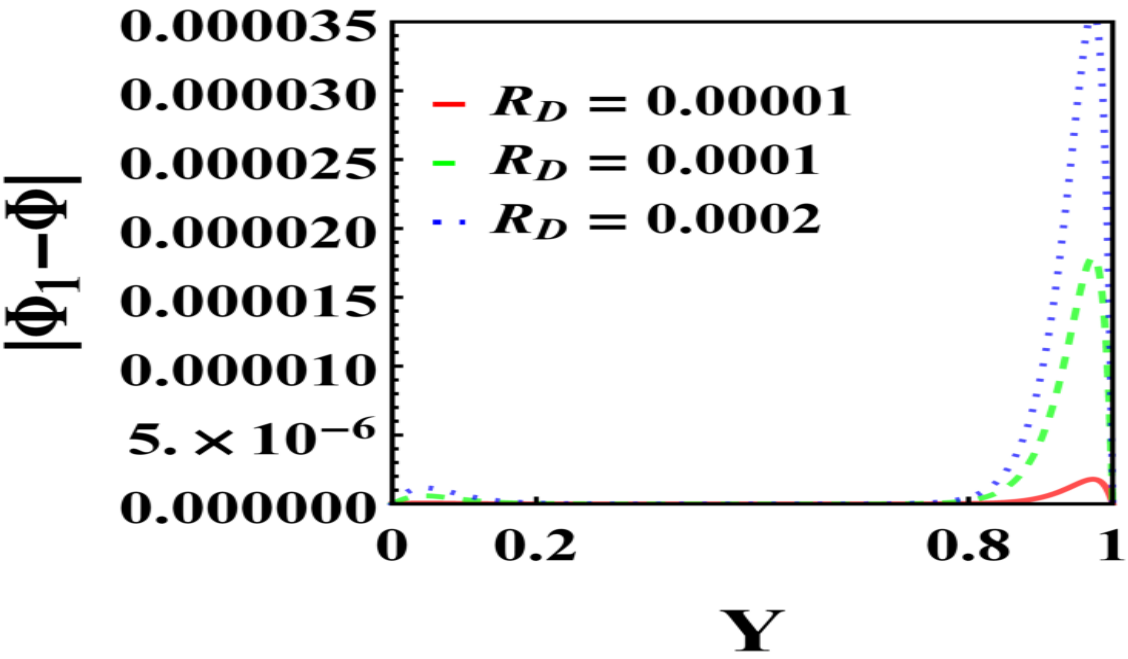

Figure 3.2: Illustration of the point wise error terms generated due to the approximation in the potential term when $\kappa = 36$, $Z_{1,2} = -1$. The error terms show a sharp peak near upper wall where the density of the ion distribution is high following the newly introduced boundary condition in equation (14).

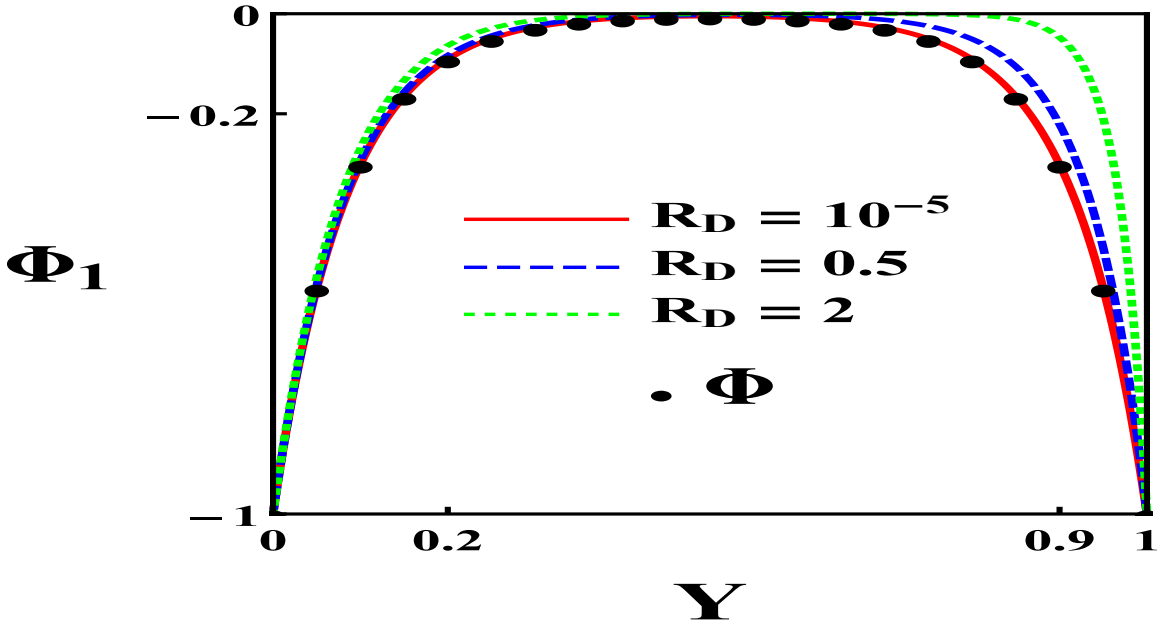

Figure 3.3: Illustration shows the effects of Diffusive Reynolds number on Zeta potential distribution when $\kappa = 12$, $Z_{1,2} = -1$. The increasing injected fluid velocity diminishes EDL thickness towards the upper wall of microchannel. It is found that, $\Phi \approx \Phi_1$ when $R_D = 10^{-5}$.

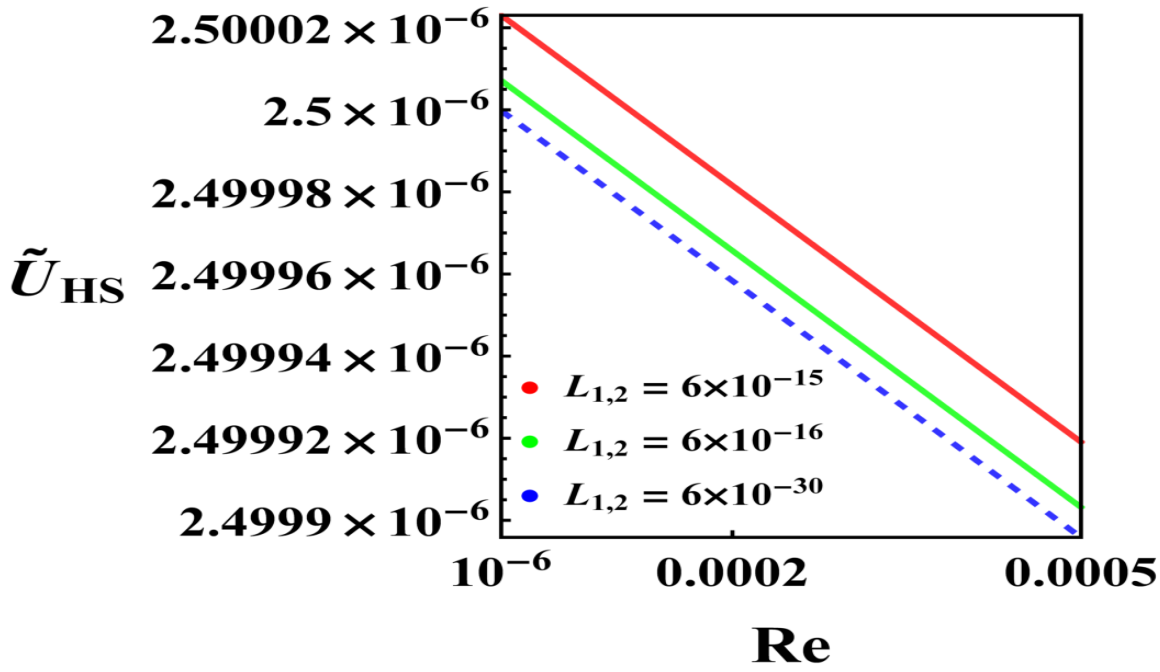

Figure 3.4: Electroosmotic slip velocity at the edge of the EDL near the lower wall converges to Smoluchowski velocity ($10^{-3}\beta$) when permeability $k_1 \to 0$ and injected nanofluid velocity Ve is very small.

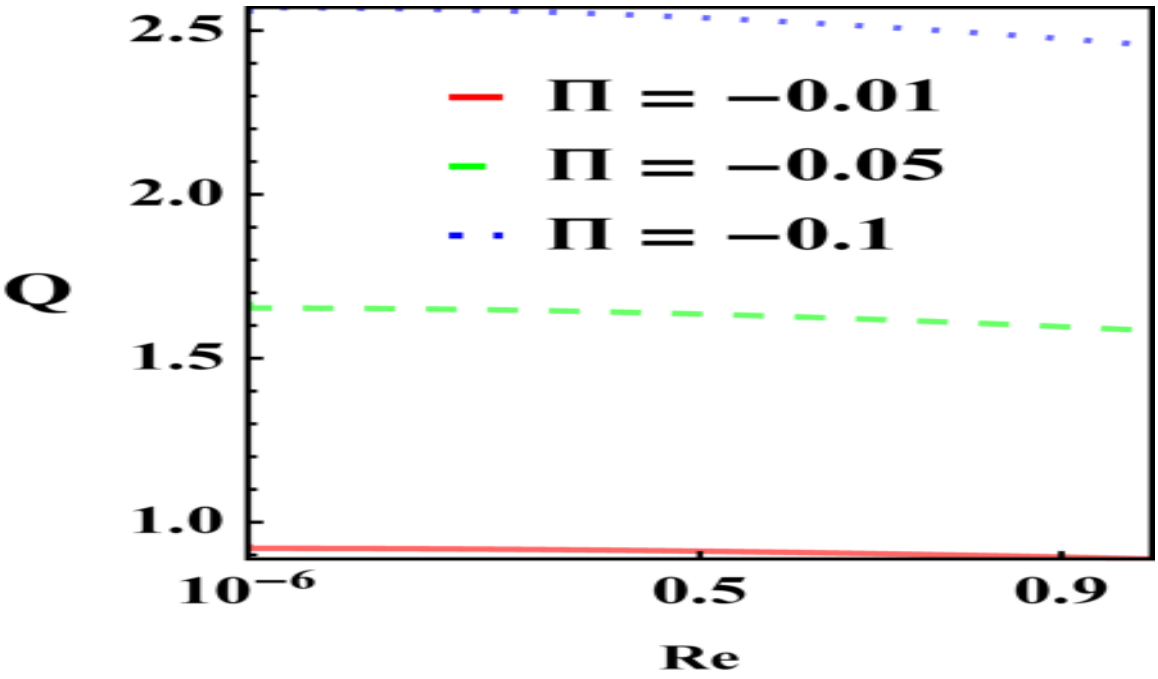

Figure 3.5: The bulk nanofluid flow rate follows an decreasing trend with Reynolds number for different pressure gradient.

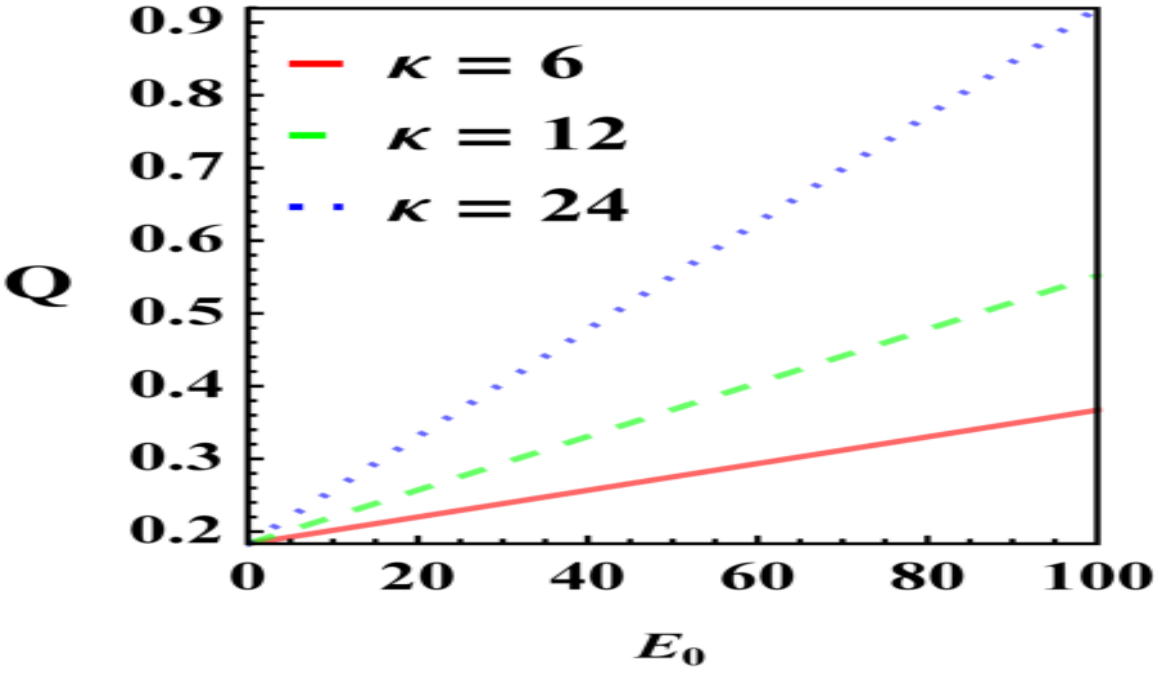

Figure 3.6: The bulk nanofluid flow rate follows an increasing trend with enhancement of electroosmotic parameter and electric field strength (when $Re = 10^{-2}$).

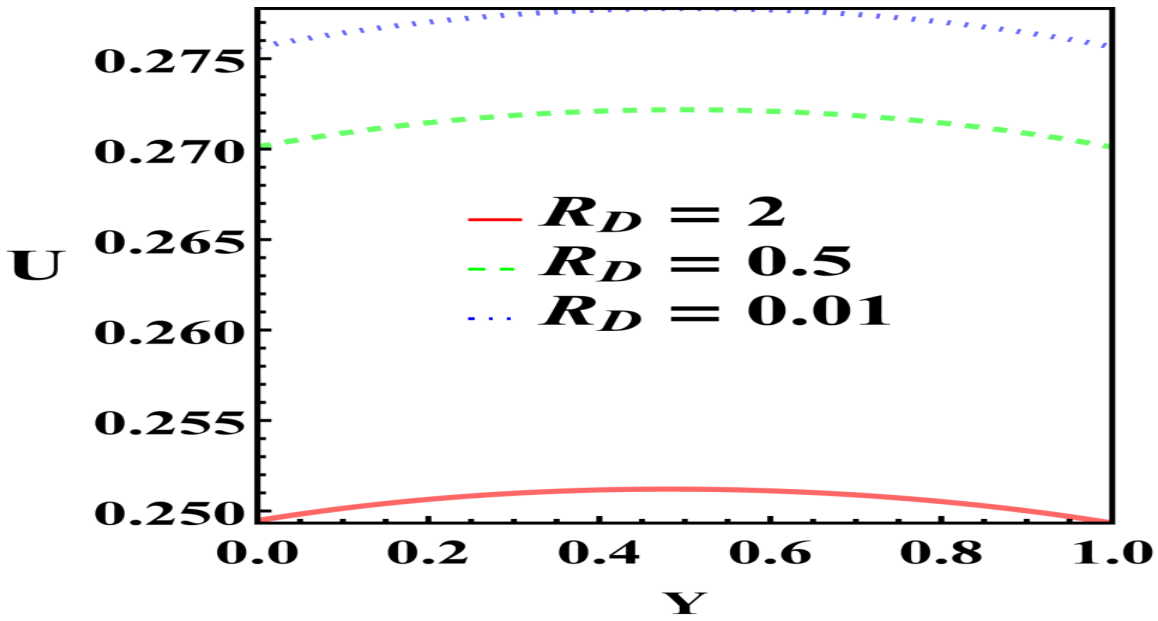

Figure 3.7: The nanofluid velocity decreases with enhancement of diffusive Reynolds number when, $\kappa = 2$, $Re = 10^{-2}$. This diagram is obtained by solving $Re\,\frac{\partial U}{\partial Y} = -\Pi + \nu\,\frac{\partial^2 U}{\partial Y^2} + \frac{\kappa^2\beta}{Z_1}\Phi_1$ and equation 3.8 using the power series method as described in Shit and Mukherjee [2019].

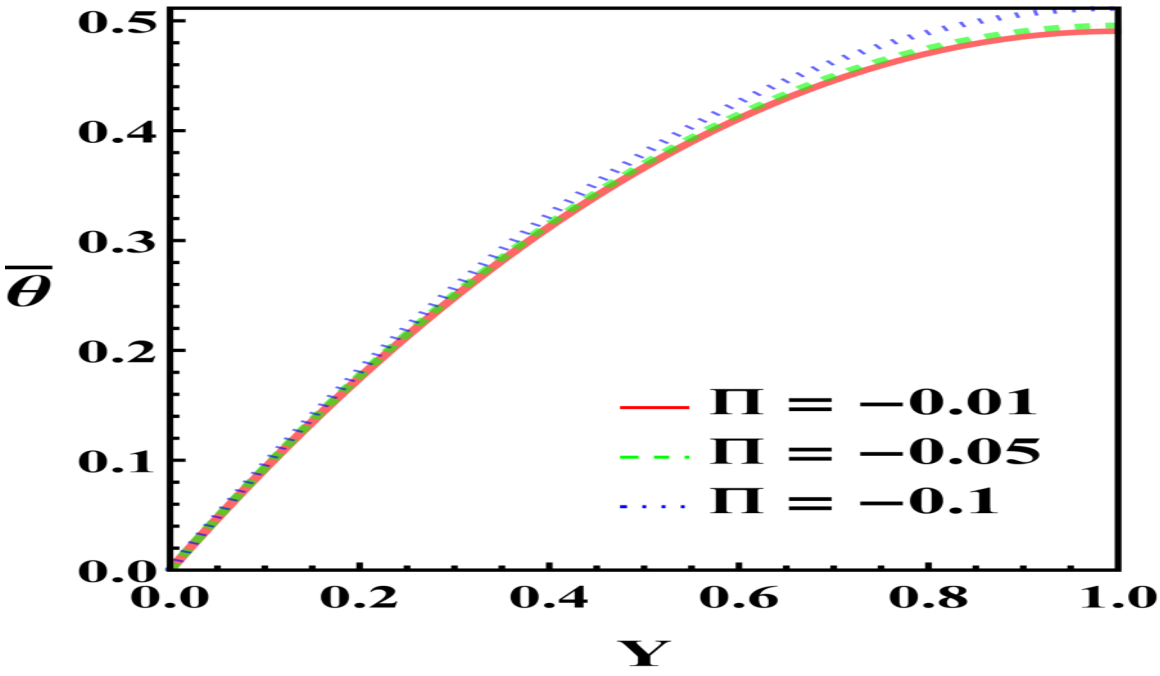

Figure 3.8: Effects of applied pressure gradient on normalized nanofluid temperature when $E_0 = 20\ Volts/m$, $Re = 10^{-2}$. Moreover, the bulk temperature follows an almost quadratic relationship with pressure gradient.

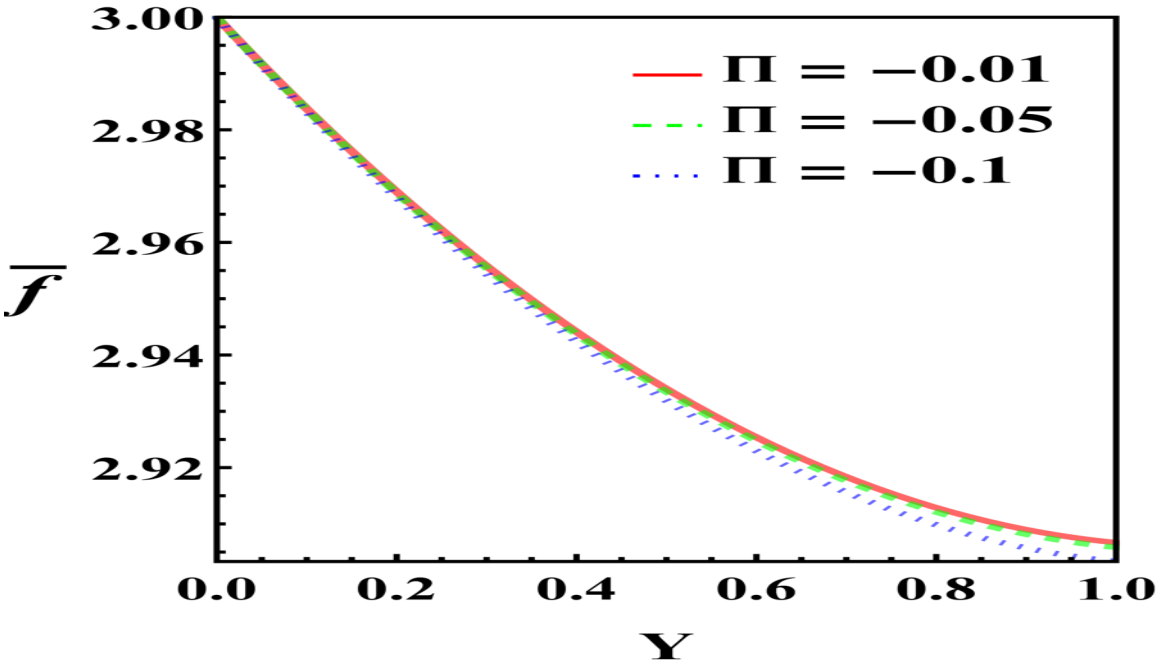

Figure 3.9: Effects of applied pressure gradient on normalized nanoparticle concentration when $E_0 = 20\ Volts/m,\ Re = 10^{-2},\ \phi_1 = 2 \times 10^{-10}$.

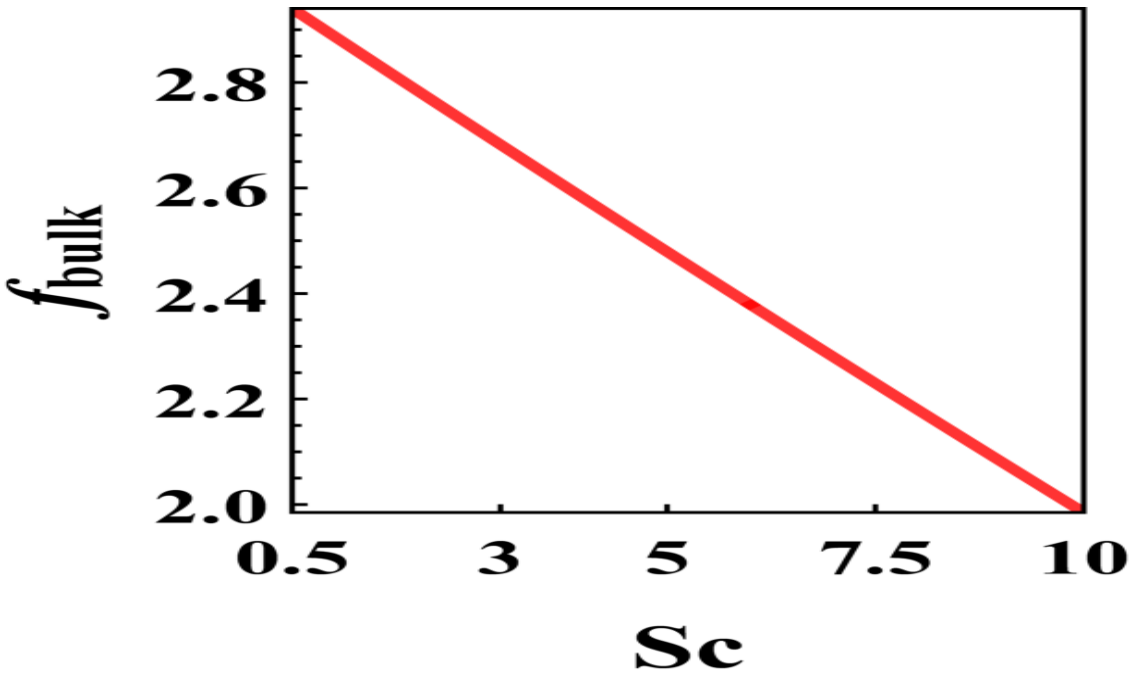

Figure 3.10: The normalized bulk nanofluid concentration follows a decreasing trend with enhancement of Schmidt number (when $E_0 = 20\ Volts/m$) when $Re = 10^{-2},\ \phi_1 = 2 \times 10^{-10}$.

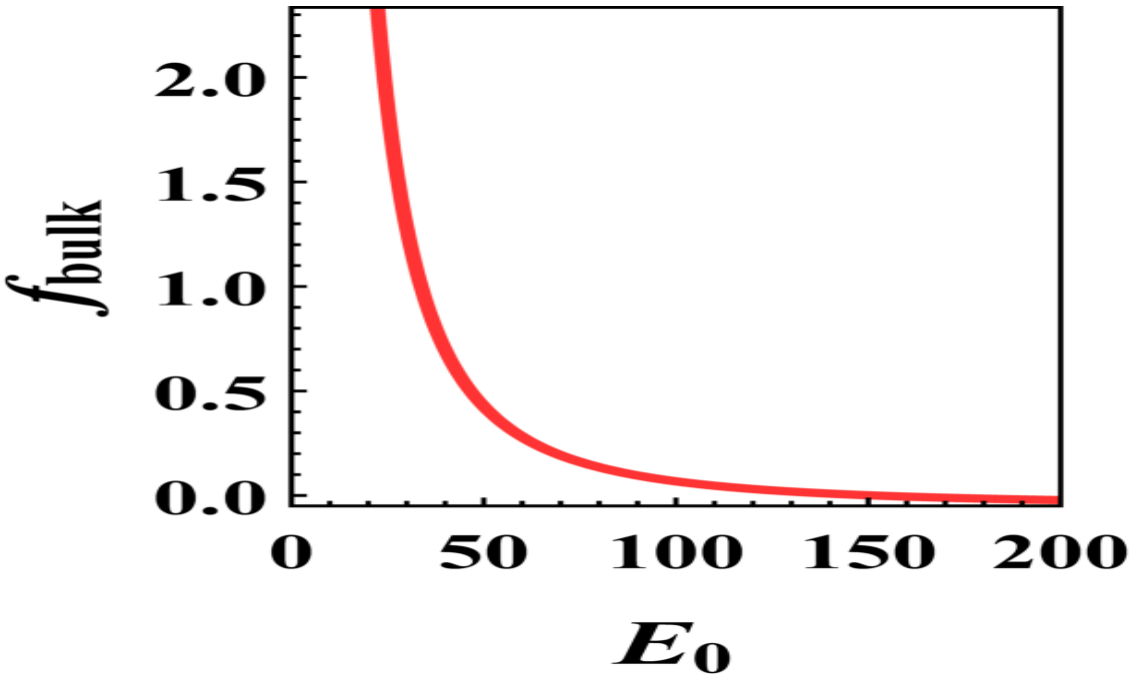

Figure 3.11: The normalized bulk nanofluid concentration follows a decreasing trend with enhancement of electric field strength when $Re = 10^{-2},\ \phi_1 = 2 \times 10^{-10}$.

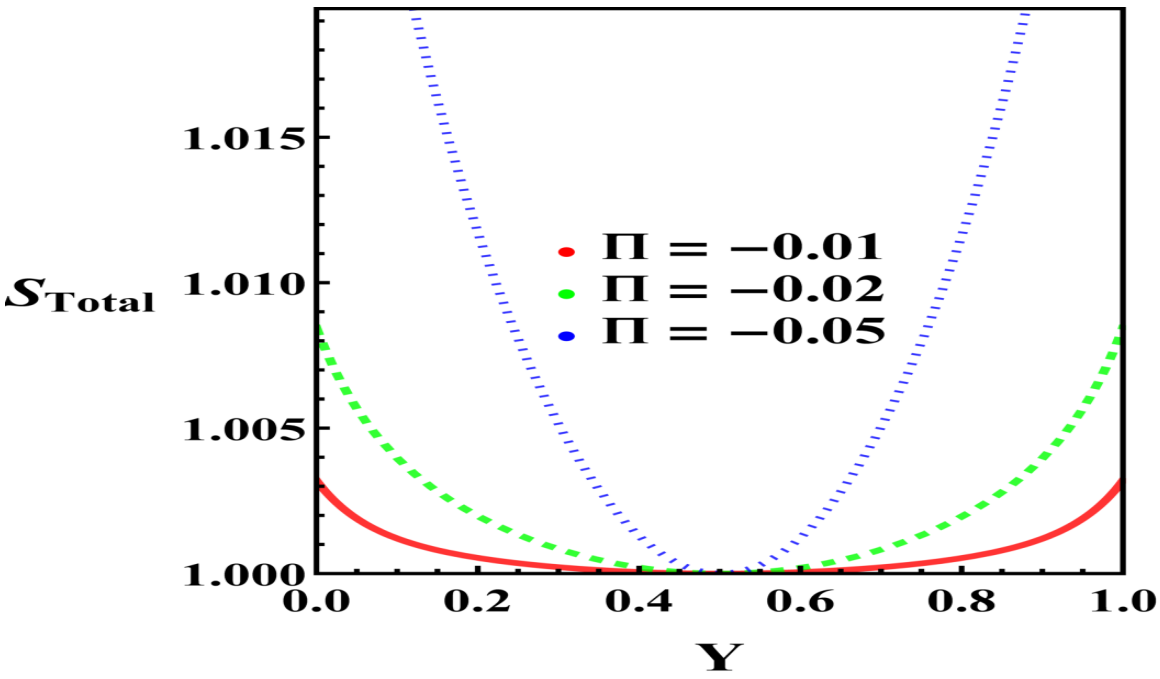

Figure 3.12: The normalized total entropy generation follows an increasing trend with enhancement of both absolute value of pressure gradient (negative value of Π indicates the pressure drives flow in the positive x direction) when $E_0 = 20\ Volts/m,\ Re = 10^{-2}$.

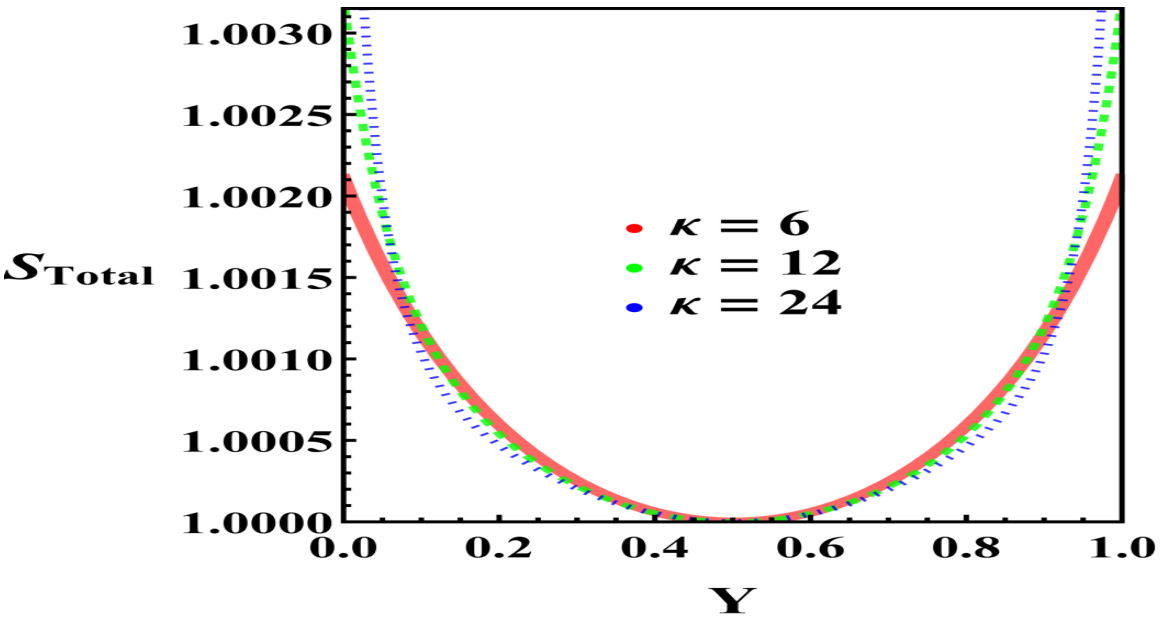

Figure 3.13: The normalized total entropy generation follows an increasing trend with enhancement of electroosmotic parameter (proportional to the ion concentration in nanofluid) near channel walls when $E_0 = 20$ Volts m^{-1}, $Re = 10^{-2}$.

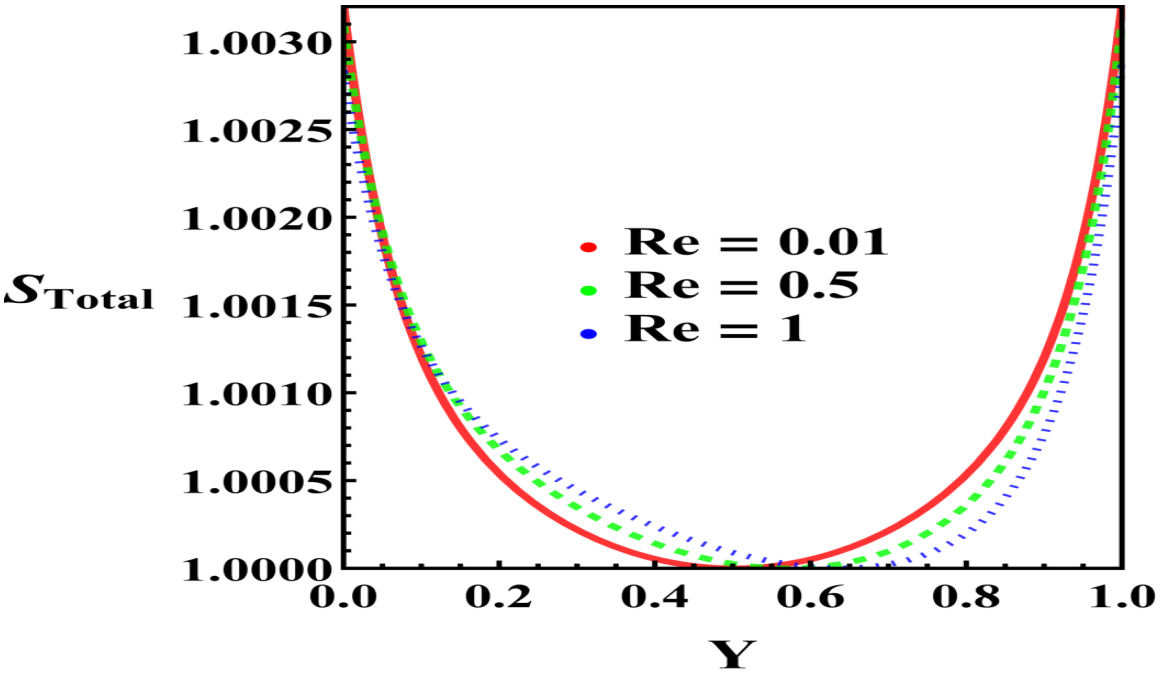

Figure 3.14: The normalized total entropy generation follows an decreasing trend with increment in Reynolds number near the channel walls, whereas, the reverse trend is visible in middle like region when $E_0 = 20$ Volts m^{-1}. Moreover, the variations in magnitude of contribution of injection velocity in total entropy generation near channel walls is smaller compared to κ, Π.

Chapter 4

Effects of diffusive Reynolds number on electroosmotic pulsating nanofluid flow[3]

4.1 INTRODUCTION

The study of ion diffusion coefficient (Nielsen et al. [1952], Zhong and Friedman [1988], Sato et al. [2012]) in an electrolyte solution is an important domain of experimental research that has several applications in building electrical double layer capacitors (EDLCS (Conway [1991], Miller and Simon [2008])) and microfluidic devices (Selvaganapathy et al. [2002], Johnson and Locascio [2002], Wang et al. [2004]). Kong et al. [2017] experimentally investigated the effects of temperature on ion diffusion coefficient in NaCl electrolyte solution in a Graphene nanochannel. It is revealed from their study that the enhancement of temperature leads to increase thermal motion of ions than bulk motion of liquid, results in a stable ion diffusion coefficient. Being motivated by their findings, we propose to investigate a converse problem (Mukherjee and Shit [2022]) mathematically to examine the effects of ion diffusion coefficient on nanofluid (CHOI [1995]) temperature for a steady couple stress nanofluid flow in a microchannel. We found that nanofluid temperature increases with an enhancement of ion diffusion coefficient. In fact, the effects of ion diffusion coefficient on temperature increases as the channel height gets thinner. This chapter intends to extend our earlier mathematical model (Mukherjee and Shit [2022]) under a pulsating pressure gradient scenario thereby incorporating several new complex physiological fluid flow phenomena.

In addition to pulsating pressure-driven flow in a micro-channel, the pressure drop phenomena across porous walls (Berman [1953], Sellars [1955], Yuan [1956], Morduchow [1956], Esmond and Clark [1966], Beavers and Joseph [1967], Wang [1971], Radhakrishnamacharya and Maiti [1977], Rajagopal and Tao [1995], Elshehawey et al.

[3]The content of this chapter has been submitted to *Physics of Fluids* (AIP)

[2000], Vajravelu et al. [2003], Malathy and Srinivas [2008], Bitla and Iyenger [2014]) is considered in terms of a slip boundary condition. It was observed from the work of Beavers and Joseph [1967] that for a steady fluid flow over a permeable bed, the effects of slip condition at channel-bed interface plays an important part in flow dynamics. They postulated a boundary condition in their paper, wherein they also experimentally calculated the slip coefficients. This boundary conditions were incorporated by several researchers Vajravelu et al. [2003], Malathy and Srinivas [2008], Bitla and Iyenger [2014] in their respective studies while analyzing fluid flow phenomena in a channel in the presence of injected velocity. However, most of their studies are limited to the investigation of the velocity profiles. In this chapter, a novel boundary condition is introduced to explore the effects of a frictional coefficient near rough microchannel walls on the nanofluid temperature. The effects of injected velocity and ion diffusion coefficient on the zeta potential distribution as well as Smoluchowski velocity have been briefly discussed in this context. In our earlier work Mukherjee and Shit [2022], we have shown that electric double layer (EDL) thickness near the lower microchannel wall, denoted by d_L, can be expressed as,

$$d_L \approx \frac{1}{R_D} ln|a\Big(\frac{R_D}{m^2} + \frac{1}{R_D}\Big) + b|,$$

where $a, b \in \mathcal{R}$, m denotes the electroosmotic parameter and R_D denotes the diffusive Reynolds number. Moreover, the electroosmotic slip velocity ($\tilde{U}_{HS}$) near the lower microchannel wall can be presented as,

$$\tilde{U}_{HS} = \frac{\sqrt{k_1}}{\alpha}\frac{\partial u}{\partial y}|_{y=0} - \frac{E_0\epsilon}{\mu}\int e^{\frac{Ve}{\nu}y}\int e^{-\frac{Ve}{\nu}y}\frac{\partial^2\psi}{\partial y^2}dydy|_{y=0},$$

where Ve denotes the injected nanofluid velocity. The non-linear coupled ODEs governing the nanofluid flow and heat transfer phenomena are solved by applying the differential transform method (DTM). Zhou [1986] pioneered the idea of DTM. Then, Chen and Ho [1999] incorporated this method to solve PDEs. This method yields a truncated power series solution where the series coefficients are calculated recursively by applying algebraic identities. We have briefly described this method in Section 4.3.

This chapter analytically examines the effect of ion diffusion coefficient, Womersely number, oscillating pressure gradient and frictional drag coefficients on pulsating electroosmotic nanofluid flow, heat and mass transfer process in a micro-nano channel between two permeable walls in the presence of wall slip-velocity. The temperature distribution in the microchannel depends on the Joule heating and temperature at the channel surface. The structure of this article can be summarized as follows. Section 4.2 states the governing flow equations under certain assumptions on the microchannel width. Section 4.3 introduces a discussion on the method of solution used in the present study. Moreover, a validation part is also presented to show the convergence of solution. Section 4.4 is devoted to the findings on the heat and mass transport flow characteristics through the graphical illustrations. The important findings are summarized in Section 4.5.

4.2 Mathematical description of the problem

The pulsating flow of viscous incompressible Newtonian nanofluid between two permeable walls of micrometer height (h) is considered for this study in the presence of an externally applied electric field of strength E_0. The physical diagram of the problem in the Cartesian coordinates is presented in Figure 4.1. The nanofluid is injected into microchannel from lower permeable wall with a velocity Ve and is assumed to be absorbed at the upper wall with same velocity. The permeability of lower and upper walls are denoted by k_1 and k_2 respectively. The flow through the permeable walls is assumed to follow the Darcy's law and slip boundary condition is implemented at the fluid-wall interface. The following assumptions are made for conducting the analysis of the problem:

- The flow takes place between two parallel plates of semi-infinite length. The microchannel height (h) is small compared to its length thereby the longitudinal gradient field $\frac{\partial}{\partial x} << \frac{\partial}{\partial y}$. Thus, the longitudinal convective terms $u\frac{\partial}{\partial x}$ are ignored from the flow equations. Moreover, velocity profile is represented as $q = (u(y), Ve)$.
- The flow is fully developed and laminar.
- Homogeneous permeable walls are assumed for this study.
- The pulsatile pressure gradient that drives the fluid flow is expressed as,

$$\frac{1}{\rho}\frac{\partial p}{\partial x} = A + Be^{i\omega t},$$

  where ω is the frequency and A, B are two negative real numbers which denote the steady and unsteady parts of the pressure gradient respectively.

Based on the above assumptions, the governing equations for nanofluid flow, in the Cartesian coordinates can be expressed as follows, (Bitla and Iyenger [2014], Seth et al. [2018])

$$\frac{\partial u}{\partial t} + Ve\,\frac{\partial u}{\partial y} = -\frac{1}{\rho}\,\frac{\partial p}{\partial x} + \nu\,\frac{\partial^2 u}{\partial y^2} + \frac{\rho_e}{\rho}\,E_0, \tag{4.1}$$

$$\frac{\partial p}{\partial y} = 0, \tag{4.2}$$

$$\frac{\partial T}{\partial t} + Ve\,\frac{\partial T}{\partial y} = \frac{k}{\rho\,C_p}\,\frac{\partial^2 T}{\partial y^2} + \sigma\,\frac{{E_0}^2}{\rho\,C_p} + F_r, \tag{4.3}$$

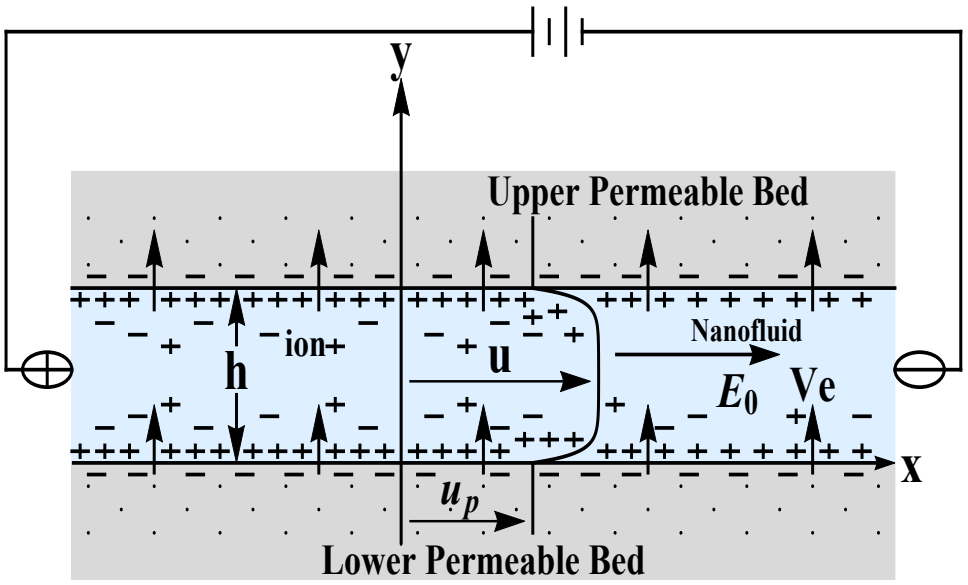

Figure 4.1: Physical sketch of the problem

$$\frac{\partial C}{\partial t} + Ve\,\frac{\partial C}{\partial y} \;=\; D_B\,\frac{\partial^2 C}{\partial y^2} + \frac{D_T}{T_h}\,\frac{\partial^2 T}{\partial y^2}, \tag{4.4}$$

where, $F_r = \frac{2\lambda_1\mu}{\rho C_p}\left[\left(\frac{\partial u_s}{\partial y}\right)^2 + \frac{\partial u_s}{\partial y}\frac{\partial u_o}{\partial y}e^{i\omega t}\right]$ denotes the contribution of time dependent viscous drag force in heat generation and λ_1 is a proportionality constant. The velocity components of nanofluid are denoted by u in the x-direction and Ve in the y-direction respectively. The nanofluid temperature is denoted by T and C denotes the concentration of nanoparticles present in the nanofluid. Here, ν denotes the kinematic viscosity, ρ the density, k the thermal conductivity, C_p the specific heat of the nanofluid, ρ_e the net charge density, D_B the Brownian diffusion parameter and D_T the thermophoresis parameter respectively. The pulsating nature of the pressure gradient suggests the following forms for the velocity, temperature and volume fraction of the nanoparticle fields:

$$\begin{aligned} u(y,t) &= u(y)_s + Real(u(y)_o e^{i\omega t}),\\ T(y,t) &= T(y)_s + Real(T(y)_o e^{i\omega t}),\\ C(y,t) &= C(y)_s + Real(C(y)_o e^{i\omega t}), \end{aligned} \tag{4.5}$$

where *Real* denotes real part of the function. The subscripts s, o denote steady and unsteady parts respectively.

Table 4.1: Physical parameter values used in this study (Ranjit et al. [2019], Zhao et al. [2014])

Physical Parameters	Values [Unit]
Channel height (h)	100 μm
Density of the fluid (ρ)	1000 kg/m^3
Charge of proton (e)	1.6×10^{-19} C
Electrical Potential at the walls (ζ_1, ζ_2)	-25 mV
Boltzmann Constant (K_B)	1.38×10^{-23} J/K
Average absolute temperature (T_{av})	300 K
Valency of ions (z)	1
Permittivity of the medium (ϵ)	8×10^{-10} C/Vm
Kinematic viscosity (ν)	10^{-6} m^2/s
Electrical Conductivity (σ_e)	5×10^{-3} S/m
Thermal Conductivity (k)	0.5 W/mK
Specific heat (C_p)	3000 J/kgK
Material parameter (α)	0.1
Permeability of the beds (k_1, k_2)	10^{-7} m^2
Brownian Diffusion Coefficient (D_B)	2×10^{-6} m^2/s
Thermophoretic Diffusion Coefficient (D_T)	10^{-6} m^2/s
Permeability of the medium (k_p)	10^{-4} m^2

4.2.1 Electric Zeta Potential Distribution

The electric potential distribution ψ developed inside the microchannel, is governed by the Poisson equation (Ranjit and Shit [2017]) as follows,

$$\frac{\partial^2 \psi}{\partial y^2} = -\frac{\rho_e}{\epsilon}, \tag{4.6}$$

where ϵ denotes the medium permittivity. The electrolytes are assumed to be $1:1$ symmetric. The expression for the net charge density (Ranjit and Shit [2017]) is described as,

$$\rho_e = ezN_A(n^+ - n^-), \tag{4.7}$$

where N_A represents the Avogadro number, z the valence of the ions, e the electron charge and $(n^{\pm})$ the average number of the positive or negative ions respectively. The ionic distribution is calculated by using the following Nernst-Planck equation along with a set of boundary conditions,

$$\begin{aligned} \frac{\partial n^{\pm}}{\partial t} + Ve\ \frac{\partial n^{\pm}}{\partial y} &= D\ \frac{\partial^2 n^{\pm}}{\partial y^2} \pm \frac{D\ z\ e}{K_B\ T_{av}} \frac{\partial}{\partial y}(n^{\pm}\ \frac{\partial \psi}{\partial y}), \\ n^{\pm} &= 0 \quad \text{at } \frac{\partial \psi}{\partial y} = 0, \\ n^{\pm} &= n_0\ e^{\frac{Ve}{D} y} \quad \text{at } \psi = 0, \end{aligned} \tag{4.8}$$

where D denotes the ion diffusivity, K_B the Boltzmann constant, T_{av} the average temperature of nanofluid, n_0 the ion density. Under an additional assumption that the ion concentration does not vary with time, after solving Eq. 4.8, we obtain the following expressions for the ion concentration,

$$n^{\pm} = n_0 \, e^{\mp \frac{z}{K_B} \frac{e}{T_{av}} \psi + \frac{Ve}{D} y}. \tag{4.9}$$

Combining Eqs. 4.6 and 4.9 and using the Debye-Hückel approximations (Bandopadhyay et al. [2013]), we obtain,

$$\frac{\partial^2 \psi}{\partial y^2} = \frac{2 n_0 \, ez \, N_A}{\epsilon} \, e^{\frac{Ve}{D} y} \left(\frac{ez}{K_B T_{av}} \psi \right). \tag{4.10}$$

The channel walls are assumed to have constant but different Zeta potentials thereby ψ satisfies the following boundary conditions,

$$\begin{aligned} \psi &= \zeta_1 \quad \text{at } y = 0, \\ \psi &= \zeta_2 \quad \text{at } y = h, \end{aligned}$$

where ζ_1, ζ_2 are the different zeta potentials at the channel walls.

4.2.2 Boundary Conditions

i. The following boundary conditions for velocity at channel walls have been set:

$$\begin{aligned} \frac{\partial u}{\partial y} &= \frac{\alpha}{\sqrt{k_1}} \left(u + \frac{k_1}{\mu} \frac{\partial p}{\partial x} \right) \text{ at } y = 0, \\ \frac{\partial u}{\partial y} &= -\frac{\alpha}{\sqrt{k_2}} \left(u + \frac{k_2}{\mu} \frac{\partial p}{\partial x} \right) \text{ at } y = h. \end{aligned} \tag{4.11}$$

ii. The constant temperature is imposed at lower channel wall and the variable temperature at the upper wall:

$$\begin{aligned} T &= T_0 \quad \text{at } y = 0, \\ Ve \frac{\partial T}{\partial y} &= \frac{bBr\nu}{C_p} \left[\left(\frac{\partial u_s}{\partial y} \right)^2 + \frac{\partial u_s}{\partial y} \frac{\partial u_o}{\partial y} e^{i\omega t} \right] \quad \text{at } y = h. \end{aligned} \tag{4.12}$$

The lower wall is assumed to be kept at a fixed temperature. It is assumed that the rate of change of the net heat energy is proportional to the viscous dissipation energy near upper channel wall where b is a frictional constant.
iii. Fractional distribution of nanoparticles at the channel walls:

$$\begin{aligned} C &= C_h + \phi_1^* \, k_1 \, \frac{\rho Ve}{M n_0} \quad \text{at } y = 0, \\ \frac{\partial C}{\partial y} &= -\phi_2^* \, k_2 \, \frac{\rho Ve}{M n_0} \quad \text{at } y = h. \end{aligned} \tag{4.13}$$

where ϕ_1^*, ϕ_2^* are boundary deposition parameters, C_h denotes the concentration of nanoparticle at the upper channel wall and M denotes Molar mass of the nanoparticles.

4.2.3 Transformation of the variables and equations

The following transformations are applied to make the governing equations dimensionless.

$$Y = \frac{y}{h},\ \tilde{t} = \frac{tVe}{h},\ U = \frac{u}{\lambda U_{HS}},\ U_s = \frac{u_s}{\lambda U_{HS}},\ U_o = \frac{u_o}{\lambda U_{HS}},$$
$$f = \frac{C - C_h}{Br(C_0 - C_h)},\ Z_1 = \frac{ez}{K_B T_{av}}\zeta_1,\ Z_2 = \frac{ez}{K_B T_{av}}\zeta_2,$$
$$\theta = \frac{T - T_0}{Br(T_h - T_0)},\ \tilde{\omega} = \frac{h\omega}{Ve},\ \Phi = \frac{ez}{K_B T_{av}}\psi,\ \lambda = \frac{h}{\epsilon|\zeta_1|}\sqrt{\frac{\sigma\mu}{S}}.$$

where S is a sensitivity material parameter, T_0 is the lower wall temperature, T_h is a reference temperature, U_s is the steady dimensionless part of velocity, U_o is the unsteady dimensionless part of velocity, U_{HS} is the Smoluchowski velocity, f is the dimensionless nanoparticle concentration, θ is the dimensionless temperature, $Z_{1,2}$ are the dimensionless zeta potentials and $\tilde{\omega}$ is the dimensionless Womersley number. The dimensionless form of the equations are presented in subsequent subsections that follow.

1. Electric Potential Distribution

$$\frac{\partial^2 \Phi}{\partial Y^2} = m^2 e^{R_D\ Y}\Phi,$$

along with the wall zeta potential

$$\begin{aligned} \Phi &= Z_1 \quad \text{at } Y = 0, \\ \Phi &= Z_2 \quad \text{at } Y = 1, \end{aligned} \tag{4.14}$$

where $Re = \frac{\rho V e h}{\mu}$ denotes the Reynolds number for injection velocity, $m = \frac{h}{\lambda_D}$ the electroosmotic parameter, $M_D = \frac{\nu}{D}$ the inverse ion diffusivity parameter, $R_D = Re \times M_D$ the diffusive Reynolds number and $\lambda_D = \left(\frac{\epsilon K_B T_{av}}{2e^2 z^2 n_0\ N_A}\right)^{\frac{1}{2}}$ indicates the Debye length.

2. Momentum equation and slip boundary conditions

Eqs. 4.1 and 4.11 are expressed in the following form:

$$\begin{aligned} &\frac{\partial^2 U}{\partial Y^2} = \Pi + Re\left(\frac{\partial U}{\partial \tilde{t}} + \frac{\partial U}{\partial Y}\right) - \frac{m^2}{\lambda Z_1}\Phi, \\ &\frac{\partial U}{\partial Y} - \frac{\alpha}{\sqrt{L_1}}(U + L_1\Pi) = 0 \quad \text{at } Y = 0, \\ &\frac{\partial U}{\partial Y} - \frac{\alpha}{\sqrt{L_2}}(U + L_2\Pi) = 0 \quad \text{at } Y = 1. \end{aligned} \tag{4.15}$$

The non dimensional parameters are as follows,

$$U_{HS} = -\frac{\epsilon E_0 \zeta_1}{\mu},\ L_1 = \frac{k_1}{h^2},\ L_2 = \frac{k_2}{h^2},\ \Pi = \frac{\frac{\partial p}{\partial x}h^2}{\mu\lambda U_{HS}},$$

where $\Pi = \Pi_s + \Pi_o e^{i\tilde{\omega}\tilde{t}}$ denotes the periodic pressure parameter, U_{HS} denotes the Helmholtz-Smoluchowski velocity at the edge of the EDL, L_1, L_2 respectively denote the permeability parameters.

3. Thermal energy equation and the boundary conditions

Using the non-dimensional variables in Eqs. 4.3 and 4.12, we obtain,

$$\begin{aligned} \theta &= \Omega + \frac{S}{RePr}Y, \\ \frac{\partial^2\Omega}{\partial Y^2} + 2\lambda_1\left[\left(\frac{\partial U_s}{\partial Y}\right)^2 + \frac{\partial U_s}{\partial Y}\frac{\partial U_o}{\partial Y}e^{i\tilde{\omega}\tilde{t}}\right] &= Pr\ Re\left(\frac{\partial\Omega}{\partial\tilde{t}} + \frac{\partial\Omega}{\partial Y}\right), \\ \Omega &= 0 \quad \text{at } Y = 0, \\ \frac{\partial\Omega}{\partial Y} &= b\cdot\frac{Ec}{Re}\left[\left(\frac{\partial U_s}{\partial Y}\right)^2 + \frac{\partial U_s}{\partial Y}\frac{\partial U_o}{\partial Y}e^{i\tilde{\omega}\tilde{t}}\right] - \frac{S}{RePr} \quad \text{at } Y = 1. \end{aligned} \tag{4.16}$$

The non-dimensional parameters appearing in the Eq. 4.16 are as follows,

$$Pr = \frac{\mu\ C_p}{k},\ \gamma = \frac{\sigma h^2 {E_0}^2}{k\ (T_h - T_0)},\ Ec = \frac{\lambda^2 {U_{HS}}^2}{C_p\ (T_h - T_0)},$$

where Pr denotes the Prandtl number, Ec the Eckert number, $Br = Pr \times Ec$ the Brinkman number and γ represents the Joule heating parameter.

4. Equation of mass concentration

The non-dimensional form of Eqs. 4.4 and 4.13 become,

$$\begin{aligned} \frac{\partial^2 f}{\partial Y^2} &= Sc\ Re\left(\frac{\partial f}{\partial\tilde{t}} + \frac{\partial f}{\partial Y}\right) - S_t\frac{\partial^2\theta}{\partial Y^2}, \\ f &= ReL_1\phi_1 \quad \text{at } Y = 0, \\ \frac{\partial f}{\partial Y} &= -ReL_2\phi_2 \quad \text{at } Y = 1. \end{aligned} \tag{4.17}$$

The non-dimensional parameters are as follows,

$$\begin{aligned} Sc = \frac{\mu}{\rho\ D_B},\ S_t = \frac{D_T\ (T_h - T_0)}{T_h\ D_B\ (C_0 - C_h)},\ \phi_1 = \frac{h\mu\phi_1^*}{BrMn_0(C_0 - C_h)}, \\ \phi_2 = \frac{h^2\mu\phi_2^*}{BrMn_0(C_0 - C_h)}, \end{aligned} \tag{4.18}$$

where Sc denotes the Schmidt number, $\phi_{1,2}$ denote deposition parameters and S_t denotes the Soret number.

4.2.4 Splitting the equations in steady and unsteady parts

We assume that the solutions of the equations 4.15-4.17 take the following form,

$$\begin{aligned} U(Y,\tilde{t}) &= U_s(Y) + Real(U_o(Y)e^{i\tilde{\omega}\tilde{t}}), \\ \Omega(Y,\tilde{t}) &= \Omega_s(Y) + Real(\Omega_o(Y)e^{i\tilde{\omega}\tilde{t}}), \\ f(Y,\tilde{t}) &= f_s(Y) + Real(f_o(Y)e^{i\tilde{\omega}\tilde{t}}). \end{aligned} \tag{4.19}$$

1. Velocity Profiles: After substituting 4.19 into the equations 4.15 and equating the steady part, we obtain,

$$\begin{aligned}
&\frac{\partial^2 U_s}{\partial Y^2} - Re\ \frac{\partial U_s}{\partial Y} = \Pi_s - \frac{m^2\Phi}{\lambda Z_1},\\
&\frac{\partial U_s}{\partial Y} = \frac{\alpha}{\sqrt{L_1}}\Big(U_s + L_1\ \Pi_s\Big) \quad \text{at } Y = 0,\\
&\frac{\partial U_s}{\partial Y} = -\frac{\alpha}{\sqrt{L_2}}\Big(U_s + L_2\ \Pi_s\Big) \quad \text{at } Y = 1.
\end{aligned} \tag{4.20}$$

Similarly, the unsteady part of those equations become,

$$\begin{aligned}
&\frac{\partial^2 U_o}{\partial Y^2} - \Pi_o - i\ \tilde{\omega}\ Re\ U_o - Re\ \frac{\partial U_o}{\partial Y} = 0,\\
&\frac{\partial U_o}{\partial Y} = \frac{\alpha}{\sqrt{L_1}}\Big(U_o + L_1\ \Pi_o\Big) \text{ at } Y = 0,\\
&\frac{\partial U_o}{\partial Y} = -\frac{\alpha}{\sqrt{L_2}}\Big(U_o + L_2\ \Pi_o\Big) \text{ at } Y = 1.
\end{aligned} \tag{4.21}$$

2. Temperature Profiles
The steady part of the equations 4.16 yields

$$\begin{aligned}
&\frac{\partial^2 \Omega_s}{\partial Y^2} - Pr\ Re\ \frac{\partial \Omega_s}{\partial Y} + 2\lambda_1\left(\frac{\partial U_s}{\partial Y}\right)^2 = 0,\\
&\Omega_s = 0 \quad \text{at } Y = 0,\\
&\frac{\partial \Omega_s}{\partial Y} = b\frac{Ec}{Re}\left(\frac{\partial U_s}{\partial Y}\right)^2 - \frac{S}{RePr} \quad \text{at } Y = 1.
\end{aligned} \tag{4.22}$$

and the corresponding unsteady part satisfy

$$\begin{aligned}
&\frac{\partial^2 \Omega_o}{\partial Y^2} - Pr\ Re\ \frac{\partial \Omega_o}{\partial Y} - Pr\ Re\ i\ \tilde{\omega}\ \Omega_o + 2\lambda_1\frac{\partial U_s}{\partial Y}\frac{\partial U_o}{\partial Y} = 0,\\
&\Omega_o = 0 \quad \text{at } Y = 0,\\
&\frac{\partial \Omega_o}{\partial Y} = b\frac{Ec}{Re}\ \frac{\partial U_s}{\partial Y}\ \frac{\partial U_o}{\partial Y} \quad \text{at } Y = 1.
\end{aligned} \tag{4.23}$$

3. Concentration profiles
The differential equations and boundary conditions of the concentration in steady case become,

$$\begin{aligned}
&Sc\ Re\left(\frac{\partial f_s}{\partial Y}\right) = \frac{\partial^2 f_s}{\partial Y^2} + S_t\ \frac{\partial^2 \theta_s}{\partial Y^2},\\
&f_s = ReL_1\phi_1 \quad \text{at } Y = 0,\\
&\frac{\partial f_s}{\partial Y} = -ReL_2\phi_2 \quad \text{at } Y = 1.
\end{aligned} \tag{4.24}$$

Table 4.2: The differential transform identities used in this study

Differentiable function	DTM expression
$w(r) = \frac{d^m g(r)}{dr^m}$	$W(l) = \frac{(l+m)!}{l!} G(l+m)$
$w(r) = m(r)n(r)$	$W(l) = \sum_{i=0}^{l} M(i)N(l-i)$
$w(r) = r^n$	$W(l) = \delta(l-n)$
$w(r) = cp(r) \pm dq(r)$	$W(l) = cP(l) \pm dQ(l)$

Similarly, the differential equation for unsteady parts give rise to,

$$\begin{aligned} &Sc\ Re \left(i\tilde{\omega} f_o + \frac{\partial f_o}{\partial Y} \right) = \frac{\partial^2 f_o}{\partial Y^2} + S_t \frac{\partial^2 \theta_o}{\partial Y^2}, \\ &f_o = 0 \quad \text{at } Y = 0, \\ &\frac{\partial f_o}{\partial Y} = 0 \quad \text{at } Y = 1. \end{aligned} \tag{4.25}$$

4.3 Method of Solution and Convergence

4.3.1 Differential Transform Method (DTM)

The Differential transform method (DTM) is employed to obtain the solutions of the equations 4.20-4.25. The n^{th} order DTM transformation of a function $w(x)$ satisfying a non-linear ODE $\mathcal{N}_w(x) = 0$, denoted by $W(n)$, is expressed as follows,

$$W(n) = \frac{1}{n!} \left[\frac{d^n w(x)}{dx^n} \right]_{x=x_0}, \tag{4.26}$$

where x_0 is selected based on the problem. The Taylor series expansion of $w(x)$ around x_0 can be expressed as,

$$w(x) = \sum_{l=0}^{\infty} W(l)(x - x_0)^l. \tag{4.27}$$

Our objective is to truncate the infinite power series expansion of $w(x)$, expressed in 4.27, into a finite sum $\tilde{w}(x)$ as follows,

$$\tilde{w}(x) = \sum_{l=0}^{N} W(l)(x - x_0)^l, \tag{4.28}$$

where, N is series length. The coefficients $W(l)$ are calculated recursively by transforming the ODEs into a set of algebraic relations by using the identities from Table 4.2. The cumulative square averaged error produced due to this approximation is

measured as,

$$\epsilon_w = \frac{1}{K+1}\sum_{i=0}^{K}[\mathcal{N}_w(\tilde{w}(\frac{i}{K+1}))]^2.$$

The smaller values of ϵ_w for sufficiently large N assures convergence of the solution. Using the identities in Table 4.2, at $x_0 = 0$, the functions satisfying equations 4.15-4.17 are approximated by the expressions $\tilde{u} = \sum_{k=0}^{N} U(k)x^k$, $\tilde{\Omega} = \sum_{k=0}^{N} \Omega(k)x^k$, $\tilde{f} = \sum_{k=0}^{N} F(k)x^k$. Similarly, the boundary conditions are also transformed as follows,

$$\begin{aligned}
&\tilde{u}'(0) + \frac{\alpha}{\sqrt{L_1}}(\tilde{u}(0) + L_1\Pi) = 0, \tilde{u}''(0) = 0, \tilde{\Omega}(0) = 0,\\
&\tilde{f}(0) = ReL_1\phi_1,\\
&\tilde{u}'(1) + \frac{\alpha}{\sqrt{L_2}}(\tilde{u}(1) + L_2\Pi) = 0, \tilde{u}''(1) = 0,\\
&\tilde{\Omega}'(1) = -\frac{S}{RePr},\ \tilde{f}'(1) = -ReL_2\phi_2.
\end{aligned} \tag{4.29}$$

For example, in order to solve f satisfying the equation 4.17, we have selected $x_0 = 0$ for calculating its l-th DTM coefficient, which is expressed as an iterated term as follows,

$$\begin{aligned}
&F(l+2) = \frac{ReSc(l+1)F(l+1) - S_t(l+1)(l+2)\Omega(l+2)}{(l+1)(l+2)},\\
&F(0) = ReL_1\phi_1,\ F(1) = a.
\end{aligned} \tag{4.30}$$

To initiate the above recursion 4.30, an initial unknown value a is needed to calculate the values $F(l), \forall l \geq 0$. The missing value of a is calculated from the boundary condition $\tilde{f}'(1) = -ReL_2\phi_2$ as described in equation 4.29.

4.3.2 Convergence of the Results

The averaged squared residual error for different series length, are presented in Table 4.3, which shows that error term decreases rapidly with the increase of series length parameter, thereby showing the tail terms of the DTM series solution are negligible. Figures 4.5 and 4.6 show a comparison between the DTM solutions (when $R_D \to 0$) and the exact analytic solutions (*i.e.* when $R_D = 0$), presented in appendix 4.6, via equations 4.14 and 4.15, which show excellent agreement. Based on Table 4.3, we have selected $N = 25$ for our study.

4.4 Results and Discussion

This study focuses on examining the effects of ion diffusivity in terms of diffusive Reynolds number (R_D), sensitivity parameter (λ), Womersley number ($\tilde{\omega}$), frictional

Table 4.3: Average squared individual residual error terms for the zeta potential, velocity, temperature and nanoparticle concentration with the number of iterations in DTM when $R_D = 2,\ Re = 10^{-2},\ m = 2,\ \Pi_{s,o} = -0.1,\ L_i = 10,\ Z_{1,2} = -1,\ \lambda = \frac{10^4}{2},\ \phi_1 = 10,\ \phi_2 = 10^{-3},\ S_t = 1,\ Pr = 6,\ S = 1,\ Sc = 0.5,\ K = 1000,\ \lambda_1 = 0.1,\ b = 0.1,\ Ec = \frac{1}{3} \times 10^{-6},\ \tilde{\omega} = \frac{\pi}{4},\ \tilde{t} = 1.$

N	ϵ_Φ	ϵ_u	ϵ_Ω	ϵ_f
20	0.000256358	5.29985×10^{-15}	3.82821×10^{-19}	2.76178×10^{-26}
23	7.56046×10^{-6}	1.14337×10^{-16}	7.75409×10^{-21}	4.749×10^{-28}
25	6.2024×10^{-7}	7.74214×10^{-18}	5.18527×10^{-22}	2.84645×10^{-29}

drag parameters (b, λ_1) on nanofluid flow, heat and mass concentration profiles. The following set of default parameter values (based on Table 4.1) are used for numerical calculations conducted in this chapter:

$$Re = 10^{-2},\ m = 3,\ \tilde{\omega}\ \tilde{t} = \frac{\pi}{4},\ Z_{1,2} = -1,\ S = 1,\ Pr = 6,\ Sc = 0.5,\ S_t = 1,$$
$$\phi_1 = 10,\ \phi_2 = 10^{-3},\ \Pi_{s,o} = -0.1,\ \lambda_1 = 0.1,\ b = 0.1,\ \lambda = \frac{10^4}{2},\ Ec = \frac{1}{3} \times 10^{-6}.$$
$$L_{1,2} = 10,\ R_D = 2,$$

It is observed that, the ion diffusion coefficient D for OH^- is around $5 \times 10^{-9} m^2/s$, which makes the diffusive Reynolds number $R_D = \frac{Veh}{D} = \frac{10^{-4} \times 10^{-4}}{5 \times 10^{-9}} = 2$ for a microchannel of height $100\mu m$ with injected velocity $10^{-4} ms^{-1}$. Figures 4.2-4.4 elucidate the zeta potential distribution inside the microchannel for different physical parameters. Figure 4.2 shows that an enhancement in diffusive Reynolds number reduces the zeta potential distribution. It may be noted that, the diffusive Reynolds number $R_D = \frac{Veh}{D}$ is inversely proportional to ion diffusion coefficient. Thus, diminution of ion diffusion coefficient reduces the zeta potential distribution inside the microchannel. Moreover, we observe a shift in the peak value of electric potential distribution towards the upper channel wall as diffusive Reynolds number increases. This phenomena was discussed for the steady flow case (Mukherjee and Shit [2022]). Figure 4.3 shows that the electric potential diminishes with a rise in the electroosmotic parameter. It is observed that, electroosmotic parameter is proportional to ion density. Thus, enhancement in ionic strength dips the electric potential distribution inside microchannel. Figure 4.4 shows the variation in the electric potential distribution for different zeta potential values at the channel walls. This figure suggests that the electric potential flattens towards the channel walls as surface potential decreases. Figures 4.5, 4.6 show that as the diffusive Reynolds number tends to zero, nanofluid velocity and the electric potential distribution converge to the exact solution, which are presented in appendix, when $R_D = 0$. Figure 4.7 shows that the nanofluid velocity diminishes with diminution of the permeability of the microchannel walls. Moreover, the velocity converges to a particular value when pressure gradient is absent, and this

velocity is a Smoluchowski like velocity. Figures 4.8-4.10 show the variation of flow profiles for different values of the material sensitivity parameter. It is observed in figure 4.8 that nanofluid velocity increases with a diminution of sensitivity parameter (when $S = 1$). The expression for λ, as presented in Subsection 4.2.3, shows that λ is proportional to the channel height h. Thus, decrement in channel height while keeping other parameters fixed eventually increases nanofluid velocity. Figure 4.9 shows that nanofluid temperature increases with a diminution of sensitivity parameter and a reversal trend is visible for nanoparticle concentration profile. The enhancement in drag force for diminishing channel height is responsible for rise in the temperature, whereas the diminution in rate of change in temperature gradient enhances the rate of change in nanoparticle concentration gradient, thereby reducing mass transfer rate due to thermophoretic diffusion process. Figures 4.11-4.16 elucidate the effects of the Womersley number and diffusive Reynolds number on the flow profiles. Figures 4.11, 4.12 show that nanofluid velocity and temperature decreases with enhancement of the Womsersley number, which is proportional to unsteady pressure frequency. This result is in agreement with the earlier results available in literature Loudon and Tordesillas [1998]. However, in figure 4.13 the trend is opposite, and the variation remains small. Figure 4.14 shows that nanofluid velocity decreases with an increase in the diffusive Reynolds number. The diminution of the ion diffusion coefficient is responsible for formation of a weaker electrical potential distribution in microchannel, thereby reducing the charge density inside the microchannel, hence the electroosmotic force cause the reduction in nanofluid flow. Figure 4.15 shows that the diminution of ion diffusion coefficient diminishes the net charge density thereby producing lesser frictional heat generation due to reduced velocity gradient. The effect of ion diffusion on heat generation is significant in a nanometer height channel, as considered in terms of $\lambda = \frac{1}{2}$, $S = 1$ and is also suggested by figure 4.9. The opposite behaviour is observed in figure 4.10 for nanoparticle concentration. These results are in agreement with some graphical findings present in the work of Kong et al. [2017].

4.5 CONCLUSIONS

The effect of the ion diffusion coefficient, in terms of diffusive Reynolds number on pulsating nanofluid flow between two permeable walls in a microchannel has been analytically examined in this article. The combined effects of the ion diffusion coefficient along with the injected fluid velocity through the pores of the channel walls, sensitivity parameter, Womsersley number and viscous drag coefficients on nanofluid velocity and temperature are investigated in this chapter. The novel boundary conditions are introduced to measure the contribution of viscous drag force during heat generation. The effects of the thermophoresis phenomena in nanoparticle diffusion process is investigated. The convergence analysis for the DTM solution is presented both graphically and in Table 4.3, in terms of square averaged error estimation for different series iteration parameter. An illustration for the effects of different sur-

face zeta potential on the electric potential distribution inside the microchannel is presented. The main findings from our study can be summarized as follows:

- The electrics potential decreases with the enhancement of the diffusive Reynolds number, electroosmotic parameter.
- The nanofluid velocity decreases with a diminution of microchannel permeability parameter; moreover velocity converges to a fixed velocity in the absence of pressure gradient when the wall permeability tends to zero.
- The nanofluid velocity increases with a diminution of sensitivity parameter, Womsersley number and diffusive Reynolds number.
- The nanofluid temperature increases with diminution of sensitivity parameter, Womsersley number and diffusive Reynolds number.
- The nanoparticle concentration increases with the enhancement of sensitivity parameter and diffusive Reynolds number.

4.6 Appendix

$$\Phi = Z_1 \cosh mY + \frac{Z_2 - Z_1 \cosh m}{\sinh m} \sinh mY, \tag{4.31}$$

$$U = U_s + U_o e^{\tilde{\omega} \tilde{t}}, \tag{4.32}$$

$$U_s = d_1 + d_2 e^{ReY} - \frac{\Pi_s}{Re} Y - \tilde{\Phi}, \tag{4.33}$$

$$U_o = e_1 e^{s_1 Y} + e_2 e^{s_2 Y} - \frac{\Pi_o}{Re\ i\ \tilde{\omega}}, \tag{4.34}$$

$$T_1 = \frac{m^2}{\lambda},\ T_2 = \frac{m^2}{\lambda} \frac{\frac{Z_2}{Z_1} - \cosh m}{\sinh m}, \tag{4.35}$$

$$\tilde{\Phi} = \Big(\frac{T_1}{m^2} + Re\ \frac{m\ T_2 + Re\ T_1}{m^2\ (m^2 - Re^2)} \Big) \cosh mY + \frac{m\ T_2 + Re\ T_1}{m\ (m^2 - Re^2)} \sinh mY, \tag{4.36}$$

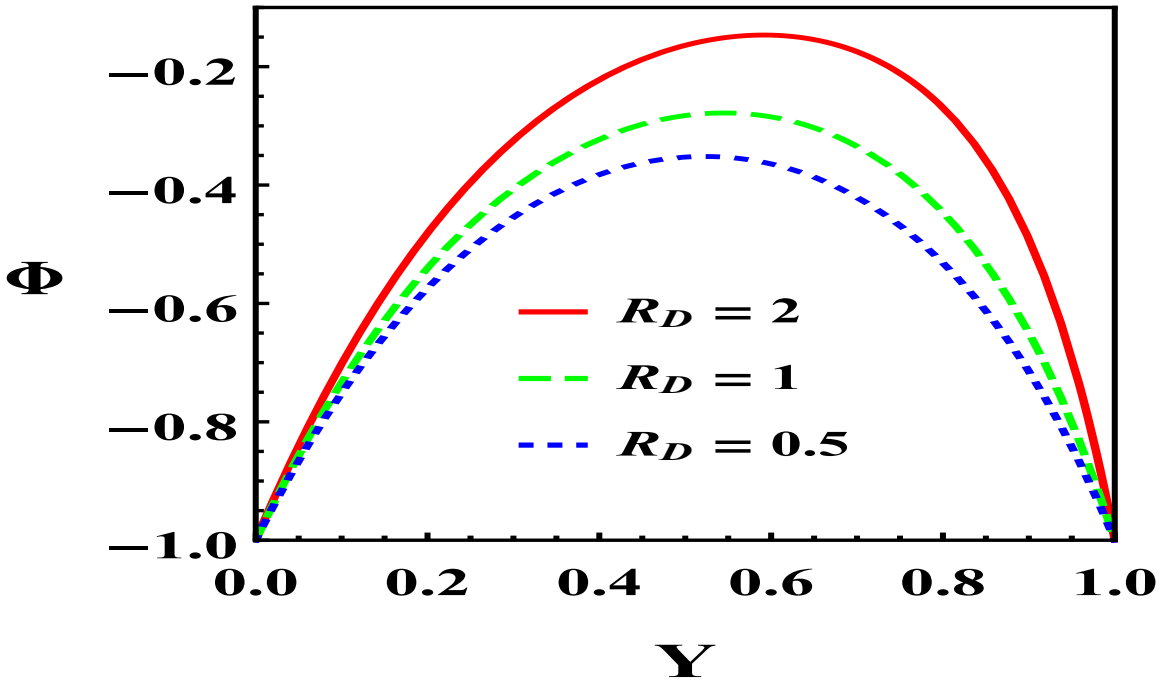

Figure 4.2: Electric potential distribution in microchannel for different values of diffusive Reynolds number when $m = 3$.

where,

$$d_1 = \frac{c_1 d - b c_2}{ad - bc},\ d_2 = \frac{c c_1 - a c_2}{bc - ad},\ a = -\frac{\alpha}{\sqrt{L_1}},$$
$$b = Re - \frac{\alpha}{\sqrt{L_1}},\ c = \frac{\alpha}{\sqrt{L_2}},\ d = Re\ e^{Re} + \frac{\alpha\ e^{Re}}{\sqrt{L_2}},$$
$$c_1 = \frac{\Pi_s}{Re} + \tilde{\Phi}'|_{Y=0} + \frac{\alpha}{\sqrt{L_1}}(L_1\ \Pi_s - \tilde{\Phi}|_{Y=0}),$$
$$c_2 = \frac{\Pi_s}{Re} + \tilde{\Phi}'|_{Y=1} - \frac{\alpha}{\sqrt{L_2}}(L_2\ \Pi_s - \tilde{\Phi}|_{Y=1} - \frac{\Pi_s}{Re}).$$
$$S_{1,2} = \frac{Re \pm \sqrt{Re^2 + 4i\tilde{\omega}Re}}{2},$$
$$e_1 = \frac{c_{13} d_3 - b_3 c_{23}}{a_3 d_3 - b_3 c_3},\ e_2 = \frac{c_3 c_{13} - a_3 c_{23}}{b_3 c_3 - a_3 d_3},\ a_3 = s_1 - \frac{\alpha}{\sqrt{L_1}},$$
$$b_3 = s_2 - \frac{\alpha}{\sqrt{L_1}},\ c_3 = e^{s_1}(s_1 + \frac{\alpha}{\sqrt{L_2}}),\ d_3 = e^{s_2}(s_2 + \frac{\alpha}{\sqrt{L_2}}),$$
$$c_{13} = \frac{\alpha}{\sqrt{L_1}}(\Pi_o\ L_1 - \frac{\Pi_o}{Re\ i\ \tilde{\omega}}), c_{23} = -\frac{\alpha}{\sqrt{L_2}}(\Pi_o\ L_2 - \frac{\Pi_o}{Re\ i\ \tilde{\omega}}).$$

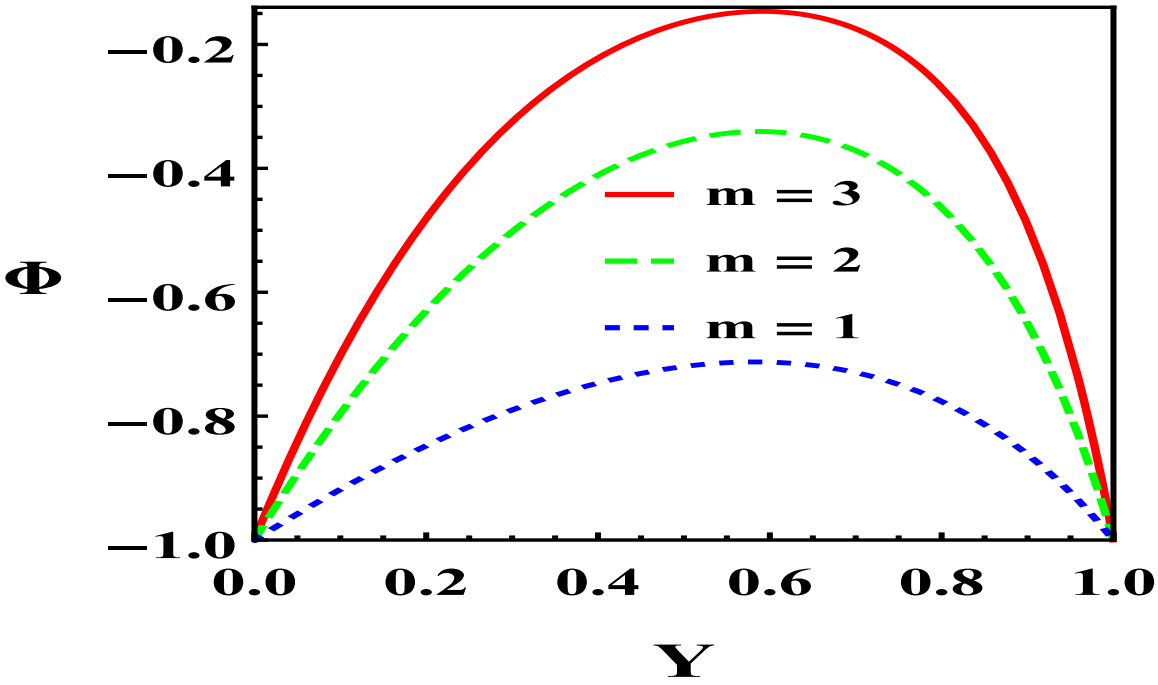

Figure 4.3: Electric potential distribution in microchannel for different values of the electroosmotic parameter when $R_D = 2$.

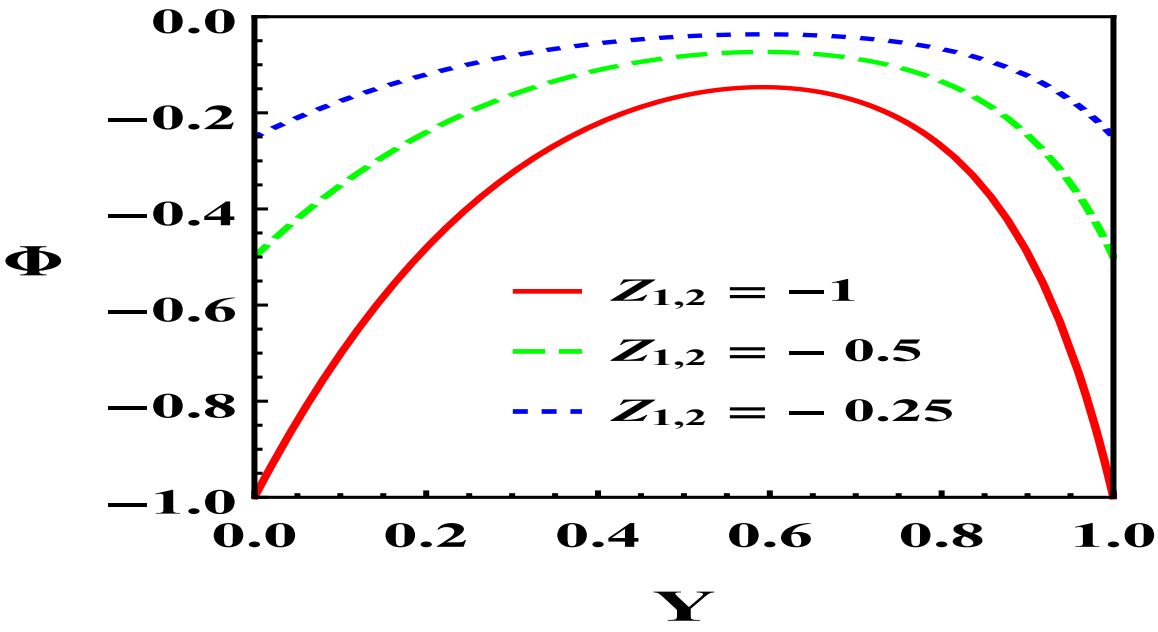

Figure 4.4: Electric potential distribution for different values of the Zeta potential in microchannel walls when $m = 3,\ R_D = 2$.

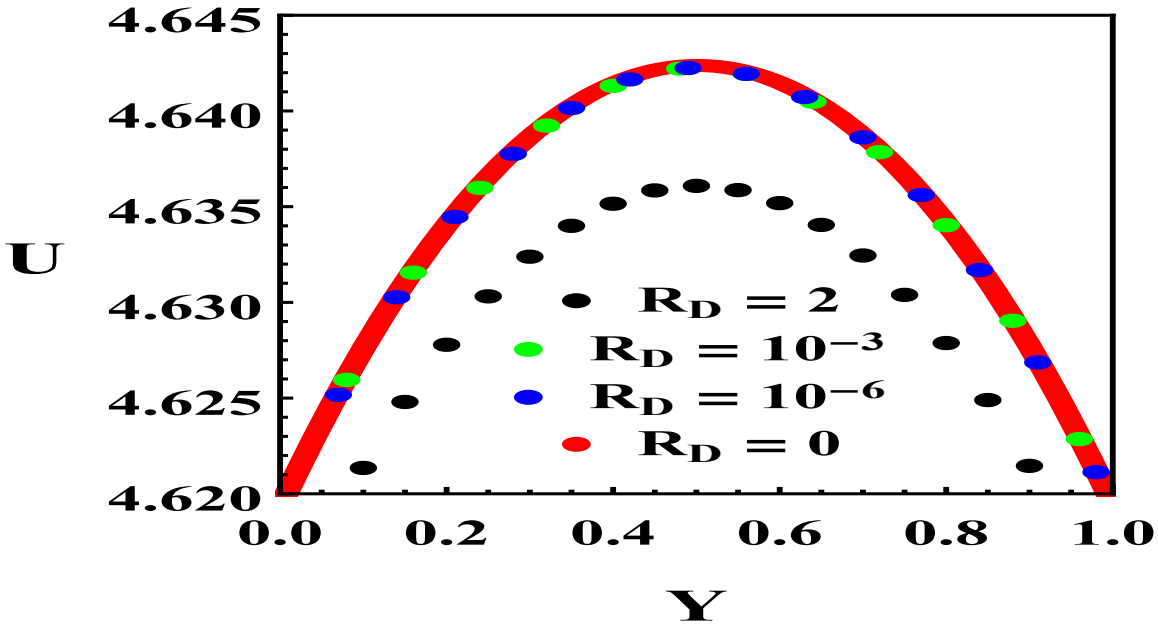

Figure 4.5: An illustrative comparison between the DTM solution U for different values of the diffusive Reynolds number R_D when $m = 3$. For, $R_D = 0$ we obtain the exact solution of the equation 4.15, plotted in red colour, presented in appendix.

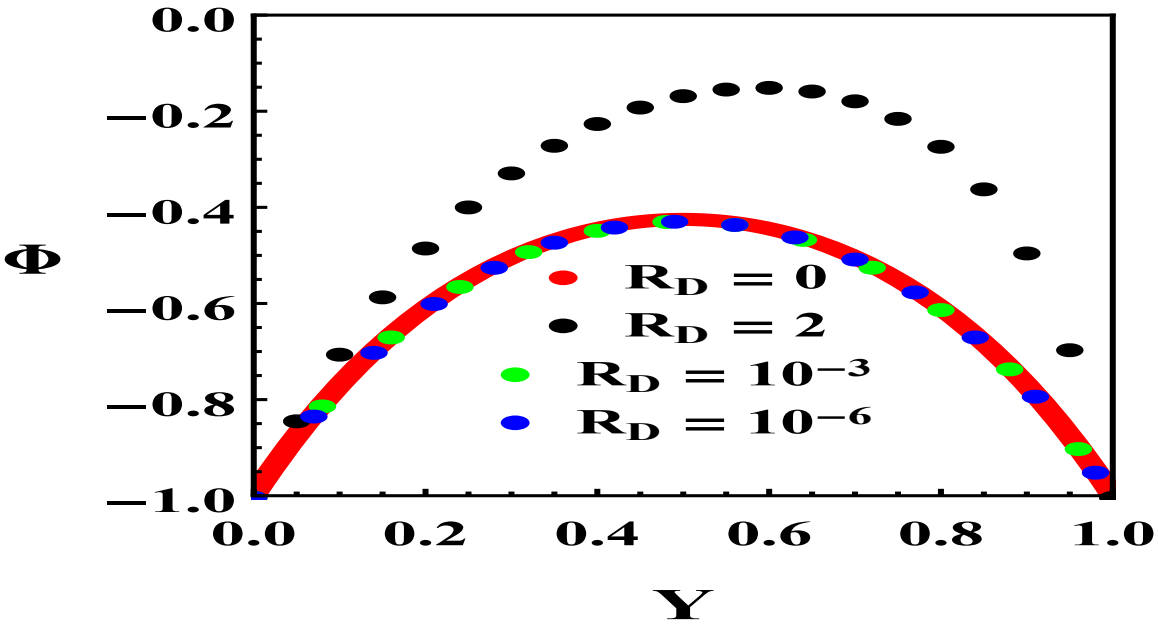

Figure 4.6: An illustrative comparison between the DTM solution Φ for different values of the diffusive Reynolds number R_D when $m = 3$. For, $R_D = 0$ we obtain the exact solution of the equation 4.14 namely Φ which satisfies $\frac{\partial^2 \Phi}{\partial Y^2} = m^2 \Phi$, plotted in red colour.

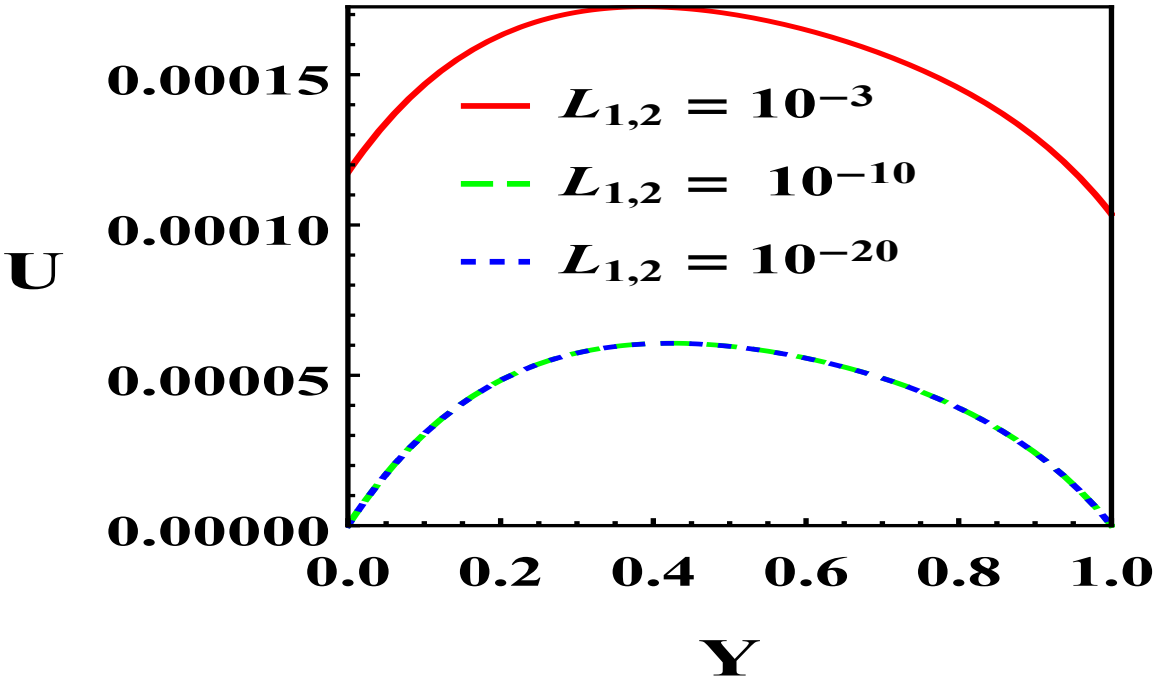

Figure 4.7: The convergence of velocity as permeability goes to zero when pressure gradient ($\Pi_{s,o} = 0$) is absent and $m = 3,\ R_D = 2,\ \tilde{t} = 1$.

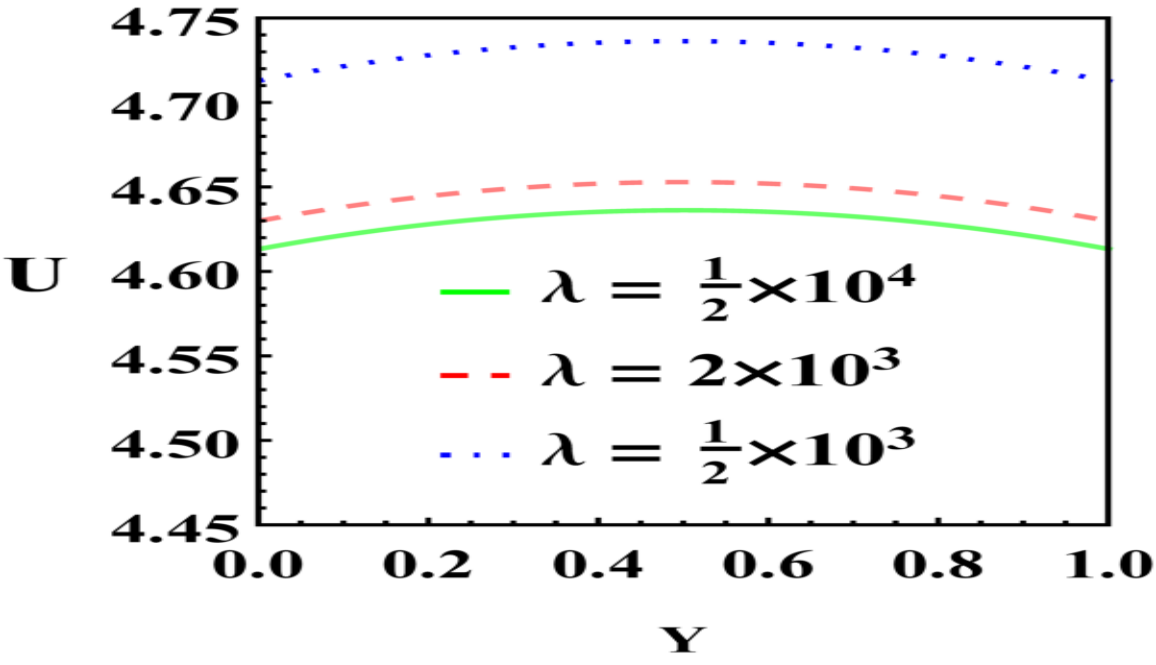

Figure 4.8: Velocity distribution for different values of sensitivity parameter when $m = 3,\ R_D = 2,\ \tilde{t} = 1,\ S = 1$.

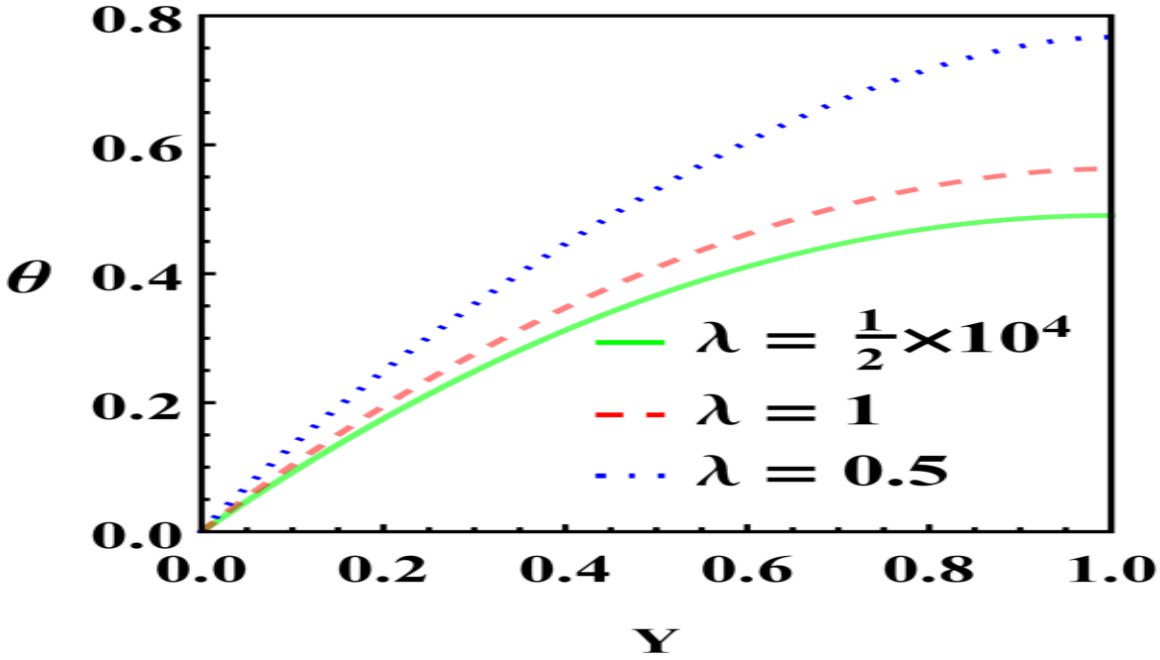

Figure 4.9: Temperature distribution for different values of sensitivity parameter when $m = 3,\ R_D = 2,\ = 1,\ Pr = 6,\ Ec = \frac{1}{3} \times 10^{-6},\ \tilde{t} = 1,\ S = 1.$

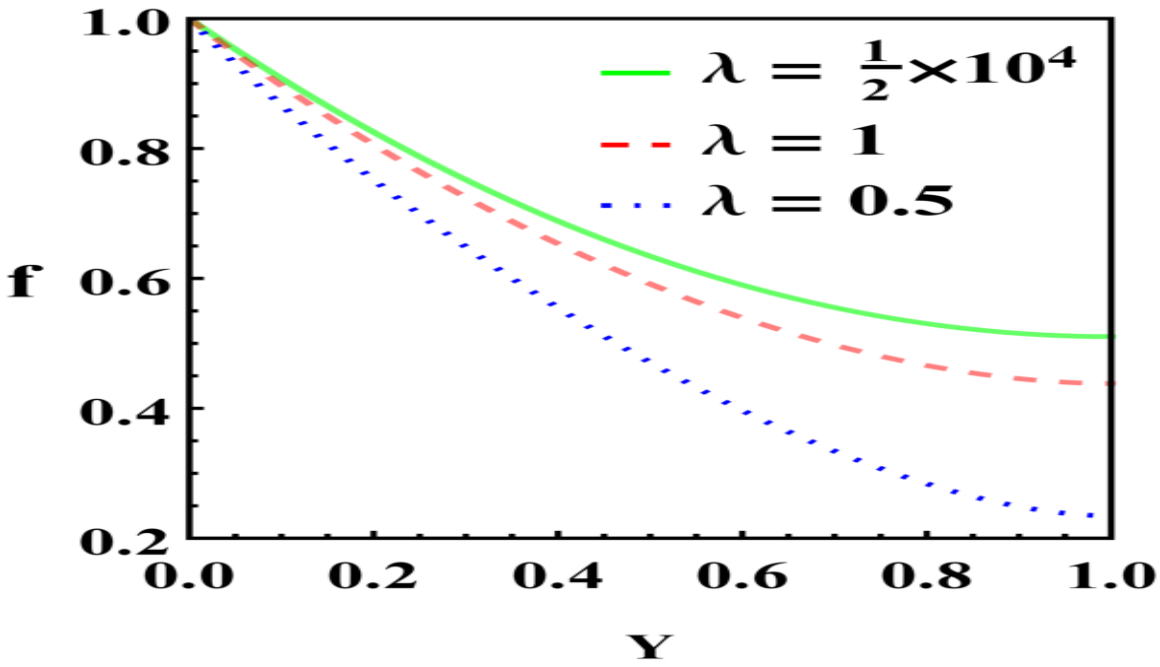

Figure 4.10: Nanoparticle concentration distribution for different values of sensitivity parameter when $m = 3,\ R_D = 2,\ = 1,\ Pr = 6,\ Ec = \frac{1}{3} \times 10^{-6},\ \tilde{t} = 1,\ S = 1.$

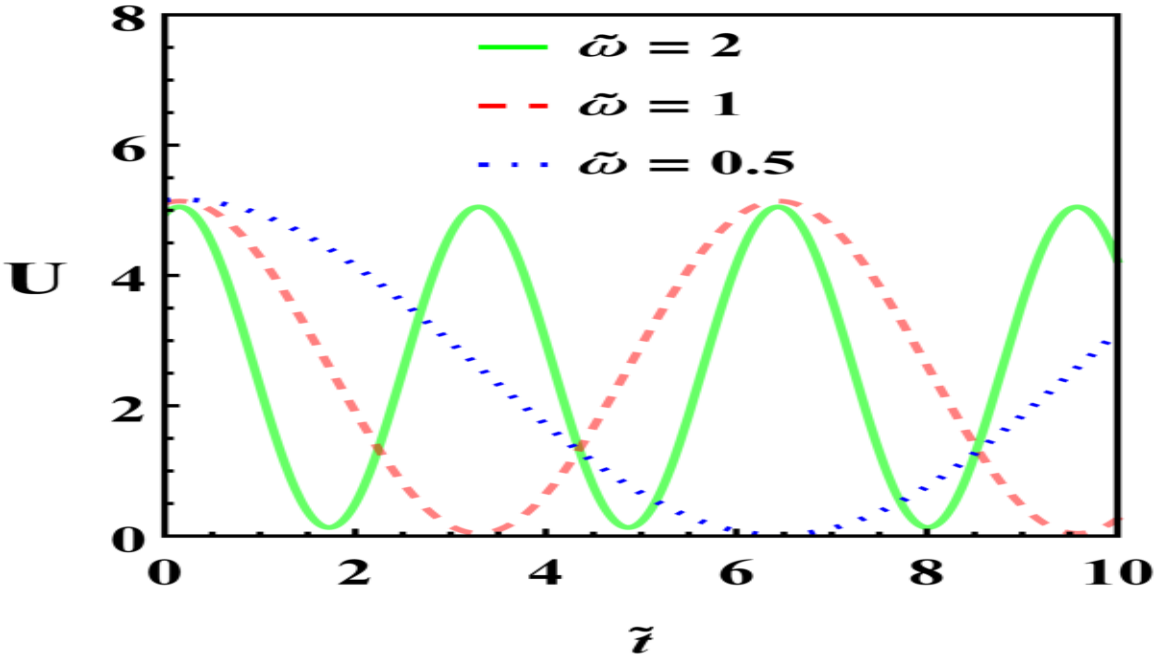

Figure 4.11: The variation in velocity for different values of Womersley number when $m = 3,\ R_D = 2,\ Y = 1$.

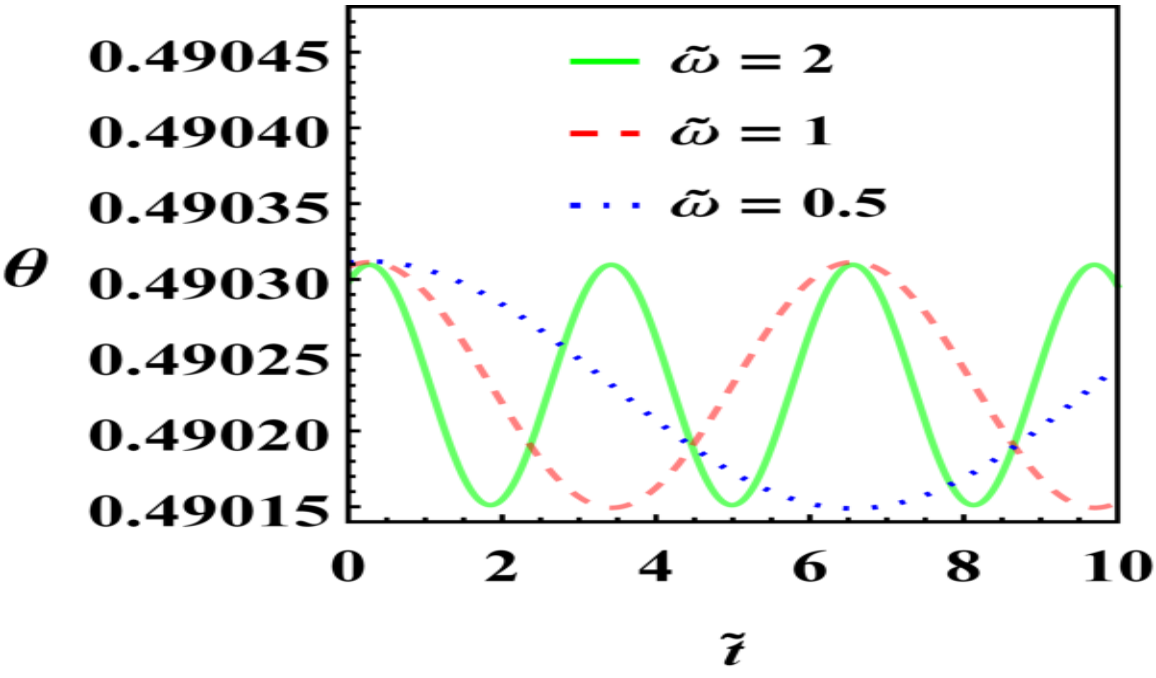

Figure 4.12: The variation in temperature for different values of Womersley number when $m = 3, Ec = \frac{1}{3} \times 10^{-6},\ Y = 1$.

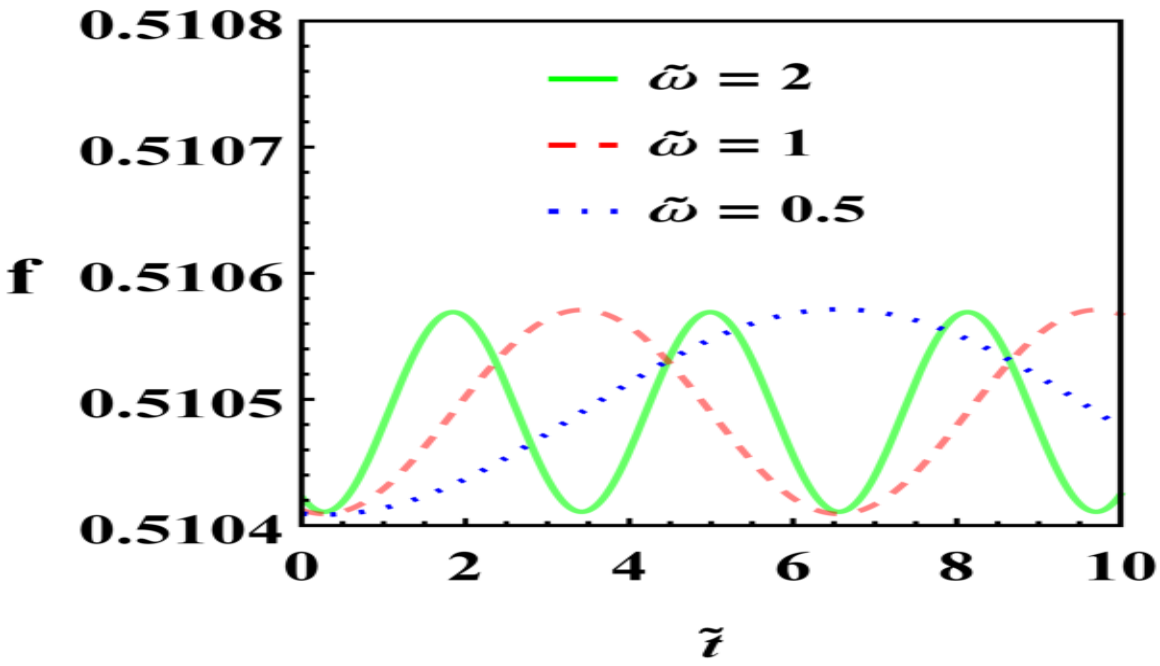

Figure 4.13: The variation in nanoparticle concentration for different values of Womersley number when $m = 3, Ec = \frac{1}{3} \times 10^{-6},\ Y = 1$.

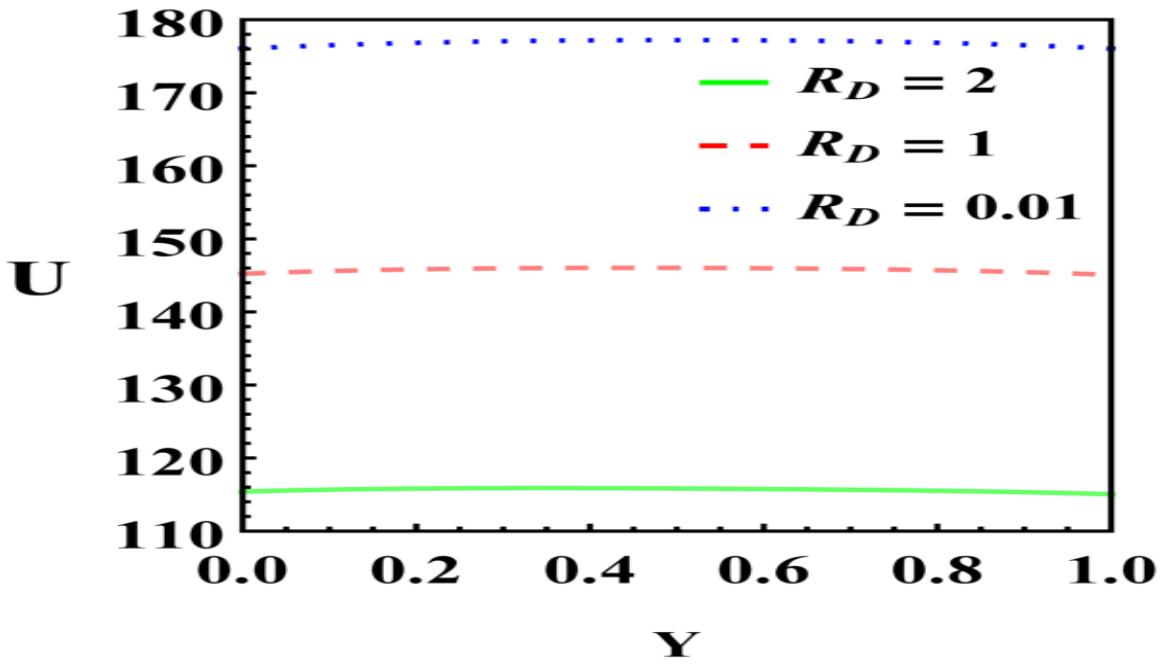

Figure 4.14: Effect of ion diffusivity on velocity when $\lambda = \frac{1}{2},\ \phi_1 = 20,\ \phi_2 = 2 \times 10^{-3}$.

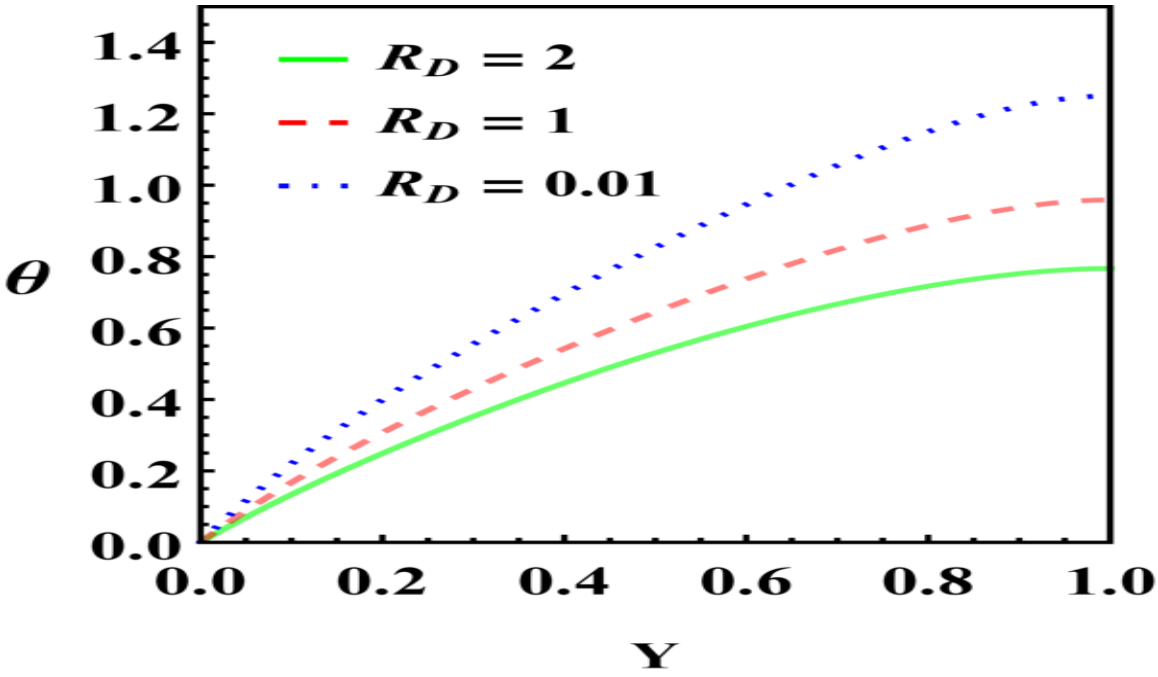

Figure 4.15: Effect of ion diffusivity on temperature when $\lambda = \frac{1}{2}$, $\phi_1 = 20$, $\phi_2 = 2 \times 10^{-3}$.

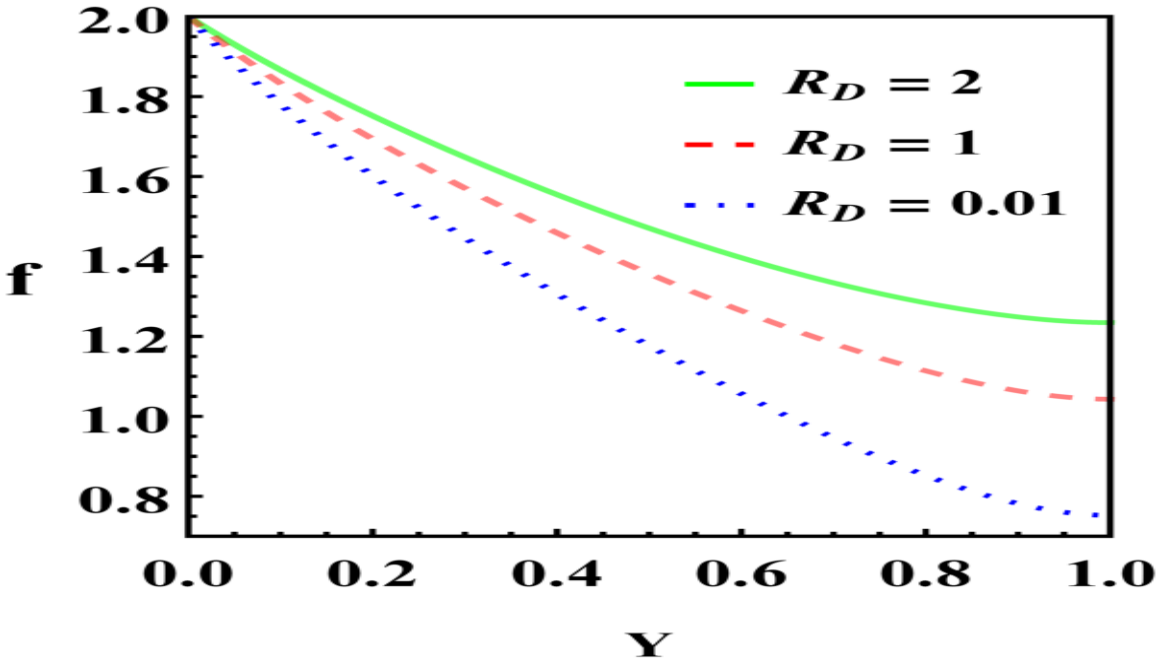

Figure 4.16: Effect of ion diffusivity on nanoparticle concentration when $\lambda = \frac{1}{2}$, $\phi_1 = 20$, $\phi_2 = 2 \times 10^{-3}$.

Chapter 5

MHD graphene-polydimethylsiloxane Maxwell nanofluid flow in a squeezing channel [4]

5.1 Introduction

Graphene-polymer composite has been the topic of serious scientific research in the recent years. Boland et al. [2016] made a phenomenal advancement in this direction by showing that Graphene-silicon nanocomposites also known as G-putty are sensitive electromechanical sensors which can even track the steps of a spider. The study of thermophysical properties of Graphene-Polydimethylsiloxane (PDMS) nanofluid has become a very important topic of research in the recent years. In this chapter, 1 cst PDMS fluid is considered for the study. Choi and Eastman [1995] first suggested the concept of nanofluid and experimentally verified that the augmentation of a small amount of highly thermally conductive nanoparticles into the base fluid increases the capacity of heat transfer of the fluid. Nanofluids are used as coolants in nuclear reactors, radiation therapy, geothermal energy extraction and in many other engineering applications. It has wide applications in polymer processing, injection modeling, loading related problems in different mechanical systems. The problem of fluid flow between two squeezing parallel plates can describe the injection modeling and loading related engineering models mathematically. In many engineering applications an external magnetic field is applied to resist the deviation of the lubrication viscosity. A list of articles in this subject can be found in Angayarkanni and Philip [2015]-Yaqing and Guo [2016].

In this chapter, we have applied an analytic method named DTM to solve the

[4]The content of this chapter has been published in *Applied Mathematics and Mechanics* (Springer), 40(9)(2019) 1269–1284.

non-linear differential equations coming out of the governing equations of the fluid flow. Zhou [1986] first employed the idea of DTM for solving differential equations in electrical engineering problems. The DTM is an recursive process to obtain analytical Taylor series solutions for the corresponding linear and non-linear differential equations. The DTM for solving partial differential equations was developed by Chen and Ho [1999]. Several articles in this method can be found in Hassan [2008], Acharya et al. [2016]. The present chapter investigates the entropy generation in an engineering system by means of a mathematical modeling in terms of various important physical parameters. The irreversible loss of thermal energy in a system is termed as entropy generation. In any engineering process, the objective of the researchers is to minimize the entropy generation. Bejan and Kestin [1983], Bejan [1979] did the significant work in this direction and formulated a number(Be) as the ratio of the entropy generation due to thermal irreversibility to the entropy generation due to fluid frictional factors (Rashidi et al. [2016]-Bhatti et al. [2016]).

Mahian et al. [2013] reviewed an article on entropy generation and they have presented many research directions in their article. These studies motivated us to investigate the Graphene-PDMS nanofluid flow between two squeezing parallel plates. The energy efficiency have been analyzed via entropy generation of the system. The influence of an external magnetic field, thermal radiation along with the volume fraction of the nanoparticles are thoroughly investigated. The novelty of this chapter lies in the study of entropy generation under the influence of thermal radiation effects of the nanoparticles. Our model has applications in polymer processing, injection modeling. In the above prescribed engineering systems, we are interested to minimize the entropy generation (Be) and try to maximize the heat transfer rate (Nu) in the system. In this chapter, Bejan number (Be) and Nusselt number (Nu) are extensively studied by varying different thermophysical parameters. We have used the DTM, which gives an approximate Taylor series solution. The velocity and temperature profiles along with the coefficient of skin-friction for different thermophysical parameter values are investigated.

5.2 Modeling of the problem

The schematic diagram of the problem is presented in Figure 5.1. We have investigated the viscous and incompressible Graphene-Polydimethylsiloxane nanofluid flow in a squeeze channel. The heat transfer properties and the entropy generation in the model is studied extensively. Our model is described by the two dimensional cartesian co-ordinate system where, the plates are lying in the x-axis direction and the normal direction to the plates are denoted by the y-axis. The gap between two parallel plates is $h(t) = H(1 - \alpha t)^{\frac{1}{2}}$ at time t (measured from $y = 0$). Here, $\alpha > 0$ determines how fast and in which direction the plates are moving. The plates moving at the speed of $v(t) = \frac{dh}{dt}$ and they will eventually meet at time $t = \frac{1}{\alpha}$. The negative values of α indicate that the plates are moving away to each other. At the beginning,

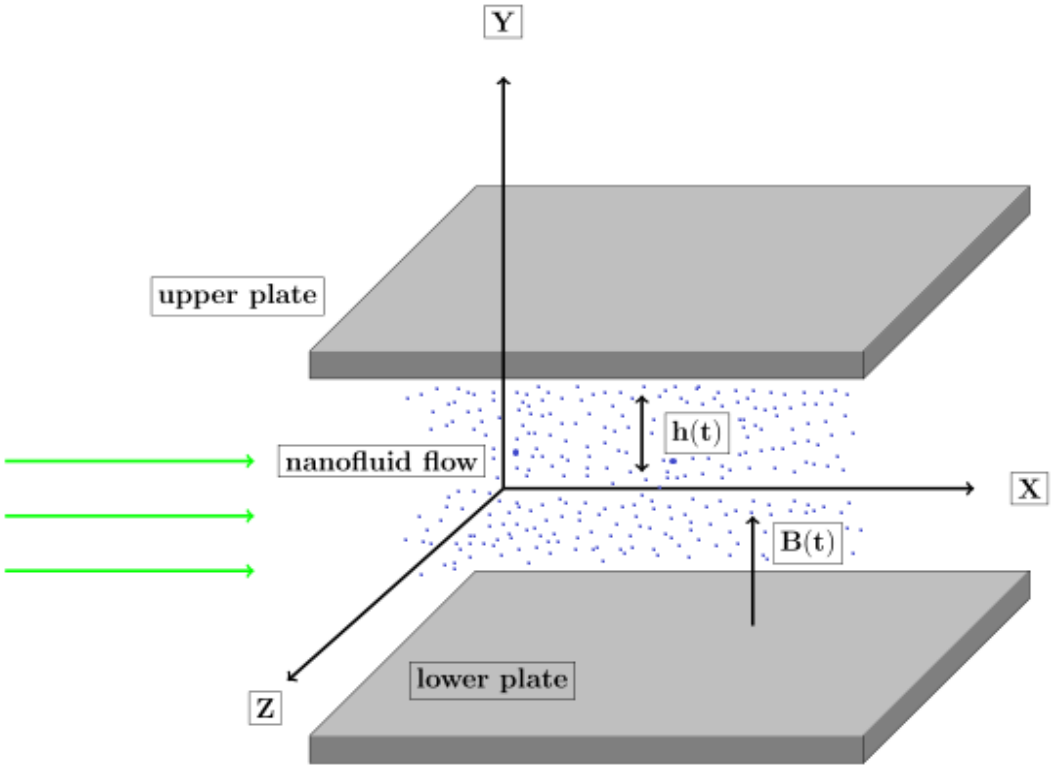

Figure 5.1: Physical sketch of the problem

the plates are at a distance H at time $t = 0$. The time dependent magnetic field of strength $B(t) = B_0(1 - \alpha t)^{-\frac{1}{2}}$ is applied in the y direction. The radiative heat flux is considered in our system and we have assumed that the chemical reactions do not take place in our system. The equations of motion and energy (Hayat et al. [2017]) for Graphene-PDMS nanofluid flow under the influence of both magnetic field and thermal radiation is described below.

$$\frac{\partial u}{\partial x} + \frac{\partial v}{\partial y} = 0, \tag{5.1}$$

$$\begin{aligned}\rho_{nf}\left(\frac{\partial u}{\partial t} + u\frac{\partial u}{\partial x} + v\frac{\partial u}{\partial y}\right) &= -\frac{\partial p}{\partial x} - \rho_{nf}\lambda_1(u^2\frac{\partial^2 u}{\partial x^2} + v^2\frac{\partial^2 u}{\partial y^2} + 2uv\frac{\partial^2 u}{\partial x \partial y}) + \\ &\mu_{nf}(\frac{\partial^2 u}{\partial x^2} + \frac{\partial^2 u}{\partial y^2}) - \sigma B(t)^2 u,\end{aligned} \tag{5.2}$$

$$\begin{aligned}\rho_{nf}\left(\frac{\partial v}{\partial t} + u\frac{\partial v}{\partial x} + v\frac{\partial v}{\partial y}\right) &= -\frac{\partial p}{\partial y} - \rho_{nf}\lambda_1(u^2\frac{\partial^2 v}{\partial x^2} + v^2\frac{\partial^2 v}{\partial y^2} + 2uv\frac{\partial^2 v}{\partial x \partial y}) \\ &+\mu_{nf}(\frac{\partial^2 v}{\partial x^2} + \frac{\partial^2 v}{\partial y^2}),\end{aligned} \tag{5.3}$$

$$\left(\frac{\partial T}{\partial t}+u\frac{\partial T}{\partial x}+v\frac{\partial T}{\partial y}\right) = \frac{k_{nf}}{(\rho C_p)_{nf}}\left(\frac{\partial^2 T}{\partial x^2}+\frac{\partial^2 T}{\partial y^2}\right)+\frac{\sigma B^2(t)}{(\rho C_p)_{nf}}u^2-\frac{1}{(\rho C_p)_{nf}}\frac{\partial q_r}{\partial y} + \frac{\mu_{nf}}{(\rho C_p)_{nf}}\left(2\left\{\left(\frac{\partial u}{\partial x}\right)^2+\left(\frac{\partial v}{\partial y}\right)^2\right\}+\left(\frac{\partial u}{\partial y}+\frac{\partial v}{\partial x}\right)^2\right), \tag{5.4}$$

where u, v denote the components of velocities in x and y directions respectively, T denotes the temperature, λ_1 the relaxation time, p the fluid pressure, ρ_{nf} the density of the nanofluid, μ_{nf} the effective dynamic viscosity, $(\rho C_p)_{nf}$ the effective heat capacity of the nanofluid, k_{nf} the effective thermal conductivity of the nanofluid, q_r the radiative heat flux of the nanofluid and σ the electrical conductivity of the nanofluid respectively. The Rosseland approximation is used to calculate the radiative heat flux as,

$$q_r = -\frac{4\sigma_1}{3k_1}\frac{\partial T^4}{\partial y},$$

where, σ_1 is the Stefan-Boltzmann constant and k_1 is the mean absorption coefficient. To linearize the temperature, we use Taylor's series expansion of T^4 and yields,

$$T^4 \cong 4{T_H}^3 T - 3{T_H}^4,$$

in which T_H represents the constant temperature at the wall.
Therefore, we obtain,

$$\frac{\partial q_r}{\partial y} = -\frac{16\sigma_1 {T_H}^3}{3k_1}\frac{\partial^2 T}{\partial y^2}. \tag{5.5}$$

The effective nanofluid properties based on the Maxwell nanofluid model is described in MAXWELL [1873], Brinkman [1952] by

$$\rho_{nf} = (1-\phi)\rho_f + \phi\rho_s, \tag{5.6}$$

$$(\rho C_p)_{nf} = (1-\phi)(\rho C_p)_f + \phi(\rho C_p)_s, \tag{5.7}$$

$$\mu_{nf} = \frac{\mu_f}{(1-\phi)^{2.5}}, \tag{5.8}$$

$$\frac{k_{nf}}{k_f} = \frac{k_s + 2k_f - 2\phi(k_f - k_s)}{k_s + 2k_f + \phi(k_f - k_s),} \tag{5.9}$$

where, ϕ denotes the volume fraction of the nanoparticle in the nanofluid, k_s the thermal conductivity of the solid Graphene, k_f the thermal conductivity of the PDMS fluid. The boundary conditions are taken as,

$$u = 0, v = \frac{dh}{dt}, T = T_H \quad at \quad y = h(t), \tag{5.10}$$

$$\frac{\partial u}{\partial y} = 0, v = 0, \frac{\partial T}{\partial y} = 0 \quad at \quad y = 0. \tag{5.11}$$

5.2. Modeling of the problem

The following similarity transformations and dimensionless variables are introduced (Sheikholeslami and domiri ganji [2013], Sheikholeslami et al. [2013b]),

$$\eta = \frac{y}{H\sqrt{1-\alpha t}}, u = \frac{\alpha x}{2(1-\alpha t)} f^{'}(\eta), v = \frac{-\alpha H}{2\sqrt{1-\alpha t}} f(\eta), \theta = \frac{T}{T_H}. \tag{5.12}$$

Use of these dimensionless variables and eliminating pressure terms by cross-differentiation of equations 5.2 and 5.3, we derive the following non-linear ordinary differential equations along with the thermal energy equation 5.4 as,

$$\begin{aligned} f^{iv} &= S \cdot A_1(1-\phi)^{2.5}(3f^{''} + \eta f^{'''} + f^{'}f^{''} - ff^{'''} - \frac{De}{2}(f^{''}f^{'2} - 3ff^{'}f^{'''} + ff^{''2} \\ &\quad -2f^2 f^{iv})) + M^2 f^{''}, \end{aligned} \tag{5.13}$$

$$\begin{aligned} (1+\frac{4R}{3})\theta^{''} + Pr \cdot S \cdot (\frac{A_2}{A_3})(f\theta^{'} - \eta\theta^{'}) + \frac{Pr \cdot Ec}{A_3(1-\phi)^{2.5}}(f^{''2} + \\ f^{'2}(M^2 + 4\delta^2)) = 0. \end{aligned} \tag{5.14}$$

Similarly the boundary conditions 5.10 and 5.11 reduce to

$$f^{''}(0) = 0, f(0) = 0, \theta^{'}(0) = 0, \tag{5.15}$$

$$f^{'}(1) = 0, f(1) = 1, \theta(1) = 1. \tag{5.16}$$

Equations 5.13 and 5.14 involved some dimensional parameters defined as $S = \frac{\alpha H^2}{2\nu_f}$ the squeeze number, $A_1 = \frac{\rho_{nf}}{\rho_f}, A_2 = \frac{(\rho C_p)_{nf}}{(\rho C_p)_f}, A_3 = \frac{k_{nf}}{k_f}$, $Pr = \frac{\mu_f(\rho C_p)_f}{\rho_f k_f}$ the Prandtl number, $Ec = \frac{\rho_f}{(\rho C_p)_f T_H}(\frac{\alpha x}{2(1-\alpha t)})^2$ the Eckert number, $De = \frac{\alpha\lambda_1}{(1-\alpha t)}$ the Deborah number, $M = HB_0\sqrt{\frac{\sigma_f}{\mu_f}}$ the magnetic number, $\delta = \frac{H\sqrt{(1-\alpha t)}}{x}$ and $R = \frac{4\sigma_1 T_H^3}{k_1 k_{nf}}$ the thermal radiation parameter.

This chapter investigates the coefficient of skin-friction C_f and the Nusselt number Nu that can be expressed as,

$$C_f = \frac{\mu_{nf}(\frac{\partial u}{\partial y})_{y=h(t)}}{\frac{1}{2}\rho_{nf}(\frac{dh}{dt})^2} = \frac{2f^{''}(1)}{S\delta A_1(1-\phi)^{2.5}}, \tag{5.17}$$

and the Nusselt number Nu has the expression,

$$\begin{aligned} Nu = \frac{-Hk_{nf}(\frac{\partial T}{\partial y})_{y=h(t)}}{k_f T_H} = \frac{-Nu_r}{\sqrt{1-\alpha t}}, \\ \text{where, } Nu_r = -A_3\theta^{'}(1). \end{aligned} \tag{5.18}$$

5.3 Entropy Generation

The irreversible loss of thermal energy in a system is termed as the entropy generation of the system. The aim of the present study is to minimize entropy generation in any engineering system to get the maximum output. This can be achieved by controlling the values of the physical parameters involved in this study. The expression for the entropy generation rate per unit volume is given as in Mkwizu and Makinde [2015], Mahian et al. [2013],

$$S_{Total} = \frac{k_{nf}}{T^2}\left(\left(\frac{\partial T}{\partial y}\right)^2 + \frac{16\sigma T_H^3}{3K_1 k_{nf}}\left(\frac{\partial T}{\partial y}\right)^2\right) + \frac{\mu_{nf}}{T}\left(\frac{\partial u}{\partial y}\right)^2 + \frac{\sigma B^2 u^2}{T}. \tag{5.19}$$

The dimensionless form of the total entropy generation E_S is given by,

$$\begin{aligned} E_S &= \frac{h(t)^2}{k_{nf}} S_{Total} = E_{ST} + E_{SFF} \\ &= \frac{1}{\theta^2}(1 + \frac{4R}{3})\theta'^2 + \frac{1}{\theta}\frac{Pr.Ec}{A_3(1-\phi)^{2.5}}(M^2 f'^2 + f''^2), \end{aligned} \tag{5.20}$$

where E_S is the total entropy generation, E_{ST} denotes the entropy generation due to the thermal effects and thermal radiation, E_{SFF} denotes the contribution of the fluid friction to the entropy generation and the effect of magnetic field. The values of E_{ST} and E_{SFF} are compared graphically to understand which factors are contributing more in the total entropy generation. The Bejan number is an important non-dimensional number that helps us to compare the entropy generation due to thermal effects to the total entropy generation. The expression for the Bejan number is as follows,

$$Be = \frac{E_{ST}}{E_S}. \tag{5.21}$$

5.4 Method of Solution

In this chapter DTM is applied to obtain approximate solutions of the equations 5.13 and 5.14 with respect to the boundary conditions 5.15 and 5.16. The idea of DTM, was first proposed by Zhou [1986]. The k^{th} order DTM of a given function $g(\eta)$ is expressed as

$$G(k) = \frac{1}{k!}\left[\frac{d^k g(\eta)}{d\eta^k}\right]_{\eta=\eta_0}, \tag{5.22}$$

where η_0 is a fixed point specified by the particular problem, $G(\eta)$ is the k^{th} differential transform of $g(\eta)$. Now expanding $g(\eta)$ around the point η_0 yields

$$g(\eta) = \sum_{k=0}^{\infty} \frac{1}{k!}\left[\frac{d^k g(\eta)}{d\eta^k}\right]_{\eta=\eta_0} (\eta - \eta_0)^k. \tag{5.23}$$

Table 5.1: The DTM conversion table

Original function	DTM Conversion
$l(\lambda) = \frac{d^m g(\lambda)}{d\lambda^m}$	$L(k) = \frac{(k+m)!}{k!} G(k+m)$
$l(\lambda) = m(\lambda)n(\lambda)$	$L(k) = \sum_{n=0}^{k} M(n)N(k-n)$
$l(\lambda) = \lambda^n$	$L(k) = \delta(k-n)$
$l(\lambda) = ag(\lambda) \pm bp(\lambda)$	$L(k) = aG(k) \pm bP(k)$

Thus, k^{th} order differential transform of g is the k^{th} Taylor's coefficient of g around the point η_0. Using 5.22 in the equation 5.23 we can write,

$$g(\eta) = \sum_{k=0}^{\infty} G(k)(\eta - \eta_0)^k. \tag{5.24}$$

It is worthwhile to mention that the DTM calculates the relative derivatives by using a recursive algebraic relation. The recursive relations are obtained by transforming the original functions with the DTM method. The DTM transformation satisfies the identities as mentioned in Table 5.1. The function $g(\eta)$ is then approximated by a finite series $\tilde{g}(\eta)$ given in the following form,

$$\tilde{g}(\eta) = \sum_{k=0}^{P} G(k)(\eta - \eta_0)^k, \tag{5.25}$$

where, P is called the length of the series. The equations 5.24 and 5.25 show that the error term $|g(\eta) - \tilde{g}(\eta)|$ is negligibly small. Using the relations for DTM at the point $\eta_0 = 0$ as given in Table 5.1, the functions $f(\eta)$ and $\theta(\eta)$ satisfying the governing equations 5.13 and 5.14 will be approximated by the equations $\tilde{f}(\eta) = \sum_{k=0}^{N} F(k)\eta^k$ and $\tilde{\theta}(\eta) = \sum_{k=0}^{N} \Theta(k)\eta^k$, where, $F(k), \Theta(k)$ are the k^{th} differential transforms of $f(\eta), \theta(\eta)$ at the point $\eta_0 = 0$. The boundary conditions for $\tilde{f}$ and $\tilde{\theta}$ defined in 5.15 and 5.16 are also transformed to,

$$\tilde{f}''(0) = 0, \tilde{f}(0) = 0, \tilde{\theta}'(0) = 0, \tag{5.26}$$

$$\tilde{f}'(1) = 0, \tilde{f}(1) = 1, \tilde{\theta}(1) = 1. \tag{5.27}$$

The l^{th} differential transforms of $f(\eta)$ and $\theta(\eta)$ satisfying the governing equations 5.13, 5.14 at the point $\eta_0 = 0$ are obtained using the above identities listed in Table

5.1 as follows,

$$
\begin{aligned}
F(l+4) \;=\; & \Bigg\{\Big(SA_1(1-\phi)^{2.5}\Big)\cdot\Bigg(3(l+1)(l+2)F(l+2)+\sum_{r=0}^{l}\Delta(l-r-1)(r+1)\\
& (r+2)(r+3)F(r+3)+\sum_{r=0}^{l}(r+1)(r+2)(l-r+1)F(r+2)\\
& F(l-r+1)-\sum_{r=0}^{l}(r+1)(r+2)(r+3)F(l-r)F(r+3)\\
& -\frac{De}{2}\Bigg(\sum_{i=0}^{l}(i+1)(i+2)F(i+2)\sum_{r=0}^{l-i}(r+1)(l-i-r+1)F(r+1)\\
& F(l-i-r+1)-3\sum_{i=0}^{l}(i+1)(i+2)(i+3)F(i+3)\sum_{r=0}^{l-i}(l-i-r+1)\\
& F(r)F(l-i-r+1)\\
& +\sum_{i=0}^{l}F(i)\sum_{r=0}^{l-i}(r+1)(r+2)(l-i-r+1)(l-i-r+2)F(r+2)\\
& F(l-i-r+2)-2\sum_{i=0}^{l}(i+1)(i+2)(i+3)(i+4)F(i+4)\sum_{r=0}^{l-i}F(r)\\
& F(l-i-r)\Bigg)\Bigg)+M^2(l+1)(l+2)F(l+2)\Bigg\}\\
& \Big/\Big((l+1)(l+2)(l+3)(l+4)\Big), \qquad (5.28)
\end{aligned}
$$

$$
\begin{aligned}
\Theta(l+2) \;=\; & -\Bigg\{Pr\;S\;(\frac{A_2}{A_3})\sum_{r=0}^{l}\Bigg((r+1)\Theta(r+1)F(l-r)\;-\;(r+1)\Delta(l-r-1)\\
& \Theta(r+1)\Bigg)+\frac{PrEc}{A_3(1-\phi)^{2.5}}\times\Bigg(\sum_{r=0}^{l}(r+1)(r+2)(l-r+1)(l-r+2)\\
& F(r+2)F(l-r+2)+\sum_{r=0}^{l}(4\delta^2+M^2)(r+1)(l-r+1)F(r+1)\\
& F(l-r+1)\Bigg)\Bigg\}\Big/\Big((1+\frac{4R}{3})(l+1)(l+2)\Big), \qquad (5.29)
\end{aligned}
$$

where $l \geq 0$, $\Delta(n)$ is defined as,

$$
\Delta(n)=\begin{cases}1 & \text{if } \; n=0\\ 0 & \text{otherwise.}\end{cases}
$$

We need the following values of $F(0), \Theta(0), F(1), \Theta(1), F(2), F(3)$ to calculate all the values of $F(l)$ and $\Theta(l)$ $\forall$ $l \geq 0$ by the above recurrence relation. From the equation 5.26 and 5.27 we have the following initial values,

$$\begin{aligned} F(0) = 0, F(1) = p, F(2) = 0, F(3) = q, \\ \Theta(0) = r, \Theta(1) = 0. \end{aligned} \tag{5.30}$$

In equation 5.30, the constants p, q, r are missing initial conditions, which are to be determined from the boundary conditions 5.26, 5.27 and the equations 5.28 and 5.29. Thus, we have,

$$\begin{aligned} &F(0) = 0, F(1) = p, F(2) = 0, F(3) = q, F(4) = 0, \\ &F(5) = \frac{1}{120}\Big(6qM^2 + A_1\Big(24q + 6p^2q \cdot De\Big)S(1-\phi)^{2.5}\Big), \cdots \\ &\Theta(0) = r, \Theta(1) = 0, \Theta(2) = -\frac{p^2 EcPr(M^2 - 4\delta^2)}{2A_3(1 + \frac{4R}{3}(1-\phi)^{2.5})}, \Theta(3) = 0, \cdots \end{aligned} \tag{5.31}$$

Using these values, the closed form solutions of f and θ are given by

$$\tilde{f}(\eta) = p\eta + q\eta^3 + \frac{1}{120}\eta^5\Big(6qM^2 + A_1\Big(24q + 6p^2q \cdot De\Big)S(1-\phi)^{2.5}\Big) + \cdots \tag{5.32}$$

and

$$\tilde{\theta}(\eta) = r - \eta^2 \frac{p^2 EcPr(M^2 - 4\delta^2)}{2A_3(1 + \frac{4R}{3}(1-\phi)^{2.5})} + \cdots \tag{5.33}$$

The boundary conditions 5.26 and 5.27 give the values for p, q, r for a particular choice of P. By substituting the values for p, q, r in the equations 5.32 and 5.33 we obtain the approximate solutions for $f(\eta)$ and $\theta(\eta)$. As an illustrative example when, $P = 20, Pr = 0.1, Ec = 0.05, M = 1, R = 0, S = 0.5, \delta = 0.1, \phi = 0.08, De = 0$, the following expressions are estimated:

$$\tilde{f}(\eta) = 1.42732\eta - 0.358219\eta^3 - 0.0655093\eta^5 - 0.00360124\eta^7 - \cdots, \tag{5.34}$$

$$\tilde{\theta}(\eta) = 1.18577 - 0.0123521\eta^2 + 0.111469\eta^4 - 0.042305\eta^6 - \cdots \tag{5.35}$$

5.5 Discussion of Results

The magnetohydrodynamic flow and its entropy generation on Graphene PDMS nanofluid in a squeeze channel via DTM has been the objective of the study in this chapter. The following range of parametric values have been used to estimate the

Table 5.2: Thermophysical properties of PDMS and Graphene (Mark [1999], Potenza et al. [2017], Pop et al. [2012], Roberts et al. [2017], KAMINSKI and JAUPART [2003])

	ρ	C_ρ	k
PDMS fluid	816	2000	0.15
Graphene	2250	710	3000

analytical approximations 5.32 and 5.33 for the velocity and temperature fields: $Pr = 11,\ Ec = 0.03,\ M = [0, 2],\ R = [0, 0.2],\ \phi = [0, 0.09],\ S = [-0.1, 0.1],\ De = [0, 5],\ \delta = 0.1$.
It is worthwhile to mention here that the thermal radiation parameter R depends on the plate temperature and measures the amount of thermal energy emitted from the plate, the magnetic parameter M is the interaction of the electromagnetic force to the viscous force, the squeeze parameter S describes how fast the parallel plates are moving towards (or away from when negative values of S are chosen) each other and the Deborah number De, which measures as the ratio of the relaxation time to observation time. The expressions for this dimensionless numbers are given at the end of the Section 5.2 of this article. The 1 cst PDMS fluid has Prandtl number around 11 (Roberts et al. [2017], KAMINSKI and JAUPART [2003], Kong et al. [2014]). The higher Deborah number De is considered as the Maxwell fluid needs higher relaxation time compared to the experimental time and the fluid is inside a squeezing channel. The lower values of S says that the squeeze process is not very rapid. The radiation number R is small for the PDMS fluid as the mean absorption coefficient is higher for this kind of fluid and the boundary temperature cannot be very high as it will change the chemical nature of the polymer. The value of the magnetic number M is kept low as we are working on a microchannel and the electrical conductivity of the base fluid is very low. The addition of Graphene although increases the electrical conductivity of the nanofluid but taking higher M values is not very reasonable. In Table 5.2, important thermophysical properties of PDMS-Graphene are given. We have compared the numerical results obtained by applying DTM for Nusselt number $-\theta'(1)$ at the channel wall with the results of Acharya et al. [2016], Mustafa et al. [2012] and Pourmehran et al. [2015]. This comparison is shown Table 5.3 where we have chosen particular parameter values to make the comparison. The computed results of the present study are in well agreement with the solutions obtained in Acharya et al. [2016], Mustafa et al. [2012], Pourmehran et al. [2015]. It is found that an increase in one of Pr or Ec, the value of $-\theta'(1)$ increases gradually when the other parameters are kept fixed. This phenomenon is also observed by the previous investigations as available in the scientific literature.

Table 5.3: Comparison table for the values of $-\theta^{'}(1)$ when $S = 0.5, \delta = 0.1, M = 0.0, \phi = 0.0, R = 0, De = 0, Pr = 6.2, Ec = 0.05$

Pr	Ec	$-\theta^{'}(1)$ Mustafa et al.	$-\theta^{'}(1)$ Pourmehran et al.	$-\theta^{'}(1)$ Kundu et al.	$-\theta^{'}(1)$ Present Work
0.5	1.0	1.5222368	1.518859607	1.5222367498	1.52237
1.0	1.0	3.026324	3.019545607	3.026323559	3.02633
2.0	1.0	5.98053	5.967887511	5.980530398	5.98053
5.0	1.0	14.43941	14.41394678	14.43941324	14.4394
1.0	0.5	1.513162	1.509772834	1.513161807	1.51316
1.0	1.2	3.631588	3.623454726	3.631588269	3.6316
1.0	2.0	6.052647	6.039091204	6.052647108	6.05266
1.0	5.0	15.13162	15.09772808	15.13161784	15.1316

5.5.1 Velocity variation

Figures 5.2 to 5.4 show how the axial velocity in the $y-$direction changes with the different values of the magnetic parameter M, the Deborah number De and the squeezing parameter S. Figure 5.2 describes the variation in axial velocity for different squeezing parameter S. If the squeezing parameter S is increased, then the velocity at the central region decreases, while the opposite trend is seen near the channel wall. Figures 5.3, 5.4 show that the velocity component have a decreasing trend with the increase of De and M up to a certain height and then follows the opposite trend. Figure 5.4 can be justified as the presence of the resistive Lorentz force during the application of graphene-PDMS nanofluid. This force reduces the fluid motion inside the channel and the opposite trend justifies the continuity equation. These results have potential applications in the injection modeling, polymer processing etc.

5.5.2 Temperature variation

Figures 5.5-5.9 describe how the thermal profiles inside the squeeze channel is affected by the different parameter values such as M, R, ϕ, S and De. Figure 5.5 shows that the thermal response increases with an increase in the magnetic parameter M. This enhancement of temperature lies in the Lorentz force that intensify the forced convection. Figure 5.6 shows that thermal response increases slowly with the increase of the volume fraction of the nanoparticle ϕ. An increase in the thermal radiation parameter R decreases the temperature as shown in Figure 5.7. Figure 5.8 shows that the increase in the Deborah number decreases the temperature. Higher De number increases the elastic nature of the Maxwell fluid and will eventually reduces the heat transfer. Figure 5.9 shows that with the positive S values the thermal response decreases and with the negative values of S the thermal response increases. The increasing S values increase the elastic nature of the Maxwell fluid therefore decreases the thermal profile.

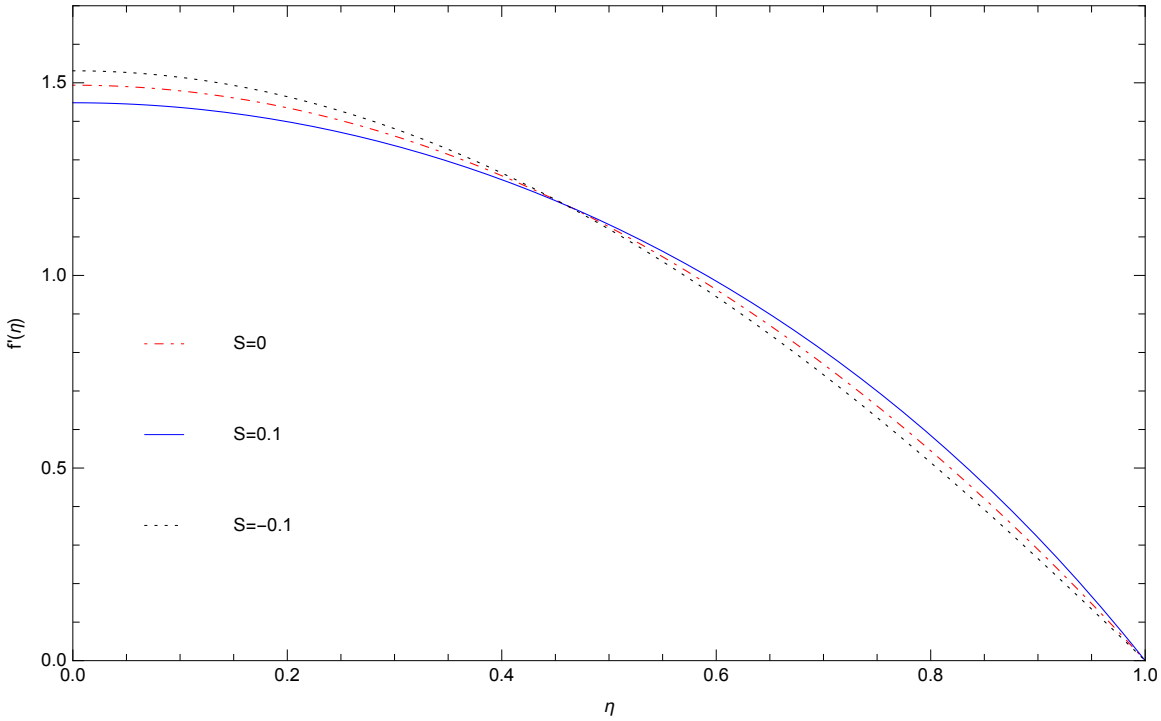

Figure 5.2: Velocity profiles for different values of S when $Pr = 11, Ec = 0.03, R = 0.1, M = 0.5, De = 5, \delta = 0.1, \phi = 0.08$

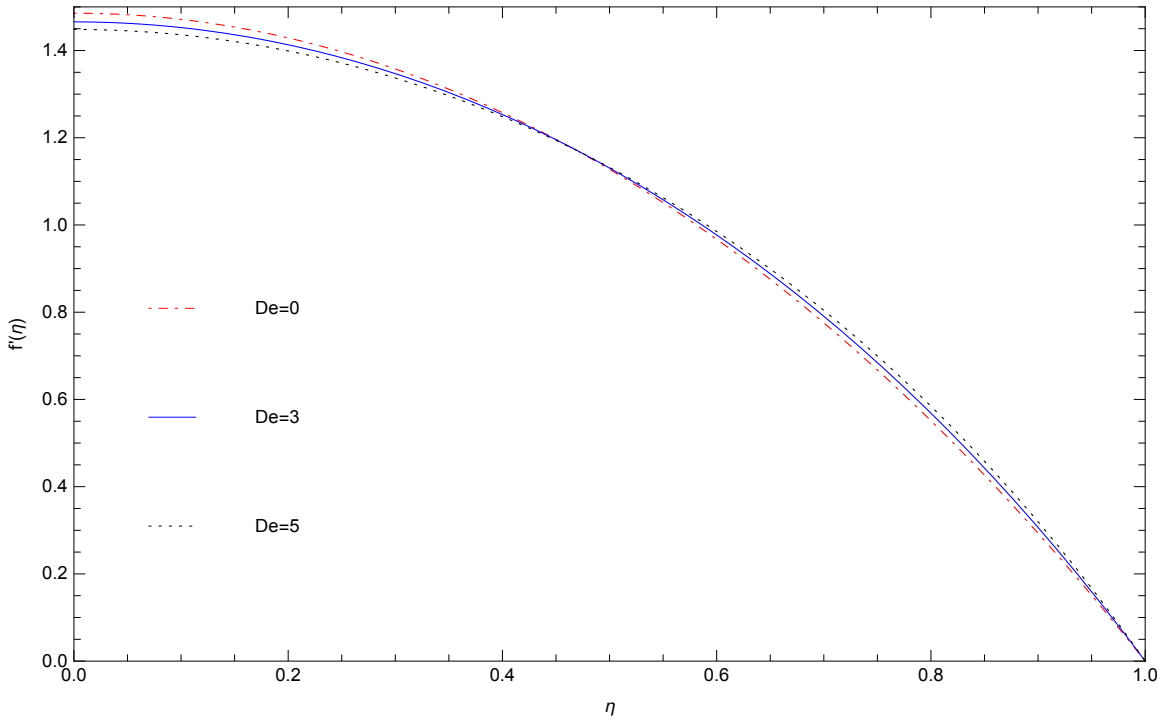

Figure 5.3: Velocity profiles for different values of De when $Pr = 11, Ec = 0.03, R = 0.1, M = 0.5, S = 0.1, \delta = 0.1, \phi = 0.08$

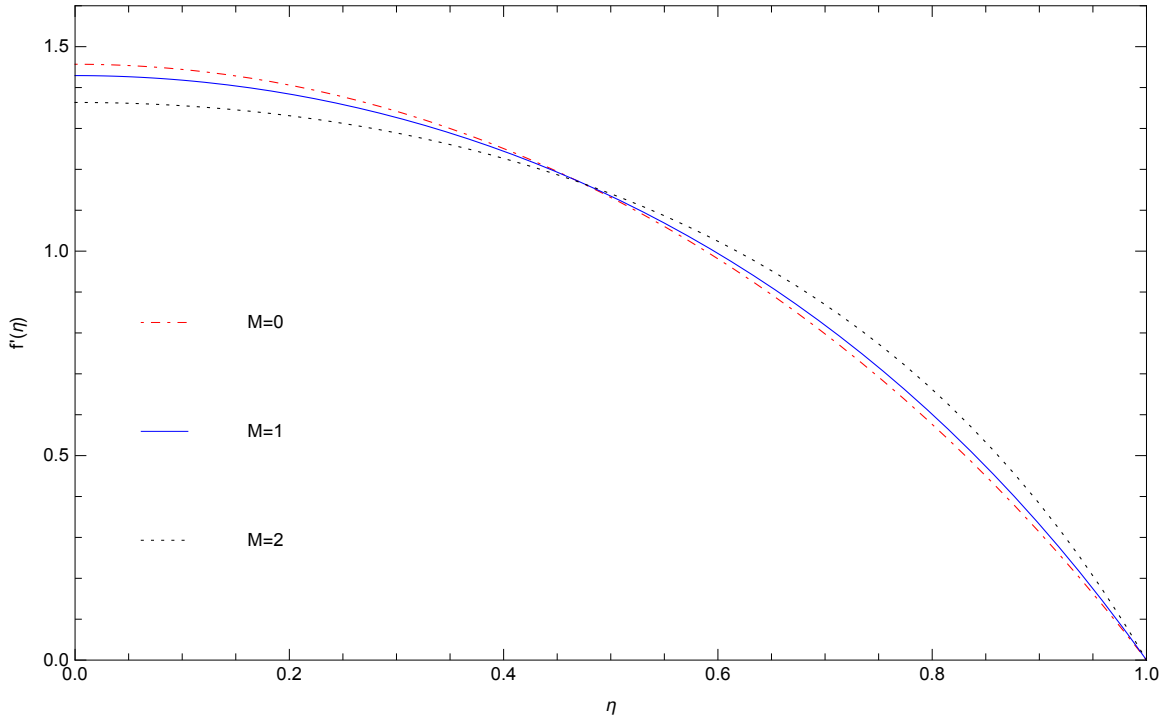

Figure 5.4: Velocity profiles for different values of M when $Pr = 11, Ec = 0.03, R = 0.1, De = 5, S = 0.1, \delta = 0.1, \phi = 0.08$

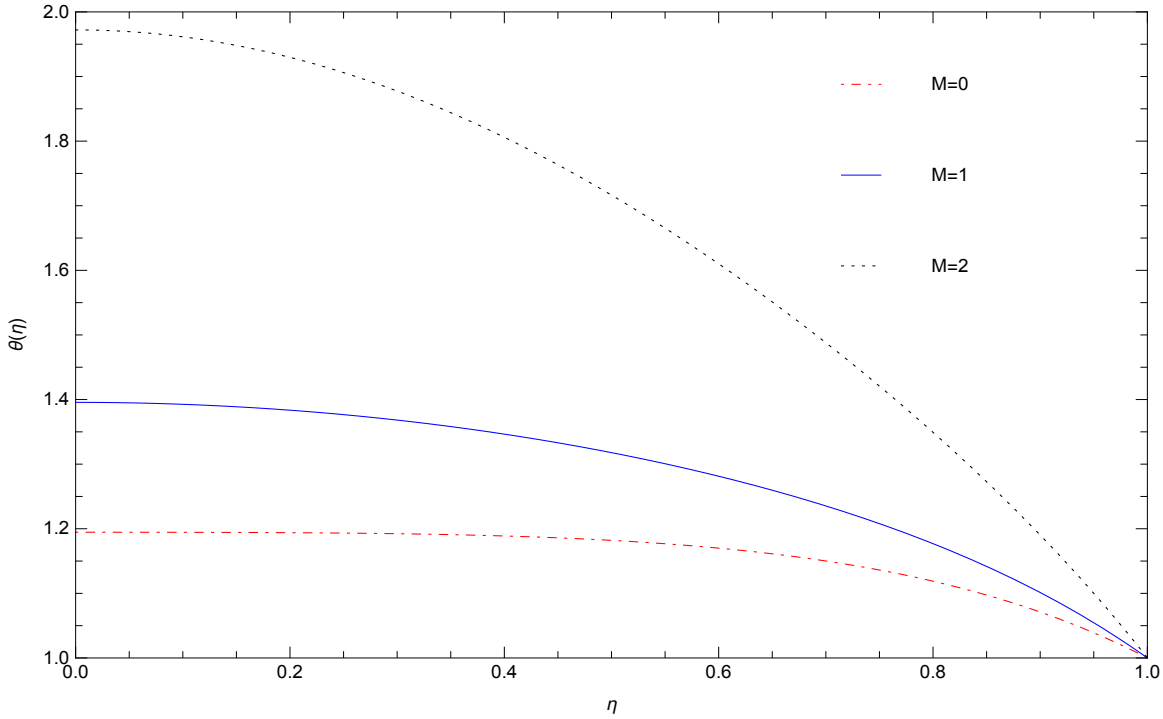

Figure 5.5: Temperature profiles for different values of M when $Pr = 11, Ec = 0.03, S = 0.1, De = 5, R = 0.1, \delta = 0.1, \phi = 0.08$

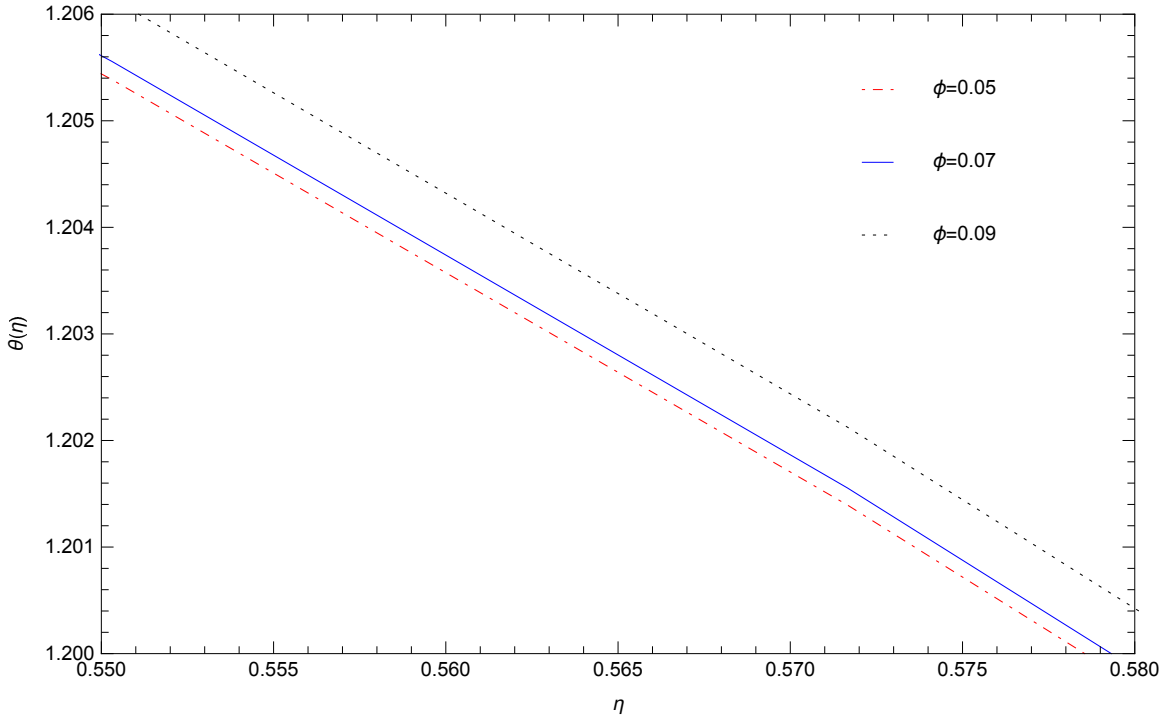

Figure 5.6: Temperature profiles for different values of ϕ when $Pr = 11, Ec = 0.03, S = 0.1, De = 5, R = 0.1, \delta = 0.1, M = 0.5$

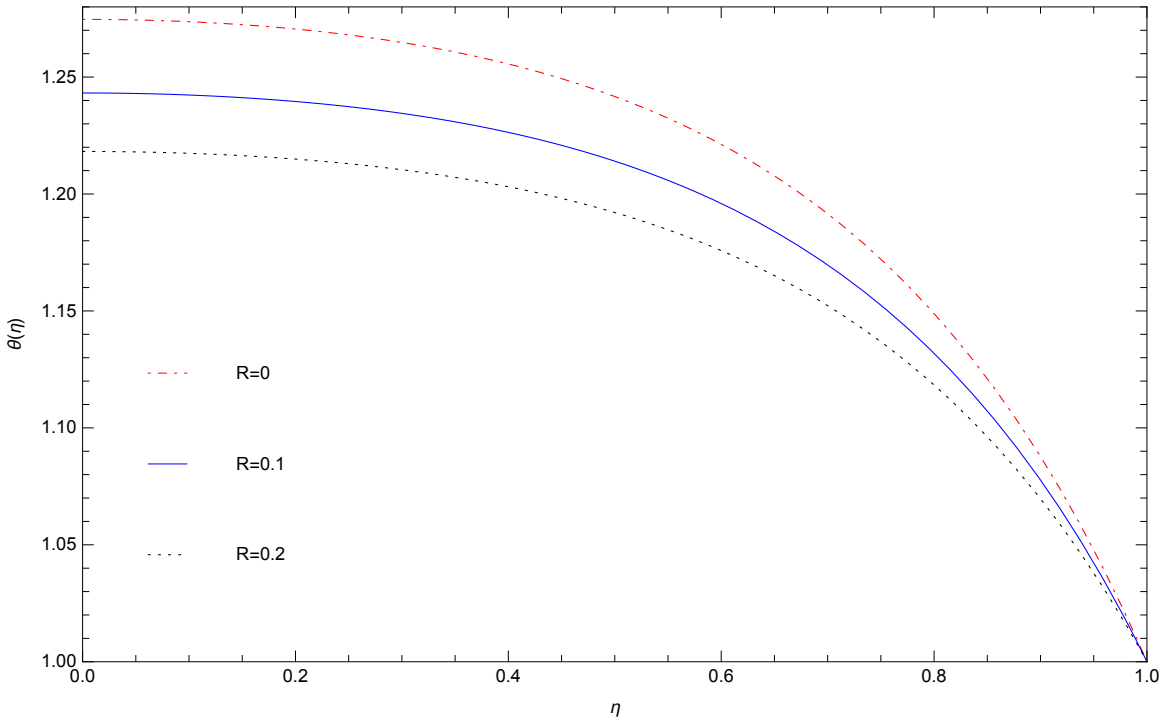

Figure 5.7: Temperature profiles for different values of R when $Pr = 11, Ec = 0.03, S = 0.1, De = 5, M = 0.5, \delta = 0.1, \phi = 0.08$

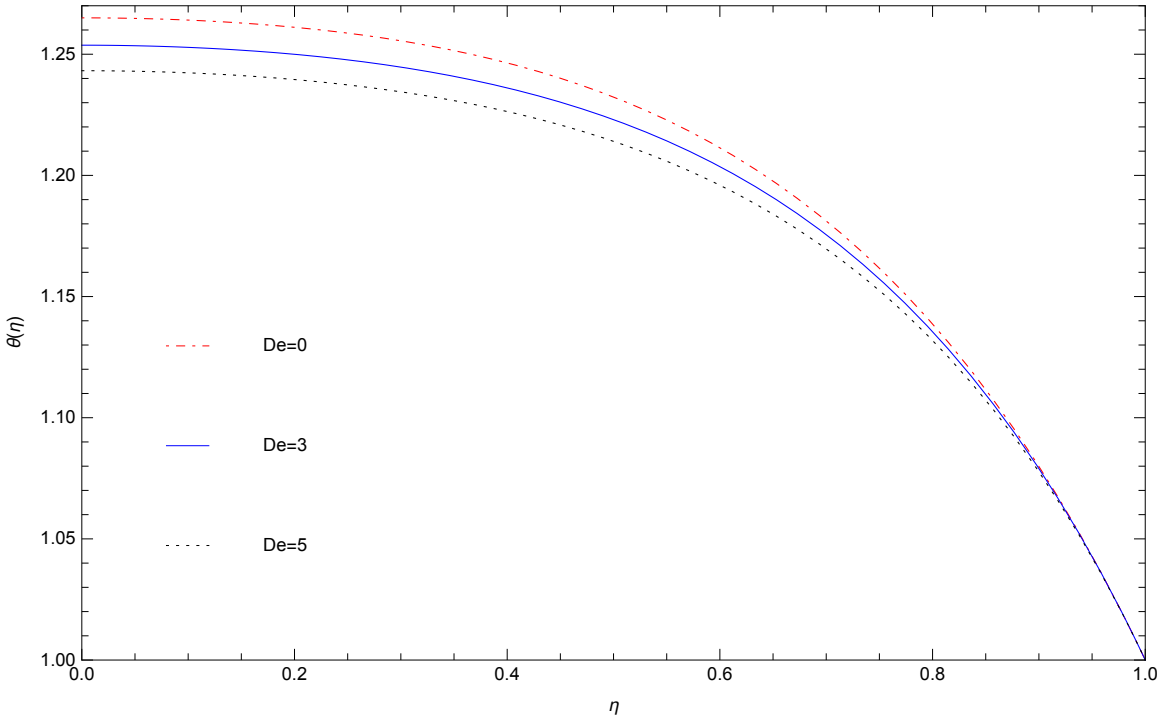

Figure 5.8: Temperature profiles for different values of De when $Pr = 11, Ec = 0.03, S = 0.1, M = 0.5, R = 0.1, \delta = 0.1, \phi = 0.08$

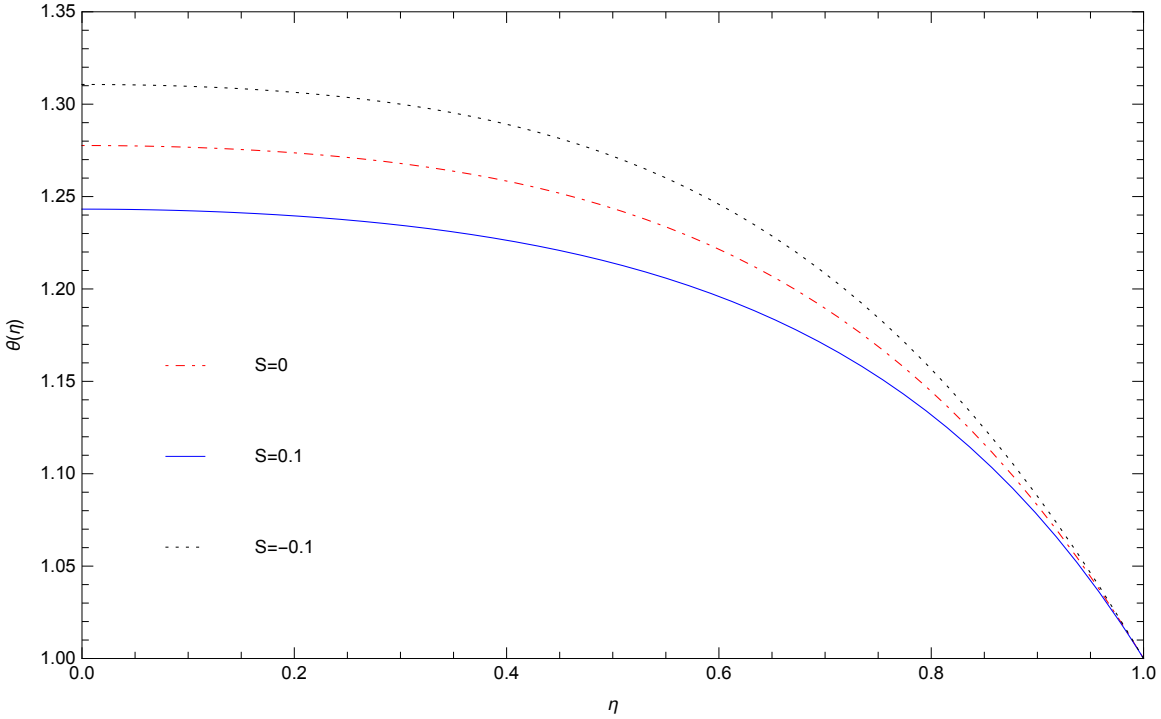

Figure 5.9: Temperature profiles for different values of S when $Pr = 11, Ec = 0.03, M = 0.5, De = 5, R = 0.1, \delta = 0.1, \phi = 0.08$

5.5.3 The study of Skin-friction and Nusselt number

The present article studies how skin-friction coefficient (C_f) and the Nusselt number (Nu) are influenced by the effect of different physical parameters. The expressions for these non-dimensional numbers are given in the equations 5.10-5.16. Figures 5.10 and 5.11 describe the effects of S on the skin-friction coefficient. Both the figures show that the skin friction coefficient increases with increase in the nanoparticle volume fraction ϕ and decreases with the increase in squeeze parameter S. Figure 5.12 depicts the relationship of De and ϕ with the local skin-friction $C_f = \frac{2f^{''}(1)}{S\delta A_1(1-\phi)^{2.5}}$. It reveals that with the increasing values of De, ϕ, skin-friction coefficient C_f increases. It can be explained as with the increase in De the elastic nature of the Maxwell fluid also increases. It is found that the skin-friction coefficient has an increasing trend with the increase of the volume fraction of the nanoparticles. Figure 5.13 gives the Nusselt number $Nu_r = -A_3\theta^{'}(1)$ in terms of the radiation parameter for different values of ϕ. It is evident that the Nusselt number decreases with the increase in the radiation parameter R. Moreover, we observed that the Nu (Nusselt number) increases with the increase in ϕ. It signifies the fact that an addition of the small amount of nanoparticles in the fluid increases the convective heat transfer capacity of the nanofluid. Figures 5.14 and 5.15 show that with a rise in the magnetic field strength the Nusselt number enhances significantly. Therefore, the nanoparticles under a strong magnetic field M increases the heat transfer capacity of the base fluid. It is also observed that under both the positive and negative values of S the Nusselt number increases with M and ϕ. Figure 5.16 shows that the Nusselt number has a decreasing trend with the increase of the Deborah number (De). The elastic nature of the Maxwell fluid increases with the increasing values of De and hence the heat transfer rate decreases.

5.5.4 Study of entropy generation

Figures 5.17 to 5.22 describe how the entropy generation is affected by the variation of the Deborah number De, the magnetic parameter M, the radiation parameter R, the squeeze parameter S and the volume fraction of the nanoparticles ϕ. Figure 5.17 gives the Bejan number profiles for different magnetic parameter M. The Bejan number increases with a rise in the magnetic field strength. The increase of Lorentz force tends to promote the enhancement of entropy generation. It is observed from Figure 5.18 that the Bejan profiles are significantly affected by R. The Bejan number (Be) decreases gradually with R. As the thermal radiation takes place in a squeeze channel, the thermal irreversibility reduces. Figure 5.19 reveals that the Bejan number Be decreases with the rise of the Deborah number De. Figures 5.20 to 5.21 reveal the comparative study of E_{SFF} and E_{ST} for different values of ϕ. It is observed that from this two figures that the entropy generation due to frictional forces are higher as compared to the entropy generation due to the thermal response. Both E_{ST} and E_{SFF} increase with the rise of the nanoparticle volume fraction. Figure 5.22 shows that Bejan number decreases with the increase of the squeeze parameter S as

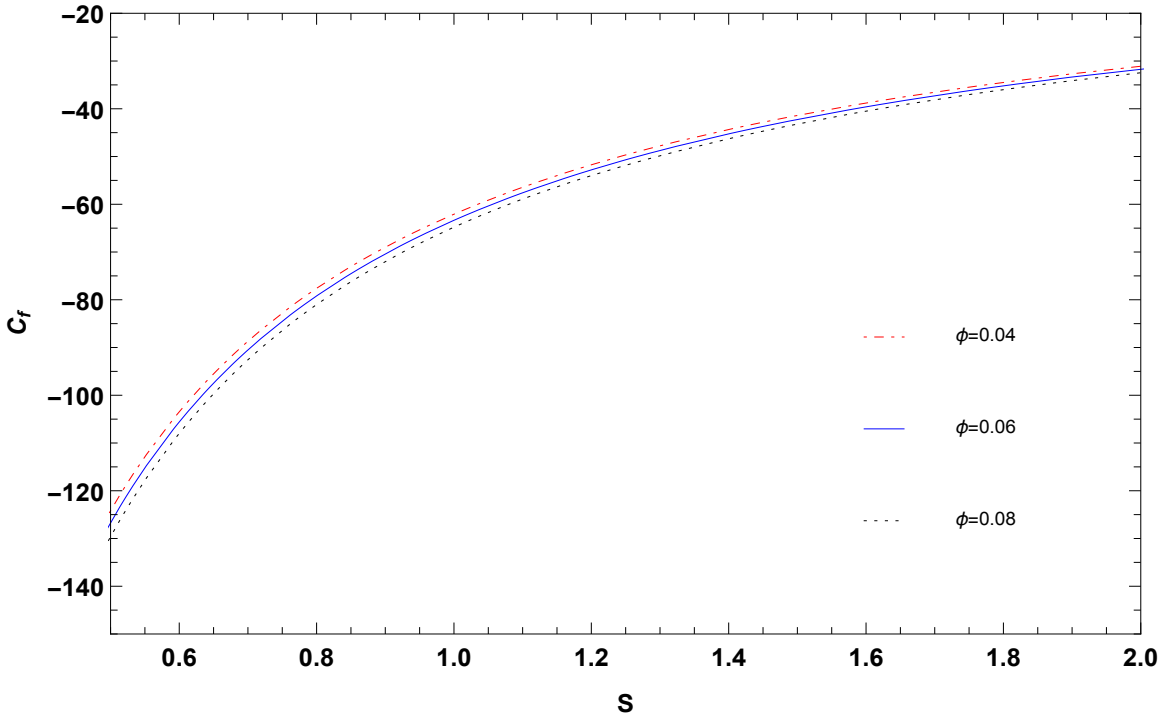

Figure 5.10: Skin-friction coefficient as a function of positive S values for different values of ϕ when $Pr = 11, Ec = 0.03, M = 0.5, De = 5, R = 0.1, \delta = 0.1$

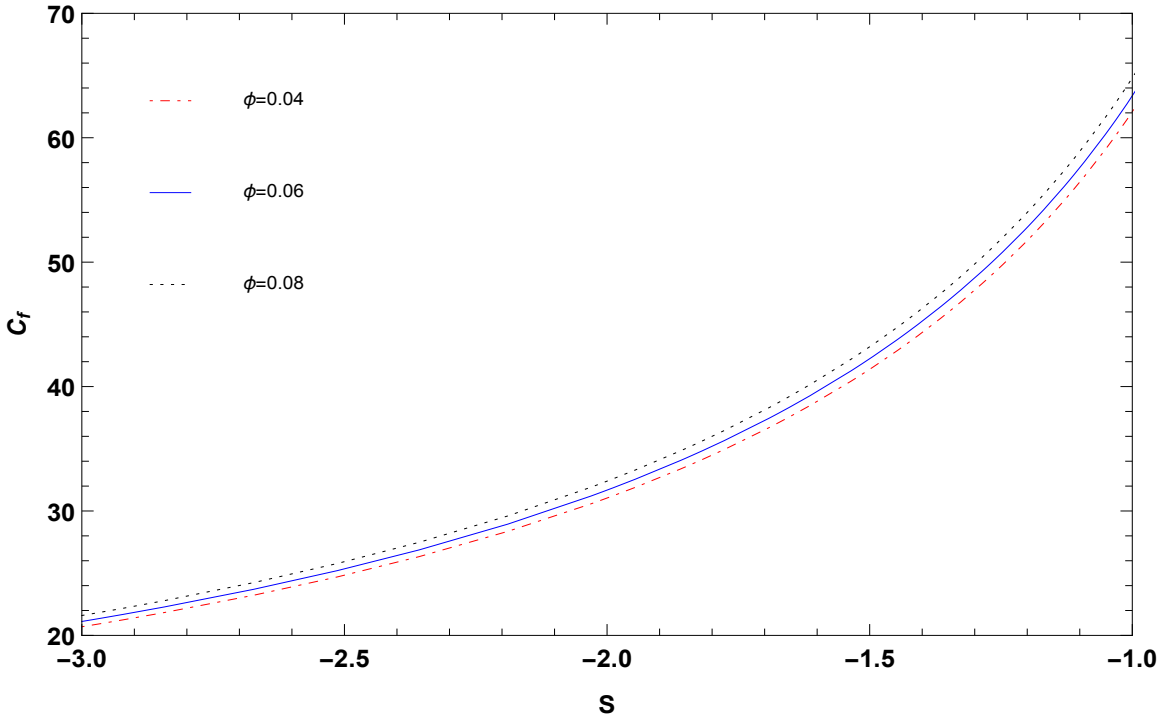

Figure 5.11: Skin-friction coefficient as a function of negative S values for different values of ϕ when $Pr = 11, Ec = 0.03, M = 0.5, De = 5, R = 0.1, \delta = 0.1$

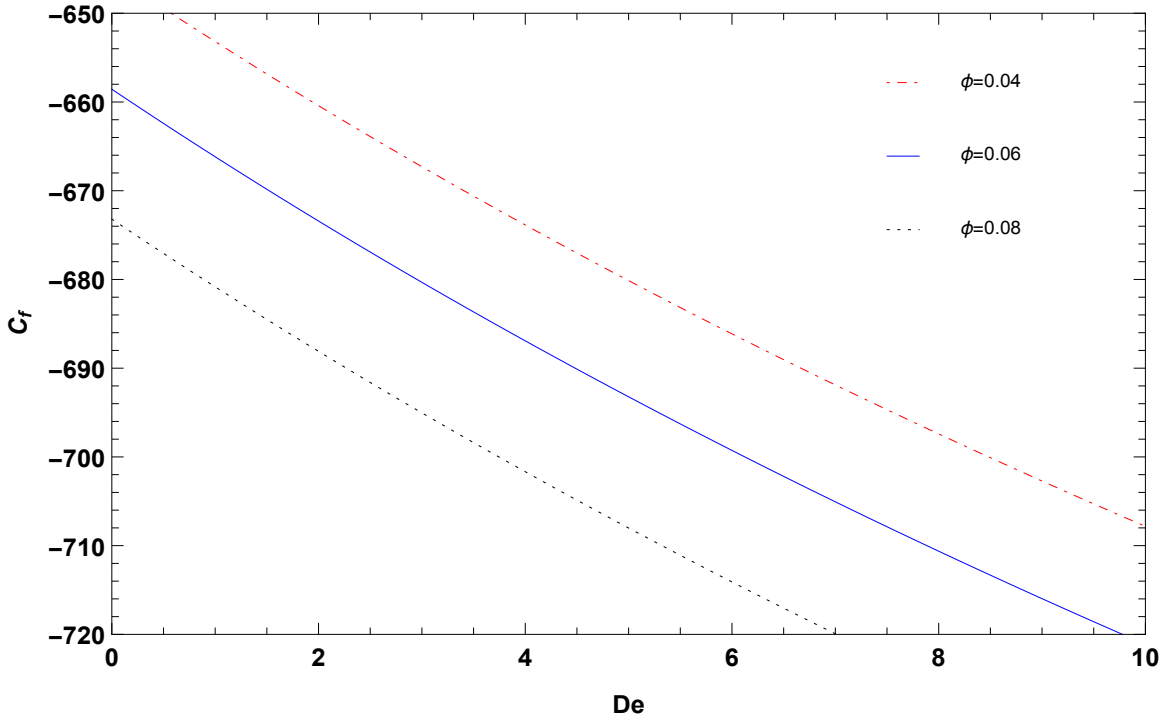

Figure 5.12: Skin-friction coefficient as a function of De for different values of ϕ when $Pr = 11, Ec = 0.03, M = 0.5, S = 0.1, R = 0.1, \delta = 0.1$

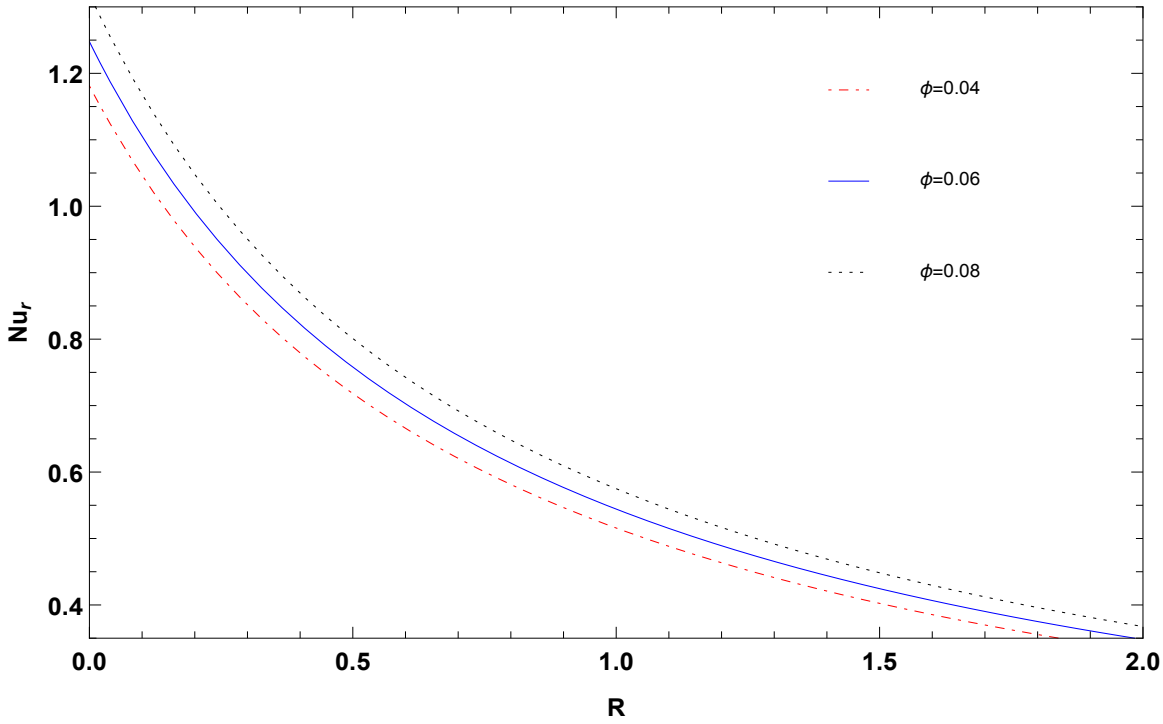

Figure 5.13: Variation of Nusselt number as a function of the thermal radiation R for different values of ϕ when $Pr = 11, Ec = 0.03, M = 0.5, De = 5, S = 0.1, \delta = 0.1$

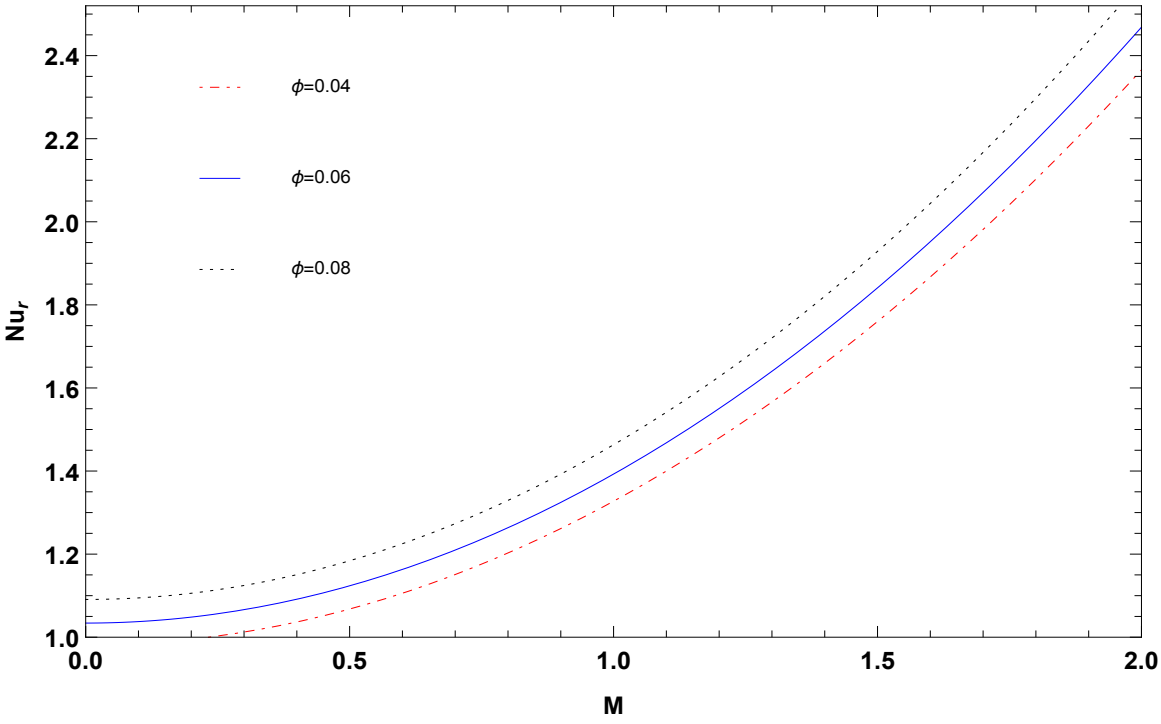

Figure 5.14: Variation of Nusselt number as a function of M for different values of ϕ when $Pr = 11, Ec = 0.03, R = 0.1, De = 5, S = -0.1, \delta = 0.1$

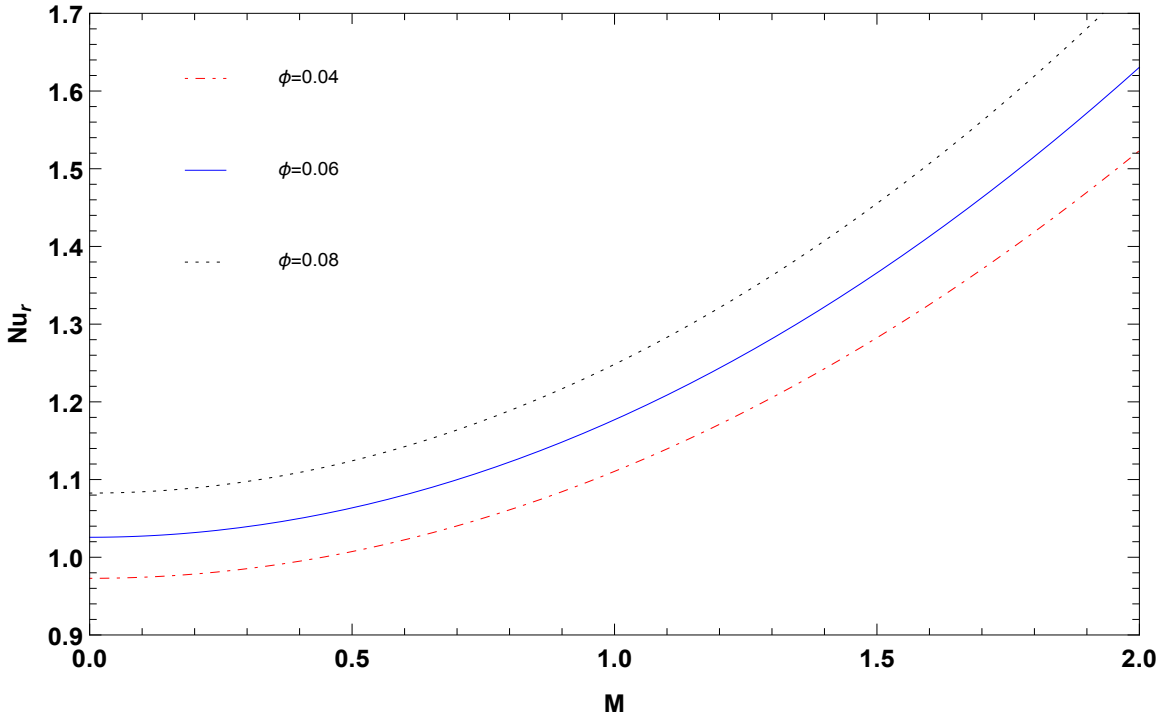

Figure 5.15: Variation of Nusselt number as a function of M for different values of ϕ when $Pr = 11, Ec = 0.03, R = 0.1, De = 5, S = 0.1, \delta = 0.1$

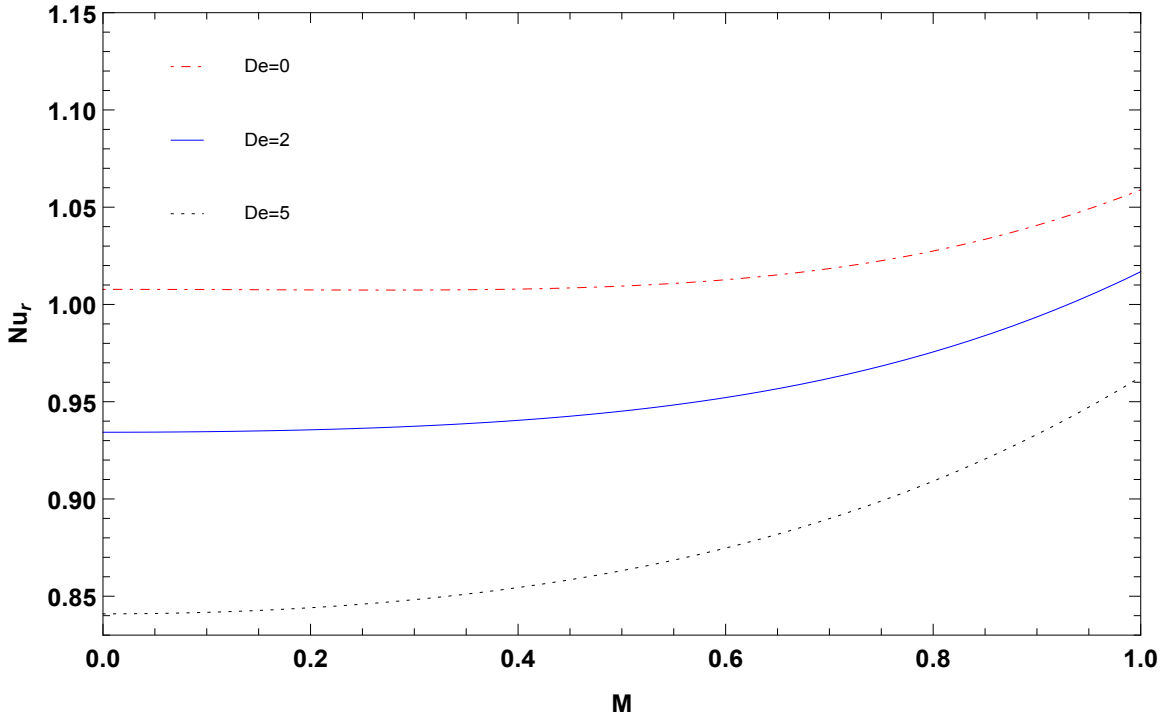

Figure 5.16: Variation of Nusselt number as a function of M for different values of De when $Pr = 11, Ec = 0.03, R = 0.1, S = 0.1, \delta = 0.1, \phi = 0.08$

the increasing squeeze parameter increases the elastic nature of the Maxwell fluid, hence increasing the frictional forces at the boundary of the channel. It is noticed from these two figures that the Bejan number is minimum at the central line of the channel whereas it is maximum at the vicinity of the channel wall. However, in the presence of strong magnetic field the Bejan number has a strong influence within the squeeze channel.

5.6 Conclusion

The energy efficiency of the squeezing Graphene-PDMS nanofluid flow between two plates under the influence of an external magnetic field as well as the radiative heat flux is examined in this article. Figure 5.1 is the physical sketch of the problem. Figures 5.2-5.22 illustrate the effects of different physical parameters such as the thermal radiation parameter R, the magnetic field strength M, the Deborah number De, the squeeze parameter S and the nanoparticle volume fraction ϕ on the velocity profiles, thermal profiles, the Nusselt number, Bejan number and the coefficient of skin-friction. The DTM has been used to solve the non-linear differential equations. The important observations from the present study are summarized below:

- Bejan number Be decreases with a rise in the Deborah number De, the squeeze parameter S.

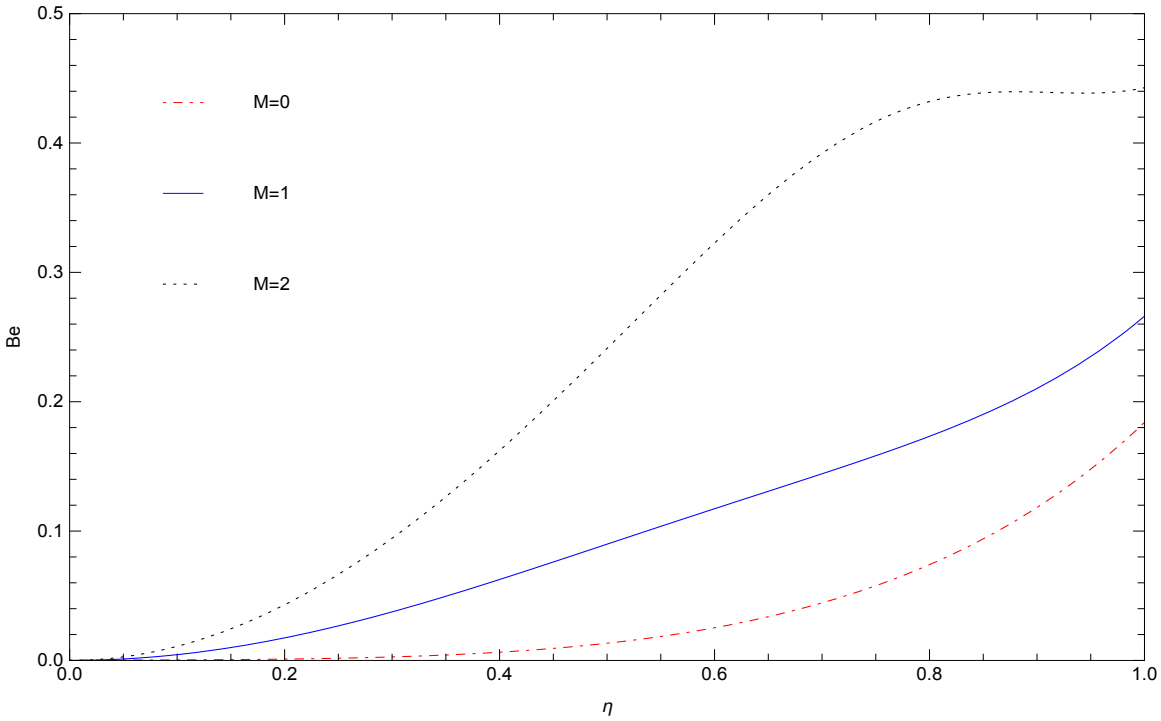

Figure 5.17: Bejan number profiles for different values of M when $Pr = 11, Ec = 0.03, De = 5, R = 0.1, S = 0.1, \delta = 0.1, \phi = 0.08$

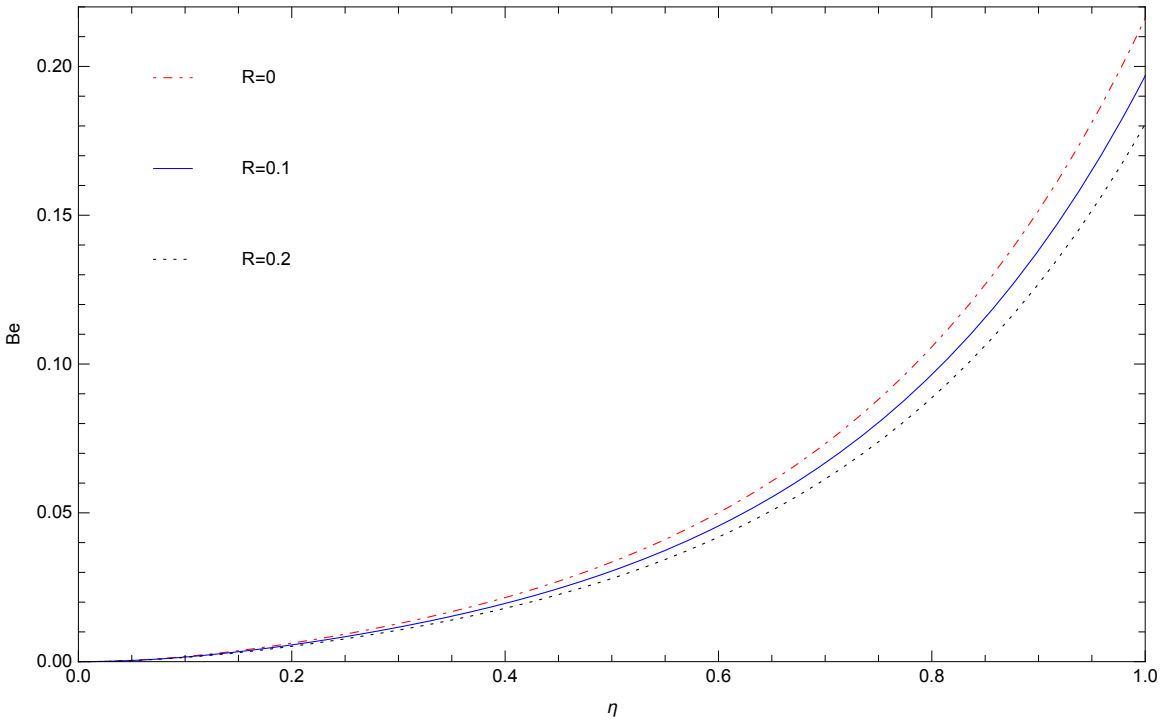

Figure 5.18: Bejan number profiles for different values of R when $Pr = 11, Ec = 0.03, De = 5, M = 0.5, S = 0.1, \delta = 0.1, \phi = 0.08$

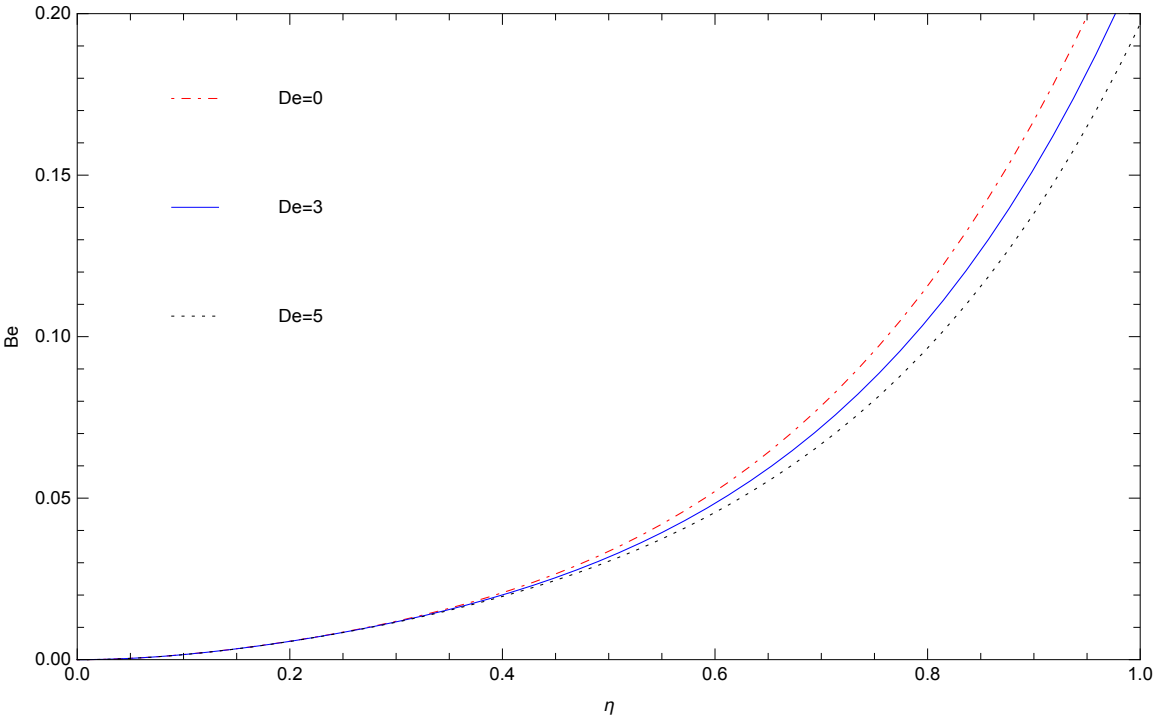

Figure 5.19: Bejan number profiles for different values of De when $Pr = 11, Ec = 0.03, M = 0.5, R = 0.1, S = 0.1, \delta = 0.1, \phi = 0.08$

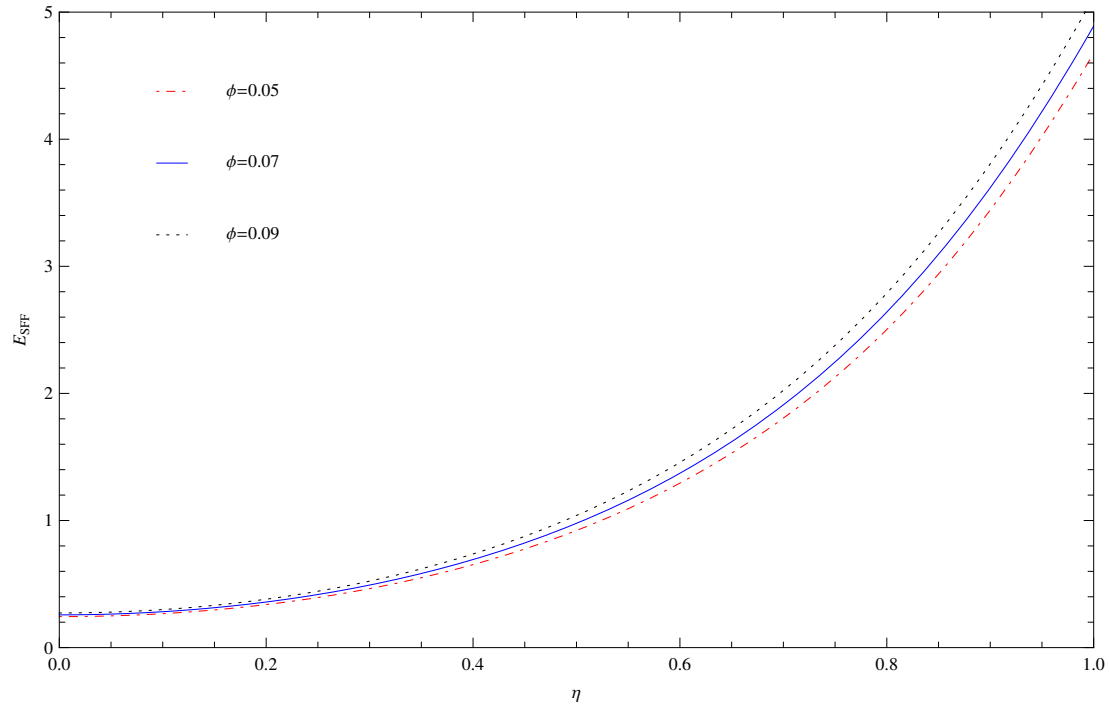

Figure 5.20: Entropy Generation via skin-friction E_{SFF} for different values of ϕ when $Pr = 11, Ec = 0.03, S = 0.1, De = 5, M = 0.5, R = 0.1, \delta = 0.1$

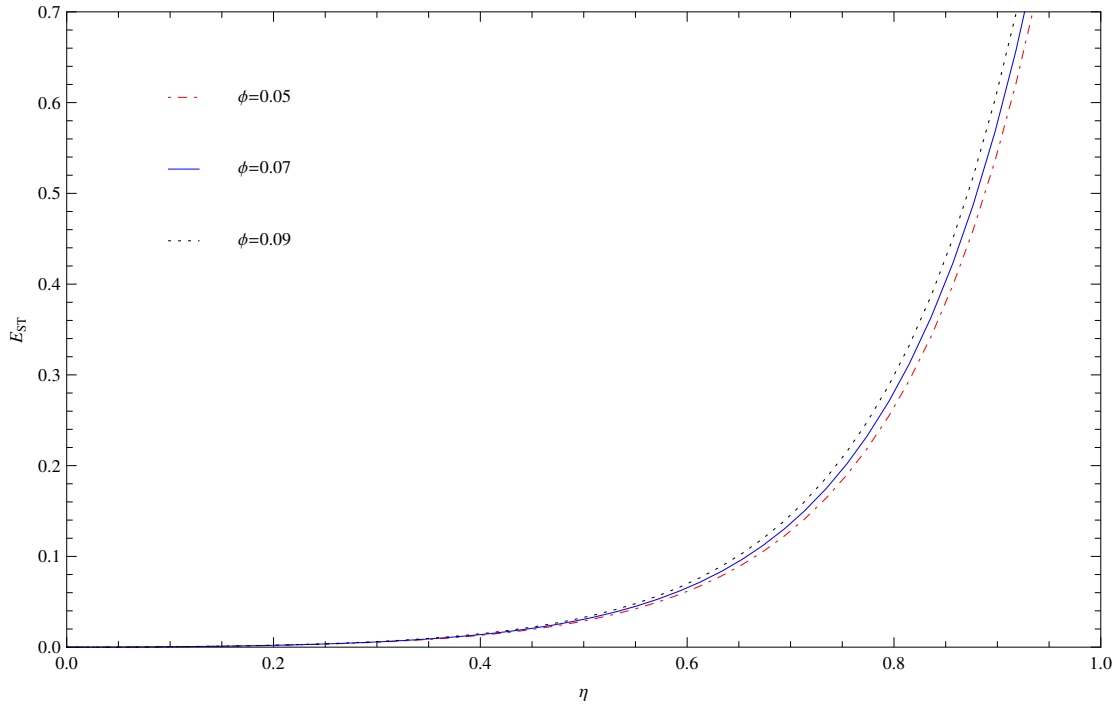

Figure 5.21: Entropy Generation via heat transfer E_{ST} for different values of ϕ when $Pr = 11, Ec = 0.03, S = 0.1, De = 5, M = 0.5, R = 0.1, \delta = 0.1$

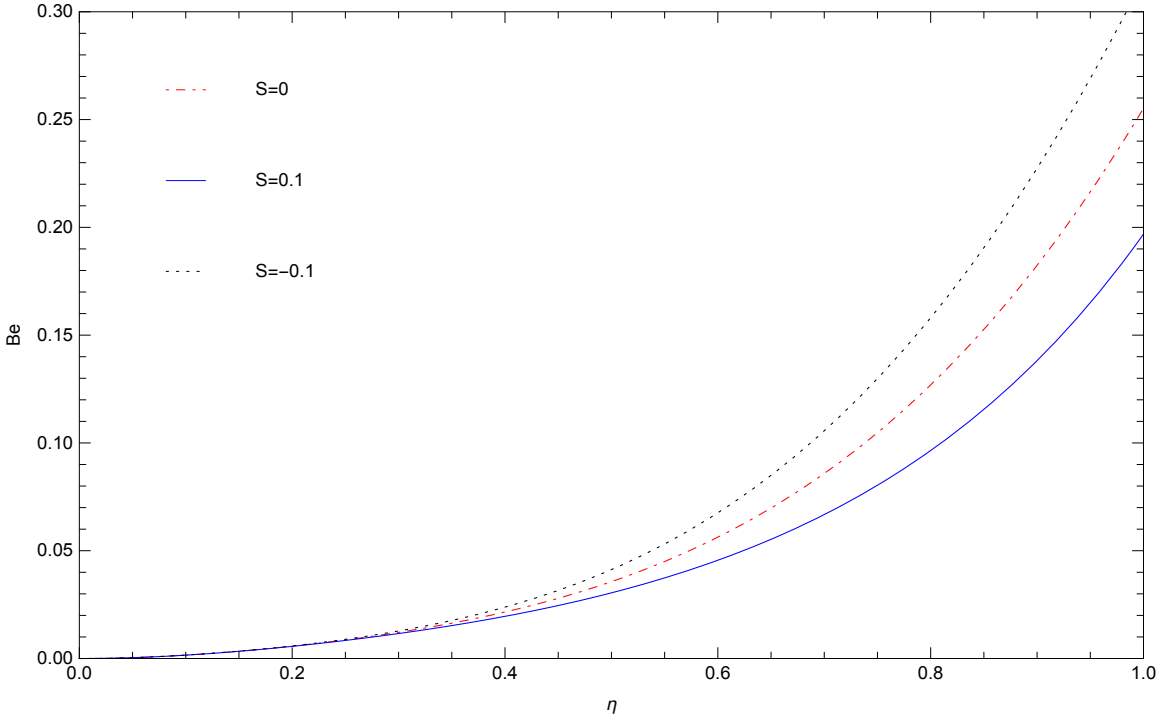

Figure 5.22: Bejan number profiles for different values of S when $Pr = 11, Ec = 0.03, M = 0.5, R = 0.1, De = 5, \delta = 0.1, \phi = 0.08$

- The Bejan number has an increasing trend with M.
- Bejan number (Be) decreases gradually with the increase of the radiation parameter R.
- Both E_{ST} and E_{SFF} increase with the enhancement of the nanoparticle size.
- E_{SFF} is much higher in comparison to the E_{ST} within the squeeze channel.
- The velocity decreases with the increase of the Deborah number De, the squeeze parameter S and the magnetic parameter M up to a certain height and then follows the opposite trend.
- The temperature within the squeeze channel increases with the increase of the applied magnetic parameter M, the nanoparticle volume fraction ϕ while the reverse trend is seen for the radiation parameter R, the squeeze parameter S as well as the Deborah number De.
- The coefficient of skin-friction coefficient C_f has an increasing trend with the Deborah number De, the nanoparticle volume fraction ϕ.
- The Nusselt number (Nu) has an increasing trend with the increasing values in M as well as the nanoparticle volume fraction (ϕ) and decreases with increasing R, the Deborah number De.

Chapter 6

Differential Transform Method for Unsteady Magnetohydrodynamic Nanofluid Flow [5]

6.1 Introduction

Nanofluid is a homogenous mixture of a base fluid with the nano-sized particles. CHOI [1995] first suggested the concept of nanofluid and experimentally verified that the augmentation of small amount of nanoparticles into the fluid increases the heat transfer capacity of the fluid. Angayarkanni and Philip [2015] provided a review article on nanofluids. Their survey include different techniques of preparing nanofluids, stability conditions of nanofluids, different methods of measuring the thermal conductivity of nanofluids. They discussed the thermal properties of nanofluids based on various experimental results. The study of nanofluid flow between two squeezing plates is an important topic of research in the recent years because of its many engineering and industrial applications. For example, the external magnetic field is applied to resist the deviation of the lubrication viscosity in some engineering cases. Nanofluids are also used as coolants in nuclear reactors, radiation therapy, geothermal energy extraction. It has wide range of applications in polymer processing, injection modeling, load capacity related problems in many mechanical systems. A fundamental work in this direction was conducted by Stefan [1874]. Reynolds [1886] experimentally studied the lubrication theory between two elliptic plates to determine the viscosity of olive oil. The squeeze flow bounded by two rectangular plates was investigated by Archibald [1956]. Rashidi et al. [2008] discussed the unsteady squeeze flow between two plates. Mahmood et al. [2007] revealed from their study that the Nusselt number increases with the increase in the Prandtl number. Their results are also supported by Mustafa et al. [2012] in their study of unsteady squeeze flow. Buongiorno et al. [2009] have carried out a joint set of experiments called INPBE on nanofluids. They have sug-

[5] The content of this chapter has been published in *Journal of nanofluids*, 8 (5) (2019) 998-1009.

gested that the thermal conductivity of the nanofluid increases considerably with an increase in nanoparticle aspect ratios. It was observed that the nanofluids are consistent under the same experimental techniques to increase the thermal conductivity of nanoparticles. Sengupta and Ghoshdastidar [2018] analyzed numerically the heat transfer enhancement of the water-based ferrofluids between micro and macro channels. Dogonchi et al. [2017] examined numerically the thermal properties and flow properties of Al_2O_3-water nanofluid by considering the thermal radiation effects, wherein they found that the nanoparticle volume fraction has an impact on the Nusselt number. Das et al. [2015] carried out the MHD nanofluid flow in a channel, which is inclined vertically. In this paper, mixed convective heat transfer properties of the fluid are investigated. Using the HPM method, Akinshilo [2018] investigated the MHD nanofluid flow in a porous stretching channel.

Zhou [1986] first employed the idea of DTM for solving differential equations in electrical engineering problems. The DTM is an recursive process to obtain analytical Taylor series solutions for the corresponding linear and non-linear differential equations. The DTM method for solving partial differential equations was developed by Chen and Ho [1999]. Sheikholeslami et al. [2013a] subsequently studied the reliability of this method. Acharya et al. [2016] studied the squeeze flow in a channel bounded by two parallel plates using DTM and have compared their results with the numerical results. In a semi-permeable channel, nanofluid flow is studied using the DTM by Sheikholeslami and Ganji [2015].

The present chapter investigates the entropy generation in terms of various important physical parameters. The irreversible loss of thermal energy in a system is termed as entropy generation. Bejan [1979], Bejan and Kestin [1983] did the significant work in this direction and formulated a number (Be) as the ratio of the entropy generation due to thermal irreversibility to the entropy generation due to fluid frictional factors. The entropy analysis of MHD blood flow of nanofluid was carried out by Bhatti and Rashidi [2016]. Wen-bin et al. [2002] investigated the entropy analysis on water-Al_2O_3 in a porous and thermally asymmetric micro-channel. Ting et al. [2015], Mkwizu and Makinde [2015] studied the entropy analysis on the unsteady nanofluid flow and considered the effects of thermophoresis. Nezhad and Shahri [2016] analyzed the entropy generation of two-immiscible MHD fluid in an inclined channel using the HAM method. Analysis of MHD nanofluid flow in a sinusoidal porous channel is studied by Hussain [2016]. They have also examined the entropy generation of the system experimentally. Shojaeian and Shojaeian [2011] numerically investigated the liquid slip flows between microchannels. Mahian et al. [2013] presented a review article on entropy generation where they pointed out further research in this direction. In most of the above works, the authors have focused in the study of viscous MHD nanofluids in the presence of thermal radiation. To the best of our knowledge, the study of entropy generation of squeeze nanofluid flow is an important area to explore the system performance and has not been examined so far in the presence of thermal radiation.

The above studies motivated us to investigate the Cu-water nanofluid flow in a squeeze

channel. The energy efficiency have been analyzed via entropy generation of the system. The influence of an external magnetic field, thermal radiation along with the volume fraction of the nanoparticles are taken into account. The novelty of this chapter lies in the study of entropy generation under the influence of thermal radiation effects of the nanoparticles. Our model has applications in polymer processing, injection modeling. In the above prescribed engineering systems, we are interested to minimize the entropy generation (Be) and try to maximize the heat transfer rate (Nu) in the system. In this chapter, Bejan number (Be) and Nusselt number (Nu) are extensively studied by varying different thermophysical parameters. We have used the DTM method which gives an approximate Taylor series solution. The convergence criteria for differential transform method in terms of its radius of convergence are presented, which may lead to major novelty of this analysis. The velocity and temperature profiles along with the coefficient of skin-friction for different non-dimensional parametric values are examined.

6.2 Modeling of the problem

The present chapter investigates the viscous, incompressible Cu-water nanofluid flow and heat transfer in a squeeze channel. We consider the two-dimensional Cartesian co-ordinate system, in which, x-axis is measured along the plate and the normal direction to the plate is denoted by y-axis. The squeezing flow in a channel is passing between two parallel plates situated at $h(t) = H(1-\alpha t)^{\frac{1}{2}}$ distance apart (measure from $y = 0$), and the corresponding physical sketch is shown in Figure 6.1. Here, $\alpha > 0$ is called the squeezing parameter. The plates have velocity $v(t) = \frac{dh}{dt}$ and they meet at $t = \frac{1}{\alpha}$. Again $\alpha < 0$ indicates that the plates are moving away to each other in time. At $t = 0$, the plates are at distance H. An external magnetic field of strength $B(t) = B_0(1-\alpha t)^{-\frac{1}{2}}$ is applied in the normal direction to the plates. The initial strength of the applied magnetic field is B_0 and then increases with time t. In this system radiative heat flux is considered by taking Rosseland approximation. It is assumed that no chemical reaction takes place. The equations of motion for Cu-water nanofluid flow with both magnetic field, thermal radiation effects are described as

$$\frac{\partial u}{\partial x} + \frac{\partial v}{\partial y} = 0, \tag{6.1}$$

$$\begin{aligned} \rho_{nf}\left(\frac{\partial u}{\partial t} + u\frac{\partial u}{\partial x} + v\frac{\partial u}{\partial y}\right) &= -\frac{\partial p}{\partial x} + \\ &\mu_{nf}\left(\frac{\partial^2 u}{\partial x^2} + \frac{\partial^2 u}{\partial y^2}\right) - \\ &\sigma B(t)^2 u, \end{aligned} \tag{6.2}$$

$$\rho_{nf}\left(\frac{\partial v}{\partial t}+u\frac{\partial v}{\partial x}+v\frac{\partial v}{\partial y}\right) = -\frac{\partial p}{\partial y}+ \mu_{nf}\left(\frac{\partial^2 v}{\partial x^2}+\frac{\partial^2 v}{\partial y^2}\right), \tag{6.3}$$

$$\begin{aligned}\left(\frac{\partial T}{\partial t}+u\frac{\partial T}{\partial x}+v\frac{\partial T}{\partial y}\right) = {} & \frac{k_{nf}}{(\rho C_p)_{nf}}\left(\frac{\partial^2 T}{\partial x^2}+\frac{\partial^2 T}{\partial y^2}\right)+ \\ & \frac{\sigma B^2(t)}{(\rho C_p)_{nf}}u^2-\frac{1}{(\rho C_p)_{nf}}\frac{\partial q_r}{\partial y} \\ & +\frac{\mu_{nf}}{(\rho C_p)_{nf}}\left(2\left\{\left(\frac{\partial u}{\partial x}\right)^2+\left(\frac{\partial v}{\partial y}\right)^2\right\}\right. \\ & \left.+\left(\frac{\partial u}{\partial y}+\frac{\partial v}{\partial x}\right)^2\right),\end{aligned} \tag{6.4}$$

where u, v denote the velocity components in x and y directions respectively, T the temperature, p denotes the fluid pressure, ρ_{nf} the density of the nanofluid, μ_{nf} the effective dynamic viscosity, $(\rho C_p)_{nf}$ the effective heat capacity of the nanofluid, k_{nf} the effective thermal conductivity of the nanofluid, q_r the radiative heat flux of the nanofluid, σ the electrical conductivity of the nanofluid respectively. The radiative heat flux is calculated using the Rosseland approximation as,

$$q_r = -\frac{4\sigma_1}{3k_1}\frac{\partial T^4}{\partial y},$$

where, σ_1 represents the Stefan-Boltzmann constant and k_1 is the mean absorption coefficient. The Taylor's series expansion of T^4 yields,

$$T^4 \cong 4{T_H}^3 T - 3{T_H}^4,$$

in which T_H represents the constant temperature at the wall.
Therefore, we obtain,

$$\frac{\partial q_r}{\partial y} = -\frac{16\sigma_1 {T_H}^3}{3k_1}\frac{\partial^2 T}{\partial y^2}. \tag{6.5}$$

In the case of nanofluid, the thermal conductivity of the nano-particle is 100 times larger than that of the base fluid. Thus, the effective nanofluid properties based on the Maxwell nanofluid model is described in Acharya et al. [2016], MAXWELL [1873], Brinkman [1952] as

$$\rho_{nf} = (1-\phi)\rho_f + \phi\rho_s, \tag{6.6}$$

$$(\rho C_p)_{nf} = (1-\phi)(\rho C_p)_f + \phi(\rho C_p)_s, \tag{6.7}$$

$$\mu_{nf} = \frac{\mu_f}{(1-\phi)^{2.5}}, \tag{6.8}$$

$$\frac{k_{nf}}{k_f} = \frac{k_s+2k_f-2\phi(k_f-k_s)}{k_s+2k_f+\phi(k_f-k_s),} \tag{6.9}$$

where, ϕ denotes the nanoparticle volume fraction, k_s the thermal conductivity of the solid Cu, k_f the thermal conductivity of the base fluid.
The boundary conditions are taken as,

$$u = 0, v = \frac{dh}{dt}, T = T_H \quad when \quad y = h(t), \tag{6.10}$$

$$\frac{\partial u}{\partial y} = 0, v = 0, \frac{\partial T}{\partial y} = 0 \quad when \quad y = 0. \tag{6.11}$$

Now, we introduce the following similarity transformations and dimensionless variables,

$$\eta = \frac{y}{H\sqrt{1-\alpha t}}, u = \frac{\alpha x}{2(1-\alpha t)} f^{'}(\eta),$$
$$v = \frac{-\alpha H}{2\sqrt{1-\alpha t}} f(\eta), \theta = \frac{T}{T_H}. \tag{6.12}$$

Use of these dimensionless variables and eliminating pressure terms by cross-differentiation of equations 6.2 and 6.3, we derive the following non-linear ordinary differential equations along with the thermal energy equation 6.4 as,

$$\begin{aligned} f^{iv} &= S \cdot A_1 (1-\phi)^{2.5} (3f^{''} + \eta f^{'''} + f^{'} f^{''} - f f^{'''}) \\ &\quad + M^2 f^{''}, \end{aligned} \tag{6.13}$$

$$\begin{aligned} &(1 + \frac{4R}{3})\theta^{''} + Pr \cdot S \cdot (\frac{A_2}{A_3})(f\theta^{'} - \eta\theta^{'}) \\ &+ \frac{Pr \cdot Ec}{A_3(1-\phi)^{2.5}} (f^{''2} + f^{'2}(M^2 + 4\delta^2)) = 0. \end{aligned} \tag{6.14}$$

Similarly the boundary conditions 6.10 and 6.11 reduce to

$$f^{''}(0) = 0, f(0) = 0, \theta^{'}(0) = 0, \tag{6.15}$$

$$f^{'}(1) = 0, f(1) = 1, \theta(1) = 1. \tag{6.16}$$

Equations 6.13 and 6.14 involved some dimensional parameters defined as $S = \frac{\alpha H^2}{2\nu_f}$ denotes the squeeze number, $A_1 = \frac{\rho_{nf}}{\rho_f}, A_2 = \frac{(\rho C_p)_{nf}}{(\rho C_p)_f}, A_3 = \frac{k_{nf}}{k_f}$, $Pr = \frac{\mu_f (\rho C_p)_f}{\rho_f k_f}$ the Prandtl number, $Ec = \frac{\rho_f}{(\rho C_p)_f T_H} (\frac{\alpha x}{2(1-\alpha t)})^2$ the Eckert number, $M = HB_0\sqrt{\frac{\sigma_f}{\mu_f}}$ the magnetic number, $\delta = \frac{H\sqrt{(1-\alpha t)}}{x}$ ad $R = \frac{4\sigma_1 T_H^3}{k_1 k_{nf}}$ the thermal radiation parameter.

This chapter investigates the skin-friction coefficient C_f and the Nusselt number Nu that can be defined as,

$$C_f = \frac{\mu_{nf} (\frac{\partial u}{\partial y})_{y=h(t)}}{\frac{1}{2}\rho_{nf} (\frac{dh}{dt})^2} = \frac{2f^{''}(1)}{S\delta A_1 (1-\phi)^{2.5}}, \tag{6.17}$$

and the Nusselt number Nu has the expression,

$$Nu = \frac{-Hk_{nf}(\frac{\partial T}{\partial y})_{y=h(t)}}{k_f T_H} = \frac{-Nu_r}{\sqrt{1-\alpha t}},$$
$$\text{where, } Nu_r = -A_3\theta^{'}(1). \tag{6.18}$$

6.3 Entropy Generation

The irreversible loss of thermal energy in a system is termed as the entropy generation of the system. The expression for the entropy generation rate per unit volume is given as in Mkwizu and Makinde [2015], Mahian et al. [2013],

$$S_G = \frac{k_{nf}}{T^2}\left(\left(\frac{\partial T}{\partial y}\right)^2 + \frac{16\sigma T_H^3}{3K_1 k_{nf}}\left(\frac{\partial T}{\partial y}\right)^2\right) + \frac{\mu_{nf}}{T}\left(\frac{\partial u}{\partial y}\right)^2 + \frac{\sigma B^2 u^2}{T}. \tag{6.19}$$

The dimensionless form of total entropy generation N_S is given by,

$$\begin{aligned} N_S &= \frac{h(t)^2}{k_{nf}} S_G = N_{ST} + N_{SFF} \\ &= \frac{1}{\theta^2}(1 + \frac{4R}{3})\theta^{'2} \\ &+ \frac{1}{\theta}\frac{Pr.Ec}{A_3(1-\phi)^{2.5}}(M^2 f^{'2} + f^{''2}), \end{aligned} \tag{6.20}$$

where N_S is the total entropy generation, N_{ST} denotes the entropy generation due to the thermal effects and thermal radiation, N_{SFF} is the entropy generation due to fluid friction and the effect of magnetic field. The Bejan number is an important non-dimensional number that helps us to compare the entropy generation due to thermal effects to the total entropy generation. The expression for the Bejan number is as follows,

$$Be = \frac{N_{ST}}{N_S}. \tag{6.21}$$

6.4 Method of Solution

This chapter concerns with the analytical approach via DTM to obtain approximate solutions of the equations 6.13 and 6.14 with respect to the boundary conditions 6.15 and 6.16. The idea of DTM, was first proposed by Zhou [1986]. The k^{th} order DTM of a given function $g(\eta)$ is expressed as

$$G(k) = \frac{1}{k!}\left[\frac{d^k g(\eta)}{d\eta^k}\right]_{\eta=\eta_0}, \tag{6.22}$$

Table 6.1: The DTM conversion table

Original function	DTM	Conversion
$l(\lambda) = \frac{d^m g(\lambda)}{d\lambda^m}$	$L(k) = \frac{(k+m)!}{k!} G(k+m)$	
$l(\lambda) = m(\lambda)n(\lambda)$	$L(k) = \sum_{n=0}^{k} M(n)N(k-n)$	
$l(\lambda) = \lambda^n$	$L(k) = \delta(k-n)$	
$l(\lambda) = ag(\lambda) \pm bp(\lambda)$	$L(k) = aG(k) \pm bP(k)$	

where η_0 is a particular point, $G(\eta)$ is the k^{th} differential transform of $g(\eta)$ around the point η_0 and is given by

$$g(\eta) = \sum_{k=0}^{\infty} \frac{1}{k!} \Big[\frac{d^k g(\eta)}{d\eta^k}\Big]_{\eta=\eta_0} (\eta - \eta_0)^k. \tag{6.23}$$

Thus, k^{th} order differential transform of g is the k^{th} Taylor's coefficient of g around the point η_0. Using 6.22 in the equation 6.23 we can write,

$$g(\eta) = \sum_{k=0}^{\infty} G(k)(\eta - \eta_0)^k. \tag{6.24}$$

It is worthwhile to mention that the DTM calculates the relative derivatives by using a recursive algebraic relation. The recursive relations are obtained by transforming the original functions with the DTM method. The DTM transformation satisfies the identities as mentioned in Table 6.1.

$g(\eta)$ is then approximated by a finite series $\tilde{g}(\eta)$ given in the following form,

$$\tilde{g}(\eta) = \sum_{k=0}^{P} G(k)(\eta - \eta_0)^k, \tag{6.25}$$

where, T is called the length of the series. The equations 6.24 and 6.25 show that the error terms $|g(\eta) - \tilde{g}(\eta)|$ is negligibly small. Using the relations for DTM at the point $\eta_0 = 0$ as given in Table 6.1, the functions $f(\eta)$ and $\theta(\eta)$ satisfying the governing equations 6.13, 6.14 will be approximated by the equations $\tilde{f}(\eta) = \sum_{k=0}^{N} F(k)\eta^k$ and $\tilde{\theta}(\eta) = \sum_{k=0}^{N} \Theta(k)\eta^k$, where, $F(k), \Theta(k)$ are the k^{th} differential transforms of $f(\eta), \theta(\eta)$ at the point $\eta_0 = 0$. The boundary conditions for $\tilde{f}$ and $\tilde{\theta}$ defined in 6.15 and 6.16 are given as,

$$\tilde{f}''(0) = 0, \tilde{f}(0) = 0, \tilde{\theta}'(0) = 0, \tag{6.26}$$

$$\tilde{f}'(1) = 0, \tilde{f}(1) = 1, \tilde{\theta}(1) = 1. \tag{6.27}$$

The k^{th} differential transforms of $f(\eta)$ and $\theta(\eta)$ satisfying the governing equations 6.13, 6.14 at the point $\eta_0 = 0$ are obtained using the above identities listed in Table

6.1 as follows,

$$
\begin{aligned}
F(l+4) \;=\; & \Bigg\{ \Big(SA_1(1-\phi)^{2.5} \Big) \\
& \Bigg(3(l+1)(l+2)F(l+2) + \\
& \sum_{j=0}^{l} \Delta(l-j-1)(j+1)(j+2) \\
& (j+3)F(j+3) \;+\; \sum_{j=0}^{l}(j+1)(j+2) \\
& (l-j+1)F(j+2)F(l-j+1) \\
& -\sum_{j=0}^{l}(j+1)(j+2)(j+3) \\
& F(l-j)F(j+3) \Bigg) \;+ \\
& +\; M^2(l+1)(l+2)F(l+2) \Bigg\} \\
& \Big/ \Big((l+1)(l+2)(l+3)(l+4) \Big), \qquad (6.28)
\end{aligned}
$$

$$
\begin{aligned}
\Theta(l+2) \;=\; & -\Bigg\{ Pr \;\; S \;\; (\frac{A_2}{A_3}) \\
& \sum_{j=0}^{l} \Bigg((j+1)\Theta(j+1) \\
& F(l-j) \\
& -\; (j+1)\Delta(l-j-1)\Theta(j+1) \Bigg) + \\
& \frac{PrEc}{A_3(1-\phi)^{2.5}} \times \\
& \Bigg(\sum_{j=0}^{k} (j+1)(j+2)(l-j+1) \\
& (l-j+2)F(j+2)F(l-j+2) \\
& +\; \sum_{j=0}^{k} (4\delta^2 + M^2)(j+1)(l-j+1) \\
& F(j+1)F(l-j+1) \Bigg) \Bigg\} \\
& \Big/ \Big((1+\frac{4R}{3})(l+1)(l+2) \Big),
\end{aligned}
\tag{6.29}
$$

where $l \geq 0$, $\Delta(n)$ is defined as,

$$
\Delta(n) = \begin{cases} 1 & \text{if } \; n = 0 \\ 0 & \text{otherwise.} \end{cases}
$$

We need the following values of $F(0), F(1), F(2), F(3), \Theta(0), \Theta(1)$ to calculate all the values of $F(l)$ and $\Theta(l) \;\; \forall \;\; l \geq 0$ by the above recurrence relation. From the equation 6.26 and 6.27 we have the following initial values,

$$
\begin{aligned}
F(0) = 0, F(1) = p, F(2) = 0, F(3) = q, \\
\Theta(0) = r, \Theta(1) = 0.
\end{aligned}
\tag{6.30}
$$

In equation 6.30, the constants p, q, r are missing initial conditions, which can be determined from the boundary conditions 6.26, 6.27 and the equations 6.28 and 6.29.

Thus, we have,

$$\begin{aligned}
&F(0)=0, F(1)=p, F(2)=0, F(3)=q,\\
&F(4)=0,\\
&F(5)=\frac{1}{120}\Big(6qM^2+24A_1qS(1-\phi)^{2.5}\Big),\cdots\\
&\Theta(0)=r, \Theta(1)=0, \Theta(2)=0, \Theta(3)=0,\\
&\Theta(4)=\Bigg(-\frac{A_2\cdot Pr\cdot S\Big(\frac{p^2EcPr(M^2+4\delta^2)}{A_3(1+\frac{4R}{3}(1-\phi)^{2.5})}-\frac{p^3EcPr(M^2+4\delta^2)}{A_3(1+\frac{4R}{3}(1-\phi)^{2.5})}\Big)}{A_3}\\
&-\frac{Ec\cdot Pr\Big(36q^2+6pq(M^2+4\delta^2)\Big)}{A_3(1-\phi)^{2.5}}\Bigg)\Bigg/12\Big(1+\frac{4R}{3}\Big)+\cdots
\end{aligned} \tag{6.31}$$

Using these values, the closed form solutions for f and θ are obtained as follows

$$\begin{aligned}
&\tilde{f}(\eta)=p\eta+q\eta^3+\frac{1}{120}\eta^5\Big(6qM^2+24A_1qS(1-\phi)^{2.5}\Big)+\\
&\frac{1}{840}\eta^7\Big(\frac{1}{6}M^2(6qM^2+24A_1qS(1-\phi)^{2.5})+\\
&A_1\cdot S\cdot\Big(12q^2+6qM^2-\cdots
\end{aligned} \tag{6.32}$$

$$\begin{aligned}
\tilde{\theta}(\eta)=r+\eta^4\Bigg(&-\frac{A_2\cdot Pr\cdot S\Big(\frac{a_1^2EcPr(M^2+4\delta^2)}{A_3(1+\frac{4R}{3}(1-\phi)^{2.5})}-\frac{p^3EcPr(M^2+4\delta^2)}{A_3(1+\frac{4R}{3}(1-\phi)^{2.5})}\Big)}{A_3}\\
&-\frac{Ec\cdot Pr\Big(36q^2+6pq(M^2+4\delta^2)\Big)}{A_3(1-\phi)^{2.5}}\Bigg)\Bigg/12\Big(1+\frac{4R}{3}\Big)+\cdots
\end{aligned} \tag{6.33}$$

The boundary conditions in 6.26 and 6.27 give the values for p, q, r for a particular choice of P. By substituting the values for p, q, r in the equations 6.32 and 6.33 we obtain the approximate solutions for $f(\eta)$ and $\theta(\eta)$. For particular values, $P = 20, Pr = 6.2, Ec = 0.05, M = 1, R = 0, S = 0.5, \delta = 0.1, \phi = 0.08$, the following expressions are estimated:

$$\begin{aligned}
&\tilde{f}(\eta)=1.42732\eta-0.358219\eta^3-0.0655093\eta^5\\
&-0.00360124\eta^7-\cdots,
\end{aligned} \tag{6.34}$$

$$\begin{aligned}
&\tilde{\theta}(\eta)=1.18577-0.0123521\eta^2+0.111469\eta^4\\
&-0.042305\eta^6-\cdots,
\end{aligned} \tag{6.35}$$

which are obviously converging series and the proof of their convergence analysis is presented in the next section.

6.4.1 Convergence of the DTM method

In this section, we show that the obtained solutions $\sum_{k=0}^{\infty} F(k)\eta^k$ and $\sum_{k=0}^{\infty} \Theta(k)\eta^k$ that we have obtained using the DTM method above are well defined. We have been able to show that the radius of convergence of these two series is 1 and it gives us the analytic solutions for the equations 6.13 and 6.14 along with the boundary conditions 6.15 and 6.16.

Theorem 1 *The series* $\tilde{f}(\eta) = \sum_{k=0}^{\infty} F(k)\eta^k$ *has the radius of convergence* ≥ 1.

Proof 1 *We will show that* $|F(k)| \leq 1 \quad \forall \quad k \geq 2$. *We want to prove this theorem inductively. Let the statement be true for* $2 \leq i \leq K$, *where* K *is any positive integer. Then we would show that the result is true for* $K+1$. *By using Mathematica, we compute that* $|F(i)| \leq 1 \quad \forall \quad 2 \leq i \leq 25$. *Therefore, we need to prove the following,*

Theorem 2 *If* $|F(i)| \leq 1 \; \forall \; 2 \leq i \leq K$ *and* $F(1) = 1.42732$, *where* $K \geq 25$ *then* $F(K+1) \leq 1$.

From the equation 6.28 we find

$$\begin{aligned} F(l+4) \;=\; & \Bigg\{ \Big(SA_1(1-\phi)^{2.5} \Big) \Bigg(3(l+1)(l+2)F(l+2) \\ & + l(l+1)(l+2)F(l+2) \sum_{j=1}^{k} (j+1)(j+2) \\ & (l-2j+1)F(j+2)F(l-j+1) \Bigg) \\ & + M^2(l+1)(l+2)F(l+2) \Bigg\} \\ & \Big/ \Big((l+1)(l+2)(l+3)(l+4) \Big), \end{aligned} \tag{6.36}$$

where, $l \geq 0$.
Therefore, we have,

$$\begin{aligned} |F(l+4)| &\leq |S \; A_1 \; (1-\phi)^{2.5}| \Big(\frac{3}{(l+3)(l+4)} + \frac{1}{l+4} + \sum_{j=0}^{l-1} \frac{(j+1)(j+2)}{(l+2)(l+3)(l+4)} \\ &\quad + \frac{|F(1)|}{l+4} \Big) + \frac{M^2}{(l+3)(l+4)} \\ &< |S \; A_1 \; (1-\phi)^{2.5}| \Big(\frac{3}{400} + \frac{1}{20} + \frac{1.5}{20} + \sum_{j=0}^{l-1} \frac{(j+1)(j+2)}{(l+2)(l+3)(l+4)} \Big) + \frac{M^2}{400}. \end{aligned}$$

$$(As \quad l \geq 20, \;\; F(1) = 1.42732)$$

We note that,

$$\sum_{t=0}^{l-1}(t+1)(t+2) = \sum_{t=0}^{l-1}(t^2+3t+2) = 2l + \frac{3l(l-1)}{2} + \frac{(l-1)l(2l-1)}{6}.$$

Therefore,

$$\frac{\sum_{j=0}^{l-1}(j+1)(j+2)}{(l+2)(l+3)(l+4)} \leq \frac{2}{400} + \frac{1}{16} + \frac{1}{6}\Big(\frac{(1-\frac{1}{l})(2-\frac{1}{l})}{(1+\frac{2}{l})(1+\frac{3}{l})(1+\frac{4}{l})}\Big)$$

$$< 0.07 + \frac{1}{3} = 0.74.$$

In our problem, $0.02 \leq \phi \leq 0.08, S = 0.5, M \leq 10$. *We find that,* $0.55 \leq |S \;\; A_1 \;\; (1-\phi)^{2.5}| \leq 0.66$.
Finally, we find

$$|F(l+4)| \leq 0.66(0.1325 + .74) + 0.25 \leq 0.58 + 0.25 = 0.84.$$

$$|F(l+4)|^{\frac{1}{l+4}} \leq 1 \quad \forall l \quad \geq 2.$$

$$\lim_{l\to\infty} |F(l)|^{\frac{1}{l}} \leq 1.$$

$$\implies \frac{1}{R} \leq 1,$$

where, radius of convergence is denoted by R.

Theorem 3 *The series* $\tilde{\theta}(\eta) = \sum_{k=0}^{\infty}\Theta(k)\eta^k$ *has the radius of convergence* ≥ 1.

Proof 2 *We will show that* $|\Theta(k)| \leq k^4 \;\; \forall \;\; k \geq 2$. *We want to prove this theorem inductively. Let the statement be true for* $2 \leq i \leq K$. *Then we would show that the result is true for* $K+1$. *By using Mathematica, we compute that* $|\Theta(i)| \leq 1 \;\; \forall \;\; 1 \leq i \leq 25$. *Therefore, we are required to prove the following,*

Theorem 4 *If* $|\Theta(i)| \leq i^4 \;\forall\; 1 \leq i \leq K$, *where* $K \geq 25$ *then* $|\Theta(K+1)| \leq (K+1)^4$.

From the equation 6.29 and using the Theorem 1, we find,

$$|\Theta(l+2)| \leq \Bigg\{ \Big|Pr \;\; S \;\; (\frac{A_2}{A_3})\Big| \sum_{j=0}^{l-1}(j+1)|\Theta(j+1)|$$

$$+ \left| \frac{PrEc}{A_3(1-\phi)^{2.5}} \right| \Bigg(\sum_{j=0}^{l}(j+1)(j+2)$$

$$(l-j+1)(l-j+2)F(j+2)F(l-j+2)$$

$$+\sum_{j=0}^{l}(4\delta^2+M^2)(j+1)(l-j+1)F(j+1)F(l-j+1)\Big)\Big|\Big\}$$
$$\Big/\Big((1+\frac{4R}{3})(l+1)(l+2)\Big),$$

where, $k \geq 0$.
By using the result proved in Theorem 1 that is $F(j) \leq 1 \ \ \forall \ \ j \geq 2$, *We note that,*

$$\Big|\frac{PrEc}{A_3(1-\phi)^{2.5}}\Big(\sum_{j=0}^{l}(j+1)(j+2)(l-j+1)(l-j+2)F(j+2)F(l-j+2)$$
$$+\sum_{j=0}^{l}(4\delta^2+M^2)(j+1)(l-j+1)F(j+1)F(l-j+1)\Big)\Big|$$
$$\Big/\Big((1+\frac{4R}{3})(l+1)(l+2)\Big)\leq$$
$$\Big|\frac{PrEc}{A_3(1-\phi)^{2.5}}\Big|\Big(\sum_{j=0}^{l}(j+1)(j+2)+(4\delta^2+M^2)l\Big).$$

In our problem, $\delta = 0.1, M \leq 10$ *and* $\Big|\frac{PrEc}{A_3(1-\phi)^{2.5}}\Big| \leq 0.4$ *for the different possible choices of the values of* ϕ. *Now, we have,*

$$\Big|\frac{PrEc}{A_3(1-\phi)^{2.5}}\Big|\Big(\sum_{j=0}^{l}(j+1)(j+2)+(4\delta^2+M^2)l\Big)$$
$$\leq\sum_{j=0}^{l}(j+1)(j+2)+(4\delta^2+M^2)l$$
$$\leq\sum_{j=0}^{l}(j^2+3j+2)+(4\delta^2+M^2)l=\frac{l^3}{3}+2l^2+\frac{11}{3}l+(4\delta^2+M^2)l$$
$$\leq\frac{l^3}{3}+\frac{l^3}{10}+\frac{l^3}{100}+\frac{l^3}{25}.$$
$$(As,\ l\geq 24)$$

Therefore, by using the induction hypothesis we obtain,

$$|\Theta(l+2)|\leq\Big|Pr\ \ S\ \ (\frac{A_2}{A_3})\Big|\sum_{j=0}^{l-1}(j+1)^5\Big/\Big((1+\frac{4R}{3})(l+1)(l+2)\Big)$$

$$+\frac{l^3}{3}+\frac{l^3}{10}+\frac{l^3}{100}+\frac{l^3}{25}$$

$$=\left|Pr\ S\ (\frac{A_2}{A_3})\right|\sum_{j=1}^{l} j^5 \Big/ \Big((1+\frac{4R}{3})(l+1)(l+2)\Big)+\frac{l^3}{3}+\frac{l^3}{10}+\frac{l^3}{100}+\frac{l^3}{25}.$$

In our case, $\left|Pr\ S\ (\frac{A_2}{A_3})\right| \leq 3.$
Therefore, we obtain,

$$|\Theta(l+2)| \leq 3\frac{\sum_{j=0}^{l} j^4}{(l+2)}+\frac{l^3}{3}+\frac{l^3}{10}+\frac{l^3}{100}+\frac{l^3}{25}$$

$$=3\frac{l(l+1)(2l+1)(3l^2+3l-1)}{30(l+2)}+\frac{l^3}{3}+\frac{l^3}{10}+\frac{l^3}{100}+\frac{l^3}{25}$$

$$\leq l\frac{(2l+1)(3l^2+3l-1)}{10}+\frac{l^3}{3}+\frac{l^3}{10}+\frac{l^3}{100}+\frac{l^3}{25}$$

$$=l\frac{6l^3+9l^2+l-1}{10}+\frac{l^3}{3}+\frac{l^3}{10}+\frac{l^3}{100}+\frac{l^3}{25}$$

$$\leq \frac{3l^4}{5}+\frac{9l^3}{10}+\frac{l^2}{10}+\frac{l^3}{3}+\frac{l^3}{10}+\frac{l^3}{100}+\frac{l^3}{25}$$

$$\leq \frac{3l^4}{5}+\frac{9l^4}{210}+\frac{l^4}{4000}+\frac{l^4}{63}+\frac{l^4}{200}+\frac{l^4}{2000}+\frac{l^4}{500} \quad (as\ l\ \geq 24)$$

$$\leq \frac{3l^4}{5}+\frac{l^4}{20}+\frac{l^4}{4000}+\frac{l^4}{60}+\frac{l^4}{200}+\frac{l^4}{2000}+\frac{l^4}{500} \leq l^4.$$

We have proved that,

$$|\Theta(l)| \leq l^4$$

$$\Rightarrow |\Theta(l)|^{\frac{1}{l}} \leq (l^{\frac{1}{l}})^4 \quad \forall l \geq 0$$

Using the result,

$$\lim_{l\to\infty} l^{\frac{1}{l}} = 1.$$

This concludes our theorem.

6.5 Discussion of Results

The study of entropy generation on magnetohydrodynamic flow of nanoparticles in a squeeze channel via DTM has been the objective of this chapter. The numerical estimation corresponding to analytical approximations 6.32 and 6.33 for velocity and temperature fields have been made based on the following values or range of values of the dimensionless parameters:
$Pr = 6.2,\ Ec = 0.05,\ M = [0, 10],\ R = [0, 2],\ \phi = [0, 0.08],\ S = [-0.5, 0.5],\ \delta = 0.1.$

In order to validate our analytical approximate solutions, we have compared the numerical results for Nusselt number $-\theta'(1)$ at the channel wall with the results of Acharya et al. [2016], Mustafa et al. [2012] and Pourmehran et al. [2015] as shown in Table 6.2.

It is found that an increase in one of Pr or Ec, the value of $-\theta'(1)$ increases gradually when the other parameters are kept fixed. This increasing variation is also observed by the previous investigations as available in the scientific literature.

6.5.1 Velocity variation

Figures 6.2 and 6.3 show how the different values of the magnetic parameter M and the squeezing parameter S affect the change in the axial velocity in the 'y' direction. Figure 6.2 shows that the velocity component decreases with the increase of the magnetic parameter up to a certain height and then follows the opposite trend. It happens because of the presence of the resistive Lorentz force during the application of Cu-water nanofluid. This force reduces the fluid motion inside the channel and the opposite trend justifies the continuity equation. Figure 6.3 describes the variation in axial velocity for different squeezing parameter S. If the squeezing parameter S is increased, then the velocity at the central region decreases, while the opposite trend is seen near the channel wall. These results have potential applications in the injection modeling, polymer processing etc.

6.5.2 Temperature variation

Figures 6.4-6.7 describe the temperature distribution for different values of the magnetic parameter M, thermal radiation parameter R, the nanoparticle volume fraction ϕ and the squeezing parameter S affect the thermal profiles inside the squeeze channel. Figure 6.4 shows that the thermal response increases with an increase in the magnetic parameter M. This enhancement of temperature lies in the Lorentz force that intensify the forced convection. The heat transfer rate increases with increasing the nanoparticles size. An increase in the thermal radiation parameter R decreases the temperature as shown in Figure 6.5. Figure 6.7 depicts that with an increase in the squeeze parameter diminishes the temperature distribution. The temperature profiles are not affected significantly with the nanoparticle volume fraction, but the temperature decreases slowly as shown in Fig. 6.6. We have checked that in the absence of thermal radiation ($R = 0$), the temperature increases slowly with the nanoparticle volume fraction, while the Fig. 6.5 shows that an increase in R decreases the temperature. This happens due to the amount of heat radiated from the squeeze channel.

6.5.3 The study of Skin-friction and Nusselt number

In the present article, we have studied how skin-friction coefficient (C_f) and the Nusselt number (Nu) are influenced by the effect of different physical parameters. The expressions for these non-dimensional numbers are given in equations 6.17-6.18. Figure 6.8 depicts the local skin-friction $C_f = \frac{2f''(1)}{S\delta A_1(1-\phi)^{2.5}}$ in terms of the magnetic field strength M for varying values of ϕ. With the increasing values of M, skin-friction coefficient C_f decreases. However, C_f increases with the nanoparticle volume fraction ϕ. Figure 6.9 gives the Nusselt number $Nu_r = -A_3\theta'(1)$ in terms of the radiation parameter for different values of ϕ. It is evident that the Nusselt number decreases with the increase in the radiation parameter R. Moreover, we observed that the Nu (Nusselt number) increases with an increase in ϕ. This shows that the addition of the small amount of nanoparticles in the fluid increases the convective heat transfer capacity of the nanofluid. Figure 6.10 shows that with a rise in the magnetic field strength the Nusselt number enhances significantly. Therefore, the presence of nanoparticles under a strong magnetic field increases the heat transfer capacity of the base fluid. Moreover, the present model provides the non-linear relation of Nusselt number with thermal radiation parameter R.

6.5.4 Study of entropy generation

Figures 6.11 to 6.13 reveal the comparative study of entropy generation due to the fluid friction N_{SFF} and entropy generation due to the thermal behavior N_{ST} for different values of the magnetic field strength M, thermal radiation parameter R and nanoparticle volume fraction ϕ. In all these cases, it is observed that the entropy generation due to frictional forces are higher as compared to the entropy generation due to the thermal response. Figure 6.11 shows that with an increase in the magnetic field strength the irreversible entropy generation due to friction increases. Figure 6.12 notice that N_{SFF} increases with the increase in the radiation parameter R. But, N_{ST} decreases with the increase in the radiation parameter R. This variation is significant near the channel wall. Figure 6.13 shows that the N_{SFF} and N_{ST} for different values of the volume fractions of the nanoparticle. The N_{SFF}, N_{ST} both increase significantly with a rise in the volume fraction of the nanoparticle. Figures 6.14 and 6.15 illustrate how the Bejan number is affected by different values of M and thermal radiation R. It is observed from Fig. 6.14 that the Bejan profiles are significantly affected by R. The Bejan number (Be) decreases gradually with R. As the thermal radiation takes place in a squeeze channel, the thermal irreversibility reduces. Fig. 6.15 gives the Bejan number profiles for different magnetic parameter M. The Bejan number increases with a rise in the magnetic field strength. The increase of Lorentz force tends to promote the enhancement of entropy generation. It is noticed from these two figures that the Bejan number is minimum at the central line of the channel and is maximum near the channel wall. However, in the presence of strong magnetic field the Bejan number has a strong influence within the squeeze channel.

6.6 Conclusion

This article examines the energy efficiency of the squeezing Cu-water nanofluid flow between two plates under the influence of an external magnetic field as well as the radiative heat flux. The physical sketch of the problem is presented in Figure 6.1. The effects of different physical parameters such as the magnetic field strength M, the thermal radiation parameter R, the squeeze parameter S and the nanoparticle volume fraction ϕ have been studied and illustrated them through the figures 6.2-6.15. The Nusselt number, Bejan number and the skin-friction coefficient have been analyzed. The DTM is used to solve the non-linear differential equations. The convergence criteria for DTM has been analyzed and observed that the series solutions for both velocity and temperature field have radius of convergence greater than or equal to 1. The important observations from the present study are summarized as follows:

- The velocity within the squeezing channel decreases with the increase of the applied magnetic parameter M and squeeze parameter S up to a certain height of the channel beyond which it increases.
- The temperature within the squeeze channel increases with the increase of the applied magnetic parameter and the reverse trend is seen for the radiation parameter as well as squeeze parameter.
- The coefficient of skin-friction increases with ϕ (nanoparticle volume fraction) and decreases with M (magnetic parameter).
- The Nusselt number (Nu) increases with a rise in M as well as the nanoparticle volume fraction (ϕ) and decreases with increasing R.
- The entropy generation by means of Bejan number (Be) increases with increasing the magnetic field strength M, while it decreases in R.
- The Bejan number is an increasing function of η for the lower values of M.
- N_{SFF} is much higher in comparison to the N_{ST} within the squeeze channel.
- N_{SFF} and N_{ST} increase with the increasing values of M.
- N_{SFF} increase with the increasing values of R and N_{ST} decreases with the thermal radiation parameter R.
- N_{SFF} and N_{ST} both increases significantly with the increase in ϕ.

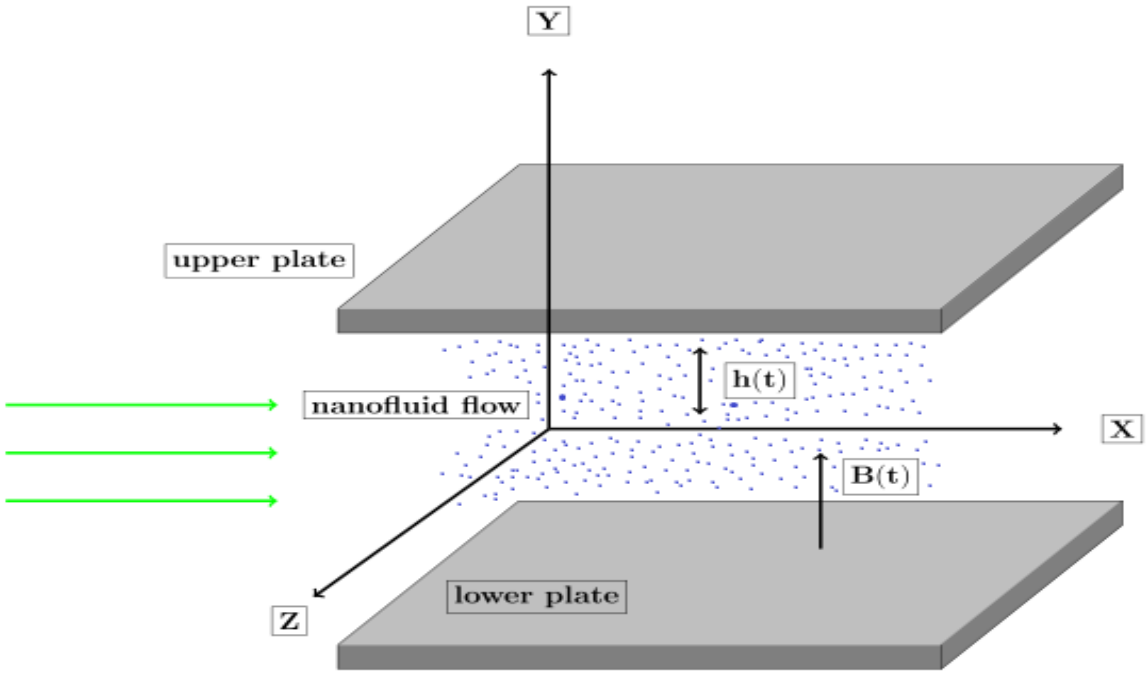

Figure 6.1: Physical sketch of the problem

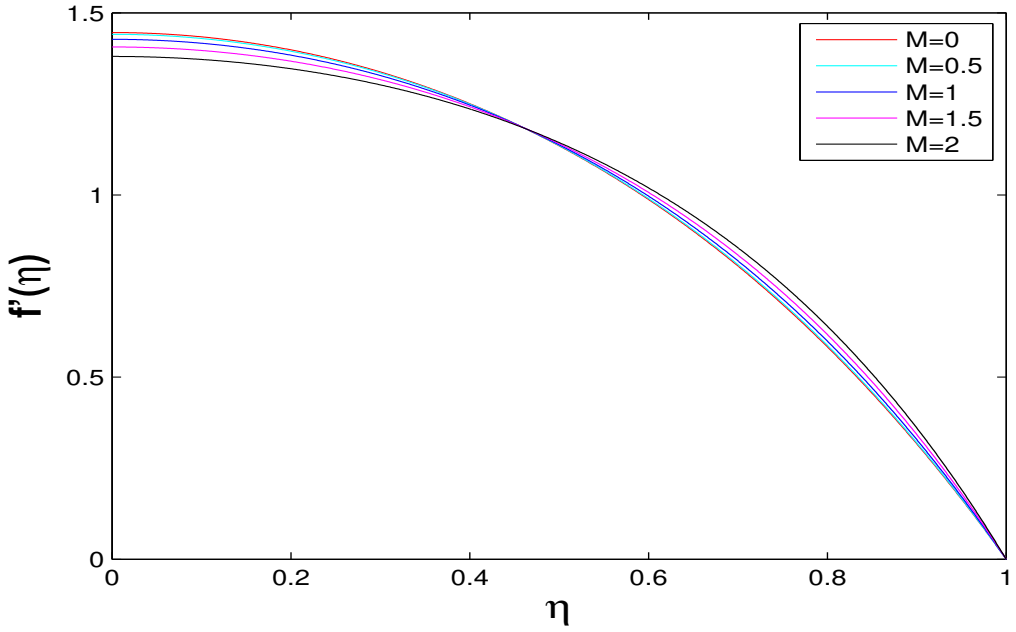

Figure 6.2: Velocity profiles for different values of M when $Pr = 6.2, Ec = 0.05, R = 1, S = 0.5, \delta = 0.1, \phi = 0.08$

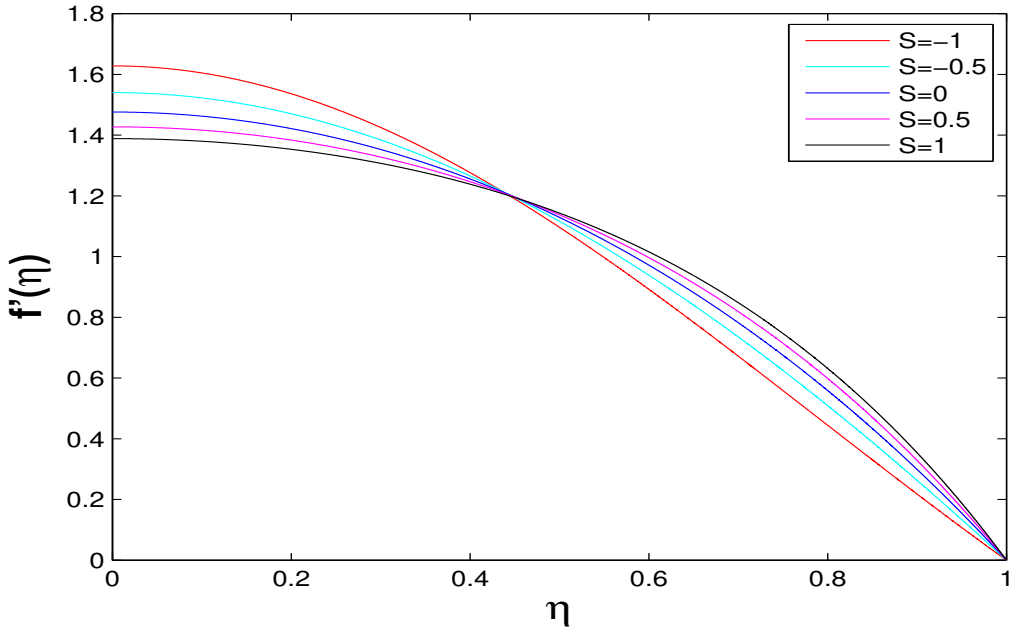

Figure 6.3: Velocity profiles for different values of S when $Pr = 6.2, Ec = 0.05, M = 1, R = 1, \delta = 0.1$

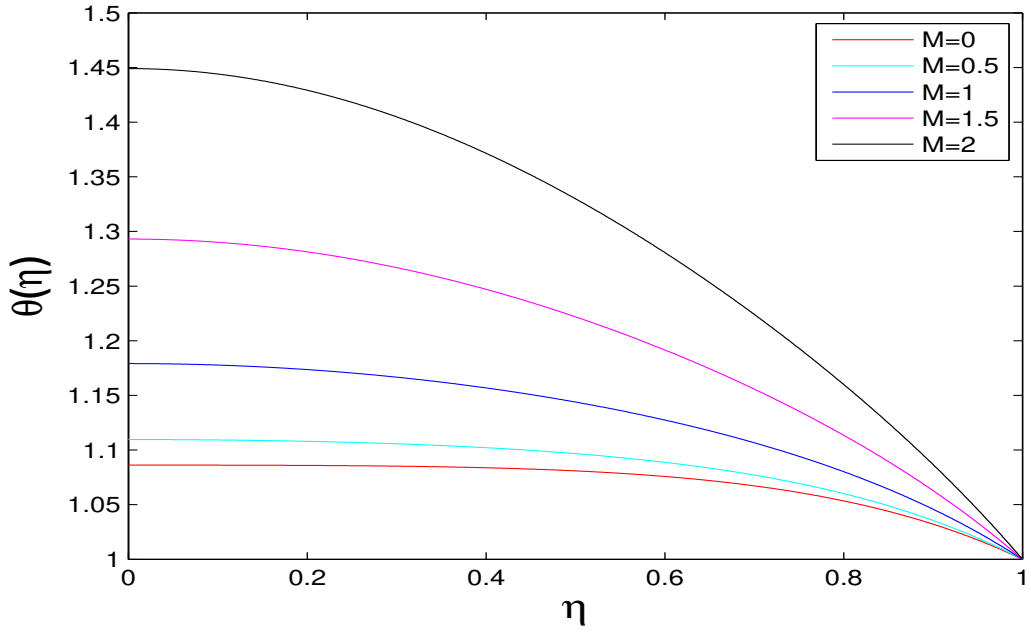

Figure 6.4: Temperature distribution for different values of M when $Pr = 6.2, Ec = 0.05, R = 1, S = 0.5, \delta = 0.1, \phi = 0.08$

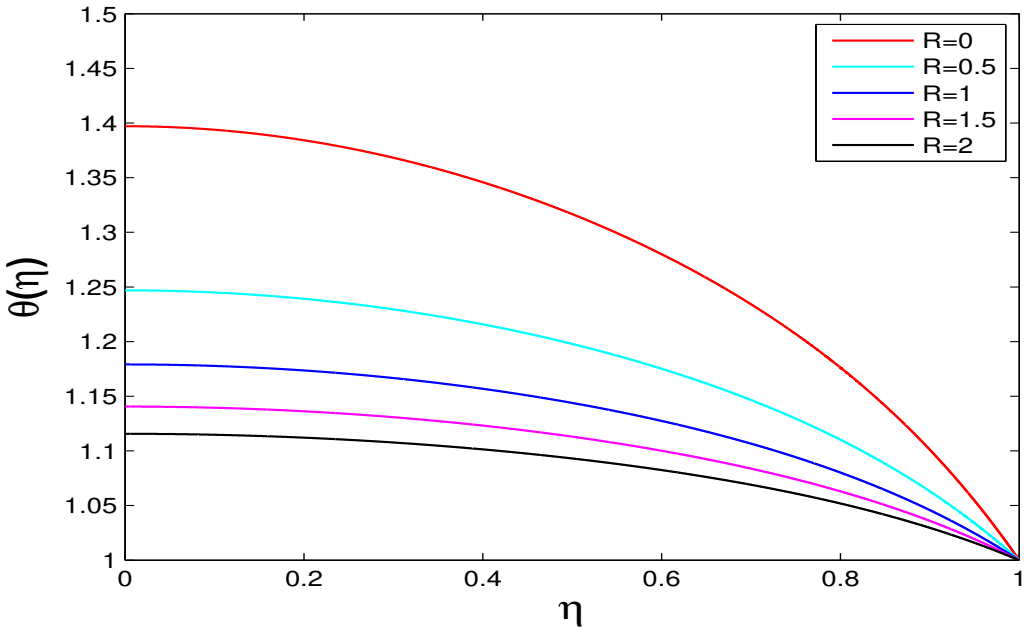

Figure 6.5: Temperature distribution for different values of R when $Pr = 6.2, Ec = 0.05, M = 1, S = 0.5, \delta = 0.1, \phi = 0.08$

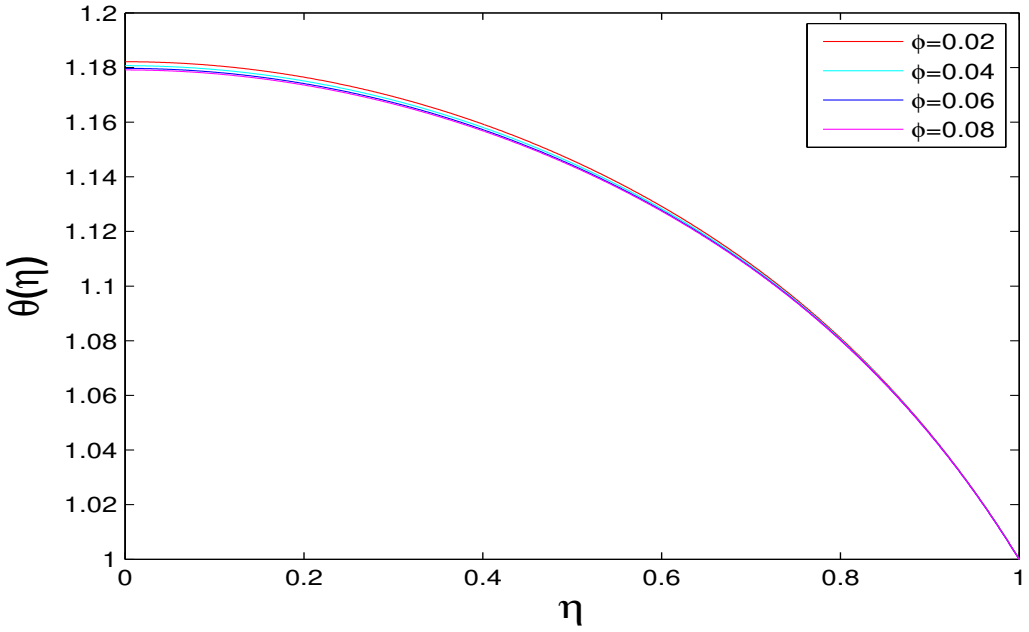

Figure 6.6: Temperature distribution for different values of ϕ when $Pr = 6.2, Ec = 0.05, M = 1, R = 1, S = 0.5, \delta = 0.1$

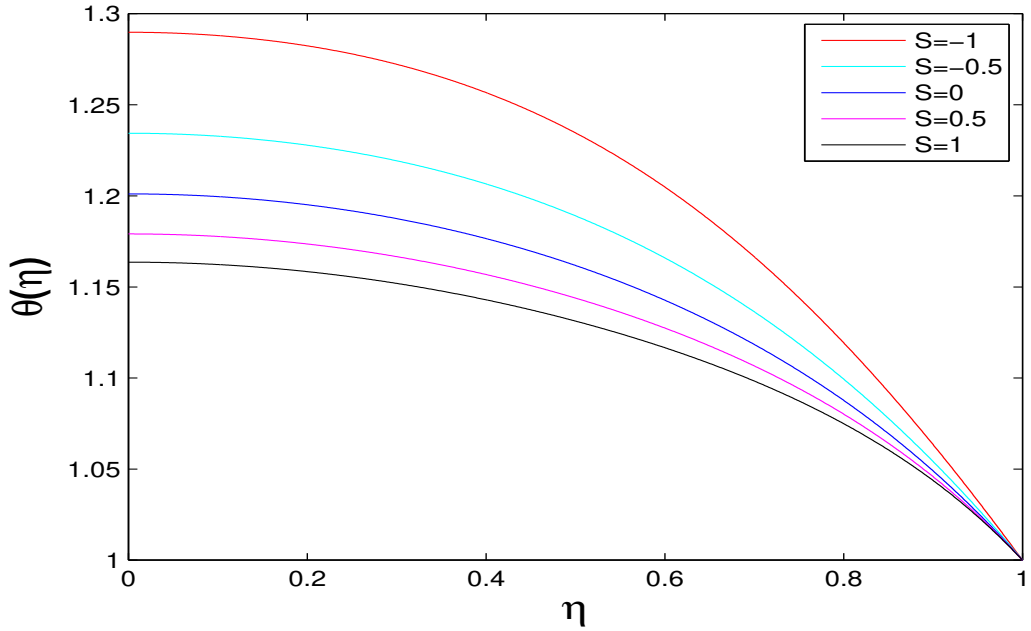

Figure 6.7: Temperature distribution for different values of S when $Pr = 6.2, Ec = 0.05, M = 1, R = 1, \delta = 0.1, \phi = 0.08$

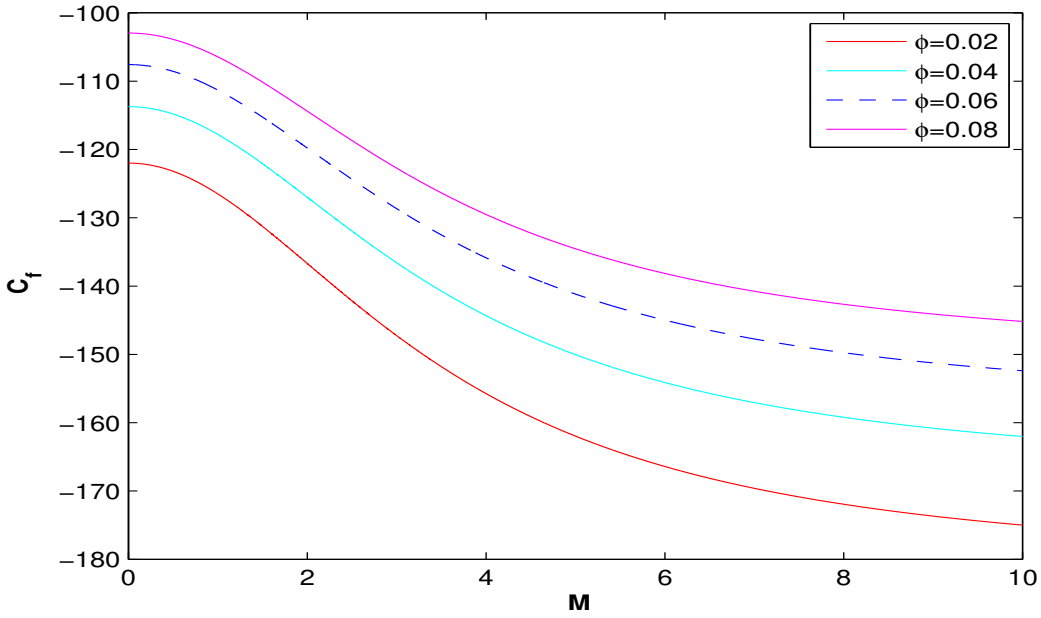

Figure 6.8: Variation of skin-friction coefficient às a function of M for different values of ϕ when $Pr = 6.2, Ec = 0.05, R = 1, S = 0.5, \delta = 0.1$

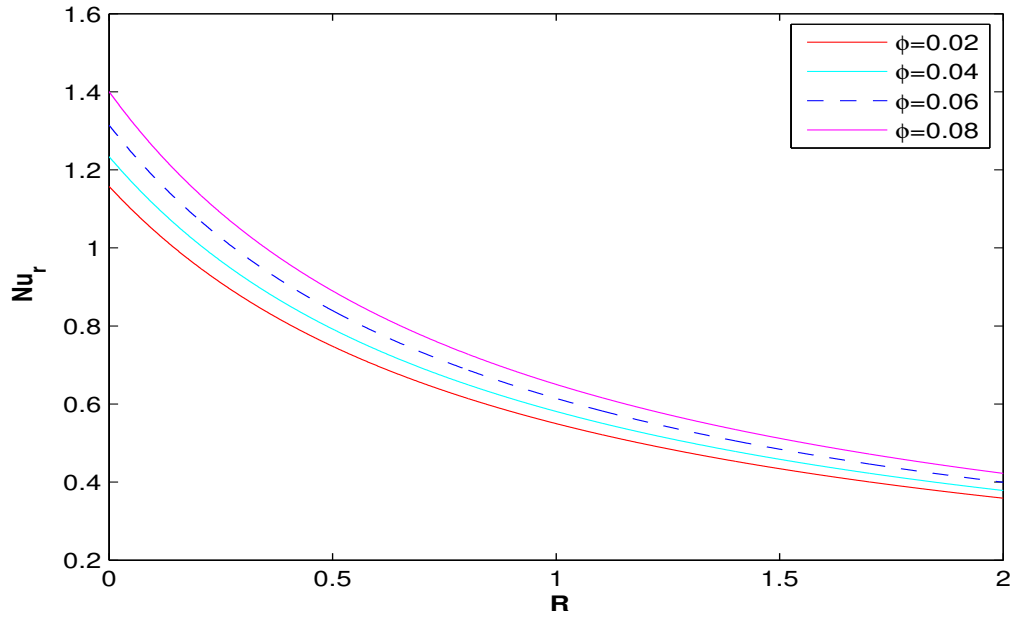

Figure 6.9: Variation of Nusselt number as a function of R for different values of ϕ when $Pr = 6.2, Ec = 0.05, M = 1, S = 0.5, \delta = 0.1$

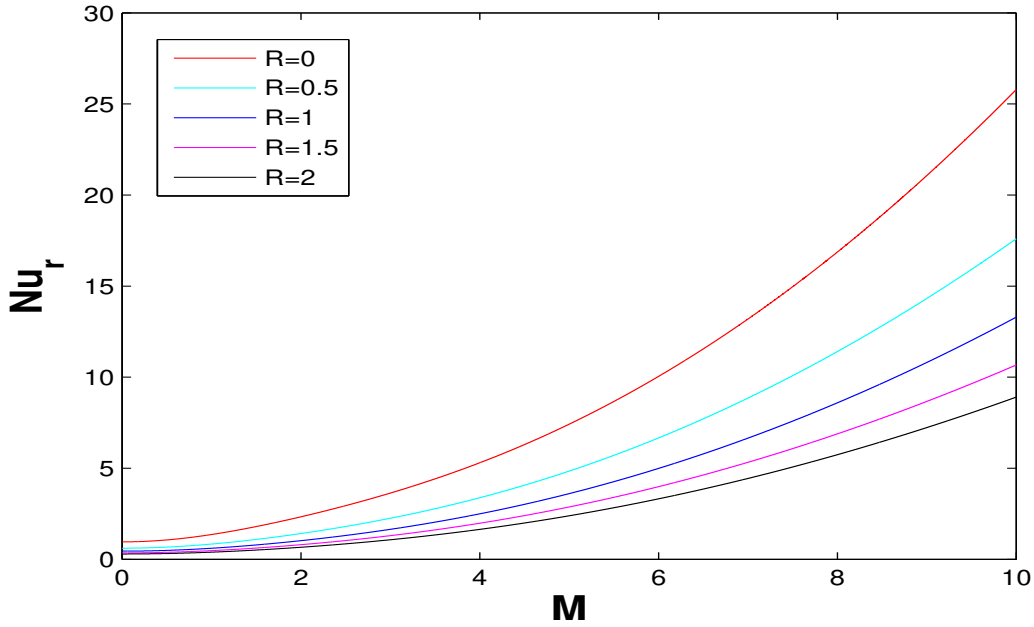

Figure 6.10: Variation of Nusselt number versus M for different values of R when $Pr = 6.2, Ec = 0.05, S = 0.5, \delta = 0.1, \phi = 0.08$

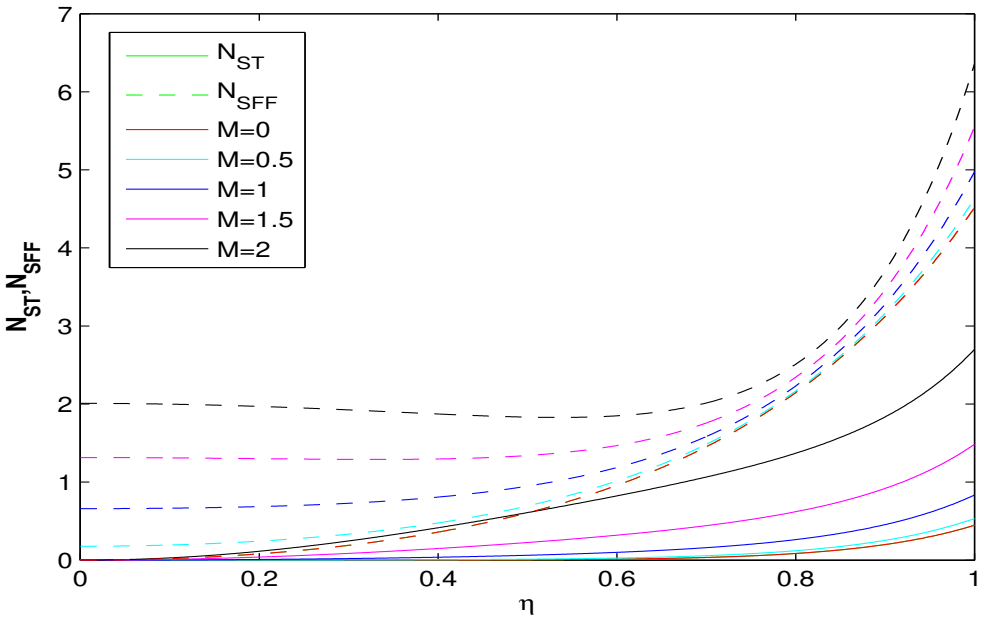

Figure 6.11: Variation of N_{ST} and N_{SFF} for different values of M when $Pr = 6.2, Ec = 0.05, R = 1, S = 0.5, \delta = .1, \phi = 0.08$

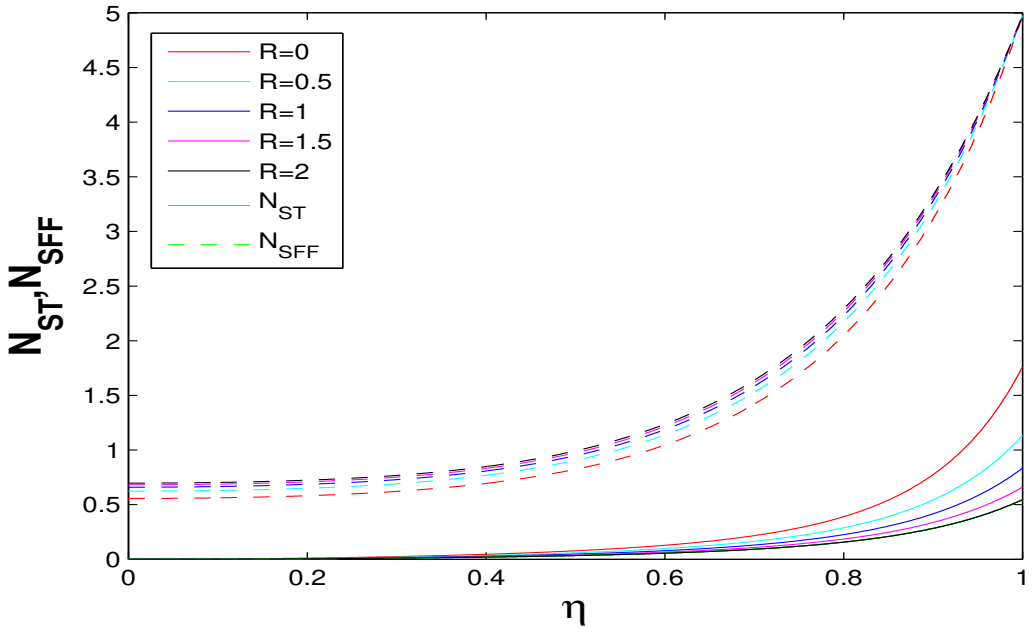

Figure 6.12: Variation of N_{ST} and N_{SFF} for different values of R when $Pr = 6.2, Ec = 0.05, M = 1, S = 0.5, \delta = 0.1, \phi = 0.08$

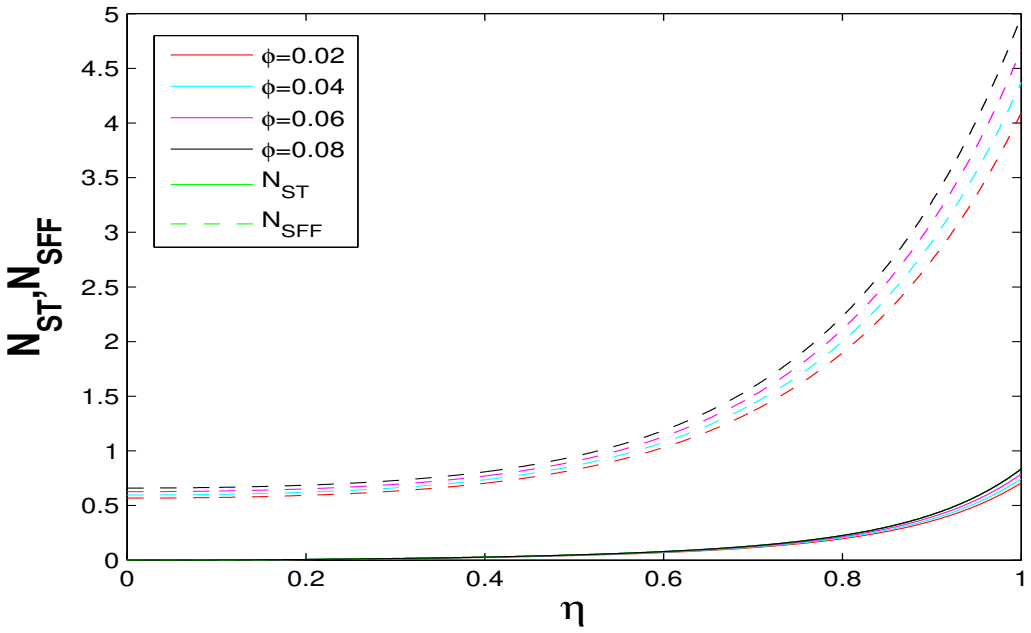

Figure 6.13: Variation of N_{ST} and N_{SFF} for different values of ϕ when $Pr = 6.2, Ec = 0.05, M = 1, R = 1, S = 0.5, \delta = 0.1$

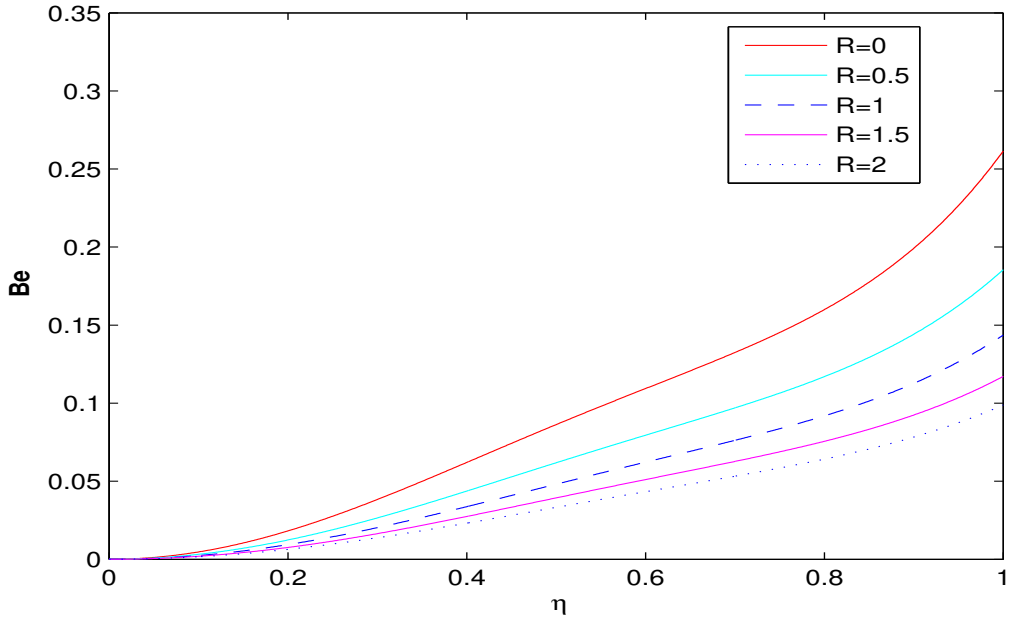

Figure 6.14: Bejan number profiles for different values of R when $Pr = 6.2, Ec = 0.05, M = 1, S = 0.5, \delta = 0.1, \phi = 0.08$

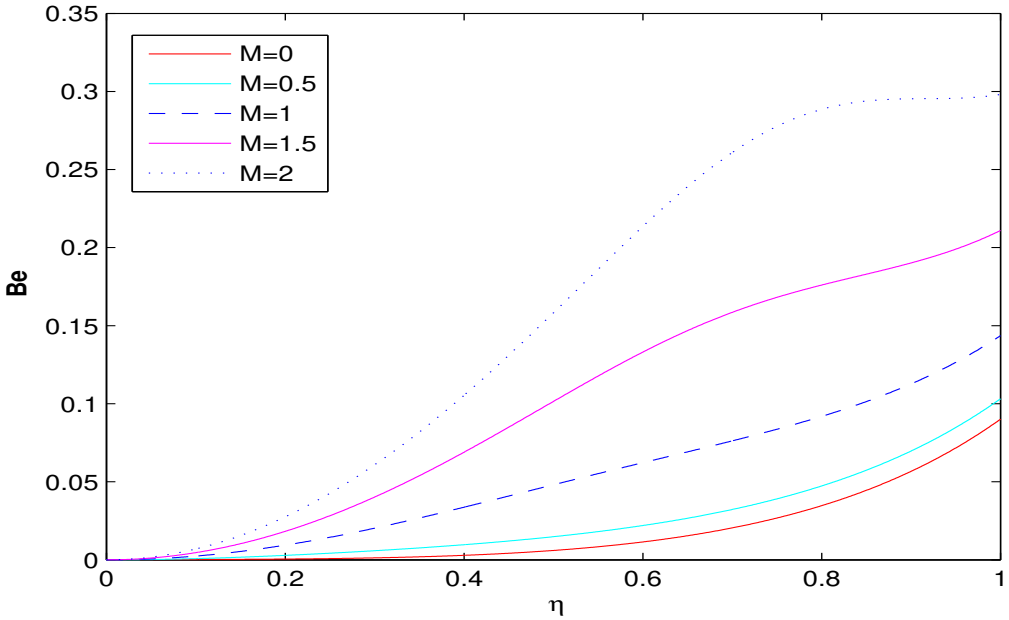

Figure 6.15: Bejan number profiles for different values of M when $Pr = 6.2, Ec = 0.05, R = 1, S = 0.5, \delta = 0.1, \phi = 0.08$

Table 6.2: Comparison table for the values of $-\theta^{'}(1)$ when $S = 0.5, \delta = 0.1, M = 0.0, \phi = 0.0, R = 0$

Pr	Ec	$-\theta^{'}(1)$ Mustafa et al.	$-\theta^{'}(1)$ Pourmehran et al.	$-\theta^{'}(1)$ Kundu et al.	$-\theta^{'}(1)$ Present Work
0.5	1.0	1.5222368	1.518859607	1.5222367498	1.52237
1.0	1.0	3.026324	3.019545607	3.026323559	3.02633
2.0	1.0	5.98053	5.967887511	5.980530398	5.98053
5.0	1.0	14.43941	14.41394678	14.43941324	14.4394
1.0	0.5	1.513162	1.509772834	1.513161807	1.51316
1.0	1.2	3.631588	3.623454726	3.631588269	3.6316
1.0	2.0	6.052647	6.039091204	6.052647108	6.05266
1.0	5.0	15.13162	15.09772808	15.13161784	15.1316

Chapter 7

Mathematical modelling of Graphene-PDMS Maxwell nanofluid flow over a stretching surface [6]

7.1 Introduction

Graphene-PDMS nanofluid has become an important topic of scientific research due to its high thermal and electrical conductivity. In order to prepare a highly conductive thermoplastic, the Graphene is often considered as a conductive filler and PDMS as a polymer (Zhang et al. [2008], Kong et al. [2014]). This study gets serious momentum after the findings of Boland et al. [2016], who showed that G-putty can be used to make extremely sensitive electrical sensor. Since then, the thermomechanical properties of Graphene-PDMS nanofluid has been widely studied by several researchers Wang et al. [2018]-Saharudin et al. [2019]. PDMS polymer shows highly viscoelastic properties thereby often considered to follow the Maxwell model as used by Lin et al. [2009] and several other researchers. Thus, the effects of viscoelastic properties under the influence of stretching surface on its thermomechanical properties are important to be explored. This chapter considers a low viscosity 1 cst PDMS as a base fluid. Choi and Eastman [1995], introduced the concept of nanofluid, experimentally verified that addition of a tiny percentage of highly thermally conductive nanoparticles into the base fluid enhances heat transfer capacity of the fluid. In this chapter, Graphene is used as nanoparticles. The problem of nanofluid flow over a stretching surface can describe the injection modeling, plastic extrusion process and loading related engineering models mathematically. A list of articles on the applications of nanofluid flow problem can be found in Angayarkanni and Philip [2015]-Seth et al. [2018].

The Homotopy Analysis Method, an analytic method which is also abbreviated

[6] The content of this chapter is submitted to *ZAMM* (Wiley)

as HAM, is applied to solve the non-linear differential equations arising from the governing equations that describe the nanofluid flow behaviour over a stretching surface. Liao [2010], first employed the idea of HAM, successfully used HAM for solving several non-linear differential equations. The HAM, a recursive analytical method, is used to obtain an approximate series solution with respect to a set of suitable basis functions for the corresponding linear and non-linear differential equations. Seth et al. [2018] applied an error minimization technique to find the convergence control parameter thereby conducting a regression analysis to study the heat-mass transfer coefficients. However, the traditional h-curve choice is implemented in this chapter. A list of articles on the applications of this method can be found in Zheng et al. [2013], Liao and Chwang [1998]. The irreversible loss of thermal energy in an engineering system, also termed as entropy generation, is investigated in this chapter with respect to different important physical regulatory parameters. It is important to minimize the entropy generation in any engineering process. The numerical ratio of the entropy generation due to thermal irreversibility to the total entropy generation (Herwig [2018], Bhatti et al. [2016]), termed as the Bejan number (Bejan and Kestin [1983], Bejan [1979]), is investigated in this chapter.

The review article by Mahian et al. [2013] on entropy generation presented many possible research directions along with a thorough literature survey which inspired us to conduct the present study. To the best of our knowledge the mathematical study of graphene-PDMS nanofluid flow, over a stretching surface embedded in a porous medium, in the presence of an external magnetic field, thermal radiation along with the volume fraction of the nanoparticles has not been conducted earlier. The study of entropy generation of graphene-PDMS nanofluid in the presence of Navier's slip boundary condition is novel. The square averaged error estimation for a particular h-value, selected from the convergence region as depicted in h-curve in Section 7.5, is also a novel attempt to address convergence. Our study bears potential applications in polymer processing, injection modeling and bio-engineering.

7.2 Mathematical description of the problem

This study investigates the viscous and incompressible graphene-PDMS (where PDMS is following the Maxwell viscoelastic fluid model) nanofluid flow over a stretching surface in the rectilinear coordinate system. The nanofluid lying over the surface is stretched in the x direction with a velocity $u_w(x,t) = \frac{ax}{1-\alpha t}$ and the y-axis denotes the normal direction to the surface. The unsteady stretching rate parameter $\alpha > 0$ determines how fast the surface is stretched, whereas, the negative values of α indicates the shrinking surface. The externally applied magnetic field of strength $B(t) = B_0(1-\alpha t)^{-\frac{1}{2}}$ is considered to be time dependent and directed towards the y axis. The nanofluid flow takes place in a porous medium with a medium permeability k_p. Moreover, the presence of Radiative heat flux as well as a non-uniform heat source/sink are considered in our system. The equations of flow and energy (Seth

et al. [2018], Zheng et al. [2013]) for Maxwell nanofluid flow under the above mentioned assumptions are expressed below,

$$\frac{\partial u}{\partial x}+\frac{\partial v}{\partial y}=0, \tag{7.1}$$

$$\begin{aligned}\rho_{nf}\left(\frac{\partial u}{\partial t}+u\frac{\partial u}{\partial x}+v\frac{\partial u}{\partial y}\right) &= -\frac{\partial p}{\partial x}-\rho_{nf}\lambda_1(v^2\frac{\partial^2 u}{\partial y^2}+2uv\frac{\partial^2 u}{\partial x\partial y})+\mu_{nf}\frac{\partial^2 u}{\partial y^2}\\ &\quad -\sigma B(t)^2 u-\frac{\mu_{nf}}{k_p}u,\end{aligned} \tag{7.2}$$

$$\frac{\partial p}{\partial y} = 0, \tag{7.3}$$

$$\begin{aligned}\frac{\partial T}{\partial t}+u\frac{\partial T}{\partial x}+v\frac{\partial T}{\partial y} &= \frac{k_{nf}}{(\rho C_p)_{nf}}\frac{\partial^2 T}{\partial y^2}+\frac{\sigma B^2(t)}{(\rho C_p)_{nf}}u^2-\frac{1}{(\rho C_p)_{nf}}\frac{\partial q_r}{\partial y}+\frac{\nu_{nf}}{(C_p)_{nf}}\left(\frac{\partial u}{\partial y}\right)^2\\ &\quad +\frac{\mu_{nf}}{(\rho C_p)_{nf}}\left(2\left\{\left(\frac{\partial u}{\partial x}\right)^2+\left(\frac{\partial v}{\partial y}\right)^2\right\}+\left(\frac{\partial u}{\partial y}+\frac{\partial v}{\partial x}\right)^2\right)+\\ &\quad \frac{q'''}{(\rho C_p)_{nf}}+\frac{\nu_{nf}}{k_p(C_p)_{nf}}u^2,\end{aligned} \tag{7.4}$$

where u, v denotes the velocity components in x and y directions respectively, T represents the temperature, λ_1 the relaxation time, p the fluid pressure, ρ_{nf} the nanofluid density, μ_{nf} the effective nanofluid dynamic viscosity, $(\rho C_p)_{nf}$ the effective nanofluid heat capacity, k_{nf} the effective nanofluid thermal conductivity, q_r the nanofluid radiative heat flux and σ the nanofluid electrical conductivity. The non uniform heat source/sink term q''' is taken as (Zheng et al. [2013]),

$$q''' = \frac{k_{nf}a}{\nu_{nf}(1-\alpha t)}(A(T_w-T_\infty)f'+B(T-T_\infty)), \tag{7.5}$$

where A denotes the spacial dependent part of source/sink and B denotes the temperature dependent part of heat source/sink. The radiative heat flux is calculated by using the Rosseland approximation,

$$q_r = -\frac{4\sigma_1}{3k_1}\frac{\partial T^4}{\partial y},$$

where, σ_1 denotes the Stefan-Boltzmann constant and k_1 the mean absorption coefficient. The radiative heat term is further reduced by using the Taylor's expansion of T^4,

$$T^4 \cong 4{T_\infty}^3 T-3{T_\infty}^4,$$

where T_∞ represents the ambient temperature of the nanofluid far away from the stretching surface. We finally obtain,

$$\frac{\partial q_r}{\partial y} = -\frac{16\sigma_1 {T_\infty}^3}{3k_1}\frac{\partial^2 T}{\partial y^2}. \tag{7.6}$$

The effective nanofluid properties are calculated based on the nanoparticle suspension model as described in the literature (MAXWELL [1873], Brinkman [1952]),

$$\rho_{nf} = (1-\phi)\rho_f + \phi\rho_s, \tag{7.7}$$

$$(\rho C_p)_{nf} = (1-\phi)(\rho C_p)_f + \phi(\rho C_p)_s, \tag{7.8}$$

$$\mu_{nf} = \frac{\mu_f}{(1-\phi)^{2.5}}, \tag{7.9}$$

$$\frac{k_{nf}}{k_f} = \frac{k_s + 2k_f - 2\phi(k_f - k_s)}{k_s + 2k_f + \phi(k_f - k_s)}, \tag{7.10}$$

where, ϕ represents the nanoparticle volume fraction, k_s the thermal conductivity of Graphene, k_f the thermal conductivity of PDMS.
The following set of boundary conditions are considered for the study,

$$u = \frac{ax}{1-\alpha t} + N\sqrt{1-\alpha t}\frac{\partial u}{\partial y},\ v = -\sqrt{\frac{\nu_f a}{1-\alpha t}}S, \tag{7.11}$$

$$-k_{nf}\frac{\partial T}{\partial y} = h_f(T_w - T)\ \ at\ \ y = 0,\ u \to 0,\ T \to T_\infty\ \ at\ \ y \to \infty. \tag{7.12}$$

We have used the following set of similarity transformations (Zheng et al. [2013]) to make the governing equations dimensionless:

$$\eta = \sqrt{\frac{a}{\nu_f(1-\alpha t)}}y,\ u = \frac{ax}{1-\alpha t}f'(\eta),\ v = -\sqrt{\frac{\nu_f a}{1-\alpha t}}f(\eta),\ \theta = \frac{T - T_\infty}{T_w - T_\infty}. \tag{7.13}$$

After eliminating the pressure term from the equations 7.2, based on the assumption of $u_\infty \to 0$ we obtain $\frac{\partial p}{\partial x} = 0$, along with applying the relations 7.13 to the equations 7.2, 7.4, we obtain the following non-linear ODEs,

$$f''' - (M+K)f' + A_1(1-\phi)^{2.5}\Big[ff'' - f'^2 - \lambda(f' + \frac{\eta}{2}f'') + De(2ff'f'' - f^2 f''')\Big] = 0, \tag{7.14}$$

$$\frac{1}{Pr}\left(1 + \frac{4R}{3}\right)\theta'' + \frac{A_2}{A_3}(f\theta' - \frac{\lambda\eta}{2}\theta') + \frac{Ec}{A_3(1-\phi)^{2.5}}(f''^2 + (M+K)f'^2) + \frac{A_1(1-\phi)^{2.5}}{Pr}(Af' + B\theta) = 0. \tag{7.15}$$

The boundary conditions 7.11, 7.12 are reduced to,

$$f^{'}(0) = 1 + \gamma f^{''}(0),\ f(0) = S,\ \theta^{'}(0) = -Bi\big(1 - \theta(0)\big), \tag{7.16}$$

$$f^{'}(\infty) = 0,\ \theta(\infty) = 0. \tag{7.17}$$

Here, $\lambda = \frac{\alpha}{a}$ denotes the stretching parameter, $A_1 = \frac{\rho_{nf}}{\rho_f}$, $A_2 = \frac{(\rho C_p)_{nf}}{(\rho C_p)_f}$, $A_3 = \frac{k_{nf}}{k_f}$, $Pr = \frac{\mu_f C_{p_f}}{\rho_f k_f}$ the Prandtl number, $Ec = \frac{(\frac{\alpha x}{1-\alpha t})^2}{C_{p_f}(T_w - T_\infty)}$ the Eckert number, $De = \frac{\alpha\lambda_1}{(1-\alpha t)}$ the Deborah number, $M = \frac{\nu_f \sigma B_0^2}{a\mu_{nf}}$ the magnetic number, $K = \frac{\nu_f(1-\alpha t)}{ak_p}$ the porous permeability parameter, $R = \frac{4\sigma_1 T_\infty^3}{k_1 k_{nf}}$ the thermal radiation parameter, $Re_x = \frac{\rho_f u_w x}{\mu_f}$ the local Reynolds number, $\gamma = N\sqrt{\frac{a}{\nu_f}}$ the slip parameter, $Bi = \frac{h_f}{k_{nf}}\sqrt{\frac{\nu_f(1-\alpha t)}{a}}$ the Biot number and $\delta = \frac{T_\infty}{T_w - T_\infty}$.

The expressions for the coefficient of skin-friction C_f and the Nusselt number Nu are given by,

$$C_f = \frac{\mu_{nf}(\frac{\partial u}{\partial y})_{y=0}}{\frac{1}{2}\rho_{nf}u_w^2} = \frac{2f^{''}(0)}{\sqrt{Re_x}A_1(1-\phi)^{2.5}},$$

$$Nu = \frac{-xk_{nf}(\frac{\partial T}{\partial y})_{y=0}}{k_f(T_w - T_\infty)} = \frac{\sqrt{Re_x}Nu_r}{\sqrt{1-\alpha t}},\quad \text{where, } Nu_r = -A_3\theta^{'}(0). \tag{7.18}$$

7.3 Entropy Generation

The study of irreversible heat loss in a physical system is termed as the entropy generation. This study is essential to investigate the present model as the irreversible heat loss due to heat transfer, thermal radiation and frictional heat generation are considerably high in our system. This quantitative study indicates the significant regulatory parameters that enhances entropy generation thereby such controlling parameters increase the energy efficiency of the system. The entropy generation rate per unit volume is presented as (Seth et al. [2018]),

$$S_{Total} = \frac{k_{nf}}{T^2}\left[\Big(\frac{\partial T}{\partial y}\Big)^2 + \frac{16\sigma T_\infty^3}{3K_1 k_{nf}}\Big(\frac{\partial T}{\partial y}\Big)^2\right] + \frac{\mu_{nf}}{T}\Big(\frac{\partial u}{\partial y}\Big)^2 + \big(\frac{\sigma B^2}{T} + \frac{\mu_{nf}}{k_p T}\big)u^2. \tag{7.19}$$

The non-dimensionless form of the total entropy generation E_S is expressed as,

$$\begin{aligned} E_S &= \frac{\nu_f(1-\alpha t)}{ak_{nf}}S_{Total} = E_{ST} + E_{SFF} \\ &= \frac{1}{(\theta+\delta)^2}(1 + \frac{4R}{3})\theta^{'2} + \frac{1}{\theta+\delta}\frac{Pr.Ec}{A_3(1-\phi)^{2.5}}((M+K)f^{'2} + f^{''2}), \end{aligned} \tag{7.20}$$

where E_S denotes the total entropy generation, E_{ST} denotes the thermal part of the entropy generation, E_{SFF} denotes the frictional and magnetic part of the entropy

generation. The Bejan number (Bejan and Kestin [1983], Bejan [1979]) is a metric that compares the ratio of entropy generation due to thermal effects to the total entropy generation. The value of the Bejan number, lies between $[0, 1]$, is expressed as follows,

$$Be = \frac{E_{ST}}{E_S}. \tag{7.21}$$

7.4 Method of Solution

The Homotopy Analysis Method (Seth et al. [2018], Liao and Chwang [1998]) is applied to obtain approximate solutions of the equations 7.14 and 7.15 with respect to the boundary conditions 7.16 and 7.17. Based on the boundary conditions, the following set of basis functions are chosen to solve the ODEs,

$$\{\eta^i exp(-j\eta) | i \geq 0, j \geq 0\}. \tag{7.22}$$

These exponential decay functions help to converge the solutions faster when η takes large values. The approximate solutions with respect these basis functions take the following form,

$$\begin{aligned} f(\eta) &= p_{0,0} + \sum_{i=0}^{\infty}\sum_{j=1}^{\infty} p_{i,j}\eta^i exp(-j\eta), \\ g(\eta) &= q_{0,0} + \sum_{i=0}^{\infty}\sum_{j=1}^{\infty} q_{i,j}\eta^i exp(-j\eta), \end{aligned} \tag{7.23}$$

where $p_{i,j}, q_{i,j}$ are coefficients that need to be obtained from the equations 7.14-7.17. Following the method of Liao with respect to the boundary conditions, the initial approximate solutions are chosen as,

$$f_0(\eta) = \frac{S + S\gamma + 1 - e^{-\eta}}{1 + \gamma},\ g_0(\eta) = \frac{Bi}{1 + Bi} e^{-\eta}. \tag{7.24}$$

The following auxiliary functions are selected to initiate the recursion process,

$$L_f = f''' + f'',\ L_\theta = \theta'' + \theta', \tag{7.25}$$

that satisfy the following properties,

$$L_f[c_1 + c_2\eta + c_3 e^{-\eta}] = 0,\ L_\theta[c_5 + c_5 e^{-\eta}] = 0, \tag{7.26}$$

where c_i are unknown constants.
The zeroth order deformation of the problem is expressed as,

$$(1-q)L_f[\tilde{f}(\eta,q)-f_0(\eta)] = qh_f H_f \mathcal{N}_f(\tilde{f}(\eta,q)) \tag{7.27}$$
$$(1-q)L_\theta[\tilde{\theta}(\eta,q)-\theta_0(\eta)] = qh_\theta H_\theta \mathcal{N}_\theta(\tilde{f}(\eta,q),\tilde{\theta}(\eta,q)) \tag{7.28}$$
$$\tilde{f}(\eta,q) = f_0(\eta)+\sum_{m=1}^{\infty} f_m(\eta)q^m,\ \tilde{\theta}(\eta,q) = \theta_0(\eta)+\sum_{m=1}^{\infty}\theta_m(\eta)q^m,$$
$$f_m(\eta) = \frac{1}{m!}\frac{\partial^m \tilde{f}}{\partial q^m}\bigg|_{q=0},\ \theta_m(\eta) = \frac{1}{m!}\frac{\partial^m \tilde{\theta}}{\partial q^m}\bigg|_{q=0}$$

with respect to the following boundary conditions,

$$\tilde{f}(0,q) = S,\ \tilde{f}'(0,q) = 1+\gamma\tilde{f}''(0,q),\ \tilde{f}'(\infty,q) = 0,\ \tilde{\theta}(\infty,q) = 0,$$
$$\tilde{\theta}'(0,q) = -Bi(1-\tilde{\theta}(0,q)). \tag{7.29}$$

where $q \in [0,1]$, $\mathcal{N}_{f,\theta}$ denotes the non-linear ODEs 7.14, 7.15 and $h_{f,\theta}, H_{f,\theta}$ are convergence control parameters. In this study, we have considered $H_{f,\theta} = e^{-\eta}$ and $h_f = h_\theta = h$. The value of h is chosen in such a way that both $\tilde{f}, \tilde{\theta}$ converge when $q = 1$. The only remaining parameters (f_m, θ_m) that we need to define are obtained from the following m-th order deformation equations,

$$L_f\Big[f_m - \chi_m f_{m-1}\Big] = h_f H_f R_m^f,\ L_\theta\Big[\theta_m - \chi_m\theta_{m-1}\Big] = h_\theta H_\theta R_m^\theta, \tag{7.30}$$
$$f_m(0) = 0,\ f_m'(0) = \gamma f_m''(0),\ f_m'(\infty) = 0,\ \theta_m(\infty) = 0,\ \theta_m'(0) = Bi\theta_m(0), \tag{7.31}$$

where

$$\begin{aligned} R_m^f(\eta) &= f_{m-1}''' - (M+K)f_{m-1}' + A_1(1-\phi)^{2.5}\Bigg[\sum_{i=0}^{m-1} f_i f_{m-1-i}'' - \sum_{i=0}^{m-1} f_i' f_{m-1-i}' - \\ &\lambda(f_{m-1}' + \frac{\eta}{2}f_{m-1}'') + De\Bigg(2\sum_{i=0}^{m-1} f_{m-1-i}\sum_{j=0}^{i} f_j' f_{j-i}'' - \\ &\sum_{i=0}^{m-1} f_{m-1-i}\sum_{j=0}^{i} f_j f_{j-i}'''\Bigg)\Bigg], \end{aligned} \tag{7.32}$$

$$\begin{aligned} R_m^\theta(\eta) &= \frac{1}{Pr}\Big(1+\frac{4R}{3}\Big)\theta_{m-1}'' + \frac{A_2}{A_3}\Bigg(\sum_{i=0}^{m-1} f_i\theta_{m-1-i}' - \frac{\lambda\eta}{2}\theta_{m-1}'\Bigg) \\ &+\frac{A_1(1-\phi)^{2.5}}{Pr}(Af_{m-1}' + B\theta_{m-1}) \\ &+\frac{Ec}{A_3(1-\phi)^{2.5}}\Bigg(\sum_{i=0}^{m-1}\Big[f_i'' f_{m-1-i}'' + (M+K)f_i' f_{m-1-i}'\Big]\Bigg). \end{aligned} \tag{7.33}$$

Table 7.1: Properties of PDMS and Graphene (Selvam et al. [2017], Roberts et al. [2017])

	ρ	C_ρ	k
PDMS fluid	816	1800	0.15
Graphene	2200	643	3000

The functions f, θ are then approximated by finite sums of the following form,

$$\overline{f} = f_0 + \sum_{i=1}^{P} f_i, \ \overline{\theta} = \theta_0 + \sum_{i=1}^{P} \theta_i \tag{7.34}$$

where P denotes the number of iteration. The convergence control parameter h is determined from the above series by first observing the h-plot and then considering the error minimizing table where error terms are defined as,

$$\epsilon_P^f = \frac{1}{L+1} \sum_{j=0}^{L} \left[\mathcal{N}_f(\sum_{i=0}^{P} f_i)(\eta_j) \right]^2, \ \epsilon_P^\theta = \frac{1}{L+1} \sum_{j=0}^{L} \left[\mathcal{N}_\theta(\sum_{i=0}^{P} \theta_i)(\eta_j) \right]^2 \tag{7.35}$$

where $\eta_j = jr$, $r = \frac{\eta_{max}}{L+1}$, $\eta_{max} = 6$, $L = 1000$ are chosen for this study. The decrements in error terms with the increasing iteration value, presented in table 7.2, indicates that $\overline{f}, \overline{\theta}$ are converging to the exact solution. The amount of precision of the iterated approximate solution as compared to the exact solution increases with the rise in number of iterations. Finally, the obtained results are shown to be in well agreement with the existing relevant results present in the literature as shown in table 7.3.

7.5 Discussion of the Results

This study focuses on analyzing the effects of the time relaxation parameter (λ_1) in terms of the Deborah number (De), surface stretching rate as well as unsteady parameter in terms of (λ), nanoparticle volume fractions (ϕ), Navier slip parameter (γ) and porous permeability of the medium (K) on nanofluid flow profiles. Moreover, the consideration of an externally applied magnetic field (M) is made along with the thermal radiation effects (R) in this study. The physical properties of PDMS-graphene that are used to obtain the parametric values are presented in the table 7.1. The following set of parametric values are used for numerical computation (Shit and Mukherjee [2019]):

$$\begin{aligned} &Pr = 10, \ Ec = 0.03, \ M = [0,1], \ R = [0,0.2], \ \phi = [0,0.2], \ \lambda = [0,2], \ De = [0,1], \\ &A = B = [-0.5,0.5], \ Bi = 0.2, \ K = 0.7, \ S = [0,0.3], \ \gamma = 0.1, \ \delta = 0.5. \end{aligned} \tag{7.36}$$

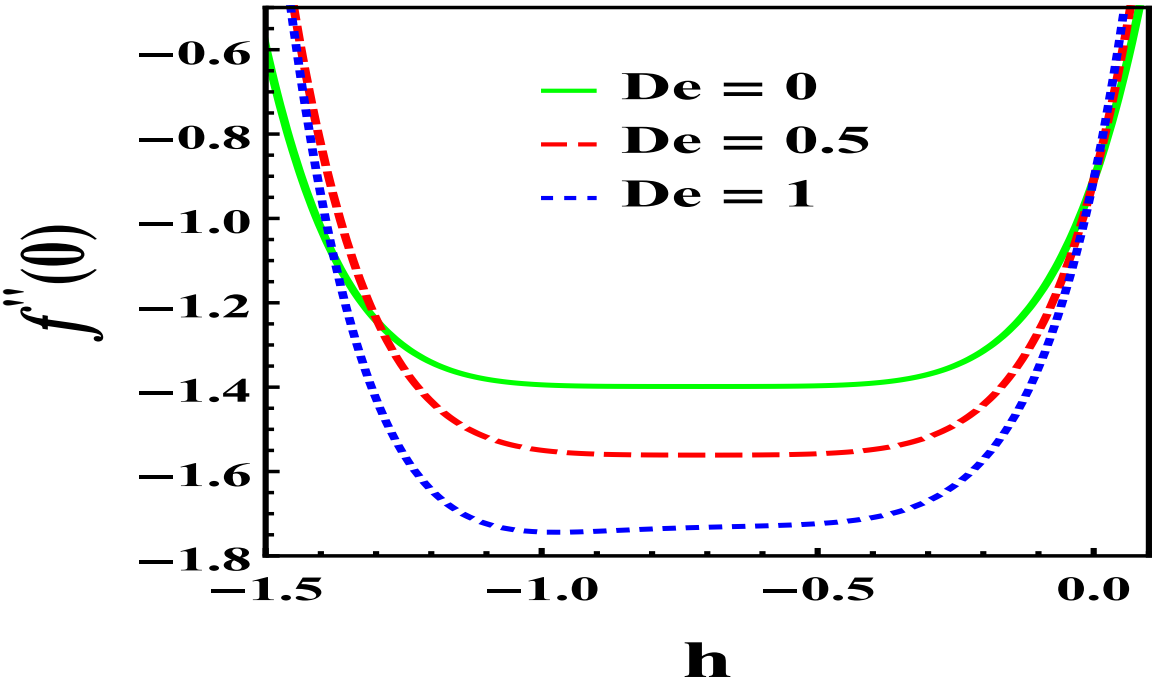

Figure 7.1: h-plot for different values of the Deborah number De when $P = 6,\ S = 0.3,\ \gamma = 0.1,\ \lambda = 0.05,\ \phi = 0.1, M, K = 0.7$.

The value $h = -0.6$ is chosen based on the h-plot (figure 7.1) which shows that $[-1, -0.5]$ is a admissible interval of h-values for which the series $\overline{f}, \overline{\theta}$ will converge subject to small variations of the physical parameters. An error estimation with such a choice of h is presented in table 7.2.

7.5.1 Validation of present results

The results of the present study have been validated with the existing previous works present in the literature Seth et al. [2018], Makinde and Aziz [2011], Reddy Gorla and Sidawi [1994]. The comparable numerical values of $-\theta'(0)$ and the results obtained from the present study are shown in table 7.3.

7.5.2 Velocity distribution

Figures 7.2-7.5 elucidate the variations of axial velocity with respect to different regulatory parameters. These figures show that nanofluid velocity decreases with an enhancement of the Deborah number De, magnetic number M, injection velocity S, Navier's slip parameter γ. The enhancement in relaxation time increases internal stress in nanofluid thereby reduces nanofluid velocity. The enhancement of the resistive Lorentz force due to higher magnetic field strength diminishes nanofluid velocity. The enhancement of Navier's slip parameter enhances drag forces at nanofluid-surface

Table 7.2: Error estimation with series iteration number when $h = -0.6, S = 0.3, \gamma = 0.1, \lambda = 0.05, \phi = 0.1, M, K = 0.7, R = 0.1, Pr = 10, A, B = -0.5, De = 0.1, Ec = 0.03, Bi = 0.2$.

P	ϵ_P^f	ϵ_P^θ
2	0.00149238	0.000163246
4	0.000196797	0.0000990327
6	0.0000570259	0.0000649834
8	0.0000224567	0.0000438791

Table 7.3: Comparison of the present study with other works when $h = -0.6$, $P = 30$, $Bi = 1000$.

Pr	$-\theta'(0)$ Refs. Seth et al. [2018]	$-\theta'(0)$ Refs. Makinde and Aziz [2011]	$-\theta'(0)$ Refs. Reddy Gorla and Sidawi [1994]	$-\theta'(0)$ Present Work
0.7	0.4537	0.4539	0.53488	0.47978
2	0.9111	0.9113	0.91142	0.90722
7	1.8907	1.8954	1.89046	1.89200
10	-	-	2.30350	2.3013

interface thereby reduces velocity. The enhancement in nanofluid injection velocity at stretching surface reduces axial velocity due to conservation of mass through a vertical section. The variations in axial velocity for change in Navier's slip parameter is found to be significant.

7.5.3 Temperature distribution

Figures 7.6-7.9 illustrate the variations of nanofluid temperature within the boundary layer for different physical parameters. These figures show that nanofluid temperature increases with enhancement of the Deborah number De, unsteadiness parameter λ, nanoparticle volume fraction ϕ, source/sink parameters A, B. The thermal convection in the horizontal direction is low, therefore, the heat generation is mostly dependent on the internal viscous dissipation and heat transfer process in the vertical direction. The higher values of both the Deborah number and unsteadiness parameter are responsible for increase in thermal diffusion process in the system thereby increase nanofluid temperature. Figure 7.8 establishes the usefulness of using nanoparticle to enhance nanofluid heat transfer rate. Figure 7.9 shows that temperature increases with enhancement of heat source term. The variations in nanofluid temperature with a small change in unsteadiness parameter and nanoparticle volume fraction are significant.

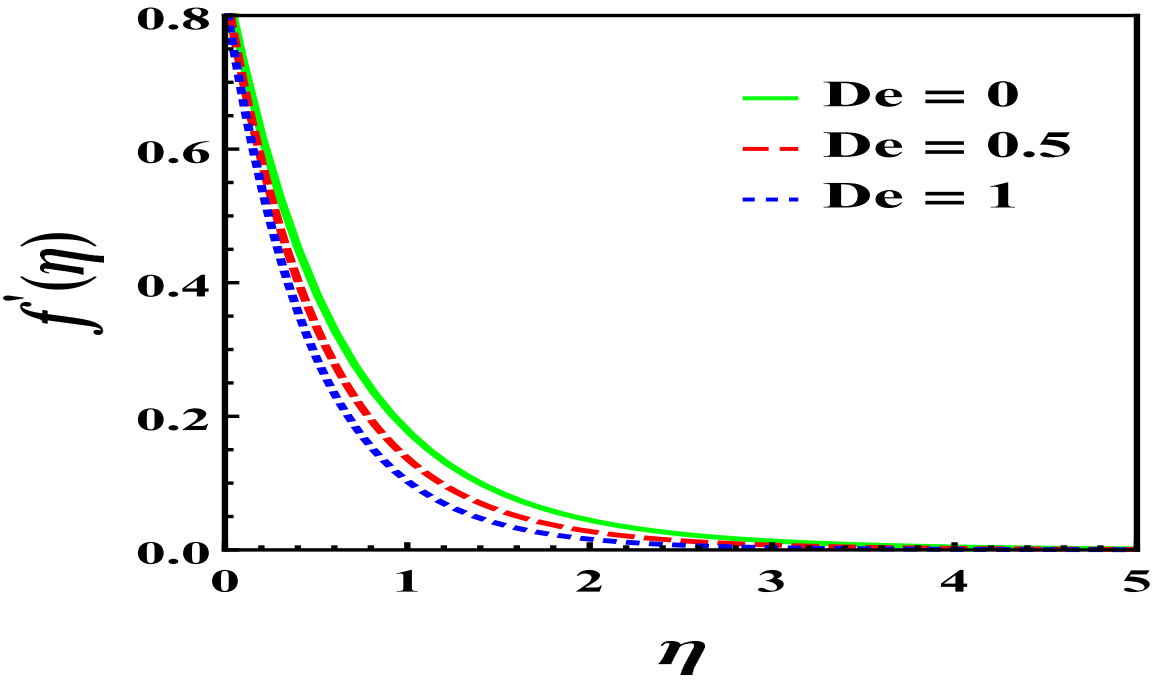

Figure 7.2: Velocity profiles for different values of De when $h = -0.6,\ S = 0.3,\ \gamma = 0.1,\ \lambda = 0.05,\ M, K = 0.7,\ \phi = 0.1$

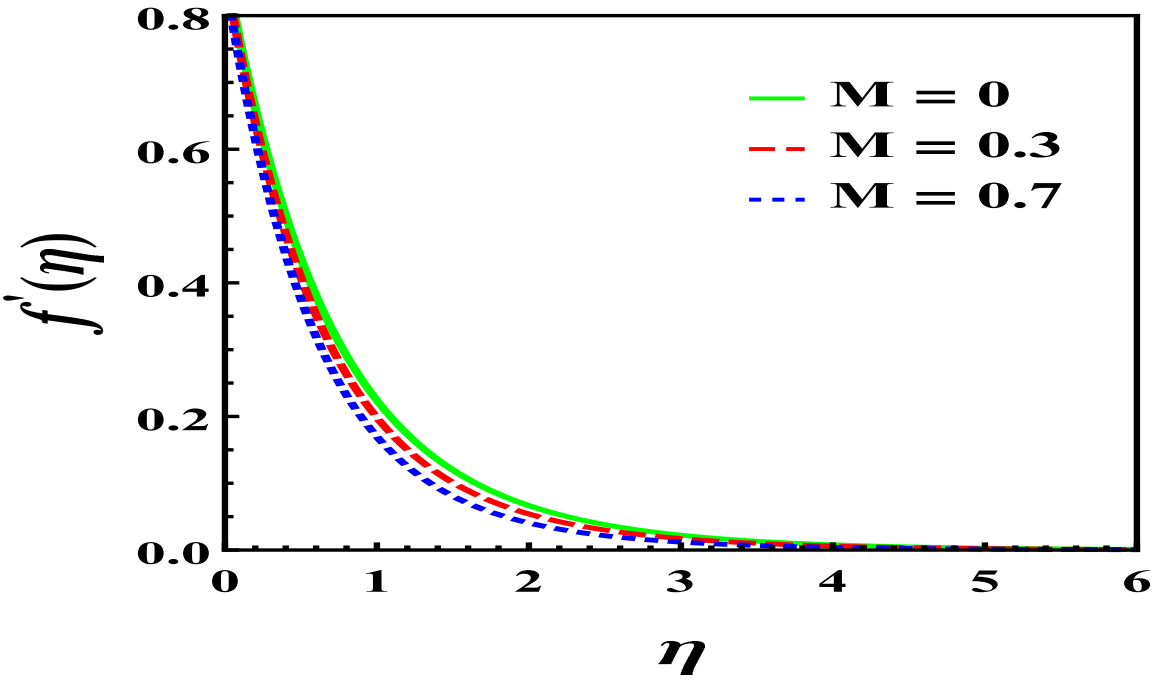

Figure 7.3: Velocity profiles for different values of M when $h = -0.6,\ S = 0.3,\ \gamma = 0.1,\ \lambda = 0.05,\ De = 0.1,\ K = 0.7,\ \phi = 0.1$

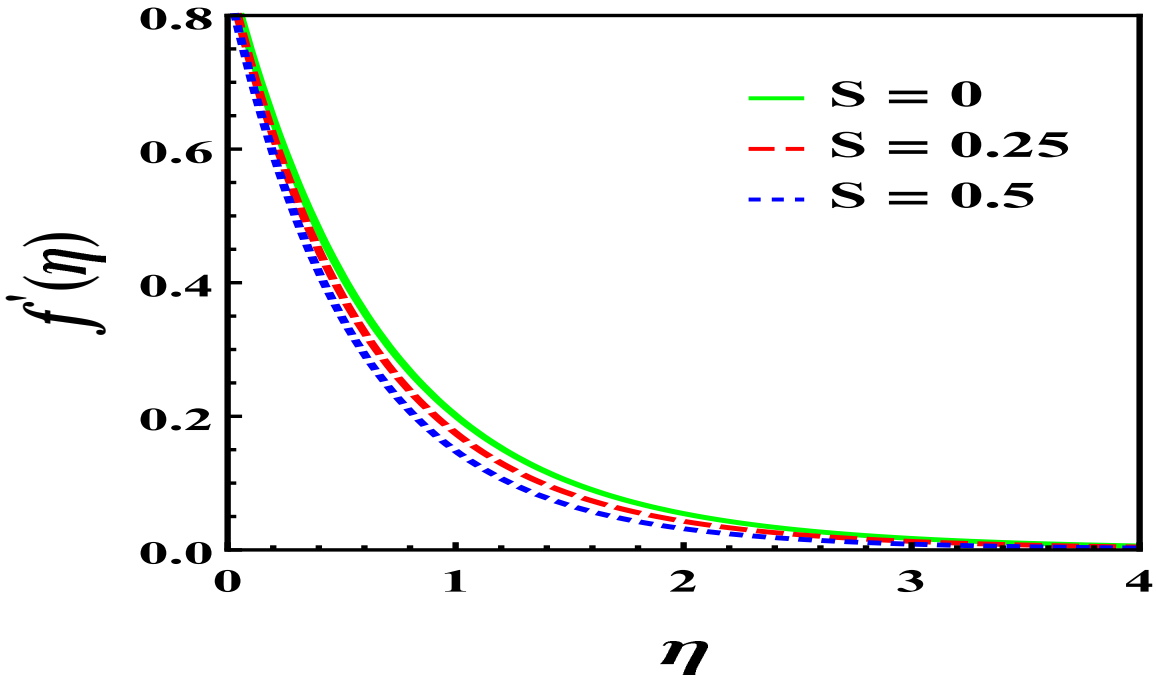

Figure 7.4: Velocity profiles for different values of S when $h = -0.6,\ \lambda = 0.05,\ \gamma = 0.1,\ De = 0.1,\ M, K = 0.7,\ \phi = 0.1$

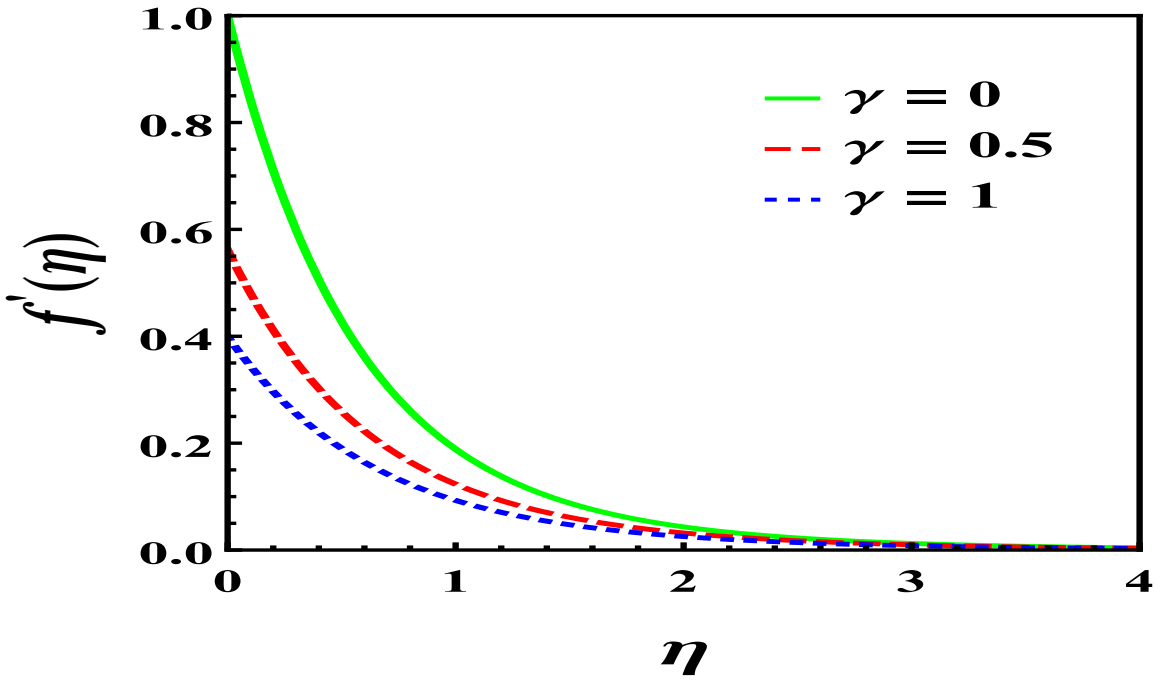

Figure 7.5: Velocity profiles for different values of γ when $h = -0.6,\ \lambda = 0.05,\ S = 0.3,\ De = 0.1,\ M, K = 0.7,\ \phi = 0.1$

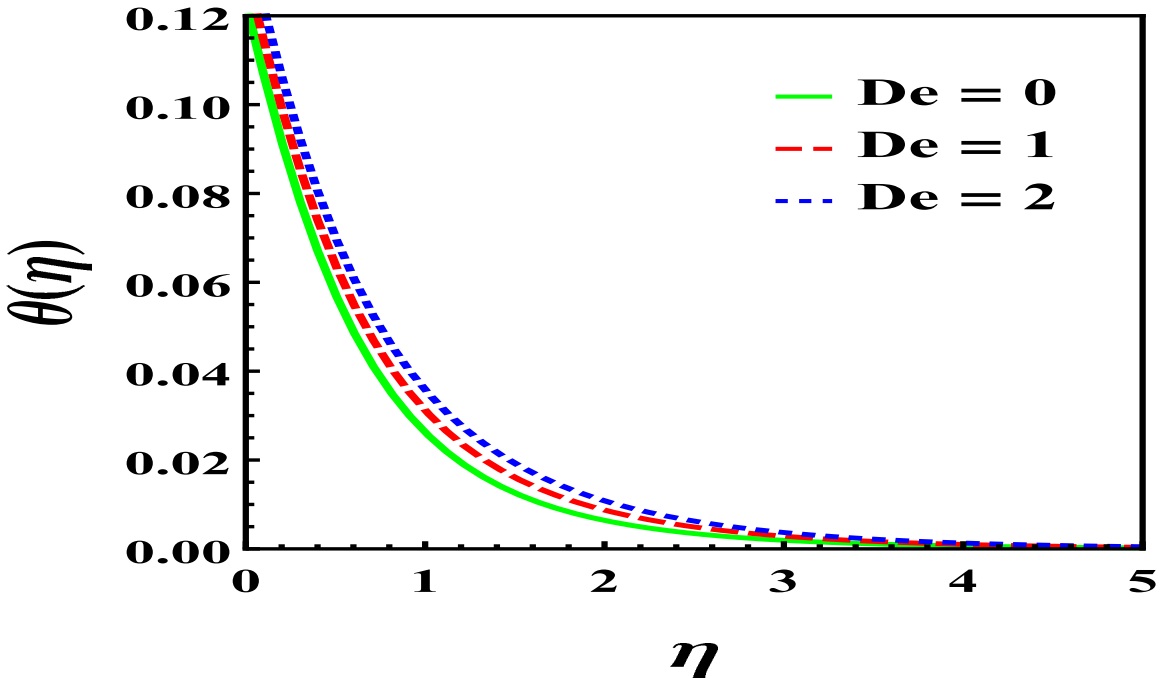

Figure 7.6: Temperature profiles for different values of De when $h = -0.6,\ S = 0.3,\ \gamma = 0.1,\ \lambda = 0.05,\ M, K = 0.7,\ \phi = 0.1,\ Ec = 0.03,\ Pr = 10,\ Bi = 0.2, R = 0.1,\ A, B = -0.5$

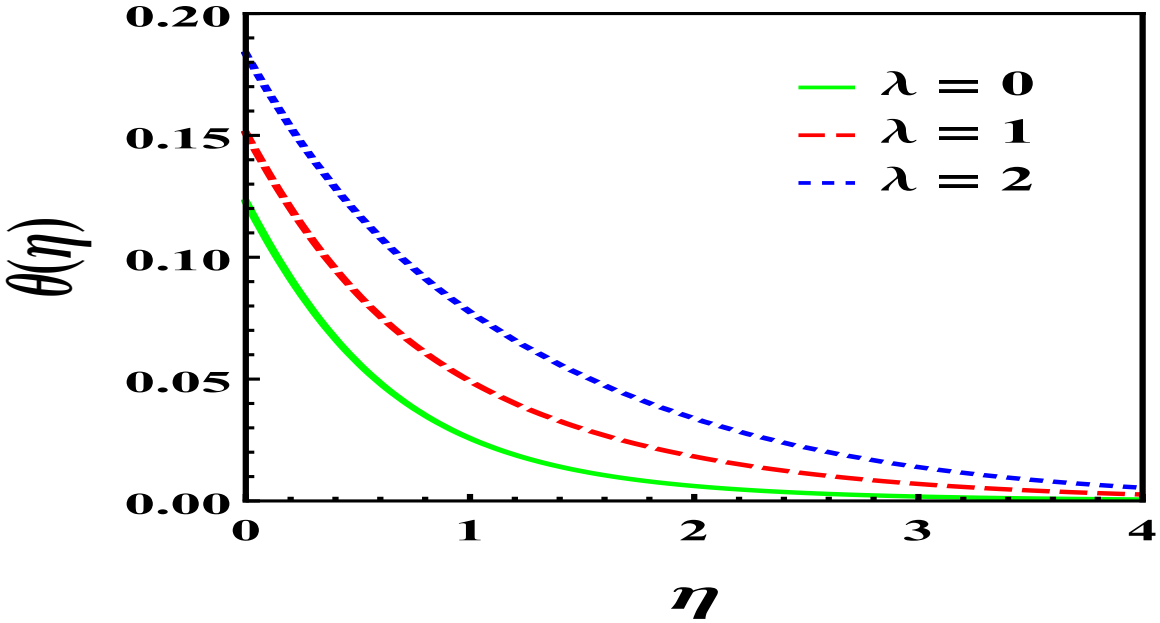

Figure 7.7: Temperature profiles for different values of λ when $h = -0.6,\ S = 0.3,\ \gamma = 0.1,\ M, K = 0.7,\ \phi = 0.1,\ Ec = 0.03,\ Pr = 10,\ Bi = 0.2, R = 0.1,\ A, B = -0.5,\ De = 0.1$

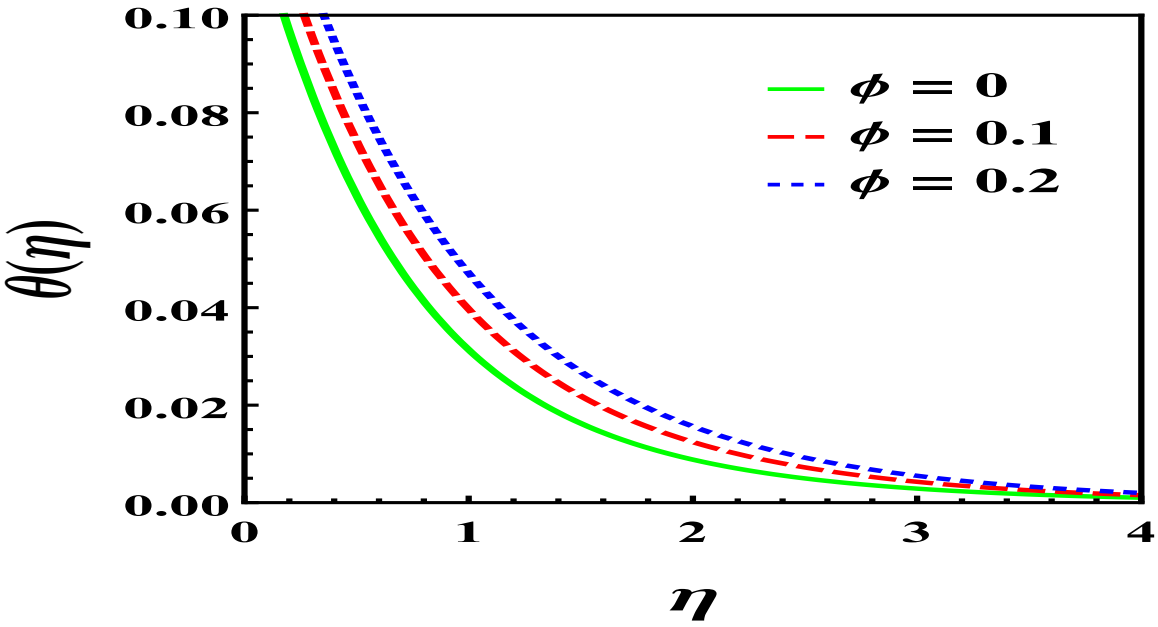

Figure 7.8: Temperature profiles for different values of ϕ when $h = -0.6$, $S = 0.3$, $\gamma = 0.1$, $M, K = 0.7$, $\lambda = 0.05$, $Ec = 0.03$, $Pr = 10$, $Bi = 0.2, R = 0.1$, $A, B = -0.5$, $De = 0.1$

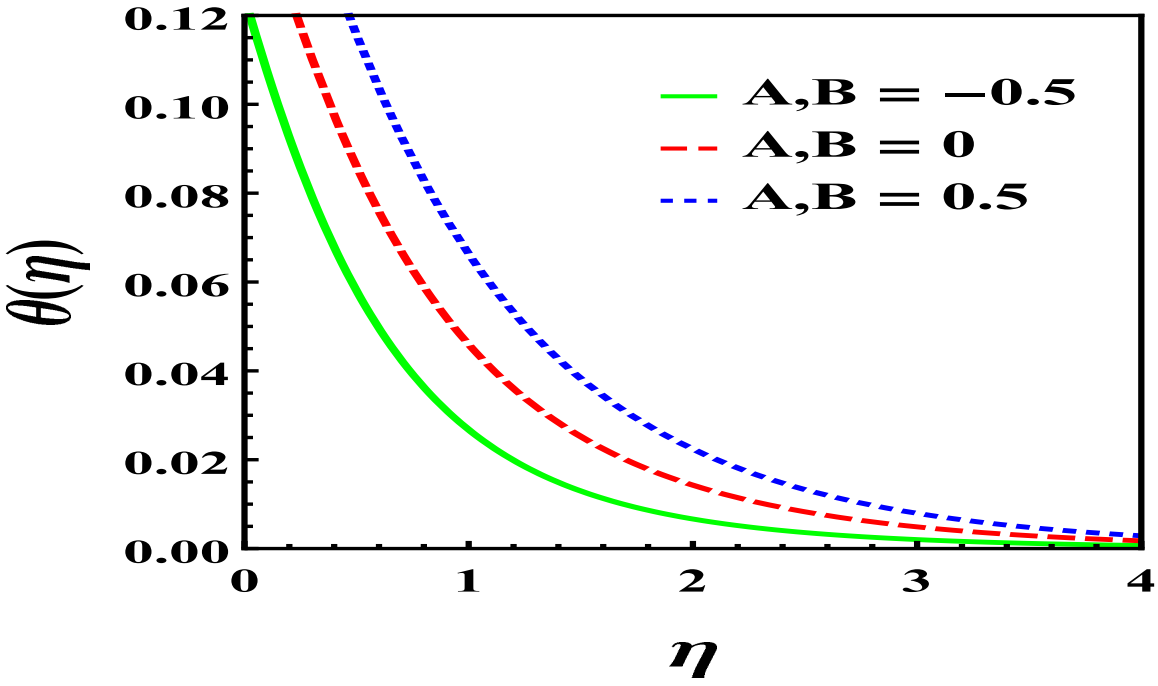

Figure 7.9: Temperature profiles for different values of A, B when $h = -0.6$, $S = 0.3$, $\gamma = 0.1$, $M, K = 0.7$, $\lambda = 0.05$, $Ec = 0.03$, $Pr = 10$, $Bi = 0.2, R = 0.1$, $\phi = 0.1$, $De = 0.1$

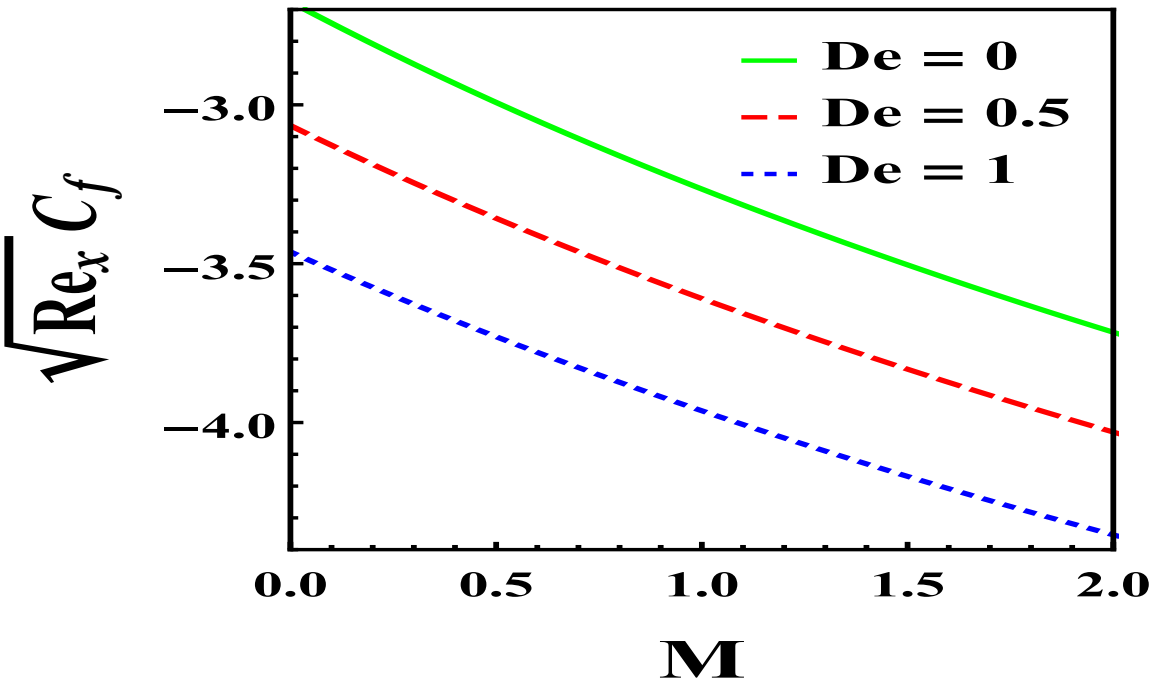

Figure 7.10: Skin-friction coefficient as a function of M for different values of De when $h = -0.6,\ S = 0.3,\ \gamma = 0.1,\ \lambda = 0.05,\ K = 0.7,\ \phi = 0.1$

7.5.4 Local skin friction coefficient and Nusselt number

Figures 7.10-7.15 depict the variations of frictional drag force in terms of skin-friction coefficient and heat transfer rate in terms of Nusselt number with respect to different regulatory parameters. Figures 7.10-7.12 show that the absolute value of the skin-friction coefficient increases with enhancement of the Deborah number De, magnetic number M, nanoparticle volume fraction ϕ, unsteadiness parameter λ. Figures 7.13-7.15 show that the Nusselt number decreases with a rise in the Deborah number De, magnetic number M, radiation parameter R but increases with the heat transfer rate in terms of the Biot number Bi and nanoparticle volume fraction ϕ. The reduction in velocity gradient due to resistive Lorentz force and internal stress generation due to high relaxation time requirement are responsible for diminution of Nusselt number, whereas, enhancement of thermal conductivity with addition of highly thermally conductive graphene nanoparticle along with increase in heat transfer rate at nanofluid-surface interface enhances Nusselt number.

7.5.5 Analysis of entropy generation

Figures 7.16-7.22 show that the Bejan number increases with enhancement of the Deborah number De, magnetic number M, nanoparticle volume fraction ϕ, unsteadiness parameter λ, Biot number Bi, porous permeability of the medium K and thermal

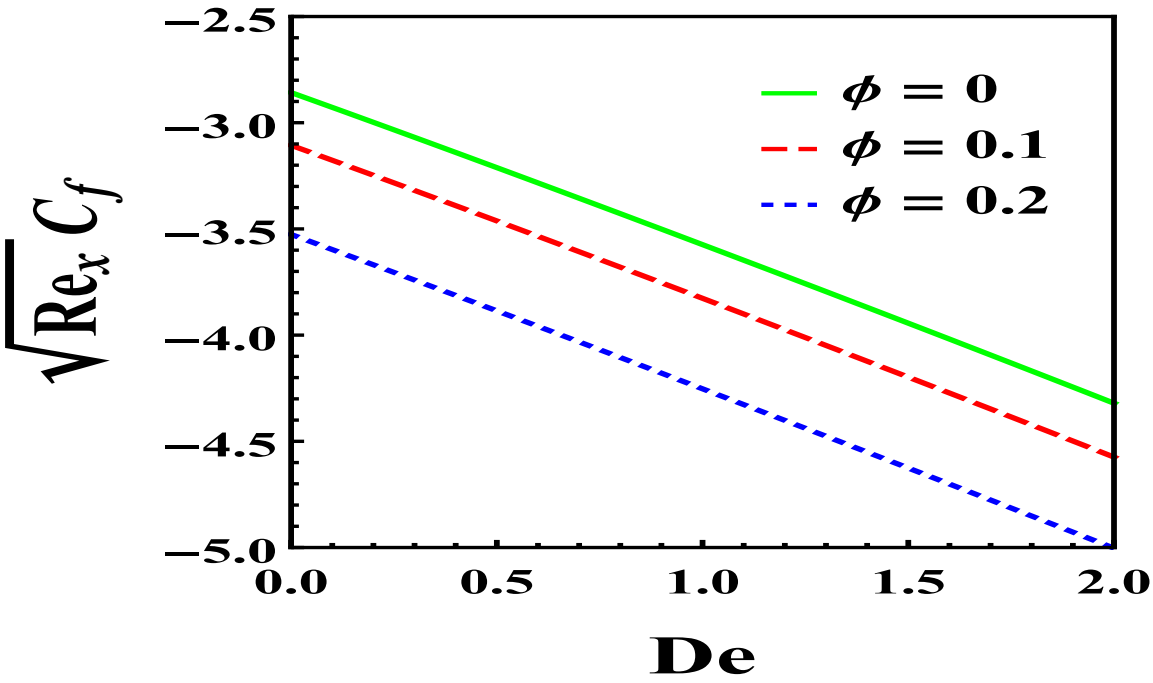

Figure 7.11: Skin-friction coefficient as a function of De for different values of ϕ when $h = -0.6,\ S = 0.3,\ \gamma = 0.1,\ \lambda = 0.05,\ M, K = 0.7$

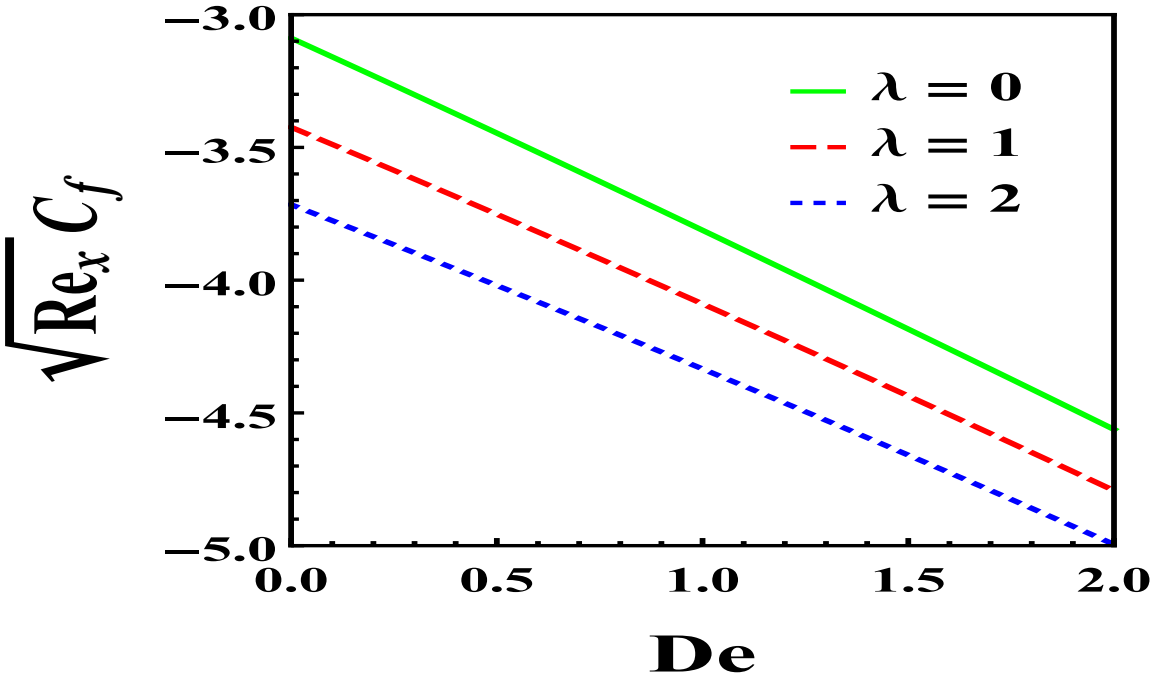

Figure 7.12: Skin-friction coefficient as a function of De for different values of λ when $h = -0.6,\ S = 0.3,\ \gamma = 0.1,\ M, K = 0.7,\ \phi = 0.1$

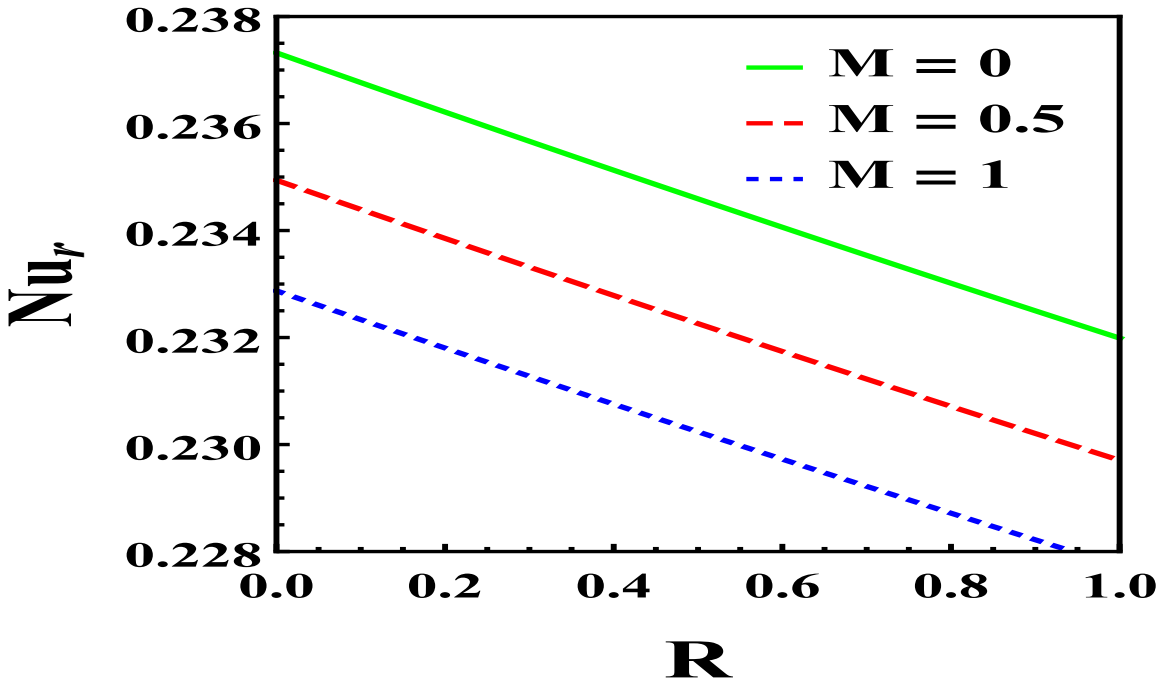

Figure 7.13: Nusselt number as a function of R for different values of M when $h = -0.6,\ S = 0.3,\ \gamma = 0.1,\ \lambda = 0.05,\ K = 0.7,\ \phi = 0.1,\ Ec = 0.03,\ De = 0.1$

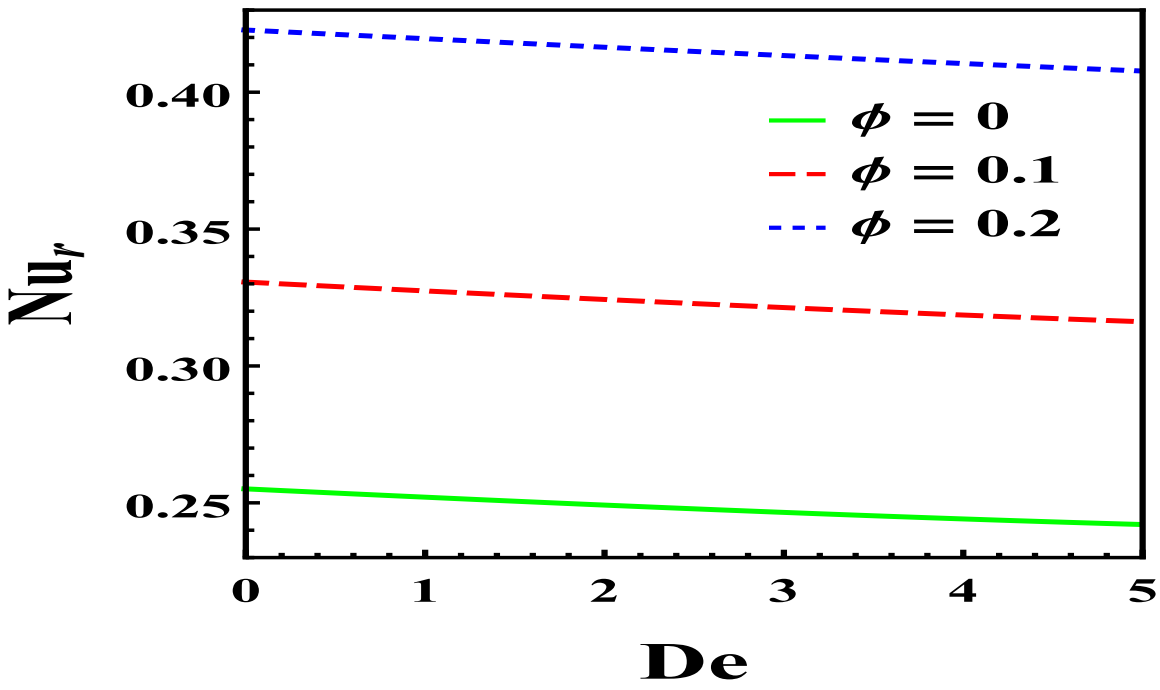

Figure 7.14: Nusselt number as a function of De for different values of ϕ when $h = -0.6,\ S = 0.3,\ \gamma = 0.1,\ \lambda = 0.05,\ M, K = 0.7,\ Ec = 0.03,\ R = 0.1$

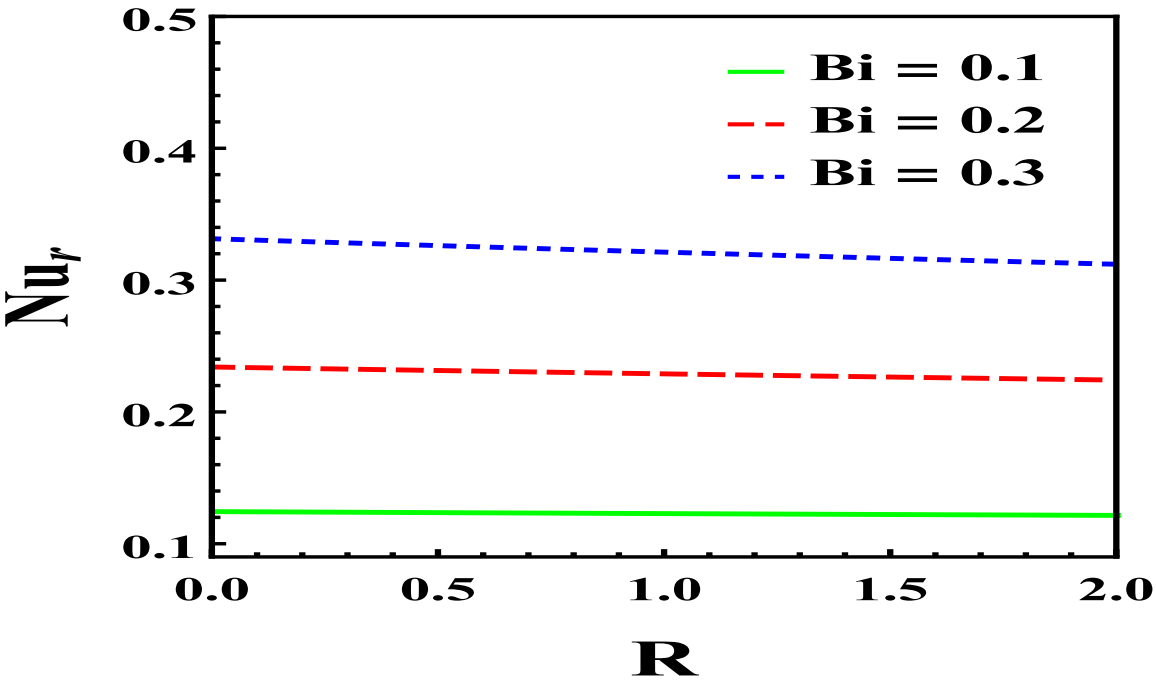

Figure 7.15: Nusselt number as a function of R values for different values of Bi when $h = -0.6,\ S = 0.3,\ \gamma = 0.1,\ \lambda = 0.05,\ M, K = 0.7,\ \phi = 0.1,\ Ec = 0.03,\ De = 0.1$

radiation parameter R. The enhancement in magnetic field strength enhances irreversible heat generation due to Lorentz force. The irreversible heat loss due to thermal radiation and heat transfer at surface-fluid interface enhances the entropy generation in the system. Figures 7.16-7.19, 7.21 show that the value of the Bejan number is low *i.e.* the entropy generation due to friction is much higher compared to the entropy generation due to heat transfer in these cases. However, figures 7.20, 7.22 show that the entropy generation due to heat transfer enhances with the rise of Biot number and nanoparticle volume fraction.

7.6 Concluding Remarks

The entropy generation of Graphene-PDMS Maxwell nanofluid flow over a stretching surface in the presence of an externally applied magnetic field and thermal radiation is examined in this chapter. The Homotopy Analysis Method (HAM) is used to solve the non-linear governing equation describing the nanofluid flow and energy balance in the system. The effects of important physical parameters such as the magnetic number M, the thermal radiation parameter R, the Deborah number De, the unsteady parameter λ, the nanoparticle volume fraction ϕ and the permeability of the medium K on the flow profiles, thermal profiles and the entropy generation are graphically illustrated. The Homotopy Analysis Method is used to solve the non-linear ODEs. The important

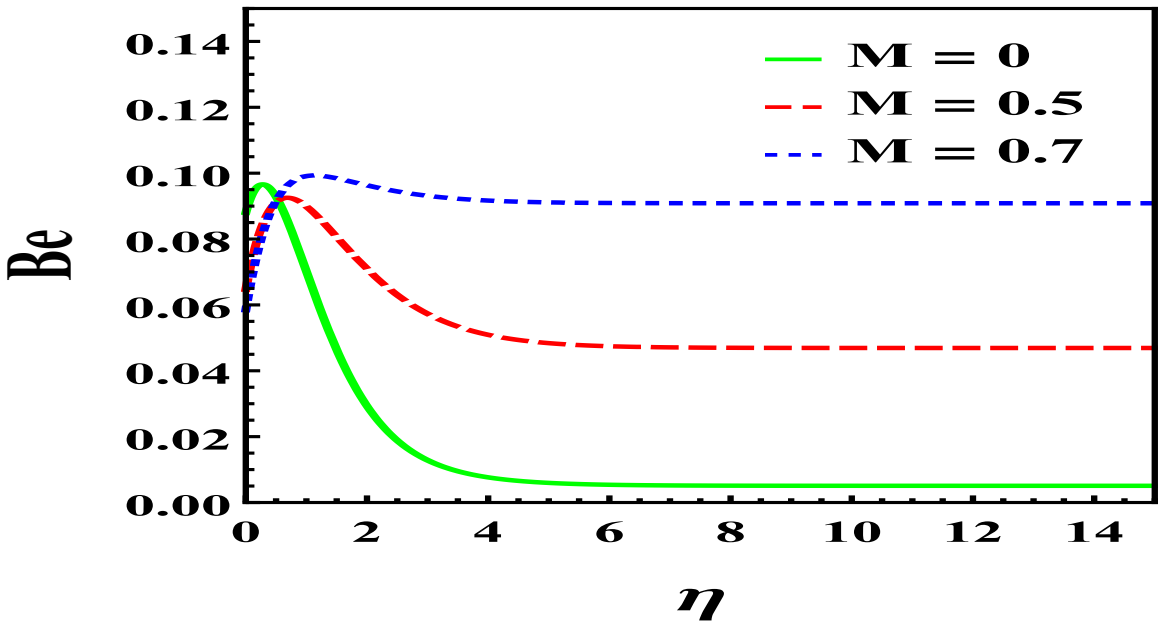

Figure 7.16: Bejan number profiles for different values of M when $h = -0.6$, $S = 0.3$, $\gamma = 0.1$, $K = 0.7$, $\lambda = 0.05$, $Ec = 0.03$, $Pr = 10$, $Bi = 0.2, R = 0.1$, $A, B = -0.5$, $De = 0.1$, $\phi = 0.1$

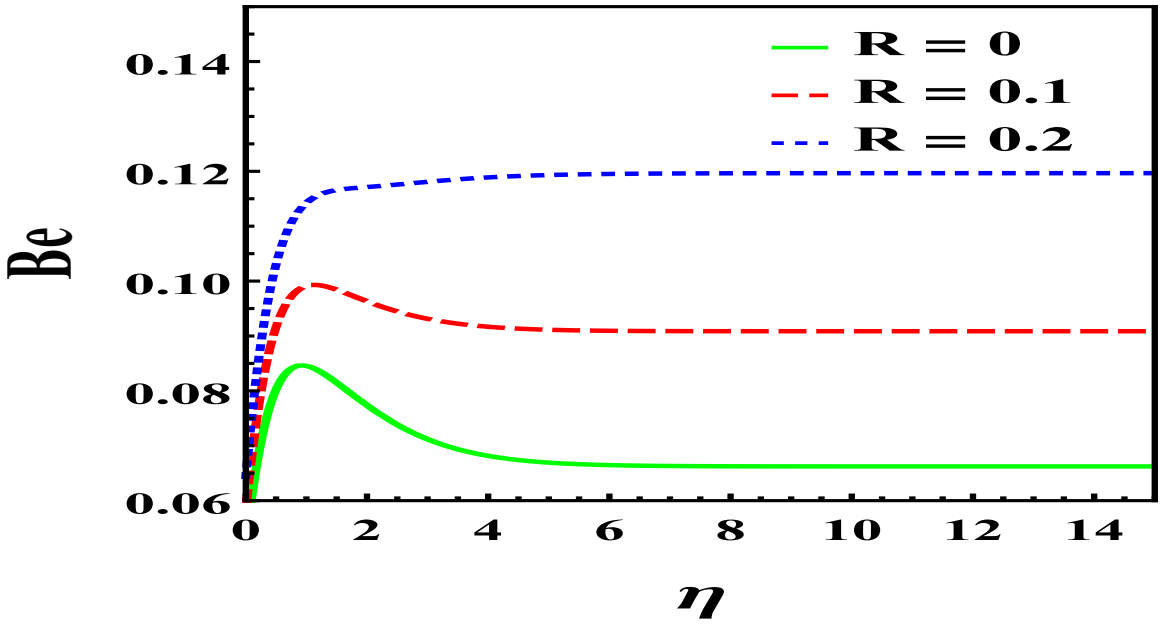

Figure 7.17: Bejan number profiles for different values of R when $h = -0.6$, $S = 0.3$, $\gamma = 0.1$, $M, K = 0.7$, $\lambda = 0.05$, $Ec = 0.03$, $Pr = 10$, $Bi = 0.2$, $A, B = -0.5$, $De = 0.1$, $\phi = 0.1$

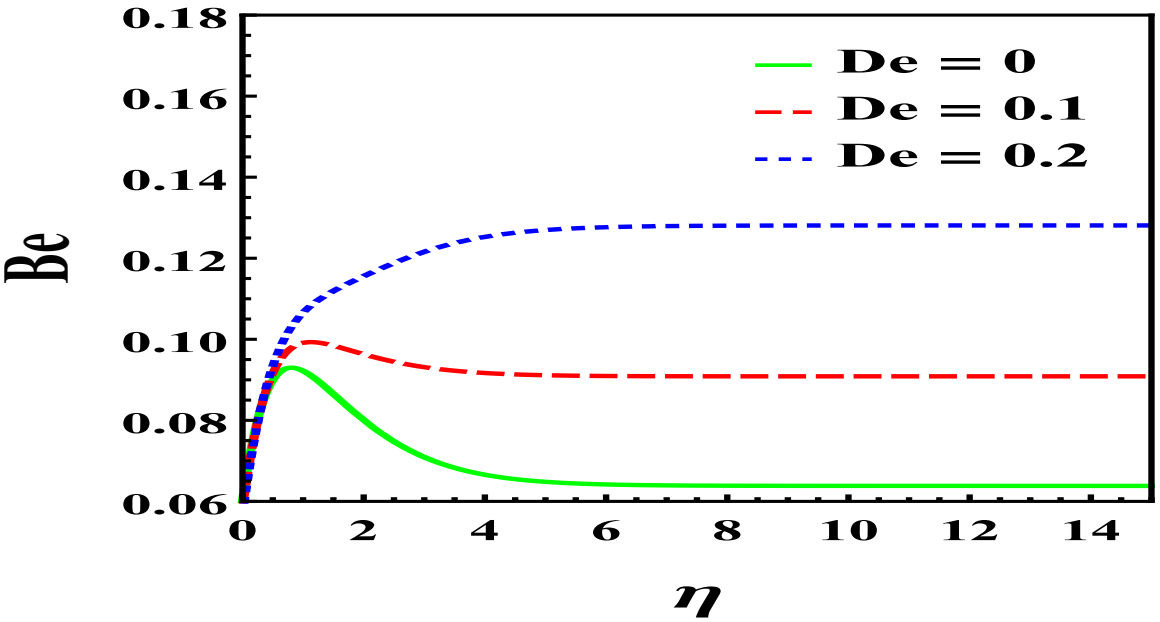

Figure 7.18: Bejan number profiles for different values of De when $h = -0.6,\ S = 0.3,\ \gamma = 0.1,\ M, K = 0.7,\ \lambda = 0.05,\ Ec = 0.03,\ Pr = 10,\ Bi = 0.2,\ A, B = -0.5,\ R = 0.1,\ \phi = 0.1$

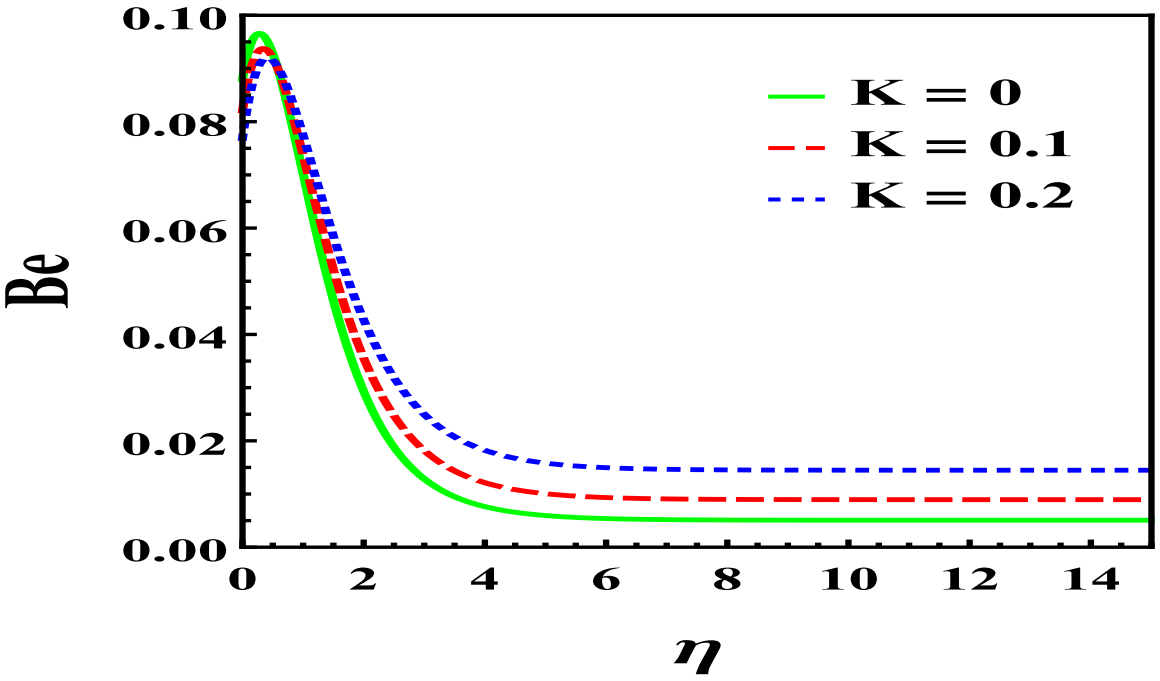

Figure 7.19: Bejan number profiles for different values of K when $h = -0.6,\ S = 0.3,\ \gamma = 0.1,\ M = 0.7,\ \lambda = 0.05,\ Ec = 0.03,\ Pr = 10,\ Bi = 0.2,\ A, B = -0.5,\ De = 0.1,\ \phi = 0.1,\ R = 0.1$

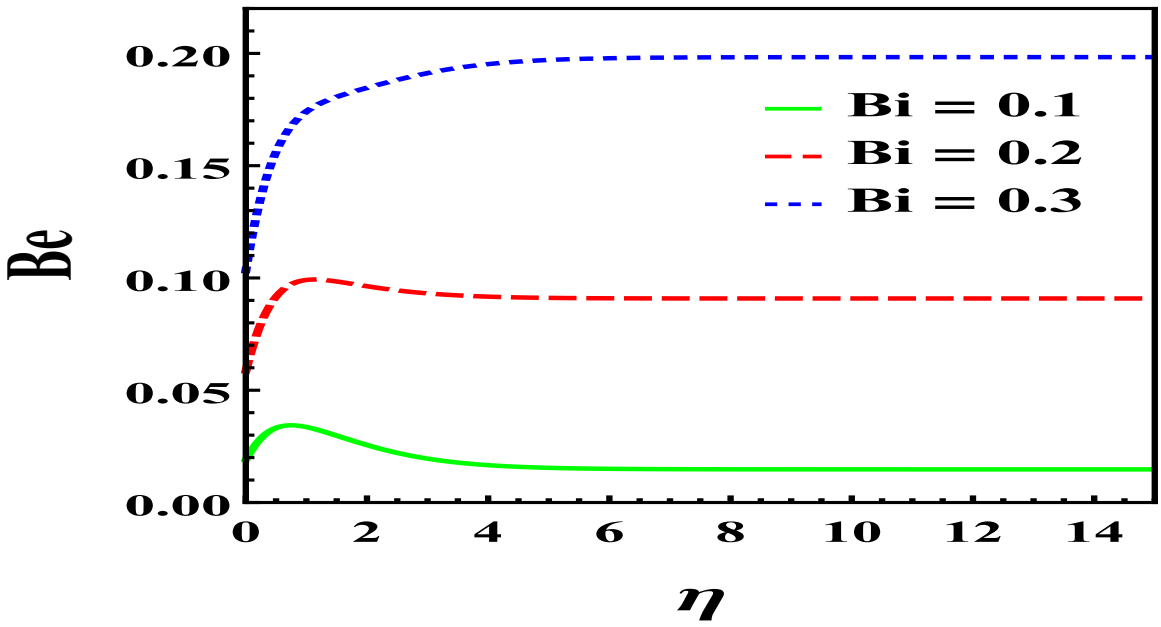

Figure 7.20: Bejan number profiles for different values of Bi when $h = -0.6$, $S = 0.3$, $\gamma = 0.1$, $M, K = 0.7$, $\lambda = 0.05$, $Ec = 0.03$, $Pr = 10$, $A, B = -0.5$, $De = 0.1$, $\phi = 0.1$, $R = 0.1$

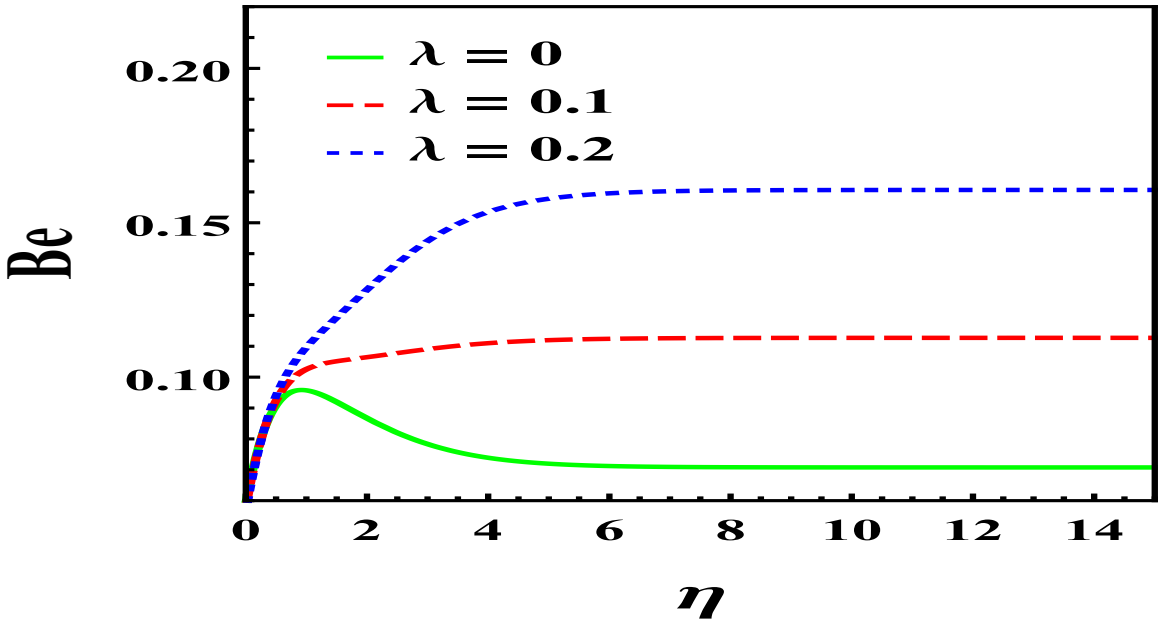

Figure 7.21: Bejan number profiles for different values of λ when $h = -0.6$, $S = 0.3$, $\gamma = 0.1$, $M, K = 0.7$, $Bi = 0.2$, $Ec = 0.03$, $Pr = 10$, $A, B = -0.5$, $De = 0.1$, $\phi = 0.1$, $R = 0.1$

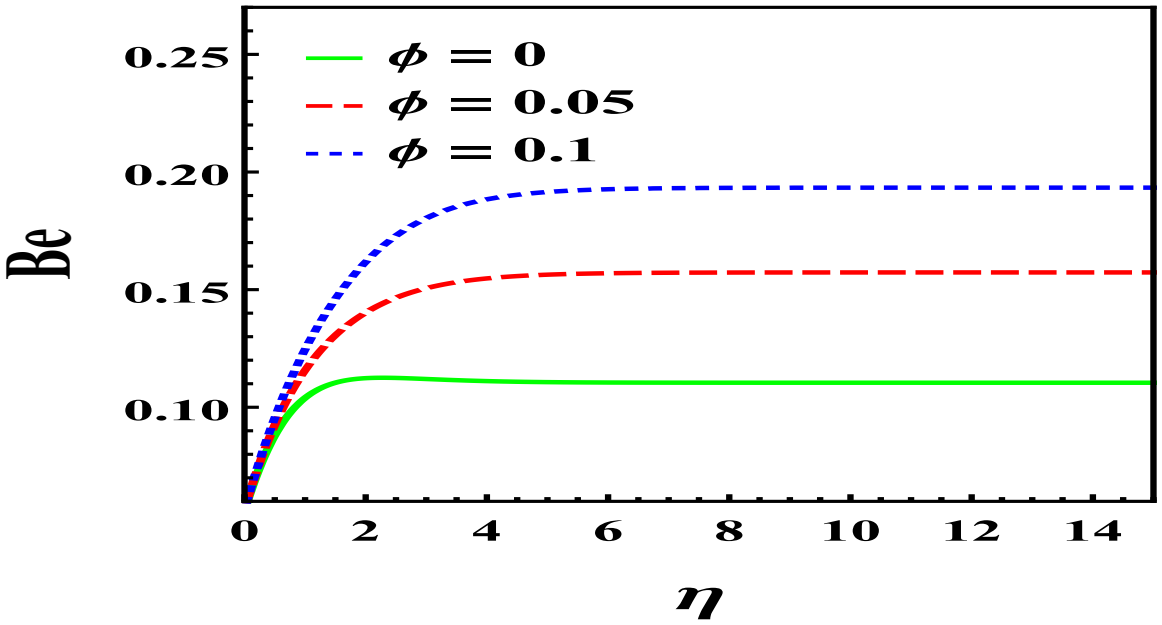

Figure 7.22: Bejan number profiles for different values of ϕ when $h = -0.6$, $S = 0.3$, $\gamma = 0.1$, $M, K = 0.7$, $Bi = 0.2$, $Ec = 0.03$, $Pr = 10$, $A, B = -0.5$, $De = 0.1$, $\lambda = 0.05$, $R = 0.1$

findings are summarized below:

- Bejan number Be increases with an enhancement in the magnetic number M, Deborah number De, thermal radiation parameter R, porous permeability parameter K, unsteadiness parameter λ, Biot number Bi and nanoparticle volume fraction ϕ.
- The nanofluid velocity decreases with an enhancement of the Deborah number De, magnetic number M, injection parameter S and Navier's slip parameter γ.
- The nanofluid temperature increases with enhancement of the Deborah number De, unsteadiness parameter λ, nanoparticle volume fraction ϕ, source/sink parameters A, B.
- The skin-friction coefficient C_f decreases with enhancement of the Deborah number De, magnetic number M, nanoparticle volume fraction ϕ, unsteadiness parameter λ.
- The Nusselt number Nu_r decreases with a rise in the Deborah number De, magnetic number M, radiation parameter R but increases with the heat transfer rate in terms of the Biot number Bi and nanoparticle volume fraction ϕ.

Chapter 8

Overall Conclusions and Future Scope of Study

8.1 Overall Conclusions

This thesis has been divided into two research directions:

- Electroosmotic nanofluid flow and heat transfer in a microchannel.
- Applications of nanofluid flow and heat transfer analysis in engineering systems by using the Differential Transform Method and Homotopy Analysis Method.

The electroosmotic nanofluid flow between two permeable walls in a microchannel has been analytically examined in this thesis. The combined effects of the injected fluid velocity and an externally applied electric field on formation of the Zeta potential is expressed analytically. The electroosmotic slip velocity at an edge of the EDL is integrally expressed under pressure drop boundary condition at the channel wall. This velocity is found to converge to the well-known Smoluchowski velocity when the fluid velocity is low and permeability of the channel tends to zero. The contribution of viscous drag force during heat generation under a weak electric field is investigated. The effects of the thermophoresis phenomena in nanoparticle diffusion process is investigated by varying the electric field strength. The effects of the electric field, pressure gradient, injection velocity and ion concentration in total entropy generation are thereafter illustrated. The energy efficiency of the squeezing Graphene-PDMS nanofluid as well as Cu-water flow between two plates under the influence of an external magnetic field as well as the radiative heat flux is examined in this thesis. The study of PDMS-graphene nanofluid flow over a stretching sheet is also conducted by using the homotopy analysis method. The effects of different physical parameters such as the thermal radiation parameter R, the magnetic field strength M, the Deborah number De, the squeeze parameter S and the nanoparticle volume fraction ϕ on the velocity profiles, thermal profiles, the Nusselt number, Bejan number and the coefficient of skin-friction are illustrated. The DTM and HAM have been used to

solve the non-linear differential equations. The main findings from our study can be summarized as follows,

1. The electroosmotic slip velocity converges to Smoluchowski velocity when the injection velocity is low and permeability $k_1 \to 0$.

2. The nanofluid velocity decreases with enhancement of injected nanofluid velocity.

3. The net flow amount increases with enhancement of the electric field strength, externally applied pressure gradient and electroosmotic parameter.

4. The nanofluid velocity decreases with enhancement of diffusive Reynolds number.

5. The increment in normalized fluid temperature with enhancement of the pressure gradient is visible when a weak electric field is applied.

6. The bulk nanofluid temperature shows an almost quadratic nonlinear relationship with the applied pressure gradient.

7. The decrements in normalized nanoparticle concentration with enhancement of the pressure gradient is visible when a weak electric field is applied.

8. The normalized bulk concentration value of the nanoparticle decreases with the enhancement of the electric field strength and Schmidt number.

9. When $Ve \approx 0$, a relationship between thermophoresis coefficient and Brownian motion coefficient of nanoparticles in terms of the cross sectional nanoparticle concentration and Joule heating parameter is obtained.

10. The normalized nanoparticle mass transfer rate rises with enhancement of Reynolds number and diminishes with Prandtl number.

11. A comparative study of normalized total entropy generation shows that the entropy generation near microchannel walls increases with the absolute pressure gradient parameter, electroosmotic parameter but decreases with injected velocity in terms of Reynolds number.

12. The total entropy generation follows a quadratic relationship with the Joule heating parameter in the absence of injection velocity and neglecting the viscous dissipation term in thermal energy equation.

13. The Zeta potential decreases with an enhancement of the diffusive Reynolds number.

14. The nanofluid velocity increases with the enhancement of porous permeability parameter, inverse couple stress parameter but decreases with diffusive Reynolds number. The bulk nanofluid flow rate is expressed as a non-linear function of couple stress parameter.

15. The nanofluid temperature increases with diminution of couple stress parameter, porous permeability of the medium but decreases with diminution of ion diffusion coefficient.

16. The total entropy generation decreases with enhancement of the diffusive Reynolds number but increases with the enhancement of inverse couple stress parameter and inverse Darcy number. The increase in entropy generation is significantly influenced due to increment in friction produced by nanofluid particles during migration through the porous media. The shape of the entropy generation graph depends on couple stress parameter.

17. Bejan number Be decreases with a rise in the Deborah number De, the squeeze parameter S.

18. The Bejan number has an increasing trend with M.

19. Bejan number (Be) decreases gradually with the increase of the radiation parameter R.

20. Both E_{ST} and E_{SFF} increase with the enhancement of the nanoparticle size.

21. E_{SFF} is much higher in comparison to the E_{ST} within the squeeze channel.

22. The velocity decreases with the increase of the Deborah number De, the squeeze parameter S and the magnetic parameter M up to a certain height and then follows the opposite trend.

23. The temperature within the squeeze channel increases with the increase of the applied magnetic parameter M, the nanoparticle volume fraction ϕ while the reverse trend is seen for the radiation parameter R, the squeeze parameter S as well as the Deborah number De.

24. The coefficient of skin-friction coefficient C_f has an increasing trend with the Deborah number De, the nanoparticle volume fraction ϕ.

25. The Nusselt number (Nu) has an increasing trend with the increasing values in M as well as the nanoparticle volume fraction (ϕ) and decreases with increasing R, the Deborah number De.

26. The nanofluid velocity decreases with an enhancement of the Deborah number De, magnetic number M, injection parameter S and Navier's slip parameter γ.

27. The nanofluid temperature increases with enhancement of the Deborah number De, unsteadiness parameter λ, nanoparticle volume fraction ϕ, source/sink parameters A, B.

8.2 Future Scope

The future scope of the present study can be extended but not limited to the following points:

1. The study of electroosmotic nanofluid flow reveals that ion diffusion coefficient is an important parameter in determining heat generation in nano-channel, which is in agreement with experimental works of Kong et al., thereby opening the scope of further experimentation on the effects of ion diffusion coefficient on fluid flow profiles. Being motivated by these findings, I would like to pursue research in experimental fluid dynamics both in microchannel and open/closed bigger channels with low and high Reynolds number respectively.

2. The study on squeezing flow between parallel plates as well as fluid flow past over an unsteady stretching surface are assumed to be laminar, however this assumption can be improved further by allowing non-laminar turbulent flow phenomena thereby making the models more realistic. The stability analysis on this models is the topic that I am currently pursuing under the guidance of my supervisor.

3. The effects of both porosity of the medium and permeability of the channel walls have remained an integral topic of our study, moreover different slip conditions are used at surface-channel interface to analyze its effect on fluid flow profiles. However, the permeability is always assumed to arise in homogeneous manner, but in reality porous obstacles are random. A novel mathematical framework to address this issue is to introduce homogenization techniques, which is available in PDE related literature, into our models.

4. The availability of large source of data and machine learning based techniques on fluid flow in natural circumstances has empowered us to conduct data-driven machine learning motivated approaches to identify patterns in fluid flow, in which I have keen interest.

References

Abate, A.R., Hung, T., Mary, P., Agresti, J.J., and Weitz, D.A. (2010). High-throughput injection with microfluidics using picoinjectors. *PNAS*, 107, 19163. 3.1

Abu Talib, A.R. and Hilo, A.K. (2021). Fluid flow and heat transfer over corrugated backward facing step channel. *Case Studies in Thermal Engineering*, 24, 100862. 3.2.2

Acharya, N., Das, K., and Kundu, P. (2016). The squeezing flow of cu-water and cu-kerosene nanofluids between two parallel plates. *AEJ - Alexandria Engineering Journal*, 55, 1177–1186. 5.1, 5.5, 5.5, 6.1, 6.2, 6.5

Afshar, S., Mishra, S., Dogonchi, A.S., Karimi, N., Chamkha, A.J., and Abulkhair, H. (2021). Dissection of entropy production for the free convection of nepcms-filled porous wavy enclosure subject to volumetric heat source/sink. *Journal of the Taiwan Institute of Chemical Engineers*, 128, 98–113. 3.1

Akinshilo, A.T. (2018). Flow and heat transfer of nanofluid with injection through an expanding or contracting porous channel under magnetic force field. *Engineering Science and Technology, an International Journal*, 21(3), 486–494. 6.1

Akram, J., Akbar, N.S., and Tripathi, D. (2020a). Blood-based graphene oxide nanofluid flow through capillary in the presence of electromagnetic fields: A sutterby fluid model. *Microvascular Research*, 132, 104062. 2.1

Akram, J., Akbar, N.S., and Tripathi, D. (2020b). Numerical study of the electroosmotic flow of $al_2o_3 - ch_3oh$ sisko nanofluid through a tapered microchannel in a porous environment. *Applied Nanoscience*, 10, 4161–4176. 2.1

Alagumalai, A., Qin, C., K E K, V., Solomin, E., Yang, L., Zhang, P., Otanicar, T., Kasaeian, A., Chamkha, A.J., Rashidi, M.M., Wongwises, S., Ahn, H.S., Lei, Z., Saboori, T., and Mahian, O. (2022). Conceptual analysis framework development to understand barriers of nanofluid commercialization. *Nano Energy*, 92, 106736. 3.1

Angayarkanni, S. and Philip, J. (2015). Review on thermal properties of nanofluids: Recent developments. *Advances in Colloid and Interface Science*, 225, 146–176. 1.2.4.3, 5.1, 6.1, 7.1

Archibald, F. (1956). Load capacity and time relations for squeeze films. *Transactions of the American Society of Mechanical Engineers*, 78(1), 29–35. 6.1

Ariman, T. and Cakmak, A.S. (1967). Couple stresses in fluids. *Physics of Fluids*, 10, 2497–2499. 2.1

Bandopadhyay, A., Goswami, P., and Chakraborty, S. (2013). Regimes of streaming potential in cylindrical nano-pores in presence of finite sized ions and charge induced thickening: An analytical approach. *The Journal of Chemical Physics*, 139, 224503. 2.2.1, 3.2.3, 4.2.1

Beavers, G. and Joseph, D. (1967). Boundary conditions at a naturally permeable wall. *Journal of Fluid Mechanics*, 30, 197. 2.1, 2.2.3, 3.1, 3.2.1, 3.2.1, 3.2.2, 4.1

Bejan, A. (1979). Study of entropy generation in fundamental convective heat transfer. *Journal of Heat Transfer*, 101, 718. 2.1, 2.4.2, 3.3.2.2, 5.1, 6.1, 7.1, 7.3

Bejan, A. and Kestin, J. (1983). Entropy generation through heat and fluid flow. *Journal of Applied Mechanics*. 5.1, 6.1, 7.1, 7.3

Berman, A.S. (1953). Laminar flow in channels with porous walls. *Journal of Applied Physics*, 24, 1232. 2.1, 3.1, 4.1

Bhandari, D.S., Tripathi, D., and Narla, V.K. (2020). Pumping flow model for couple stress fluids with a propagative membrane contraction. *International Journal of Mechanical Sciences*, 188, 105949. 2.1

Bhatti, M.M., Abbas, T., Rashidi, M.M., Ali, M.E.S., and Yang, Z. (2016). Entropy generation on mhd eyring-powell nanofluid through a permeable stretching surface. *Entropy*, 18(6), 224. 5.1, 7.1

Bhatti, M.M. and Rashidi, M.M. (2016). Effects of thermo-diffusion and thermal radiation on williamson nanofluid over a porous shrinking/stretching sheet. *Journal of Molecular Liquids*, 221, 567–573. 6.1

Bitla, P. and Iyenger, T. (2014). Pulsating flow of an incompressible micropolar fluid between permeable beds with an inclined uniform magnetic field. *European Journal of Mechanics - B/Fluids.*, 48, 174. 2.1, 2.2.2, 3.1, 3.1, 3.2, 4.1, 4.2

Boland, C.S., Khan, U., Ryan, G., Barwich, S., Charifou, R., Harvey, A., Backes, C., Li, Z., Ferreira, M.S., Möbius, M.E., et al. (2016). Sensitive electromechanical sensors using viscoelastic graphene-polymer nanocomposites. *Science*, 354(6317), 1257–1260. 5.1, 7.1

Brinkman, H.C. (1952). The viscosity of concentrated suspensions and solutions. *The Journal of chemical physics*, 20(4), 571–571. 5.2, 6.2, 7.2

Buongiorno, J., Venerus, D.C., Prabhat, N., McKrell, T., Townsend, J., Christianson, R., Tolmachev, Y.V., Keblinski, P., Hu, L.w., Alvarado, J.L., Bang, I.C., Bishnoi, S.W., Bonetti, M., Botz, F., Cecere, A., Chang, Y., Chen, G., Chen, H., Chung, S.J., Chyu, M.K., Das, S.K., Di Paola, R., Ding, Y., Dubois, F., Dzido, G., Eapen, J., Escher, W., Funfschilling, D., Galand, Q., Gao, J., Gharagozloo, P.E., Goodson, K.E., Gutierrez, J.G., Hong, H., Horton, M., Hwang, K.S., Iorio, C.S., Jang, S.P., Jarzebski, A.B., Jiang, Y., Jin, L., Kabelac, S., Kamath, A., Kedzierski, M.A., Kieng, L.G., Kim, C., Kim, J.H., Kim, S., Lee, S.H., Leong, K.C., Manna, I., Michel, B., Ni, R., Patel, H.E., Philip, J., Poulikakos, D., Reynaud, C., Savino, R., Singh, P.K., Song, P., Sundararajan, T., Timofeeva, E., Tritcak, T., Turanov, A.N., Van Vaerenbergh, S., Wen, D., Witharana, S., Yang, C., Yeh, W.H., Zhao, X.Z., and Zhou, S.Q. (2009). A benchmark study on the thermal conductivity of nanofluids. *Journal of Applied Physics*, 106(9), 094312. 6.1

Chamkha, A.J., Dogonchi, A., and Ganji, D. (2018). Magnetohydrodynamic nanofluid natural convection in a cavity under thermal radiation and shape factor of nanoparticles impacts: A numerical study using cvfem. *Applied Sciences*, 8(12). 3.1

Chen, C.K. and Ho, S.H. (1999). Solving partial differential equations by two-dimensional differential transform method. *Applied Mathematics and computation*, 106(2-3), 171–179. 1.6.1, 2.1, 4.1, 5.1, 6.1

CHOI, S.U.S. (1995). *Developments and Applications of Non-Newtonian Flows*. ASME, New York. 2.1, 3.1, 4.1, 6.1

Choi, S.U. and Eastman, J.A. (1995). Enhancing thermal conductivity of fluids with nanoparticles. Technical report, Argonne National Lab.(ANL), Argonne, IL (United States). 1.2.4.3, 5.1, 7.1

Conway, B.E. (1991). Transition from supercapacitor to battery behavior in electrochemical energy storage. *Journal of The Electrochemical Society*, 138, 1539. 2.1, 3.1, 4.1

Cosserat, E. and Cosserat, F. (1909). *Theorie des Corps Deformables, Theory of Deformable Bodies*. A. Hermann et Fils, Paris. 2.1

Craven, T.J., Rees, J.M., and Zimmerman, W.B. (2008). On slip velocity boundary conditions for electroosmotic flow near sharp corners. *Physics of Fluids*, 20, 043603. 3.3.2.1

Dahler, J.S. and Scriven, L.E. (1963). Theory of structured continua i. general consideration of angular momentum and polarization. *Proceedings of the Royal Society of London. Series A. Mathematical and Physical Sciences*, 275, 504. 2.1

Das, S., Jana, R., and Makinde, O. (2015). Magnetohydrodynamic mixed convective slip flow over an inclined porous plate with viscous dissipation and joule heating. *Alexandria Engineering Journal*, 54, 251–261. 6.1

Dhivya, M., Loganathan, P., and Vajravelu, K. (2021). Chemically reacting viscous fluid flow on a permeable cylinder susceptible to oscillations. *International Communications of Heat Mass Transfer*, 126, 105477. 3.1

Dogonchi, A.S., Mishra, S., Chamkha, A.J., Ghodrat, M., Elmasry, Y., and Alhumade, H. (2021a). Thermal and entropy analyses on buoyancy-driven flow of nanofluid inside a porous enclosure with two square cylinders: Finite element method. *Case Studies in Thermal Engineering*, 27, 101298. 2.2.4, 3.1, 3.2.2

Dogonchi, A.S., Sadeghi, M., Ghodrat, M., Chamkha, A.J., Elmasry, Y., and Alsulami, R. (2021b). Natural convection and entropy generation of a nanoliquid in a crown wavy cavity: Effect of thermo-physical parameters and cavity shape. *Case Studies in Thermal Engineering*, 27, 101208. 3.1

Dogonchi, A., Alizadeh, M., and Ganji, D. (2017). Investigation of mhd go-water nanofluid flow and heat transfer in a porous channel in the presence of thermal radiation effect. *Advanced Powder Technology*, 28(7), 1815–1825. 6.1

Dogonchi, A., Seyyedi, S.M., Hashemi-Tilehnoee, M., Chamkha, A.J., and Ganji, D. (2019). Investigation of natural convection of magnetic nanofluid in an enclosure with a porous medium considering brownian motion. *Case Studies in Thermal Engineering*, 14, 100502. 3.1

Dutta, P. and Beskok, A. (2001). Analytical solution of combined electroosmotic pressure driven flows in two-dimensional straight channels: Finite debye layer effects. *Analytical Chemistry*, 73, 1979. 2.1, 3.1

Elshehawey, E., Elbarbary, E., Afifi, N., and El-Shahed, M. (2000). Pulsatile flow of blood through a porous medium under periodic body acceleration. *International Journal of Theoretical Physics*, 39, 183. 2.1, 4.1

Eshaghi, S., Izadpanah, F., Dogonchi, A.S., Chamkha, A.J., Ben Hamida, M.B., and Alhumade, H. (2021). The optimum double diffusive natural convection heat transfer in h-shaped cavity with a baffle inside and a corrugated wall. *Case Studies in Thermal Engineering*, 28, 101541. 2.2.4, 3.1, 3.2.2

Esmond, W. and Clark, H. (eds.) (1966). *Proceedings, Biomedical Fluid Mechanics Symposium, NewYork*. ASME, New York. 2.1, 4.1

Falade, J.A., Adesanya, S.O., Ukaegbu, J.C., and Osinowo, M.O. (2016). Entropy generation analysis for variable viscous couple stress fluid flow through a channel with non-uniform wall temperature. *Alexandria Engineering Journal*, 55, 69. 2.4.2

Hadjesfandiari, A.R., Hajesfandiari, A., and Dargush, G.F. (2015). Skew-symmetric couple-stress fluid mechanics. *Acta Mechanica*, 226, 871–895. 2.1

Hassan, I. (2008). Comparison deferential transformation technique with adomian decomposition method for linear and nonlinear initial value problems. *Chaos, Solitons & Fractals*, 36, 53–65. 5.1

Hayat, T., Muhammad, T., Shehzad, S., and Alsaedi, A. (2017). Three dimensional rotating flow of maxwell nanofluid. *Journal of Molecular Liquids*, 229, 495–500. 5.2

Herwig, H. (2018). How to teach heat transfer more systematically by involving entropy. *Entropy*, 20, 791. 2.1, 3.1, 7.1

Horiuchi, K. and Dutta, P. (2004). Joule heating effects in electroosmotically driven microchannel flows. *International Journal of Heat Mass Transfer*, 47, 3085. 3.1

Hussain, S.H. (2016). Analysis of heatlines and entropy generation during double-diffusive mhd natural convection within a tilted sinusoidal corrugated porous enclosure. *Engineering Science and Technology, an International Journal*, 19(2), 926–945. 6.1

Johnson, T.J. and Locascio, L. (2002). Characterization and optimization of slanted well designs for microfluidic mixing under electroosmotic flow. *Lab on a Chip*, 2, 135. 2.1, 3.1, 4.1

KAMINSKI, E. and JAUPART, C. (2003). Laminar starting plumes in high-prandtl-number fluids. *Journal of Fluid Mechanics*, 478, 287–298. 5.2, 5.5

Khan, M.R., Mao, S., Deebani, W., and Elsiddieg, A.M. (2022). Numerical analysis of heat transfer and friction drag relating to the effect of joule heating, viscous dissipation and heat generation/absorption in aligned mhd slip flow of a nanofluid. *International Communications in Heat and Mass Transfer*, 131, 105843. 3.1

Kong, J., Bo, Z., Yang, H., Yang, J., Shuai, X., Yan, J., and Cen, K. (2017). Temperature dependence of ion diffusion coefficients in nacl electrolyte confined within graphene nanochannels. *Physical Chemistry Chemical Physics*, 19, 7678. 2.1, 3.1, 4.1, 4.4

Kong, K., Mariatti, M., Rashid, A., and Busfield, J. (2014). Enhanced conductivity behavior of polydimethylsiloxane (pdms) hybrid composites containing exfoliated graphite nanoplatelets and carbon nanotubes. *Composites Part B: Engineering*, 58, 457–462. 5.5, 7.1

Krishna, M.V. (2020a). Hall and ion slip effects on mhd free convective rotating flow bounded by the semi-infinite vertical porous surface. *Heat Transfer*, 49, 1920–1938. 3.1

Krishna, M.V. (2020b). Hall and ion slip effects on mhd laminar flow of an elastico-viscous (walter's-b) fluid. *Heat Transfer*, 49, 2311–2329. 3.1

Krishna, M.V. and Chamkha, A.J. (2020). Hall and ion slip effects on mhd rotating flow of elastico-viscous fluid through porous medium. *International Communications in Heat and Mass Transfer*, 113, 104494. 3.1

Krishna, M.V., Sravanthi, C., and Gorla, R.S.R. (2020). Hall and ion slip effects on mhd rotating flow of ciliary propulsion of microscopic organism through porous media. *International Communications in Heat and Mass Transfer*, 112, 104500. 3.1

Liao, S.J. and Chwang, A. (1998). Application of homotopy analysis method in nonlinear oscillations. *Journal of Applied Mechanics*. 7.1, 7.4

Liao, S. (2010). An optimal homotopy-analysis approach for strongly nonlinear differential equations. *Communications in Nonlinear Science and Numerical Simulation*, 15(8), 2003–2016. 1.6.2, 7.1

Lin, I.K., Ou, K.S., Liao, Y.M., Liu, Y., Chen, K.S., and Zhang, X. (2009). Viscoelastic characterization and modeling of polymer transducers for biological applications. *Journal of Microelectromechanical systems*, 18(5), 1087–1099. 7.1

Loudon, C. and Tordesillas, A. (1998). The use of the dimensionless womersley number to characterize the unsteady nature of internal flow. *Journal o Theoretical Biology*, 191, 63–78. 4.4

Mahian, O., Kianifar, A., Kleinstreuer, C., Moh'd A, A.N., Pop, I., Sahin, A.Z., and Wongwises, S. (2013). A review of entropy generation in nanofluid flow. *International Journal of Heat and Mass Transfer*, 65, 514–532. 1.5.1.2, 5.1, 5.3, 6.1, 6.3, 7.1

Mahmood, M., Asghar, S., and Hossain, M. (2007). Squeezed flow and heat transfer over a porous surface for viscous fluid. *Heat and mass Transfer*, 44(2), 165–173. 6.1

Maiti, S., Shaw, S., and Shit, G. (2019). Caputo-fabrizio fractional order model on mhd blood flow with heat and mass transfer through a porous vessel in the presence of thermal radiation. *Physica A*. 2.1

Makinde, O.D. and Aziz, A. (2011). Boundary layer flow of a nanofluid past a stretching sheet with a convective boundary condition. *International Journal of Thermal Sciences*, 50(7), 1326–1332. 7.5.1, 7.3

Malathy, T. and Srinivas, S. (2008). Pulsating flow of a hydromagnetic fluid between permeable beds. *International Communications in Heat and Mass Transfer*, 35, 681. 2.1, 3.1, 3.1, 3.2, 4.1

Mark, J.E. (1999). *Polymer Data Handbook*. Oxford University Press. 5.2

MAXWELL, A. (1873). 'a treatise on electricity and magnetism vol. ii'. 5.2, 6.2, 7.2

Miller, J.R. and Simon, P. (2008). Materials science-electrochemical capacitors for energy management. *Science*, 321, 651. 2.1, 3.1, 4.1

Misra, J.C., Mallick, B., and Steinmann, P. (2020). Temperature distribution and entropy generation during darcy forchheimer brinkman electrokinetic flow in a microfluidic tube subject to a prescribed heat flux. *Meccanica*, 55, 1079. 3.1

Mkwizu, M.H. and Makinde, O.D. (2015). Entropy generation in a variable viscosity channel flow of nanofluids with convective cooling. *Comptes Rendus Mécanique*, 343(1), 38–56. 5.3, 6.1, 6.3

Morduchow, M. (1956). On laminar flow through a channel or tube with injection - application of methods of averages. *Physics of Fluids*, 14, 361. 2.1, 3.1, 4.1

Moshfegh, B. and Sandberg, M. (1996). Investigation of fluid flow and heat transfer in a vertical channel heated from one side by pv elements, part i - numerical study. *Renewable Energy*, 8(1), 248–253. 2.2.4, 3.2.2

Mukherjee, S. and Shit, G.C. (2022). Mathematical modeling of electrothermal couple stress nanofluid flow and entropy in a porous microchannel under injection process. *Applied Mathematics and Computation*, 426, 127110. 4.1, 4.4

Mustafa, M., Hayat, T., and Obaidat, S. (2012). On heat and mass transfer in the unsteady squeezing flow between parallel plates. *Meccanica*, 47(7), 1581–1589. 5.5, 5.5, 6.1, 6.5

Narla, V.K. and Tripathi, D. (2020). Entropy and exergy analysis on peristaltic pumping in a curved narrow channel. *Heat Transfer*, 49 (6), 3357–3373. 2.1

Narla, V.K., Tripathi, D., and Beg, O.A. (2020a). Analysis of entropy generation in biomimetic electroosmotic nanofluid pumping through a curved channel with joule dissipation. *Thermal Science and Engineering Progress*, 15, 100424. 2.1

Narla, V.K., Tripathi, D., and Beg, O.A. (2020b). Electro-osmotic nanofluid flow in a curved microchannel. *Chinese Journal of Physics*, 67, 544–558. 2.1

Nezhad, A. and Shahri, M. (2016). Entropy generation case studies of two-immiscible fluids under the influence of a uniform magnetic field in an inclind channel. *Journal of Mechanics*, 32(6), 749–757. 6.1

Nielsen, J.M., Adamson, A.W., and Cobble, J.W. (1952). The self-diffusion coefficients of the ions in aqueous sodium chloride and sodium sulfate at 25^o. *Journal of the American Chemical Society*, 74, 446. 2.1, 3.1, 4.1

Park, H.M. and Kim, T.W. (2009). Extension of the helmholtz-smoluchowski velocity to the hydrophobic microchannels with velocity slip. *Lab on a Chip*, 9, 291. 3.1

Pop, E., Varshney, V., and Roy, A.K. (2012). Thermal properties of graphene: Fundamentals and applications. *MRS bulletin*, 37(12), 1273–1281. 5.2

Potenza, M., Cataldo, A., Bovesecchi, G., Corasaniti, S., Coppa, P., and Bellucci, S. (2017). Graphene nanoplatelets: Thermal diffusivity and thermal conductivity by the flash method. *AIP Advances*, 7, 075214. 5.2

Pourmehran, O., Rahimi-Gorji, M., Gorji-Bandpy, M., and Ganji, D. (2015). Retracted: Analytical investigation of squeezing unsteady nanofluid flow between parallel plates by lsm and cm. *Alexandria Engineering Journal*, 54(1), 17–26. 5.5, 5.5, 6.5

Radhakrishnamacharya, G. and Maiti, M. (1977). Heat transfer to pulsatile flow in a porous channel. *International Journal of Heat and Mass Transfer*, 20, 171. 2.1, 3.1, 4.1

Rajagopal, K. and Tao, L. (1995). *Mechanics of mixtures*. World Scientific Publishing Co. 2.1, 3.1, 4.1

Ramesh, K., Reddy, M.G., and Souayeh, B. (2021). Electro-magneto-hydrodynamic flow of couple stress nanofluids in micro-peristaltic channel with slip and convective conditions. *Applied Mathematics and Mechanics*, 42, 593. 2.1

Ranjit, N.K. and Shit, G.C. (2017). Joule heating effects on electromagnetohydrodynamic flow through a peristaltically induced micro-channel with different zeta potential and wall slip. *Physica A*, 482, 458. 1.4.1, 1.4.1, 2.2.1, 2.2.1, 2.2.2, 3.2, 3.2.3, 3.2.3, 4.2.1, 4.2.1

Ranjit, N.K., Shit, G.C., and Tripathi, D. (2019). Entropy generation and joule heating of two layered electroosmotic flow in the peristaltically induced microchannel. *International Journal of Mechanical Sciences*, 430, 153. 2.1, 2.4.2, 3.3.2.1, 3.3.2.2, 4.1

Rashidi, M.M., Bhatti, M.M., Abbas, M.A., and Ali, M.E.S. (2016). Entropy generation on mhd blood flow of nanofluid due to peristaltic waves. *Entropy*, 18(4). 5.1

Rashidi, M.M., Shahmohamadi, H., and Dinarvand, S. (2008). Analytic approximate solutions for unsteady two-dimensional and axisymmetric squeezing flows between parallel plates. *Mathematical Problems in Engineering*, 2008. 6.1

Reddy Gorla, R.S. and Sidawi, I. (1994). Free convection on a vertical stretching surface with suction and blowing. *Applied Scientific Research*, 52(3), 247–257. 7.5.1, 7.3

Reynolds, O. (1886). On the theory of lubrication and its application to mr. beauchamp tower's experiments, including an experimental determination of the viscosity of olive oil. *Philosophical Transactions of the Royal Society of London*, 177, 234. 6.1

Roberts, C.C., Graham, A., Nemer, M., Phinney, L.M., Garcia, R.M., Soehnel, M.M., and Stirrup, E.K. (2017). Physical properties of low-molecular weight polydimethylsiloxane fluids. Technical report, Sandia National Lab.(SNL-NM), Albuquerque, NM (United States). 5.2, 5.5, 7.1

Sadeghi, M.S., Dogonchi, A., Ghodrat, M., Chamkha, A.J., Alhumade, H., and Karimi, N. (2021). Natural convection of cuo-water nanofluid in a conventional oil/water separator cavity: Application to combined-cycle power plants. *Journal of the Taiwan Institute of Chemical Engineers*, 124, 307–319. 3.1

Saharudin, K., Karim, M., and Sreekantan, S. (2019). Preparation of a polydimethylsiloxane (pdms)/graphene-based super-hydrophobic coating. *Materials Today: Proceedings*, 17, 752–760. 7.1

Sato, H., Yui, M., and Yoshikawa, H. (2012). Ionic diffusion coefficients of cs+, pb2+, sm3+, ni2+, seo_4^{2-} and tco_4^- in free water determined from conductivity measurements. *Journal of Nuclear Science and Technology*, 33, 950. 2.1, 3.1, 4.1

Sellars, J.R. (1955). Laminar flow in channels with porous walls at high suction reynolds numbers. *Journal of Applied Physics*, 26, 489. 2.1, 3.1, 4.1

Selvaganapathy, P., Ki, Y.S.L., Renaud, P., and Mastrangelo, C.H. (2002). Bubble-free electrokinetic pumping. *Journal of Microelectromechanical Systems*, 11, 448. 2.1, 3.1, 4.1

Selvam, C., Mohan Lal, D., and Harish, S. (2017). Thermal conductivity and specific heat capacity of water–ethylene glycol mixture-based nanofluids with graphene nanoplatelets. *Journal of Thermal Analysis and Calorimetry*, 129(2), 947–955. 7.1

Sengupta, A. and Ghoshdastidar, P.A. (2018). Heat transfer enhancement in ferrofluids flow in micro and macro parallel plate channels: A comparative numerical study. *Journal of Thermal Science and Engineering Applications*, 021012. 6.1

Seth, G.S., Bhattacharya, A., Kumar, R., and Chamkha, A.J. (2018). Entropy generation in hydromagnetic nanofluid flow over a non-linear stretching sheet with navier's velocity slip and convective heat transfer. *Physics of Fluids*, 30, 122003. 2.2.2, 2.2.3, 2.4.2, 3.2, 3.2.1, 4.2, 7.1, 7.2, 7.3, 7.4, 7.5.1, 7.3

Shaw, S., Sibanda, P., Sutradhar, A., and Murthy, P. (2014). Magnetohydrodynamics and soret effects on bioconvection in a porous medium saturated with a nanofluid containing gyrotactic microorganisms. *International Journal of Heat and Mass Transfer*, 136 (5), 052601. 2.1

Sheikholeslami, M., Ashorynejad, H., Barari, A., and Soleimani, S. (2013a). Investigation of heat and mass transfer of rotating mhd viscous flow between a stretching sheet and a porous surface. *Engineering Computations*, 30. 6.1

Sheikholeslami, M. and domiri ganji, D. (2013). Heat transfer of cu-water nanofluid flow between parallel plates. *Powder Technology*, 235, 873–879. 5.2

Sheikholeslami, M., domiri ganji, D., and Ashorynejad, H. (2013b). Investigation of squeezing unsteady nanofluid flow using adm. *Powder Technology*, 239, 259–265. 5.2

Sheikholeslami, M. and Ganji, D.D. (2015). Nanofluid flow and heat transfer between parallel plates considering brownian motion using dtm. *Computer Methods in Applied Mechanics and Engineering*, 283, 651–663. 6.1

Shit, G.C. and Mukherjee, S. (2019). Mhd graphene-polydimethylsiloxane maxwell nanofluid flow in a squeezing channel with thermal radiation effects. *Applied Mathematics and Mechanics*, 40, 1269. 3.3.1, 3.7, 7.5

Shojaeian, M. and Shojaeian, M. (2011). Analytical solution of mixed electromagnetic/pressure driven gaseous flows in microchannels. *Microfluidics and Nanofluidics*, 12. 6.1

Siddabasappa, C., Siddheshwar, P.G., and Makinde, O.D. (2021). A study on entropy generation and heat transfer in a magnetohydrodynamic flow of a couple stress fluid through a thermal nonequilibrium vertical porous channel. *Heat Transfer*, 50, 6377. 2.1

Siva, T., Kumbhakar, B., Jangili, S., and Mondal, P.K. (2020). Unsteady electroosmotic flow of couple stress fluid in a rotating microchannel: An analytical solution. *Physics of Fluids*, 32, 102013. 2.1, 2.2.2

Stefan, M. (1874). Akademie der wissenschaften in wien. *Mathematisch-Naturwissenschaftliche Klasse*, 69, 713. 6.1

Stokes, V.K. (1966). Couple stresses in fluid. *Physics of Fluids*, 9 (9), 1709–1715. 2.1

Subramaniam, C.G. and Mondal, P.K. (2020). Effect of couple stresses on the rheology and dynamics of linear maxwell viscoelastic fluids. *Physics of Fluids*, 32, 013108. 2.1

Tayebi, T. and Chamkha, A. (2020). Magnetohydrodynamic natural convection heat transfer of hybrid nanofluid in a square enclosure in the presence of a wavy circular conductive cylinder. *Journal of Thermal Science and Engineering Applications*, 12, 031009. 3.1

Tayebi, T., Sattar Dogonchi, A., Karimi, N., Ge-JiLe, H., Chamkha, A.J., and Elmasry, Y. (2021). Thermo-economic and entropy generation analyses of magnetic natural convective flow in a nanofluid-filled annular enclosure fitted with fins. *Sustainable Energy Technologies and Assessments*, 46, 101274. 3.1

Ting, T.W., Hung, Y.M., and Guo, N. (2015). Entropy generation of viscous dissipative nanofluid flow in thermal non-equilibrium porous media embedded in microchannels. *International Journal of Heat and Mass Transfer*, 81, 862–877. 6.1

Toupin, R.A. (1962). Elastic materials with couple-stresses. *Archive for Rational Mechanics and Analysis*, 11, 385. 2.1

Tripathi, D., Ashu, Y., and Beg, A. (2017). Electroosmotic flow of couple stress fluids in a micro-channel propagated by peristalsis. *European Physical Journal Plus*, 132, 173. 2.1

Tripathi, D., Prakash, J., Reddy, M.G., and Kumar, R. (2021). Numerical study of electroosmosis-induced alterations in peristaltic pumping of couple stress hybrid nanofluids through microchannel. *Indian Journal of Physics*, 95, 2411. 2.1

Turan, O. and Cuhadaroglu, B. (2020). The effects of uniform injection and suction on heat transfer with viscous dissipation through a permeable surface in zero pressure gradient. *International Communications in Heat and Mass Transfer*, 119, 104972. 3.1

Vajravelu, K., K. Ramesh, S.S., and Arunachalam, P.V. (2003). Pulsatile fow between permeable beds. *International Journal of Non Linear Mechanics*, 38, 999. 2.1, 3.1, 3.1, 3.2, 3.2.2, 4.1

Veera Krishna, M. (2020). Hall and ion slip impacts on unsteady mhd free convective rotating flow of jeffreys fluid with ramped wall temperature. *International Communications in Heat and Mass Transfer*, 119, 104927. 3.1

Veera Krishna, M., Ameer Ahamad, N., and Aljohani, A. (2021a). Thermal radiation, chemical reaction, hall and ion slip effects on mhd oscillatory rotating flow of micropolar liquid. *Alexandria Engineering Journal*, 60(3), 3467–3484. 3.1

Veera Krishna, M., Ameer Ahamad, N., and Chamkha, A.J. (2021b). Hall and ion slip impacts on unsteady mhd convective rotating flow of heat generating/absorbing second grade fluid. *Alexandria Engineering Journal*, 60(1), 845–858. 3.1

Veera Krishna, M. and Chamkha, A. (2018). Hall effects on unsteady mhd flow of second grade fluid through porous medium with ramped wall temperature and ramped surface concentration. *Physics of Fluids*, 30, 053101. 3.1

Veera Krishna, M. and Chamkha, A.J. (2019). Hall and ion slip effects on mhd rotating boundary layer flow of nanofluid past an infinite vertical plate embedded in a porous medium. *Results in Physics*, 15, 102652. 3.1

Veera Krishna, M., Subba Reddy, G., and Chamkha, A. (2018). Hall effects on unsteady mhd oscillatory free convective flow of second grade fluid through porous medium between two vertical plates. *Physics of Fluids*, 30, 023106. 3.1

Wang, Y.C., Choi, M., and Han, J. (2004). Two-dimensional protein separation with advanced sample and buffer isolation using microfluidic valves. *Analytical Chemitry*, 76, 4426. 2.1, 3.1, 4.1

Wang, Y. (1971). Pulsatile flow in a porous channel. *Journal of Applied Mechanics*, 38, 553. 2.1, 3.1, 4.1

Wang, Z., Gao, W., Zhang, Q., Zheng, K., Xu, J., Xu, W., Shang, E., Jiang, J., Zhang, J., and Liu, Y. (2018). 3d-printed graphene/polydimethylsiloxane composites for stretchable and strain-insensitive temperature sensors. *ACS Applied Materials & Interfaces*, 11(1), 1344–1352. 7.1

Wen-bin, H., Yong, X., Guo-ping, L., and Hong-yan, L. (2002). Squeeze flow of a power-law fluid between two rigid spheres with wall slip. *Applied Mathematics and Mechanics*, 23(7), 811–818. 6.1

Yang, P., Jiang, T., Zhang, Y., and Li, Z. (2018). Effect of osmotic pressure on migration behavior of nzno in gcls. *Geomaterials in Geotechnical Engineering*, 2019. 3.3.2.1

Yaqing, L. and Guo, B. (2016). Coupling model for unsteady mhd flow of generalized maxwell fluid with radiation thermal transform. *Applied Mathematics and Mechanics*, 37, 137–150. 5.1

Yuan, S.W. (1956). Further investigation in laminar flow in channels with porous walls. *Journal of Applied Physics*, 27, 267. 2.1, 4.1

Zhang, X.M., Yang, X.L., and Wang, K.Y. (2008). Conductive graphene/polydimethylsiloxane nanocomposites for flexible strain sensors. *Physics of Fluids*, 20, 043603. 7.1

Zhao, C., Fu, J., Oztekin, A., and Cheng, X. (2014). Measuring the soret coefficient of nanoparticles in a dilute suspension. *International Journal of Mechanical Sciences*, 430, 153. 2.1, 3.3.2, 3.3.2.1, 4.1

Zheng, L., Liu, N., and Zhang, X. (2013). Maxwell fluids unsteady mixed flow and radiation heat transfer over a stretching permeable plate with boundary slip and nonuniform heat source/sink. *Journal of Heat Transfer*, 135(3). 7.1, 7.2, 7.2, 7.2

Zheng, Q. and Wei, G.W. (2011). Poisson-boltzmann–nernst-planck model. *The Journal of Chemical Physics*, 134, 194101. 2.1

Zhong, E.C. and Friedman, H.L. (1988). Self-diffusion and distinct diffusion of ions in solution. *The Journal of Physical Chemistry*, 6, 1685. 2.1, 3.1, 4.1

Zhou, J. (1986). Differential transformation and its applications for electrical circuits. 1.6.1, 2.1, 2.3.1, 3.3.1, 4.1, 5.1, 5.4, 6.1, 6.4

List of Publications

1. **S. Mukherjee**, G. C. Shit, Mathematical modeling of electrothermal couple stress nanofluid flow and entropy in a porous microchannel under injection process, ***Applied Mathematics and Computation (SCI)***, *Elsevier*, ***Impact Factor 4.397***, ***426 (2022) 127110***.

2. G. C. Shit, **S. Mukherjee**, MHD graphene-polydimethylsiloxane Maxwell nanofluid flow in a squeezing channel with thermal radiation effects, ***Applied Mathematics and Mechanics (SCIE)***, *Springer*, ***Impact Factor 3.918***, ***40 (2019) 1269–1284***.

3. G. C. Shit, **S. Mukherjee**, Differential Transform Method for Unsteady Magnetohydrodynamic Nanofluid Flow in the Presence of Thermal Radiation, ***Journal of nanofluids (Web of Science)***, *American Scientific Publishers*, ***8 (2019) 998–1009.***

4. **S. Mukherjee**, G. C. Shit, K. Vajravelu, Entropy Generation of Electrothermal Nanofluid Flow Between Two Permeable Walls Under Injection Process, ***Journal of nanofluids (Web of Science)***, *American Scientific Publishers*, ***11 (2022) 714-727***.

5. **S. Mukherjee**, G. C. Shit, K. Vajravelu, Mathematical modelling of Graphene-PDMS Maxwell nanofluid flow over a stretching surface: A study on the efficient energy management, ***Communicated to ZAMM - Zeitschrift für Angewandte Mathematik und Mechanik*** **(2022)**.

6. **S. Mukherjee**, G. C. Shit, Effects of diffusive Reynolds number on electroosmotic pulsating nanofluid flow, ***Communicated to Physics of Fluids*** **(2022)**.

Satwik Mukherjee
15/09/2022